Durham E-Theses

Magnetic trapping of an ultracold (^87)Rb -(^133)Cs atomic mixture

Tierney, Patrick

Magnetic Trapping of an Ultracold ^{87}Rb -^{133}Cs Atomic Mixture

Patrick Tierney

A thesis submitted in partial fulfilment
of the requirements for the degree of
Doctor of Philosophy

Durham
University

Department of Physics
Durham University

July 14, 2009

2 7 JUL 2009

Magnetic Trapping of an Ultracold ^{87}Rb -^{133}Cs Atomic Mixture

Patrick Tierney

Abstract

This thesis reports on the realisation and characterisation of a magnetically trapped ultracold atomic mixture of ^{87}Rb and ^{133}Cs in the $F = 1$, $m_F = -1$ and $F = 3$, $m_F = -3$ hyperfine states respectively.

A compact two-species double magneto-optical trapping (MOT) apparatus is constructed in which a pyramid MOT acts to provide an independent flux of both atomic species for capture in the ultra-high vacuum science region of the apparatus. For the two-species science MOT in which this atom flux is captured, interspecies light assisted inelastic collisions are found to be a highly significant loss mechanism. A novel optical pressure spatial displacement technique is developed to minimise such losses, allowing near independent simultaneous loading of up to $\simeq 8 \times 10^8$ ^{87}Rb and $\simeq 3 \times 10^8$ ^{133}Cs atoms into an Ioffe-Pritchard 'baseball' magnetic trap at magnetic bias fields of 166.70(6) and 165.50(6) G respectively.

At the loaded ^{87}Rb and ^{133}Cs atom number densities of 1.78(6) $\times$ 10^9 and 2.53(6) $\times$ 10^9 cm^{-3} respectively the magnetic trap lifetime of each atomic species is shown to be 100(10) s and independent of the presence of the second atomic species. Radio-frequency evaporative cooling trajectories for ^{87}Rb and ^{133}Cs of 129 s duration are separately optimised under single species magnetic trap operation to achieve phase-space densities of 6(1) $\times$ 10^{-7} and 3(1) $\times$ 10^{-4} respectively at temperatures of 7.6(1) μK and 520(10) nK.

^{133}Cs Feshbach resonances at 118.06(8) and 133.4(1) G are characterised through the measurement of magnetic field dependent losses at the increased phase-space density. Implementation of simultaneous evaporative cooling following the single species trajectories is found to be ineffective below $\simeq$ 10 μK due to the increased thermal load imposed upon the ^{133}Cs atoms as the ^{87}Rb single species elastic collision cross section approaches the low energy limit. Following simultaneous evaporation to $\simeq$ 15 μ K thermalisation of the mixtures axial and radial temperature components suggests a ^{87}Rb-^{133}Cs interspecies elastic collision rate 3(1) and 7(1) times greater than the calculated single species ^{133}Cs and ^{87}Rb elastic collision rates respectively.

An interspecies Feshbach resonance search is undertaken by measuring the number of atoms of each species remaining in the magnetic trap as a function

of applied magnetic field following simultaneous evaporation. The absence of magnetic field dependent losses in conjunction with analysis of the measurement sensitivity demonstrates that no interspecies Feshbach resonances wider than 1 G with two-body inelastic collision rate constants greater than 5×10^{-10} cm^3 s^{-1} are present over the magnetic field range $166 < B < 370$ G in the trapped states. The sensitivity of this measurement is found to be highly dependent upon the magnetic field induced differential gravitational sag of the mixtures components.

Declaration

I confirm that no part of the material offered has previously been submitted by myself for a degree in this or any other University. Where material has been generated through joint work, the work of others has been indicated.

Patrick Tierney
Durham, July 14, 2009

For Mum, Dad, and Lizzie.
You have shown me more love
than I could ever repay.

Acknowledgements

Contents

Chapter 1

Introduction

The phenomenon of Bose-Einstein condensation, first predicted in 1924 [1, 2] was observed over 70 years later in dilute vapors of ^{87}Rb, ^{7}Li and ^{23}Na alkali atoms [3–5] through the combined application of laser-cooling [6–8] and forced evaporative cooling techniques [9, 10]. This new state of matter, analogous to superfluid liquid helium, provided a macroscopic window through which exotic quantum behavior could be investigated. Initial work to probe these novel quantum systems was accompanied by an expansion in the number of elements and isotopes successfully condensed. The ability to magnetically tune atomic scattering lengths via Feshbach resonances [11] provided unprecedented control of atomic interactions, allowing the production of stable condensates of ^{85}Rb [12] and efficient condensation of ^{133}Cs [13]. Whilst the range of disciplines in which atomic condensates were breaking new ground broadened into areas including investigation of solitary waves [14], matter wave interferometry [15] and molecular spectroscopy [16], the potential rewards offered by the emerging field of atomic mixtures also became apparent. Many experiments with mixtures utilised a 'buffer gas' species to sympathetically cool a second species with less favorable prospects for direct evaporation [17, 18]. This technique proved essential to the realisation of quantum degeneracy in Fermionic ensembles [19, 20], from which the first molecular Bose-Einstein condensates were engineered [21, 22]. Mixtures with tunable interactions have been utilised to investigate phase separation and interpenetration of superfluids [23] and crucially to create ultracold heteronuclear molecules in ro-vibrationally excited states [24].

The transfer into ro-vibrational ground states of $^7\mathrm{Li}^{133}\mathrm{Cs}$ molecules [25] through photoassociation and $^{40}\mathrm{K}^{87}\mathrm{Rb}$ [26] molecules using the two photon stimulated Raman adiabatic passage (STIRAP) technique [27] in 2008 heralded a new dawn in quantum physics, the era of strongly interacting dipolar gases. Bringing Bosonic dipolar molecules to quantum degeneracy is eagerly anticipated to revolutionise the fields of precision measurement [28–30], ultracold chemistry [31], and quantum information processing [32]. Access to this rich seam of quantum physics is the motivation behind the long term goal of this project: The realisation of a dipolar molecular Bose-Einstein condensate. This chapter describes the nature of Bose-Einstein condensation before discussing the additional physics afforded by quantum degenerate mixtures and the proposed route to create molecular condensates from such systems. Attention is then focussed upon the scope of the work carried out by myself towards this goal, encompassing an overview of this document.

1.1 Bose-Einstein Condensation

A Bose-Einstein Condensate is a state of matter in which a large fraction of an ensemble of identical atomic or molecular species occupies the lowest energy quantum state. The indistinguishable nature of the constituent components results in the ensemble displaying collective quantum behavior on a macroscopic scale.

1.1.1 What is a Bose-Einstein Condensate?

For an ideal (noninteracting) gas of Bosons at thermodynamic equilibrium, the mean number of particles occupying a state i with energy ϵ_i as a function of temperature T is given by the Bose distribution [33]:

$$n_i = \frac{1}{e^{(\epsilon_i - \mu)/k_B T} - 1} \quad , \tag{1.1}$$

where k_B is the Boltzmann constant and μ is the chemical potential (the energy required to add a particle to the system). As the temperature is reduced, there is a corresponding reduction in the mean occupation number of each excited state. When the mean occupation numbers are reduced to the

extent that the total density of particles is no longer accommodated within the excited states alone, particles begin to accumulate in the ground state. The particles condensed into the lowest energy quantum state constitute a Bose-Einstein condensate, whilst the excited state population retains a thermal distribution. One parameter with which the onset of Bose-Einstein condensation may be quantified is the phase-space density (PSD):

$$\text{PSD} = n\lambda_{\text{dB}}{}^3 \quad , \tag{1.2}$$

where n is the particle number density of the ensemble and λ_{dB} the particles thermal de Broglie wavelength, which is:

$$\lambda_{\text{dB}} = \sqrt{\frac{h^2}{2\pi m k_{\text{B}} T}} \quad , \tag{1.3}$$

for particles of mass m in an ensemble at temperature T. Planck's constant is denoted h. In the case of a uniform ideal Bose gas confined in three dimensions, the phase transition to a Bose-Einstein condensate occurs when the phase space density exceeds $\simeq 2.612$ [34].

1.1.2 Interactions in a BEC

As the particles within a BEC are indistinguishable the condensate may be described by a single wave function $\psi(\mathbf{r})$ normalised to the total particle number. To first order collisions between weakly interacting particles within the condensate are included in the time independent Schrödinger equation using a 'mean field' treatment, from which the Gross-Pitaevskii equation (GPE) is obtained [35]:

$$\left[-\frac{\hbar^2}{2m}\nabla^2 + V(\mathbf{r}) + g\left|\psi(\mathbf{r})\right|^2 \right] \psi(\mathbf{r}) = \mu\psi(\mathbf{r}) \quad , \tag{1.4}$$

where m is the particle mass, μ the chemical potential and $\hbar$ the reduced Planck's constant. Here the first two terms account for the wave function's kinetic energy and the influence of an external potential (*e.g.* the presence of a harmonic trap) respectively. Interactions between the particles are accounted for by the nonlinear $g\left|\psi(\mathbf{r})\right|^2$ term, where:

$$g = \frac{4\pi\hbar^2 a}{m} \quad , \tag{1.5}$$

is the energy of the condensate due to interactions between its constituent particles. Both the magnitude and sign of this interaction term are determined by the value of a, the scattering length (see section 2.3.1), the magnitude of which characterises the length scale over which particles interact, whilst the sign determines the nature of the interaction: for $a < 1$ collisions are attractive, limiting the atom number for which the condensate is stable against collapse, for $a > 1$ collisions are repulsive, and there is no corresponding limit. This influence of the scattering length upon the collective behavior of a condensate makes tunability of the scattering length a highly desirable feature within an ultracold system: Varying the magnetic field applied to a ^{133}Cs BEC for example, allows the scattering length to be tuned from $-\infty$ to $+\infty$ via a Feshbach resonance (section 2.4). This feature has been utilised to optimise the production of ^{133}Cs condensates [36] and enabled the creation of ^{133}Cs$_2$ molecules [37].

1.1.3 Realisation of Bose-Einstein Condensation

As there is a wealth of excellent literature detailing the experimental techniques with which BECs are created, I shall present only a brief overview of the generalised route to atomic Bose-Einstein condensation in the alkali metals, referring the reader to already published works which best encompass the wider material.

Laser Cooling

The phase-space density at which the phase transition to BEC occurs of PSD$\simeq 2.612$ is most readily approached through reducing the temperature of an atomic ensemble. In order to effect significant cooling it is essential to isolate the atoms being cooled from all thermal sources. For this reason all atom cooling experiments take place within a vacuum system. Predominantly the alkali atoms to be cooled are placed in the vacuum chamber upon construction in either elemental form or in the form of a salt contained within alkali-metal dispensers. In both cases release of atoms is instigated upon heating, in an oven or through dissipation of electrical power respectively. Atoms from the low energy tail of this 'thermal' distribution are then

subjected to laser cooling [38, 39] in, for example, a Zeeman slower, two dimensional Magneto-Optical trap (MOT) [40], pyramid MOT [41], conventional MOT [42] *etc.*, before being transferred into a second 'science' region of the vacuum apparatus in which the pressure is significantly lower. This transfer is commonly effected through optical pressure or the application of inhomogeneous magnetic fields [42, 43].

Once in the 'science' region the parameters of the MOT can be transiently altered in order to increase the ensemble density [44, 45] before implementing polarisation gradient cooling in a transient 'optical molasses' phase [46]. The maximum phase-space density achievable in such a dissipative trap is limited to $\simeq 10^{-5}$ [34], hence it is essential to transfer atoms into a conservative trap to achieve the required PSD for condensation to occur.

Conservative Trapping

Conservative trapping necessitates the realisation of a localised region of space for which an atoms potential energy is a minimum. This may be provided by the local minimum of an inhomogeneous magnetic field or local maximum (or minimum) laser beam intensity, or a hybrid of the two. Magnetic trapping relies upon the interaction between the applied magnetic field and the atoms permanent magnetic dipole moment. As it is not possible to create a local maximum magnetic field in all three dimensions [47], trapping is limited to atoms with positive magnetic dipole moments, the so-called 'weak field seeking' states. Optical trapping [48], relying instead upon the interaction between the laser beam's oscillating electric field and the laser-induced electric dipole moment of the atom, is not subject to such a constraint.

To achieve condensation it is essential to polarize atoms into a single magnetic sub-level of a ground state (thus reducing losses and heating due to inelastic fine-structure and hyperfine structure changing collisions). This is commonly achieved through making the desired sub-level a 'dark state' into which atoms are optically pumped using a combination of polarised laser beams and a magnetic quantisation field.

Evaporative Cooling

Further increases in the phase-space density are achieved through implementation of forced evaporative cooling. 'Hot' atoms, *i.e.* those with above average potential energy, are preferentially removed from magnetic traps by inducing radio-frequency (RF) or microwave transitions into non-trapped states. In optical traps preferential removal of 'hot' atoms is conventionally achieved through reducing the intensity of the trapping laser beams.

As the phase-space density varies with atom number N and temperature T as N/T^3, the loss of atoms resulting from evaporation may be more than compensated for by the corresponding reduction in temperature. The efficiency of evaporation depends upon the ratio of 'good' thermalising elastic collisions and 'bad' inelastic collisions which result in heating. Elastic collision rates may be increased by increasing the trapping frequencies through modification of trap geometry *e.g.* reducing the bias field of a magnetic trap, or adding a 'dimple' laser beam to an optical trap, whilst 'tuning' the scattering length via a magnetic or optical Feshbach resonance greatly affects the rate of both types of collision.

There is much parameter space to explore in order to optimise both laser cooling and forced evaporative cooling schemes, and for some atomic species it is necessary to add additional steps in the cooling process described here (*e.g.* implementing a dark spot MOT, Raman sideband cooling *etc.*) to reach the requisite 2.612 PSD. The route to Bose-Einstein condensation described here may be recognised in virtually all successful schemes for condensing Bosonic alkali atoms in single species traps. Condensation of the Fermionic alkalis, non-alkali atoms, mixtures of atomic species and molecules is considerably more complex.

1.2 Ultracold Mixtures

Mixtures of ultracold atomic gases provide access to a wealth of physics beyond that offered by single species systems. Initial work with mixtures focussed on utilising an 'easily' condensed atomic species, ^{87}Rb for example, as a refrigerant for a Fermionic (or Bosonic) species less suited to direct

evaporation, a process described as 'sympathetic cooling'. Bose-Einstein condensation of ^{41}K was first achieved in this manner through evaporation of ^{87}Rb 'buffer gas' atoms [18].

1.2.1 Fermi Degeneracy

At ultracold temperatures in the absence of a second component (a different atomic species, or the same species in a different spin-state) the Pauli exclusion principle renders direct evaporative cooling of spin polarised Fermionic species totally ineffective. A variation of sympathetic cooling in which two spin states of ^{40}K were simultaneously evaporatively cooled in a single trap through mutual mediation of interatomic collisions proved instrumental in achieving Fermi degeneracy for the first time [19].

1.2.2 Mixture Dynamics

Ultracold mixtures provide a medium in which the interactions of two-component superfluids can be observed, and in the case of tunable interactions controlled [23]. The simultaneous presence of quantum degenerate ensembles of two atomic species (or one atomic species in two distinct states) results in an additional interaction term entering the Gross-Pitaevskii equation for each species in a 'mean field' treatment. The combined system is approximated by a pair of coupled GPE equations [49]:

$$\left[-\frac{\hbar^2}{2m_1} \nabla^2 + V_1\left(\mathbf{r}\right) + g_{11}\left|\psi_1\left(\mathbf{r}\right)\right|^2 + g_{12}\left|\psi_2\left(\mathbf{r}\right)\right|^2 \right] \psi_1\left(\mathbf{r}\right) = \mu_1\psi_1\left(\mathbf{r}\right) \quad , \quad (1.6)$$

$$\left[-\frac{\hbar^2}{2m_2} \nabla^2 + V_2\left(\mathbf{r}\right) + g_{21}\left|\psi_1\left(\mathbf{r}\right)\right|^2 + g_{22}\left|\psi_2\left(\mathbf{r}\right)\right|^2 \right] \psi_2\left(\mathbf{r}\right) = \mu_2\psi_2\left(\mathbf{r}\right) \quad , \quad (1.7)$$

where m_1 (m_2) and μ_1 (μ_2), are the particle mass and chemical potential of species 1 (2) with wavefunction $\psi_1\left(\mathbf{r}\right)$ $(\psi_2\left(\mathbf{r}\right))$. The first two terms of each equation account for the corresponding wave function's kinetic energy and the influence of an external potential respectively. Interactions between degenerate particles are accounted for by the interaction terms $g_{11}\left|\psi_1\left(\mathbf{r}\right)\right|^2$ and $g_{22}\left|\psi_2\left(\mathbf{r}\right)\right|^2$ respectively whilst interactions between the two components of the mixture are encompassed in the $g_{12}\left|\psi_2\left(\mathbf{r}\right)\right|^2$ and $g_{21}\left|\psi_1\left(\mathbf{r}\right)\right|^2$ terms

where:

$$g_{11} = \frac{4\pi\hbar^2 a_{11}}{m_1} \ , \quad g_{22} = \frac{4\pi\hbar^2 a_{22}}{m_2} \quad \text{and} \tag{1.8}$$

$$g_{12} = g_{21} = 2\pi\hbar^2 a_{12} \left(\frac{m_1 + m_2}{m_1 m_2} \right) \quad , \tag{1.9}$$

for the single species scattering lengths a_{11} and a_{22}, and the interspecies scattering length a_{12} respectively. The relative strength of single species and interspecies interactions can be characterised by the ratio:

$$\Delta = \frac{g_{12}}{\sqrt{g_{11}g_{22}}} = \frac{a_{12}}{\sqrt{a_{11}a_{22}}} \sqrt{\frac{(m_1 + m_2)^2}{4m_1 m_2}} \simeq \frac{a_{12}}{\sqrt{a_{11}a_{22}}} \quad , \tag{1.10}$$

to reveal three distinct regimes of the dual BEC topology [49], as shown in figure 1.1: unstable miscible condensates with attractive interactions, stable interpenetrating superfluids [50], and phase separation of stable condensates.

The ability to control the value of the interspecies scattering length, or either of the single species scattering lengths, allows the relative strength of interactions and hence the miscibility of the mixture to be tuned across these three regimes. This has been demonstrated in a ^{85}Rb-^{87}Rb mixture through control of the ^{85}Rb scattering length via a ^{85}Rb Feshbach resonance [23]. Although
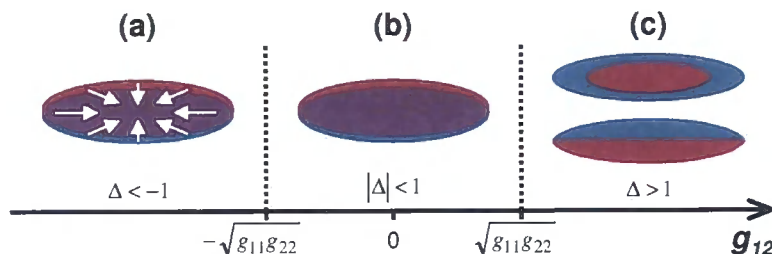
Figure 1.1: Miscibility characteristics of two interacting Bose-Einstein condensates as a function of the interaction parameter $\Delta = g_{12}/\sqrt{g_{11}g_{22}}$ (see text). For large negative values of Δ (a) the dominant attractive interspecies interactions make the two components miscible but lead to simultaneous collapse of both condensates. For large positive values of Δ (c) the dominant repulsive interspecies interactions lead to phase separation of the two condensates, with no appreciable overlap. When single species interactions are dominant (b) the two condensates are miscible and stable (neglecting the relative sag of the two components within the trapping potential).

there is much value in investigating the properties of ultracold mixtures with tunable interactions, the key motivation for utilising such an atomic mixture in this work is the prospect of creating ultracold molecules from the mixtures components.

1.3 Ultracold Molecules

The attainment of molecular Bose-Einstein condensates is presently being approached from many different angles by research groups from around the globe. The approaches taken can broadly be categorised into two areas: making thermal molecules ultracold, and combining ultracold atoms to make molecules.

1.3.1 Direct Cooling

Directly cooling molecules is by no means trivial, as the added complexities of vibrational and rotational structure preclude the implementation of laser cooling [51]. Current methods of direct cooling include cryogenic buffer gas cooling, Stark deceleration of supersonic molecular beams, and collisional cooling in crossed molecular beams [52]. These techniques can be applied to a wide variety of dipolar molecules, and promise direct access to molecules such as YbF for which there is already an experimental demand [53]. The temperatures presently realisable via these schemes of 1-1000 mK however, are orders of magnitude greater than the sub μK temperatures routinely obtained in ensembles of ultracold alkali atoms.

1.3.2 Association of Cold Atoms

A number of techniques have been developed to produce molecules in electronic ground states from ultracold atomic ensembles [24]. All of these techniques are limited to donor atomic species which can be successfully brought to ultracold temperatures using conventional techniques.

Photoassociation in a Magneto-Optical Trap

Photoassociation of laser-cooled atoms [54] both using fixed optical frequencies [55], and broadband shaped femtosecond laser pulses [56] can be used to create vibrationally excited diatomic molecules in the electronic ground state. The temperature of the resulting molecules is however limited to that of the laser cooled atoms from which they are created. These photoassociation techniques provide an excellent means by which to carry out spectroscopy on the molecular ground states.

Feshbach Association

Magnetic Feshbach resonances (section 2.4) can be used to couple a bound molecular state with that of two (or more) 'free' atoms in a conservative magnetic or optical trap. The coupling is achieved by bringing the energy of the molecular state into coincidence with the atomic threshold through the application of a magnetic field ramp. With appropriated selection of B-field ramp rate ultracold molecules can be formed with the phase space density of the constituent atoms. Such Feshbach association was instrumental in the formation of molecular Bose-Einstein condensates from Fermionic ^{40}K atoms [22], and allowed the exploration of the crossover between BEC and Bardeen-Cooper-Schrieffer (BCS) superfluids [57]. A large number of single species Feshbach resonances have been utilised in the creation of Feshbach molecules, whilst recently interspecies Feshbach resonances have also been exploited to create heteronuclear molecules. Feshbach association by its nature creates very weakly bound molecules in vibrationally excited states which are liable to dissociation into other (internal, atomic) states. Feshbach association brings the realm of ground state ultracold molecules a step closer, but does not entirely bridge the gap between ultracold atoms and dipolar molecules.

Stimulated Raman Adiabatic Passage

Recently a great deal of progress has been made in the transfer of weakly bound molecules (produced through Feshbach association or photoassociation schemes) into more deeply bound molecular states using a stimulated

Raman adiabatic passage (STIRAP) technique [27, 58]. This method relies upon the creation of a dark state superposition of the initial molecular state and the target deeply bound state via an intermediate excited 'dark' state using a sequence of two partially overlapping laser pulses. This method has been used to transfer $^{87}Rb_2$ molecules into the triplet rovibrational ground state [59]. The application of this technique to heteronuclear molecules has led to the creation of $^{40}K^{87}Rb$ [26] polar molecules in the absolute ground states. The proposed route for converting ^{87}Rb and ^{133}Cs atoms into ground state molecules [60] is shown in figure 1.2.
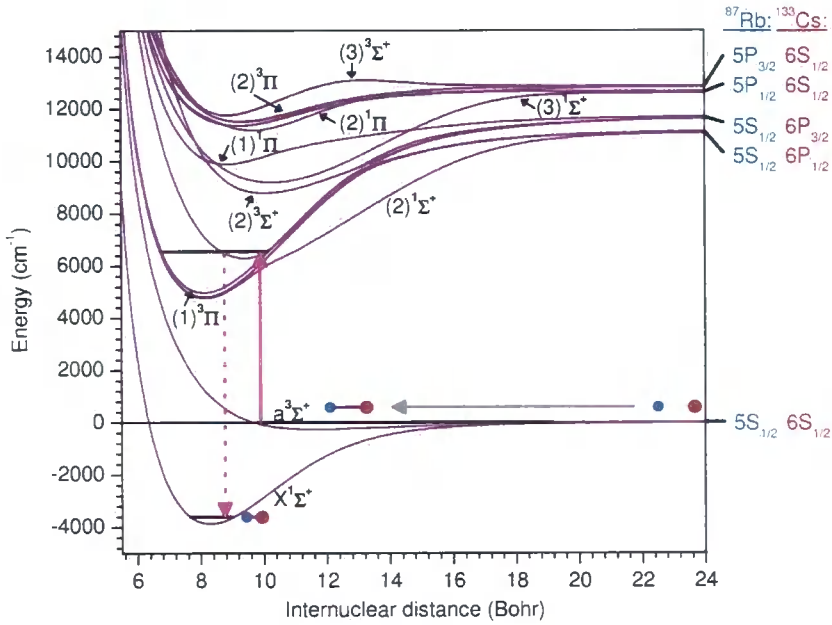
Figure 1.2: Scheme for the creation of deeply bound $^{87}Rb^{133}Cs$ dipolar molecules from ultracold atoms [60]. Ground state ultracold atoms are converted into rotationally and vibrationally excited heteronuclear molecules via a magnetic field sweep through an interspecies Feshbach resonance (grey arrow). The excited molecules are then coherently transferred into the vibrational and rotational ground state via a stimulated Raman transition in which two laser frequencies (pink solid and dashed arrows) couple the initial and final molecular states via an intermediate 'dark state'. The theoretical $^{87}Rb^{133}Cs$ molecular potentials presented here are taken from the *ab initio* calculations of Allouche *et al.* [61].

By performing a magnetic field sweep across an interspecies Feshbach resonance, ultracold heteronuclear atoms are converted into vibrationally excited ^{87}Rb^{133}Cs molecules. Coupling of this excited state to the rovibrational ground state via the intermediate excited state of the mixed b$^3\Pi$ and A$^1\Sigma^+$ potentials may be achieved using temporally overlapping pulses of $\simeq$ 970 and $\simeq$ 1530 nm laser wavelengths.

1.4 Rubidium and Caesium

Of the candidates for the creation of dipolar ultracold molecules via Feshbach association, a mixture of ^{87}Rb and ^{133}Cs has a number of highly desirable qualities. Bose-Einstein condensation of both components of this bi-alkali pairing has been achieved [3, 13], whilst the existence of a large number of ^{133}Cs Feshbach resonances in the $|F = 3, m_F = -3\rangle$ state (figure 1.3) offers a means by which to tune the miscibility of the ^{87}Rb-^{133}Cs mixture. Although the route to direct condensation of ^{133}Cs is by no means trivial, ^{87}Rb has proved to be an excellent 'buffer gas' for sympathetic cooling in a number of atomic species due to the relative simplicity with which direct evaporation of ^{87}Rb may be implemented [18]. One technical advantage over many bi-alkali mixtures is that ^{87}Rb and ^{133}Cs in the $|F = 1, m_F = \pm 1\rangle$ and $|F = 3, m_F = \pm 3\rangle$ states have near identical magnetic moment to mass ratios (section 2.2.4), resulting in a large degree of spatial overlap of the two components when the mixture is magnetically levitated. The ready availability of diode lasers at the 780 and 852 nm wavelengths required for laser cooling is also a distinct advantage.

1.5 Scope Of This Work

The goal of this work is the realisation and characterisation of a magnetically trapped ultracold mixture of ^{87}Rb and ^{133}Cs atoms in the $|F = 1, m_F = -1\rangle$ and $|F = 3, m_F = -3\rangle$ states respectively, providing the foundation for a project to create a quantum gas of ultracold ^{87}Rb^{133}Cs polar molecules.
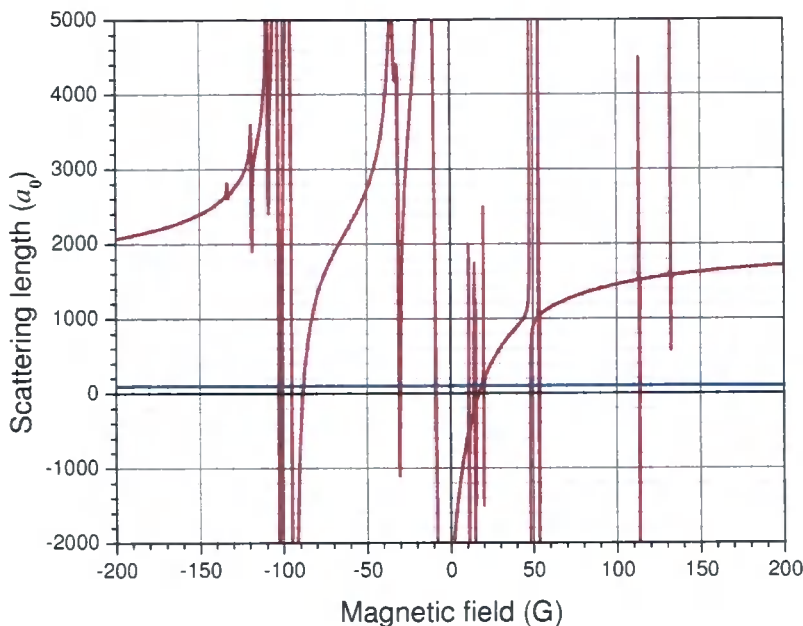
Figure 1.3: Single species scattering length as a function of magnetic field for ^{87}Rb (blue) and ^{133}Cs (red) in the $|F = 1, m_F = \pm 1\rangle$ and $|F = 3, m_F = \pm 3\rangle$ states respectively. The negative region of magnetic field corresponds to the $|F = 1, m_F = -1\rangle$ and $|F = 3, m_F = -3\rangle$ low field seeking spin states, whilst the positive region corresponds to the $|F = 1, m_F = +1\rangle$ and $|F = 3, m_F = +3\rangle$ high field seeking spin states. The data for this figure is taken from reference [62].

My participation in this project began in October 2004 with two empty optical benches in an empty lab. Everything from the construction of a vacuum system and winding of magnetic coils to the optical setup and apparatus computer control had yet to be embarked upon before even magneto-optical trapping of a single atomic species could be contemplated. The work encompassed in this thesis describes the construction, optimisation, and characterisation of a robust and reliable apparatus with which an ultracold mixture of ^{87}Rb and ^{133}Cs atoms is magnetically trapped, along with characterisation of single and interspecies collisions in a magneto-optical trap and magnetic trap. Key results of this work include the development of a novel two-species MOT loading scheme incorporating optical displacement, measurement of ^{133}Cs Feshbach resonances at 118.06(8) and 133.4(1) G, simultaneous evaporative

cooling of the two-component mixture, and the undertaking of an interspecies Feshbach resonances search over the magnetic field range $166 < B < 370$ G.

1.5.1 Overview of Thesis

The technical nature of this document reflects both the nature of the work undertaken in establishing the first ultracold atomic mixture experiment in the United Kingdom, and my personal objective in laying an experimental foundation stone upon which present and future members of the experimental BEC community at Durham University may build.

The theoretical background required to understand the results presented in this document is contained in chapter 2 and the references therein. This is not intended to be an exhaustive guide to the field of ultracold physics. The apparatus developed in this work is presented in chapter 3 with the results of subsequent single species optimisation and characterisation for ^{87}Rb and ^{133}Cs detailed in chapter 4. The interspecies collisional behavior of the ^{87}Rb-^{133}Cs mixture in both the magneto-optical trap and the magnetic trap is explored in chapter 5, alongside measurements of ^{133}Cs Feshbach resonances. The final chapter describes brings together the results achievements of this work and provides an outlook for the field of ultracold polar molecules with a particular focus on the forthcoming developments at Durham University. Also included in this document are a range of appendices focusing on specific technical aspects of this work.

Nomenclature

All of the abbreviations, constants and conversion factors used in this document are defined in the nomenclature section on page 237. Specific products used in this project, along with suppliers are also listed in the nomenclature.

1.5.2 Publications

A number of the results included in this thesis have been previously published in journals. Section 3.2.4 contains results published in references [63] and [64],

whilst the general apparatus (chapter 3) is presented in reference [65], along with the data of section 5.1.

1.5.3   Contributions of Others

The project described in this document is a collaboration between the principle investigator Dr Simon L. Cornish, fellow PhD students (at the time) Dr Margaret Harris (October 2004 to October 2007), Danny McCarron (October 2007 to present) and myself (October 2004 to May 2008). Of the apparatus construction (chapter 3) Dr Harris and I contributed equally to the laser frequency generation aspects. Dr Harris developed the absorption imaging apparatus, image acquisition, and processing software whilst the vacuum apparatus, magnetic trap, and MOT optics were developed predominantly by myself with the aid of Dr Cornish. Computer control of the apparatus via LabVIEW was implemented by Dr Cornish and I with input from Dr Harris on the imaging aspects of the control sequence. In terms of data acquisition Dr Harris's work focussed on the analysis of inelastic losses in the two species magneto-optical trap, whilst optimisation of the MOT and magnetic trapping for single and two species operation was predominantly my work. All aspects of investigation within the magnetic trap were carried out by me, with the exception of the interspecies Feshbach resonance search for which Mr McCarron was of great assistance.

Chapter 2

Experimental Guide

The majority of techniques used in laser cooling, and Bose-Einstein condensation experiments are exceedingly well documented in widely available literature, as is the theory behind these phenomena. Hence there is little value in presenting an in-depth analysis of all theoretical aspects of the field here. This chapter is highly focussed upon aspects of theory directly relevant to the work presented in this document. More general techniques are given only a brief description, leaving the reader to obtain any additional detail from the publications referenced herein.

2.1 Laser Cooling and Trapping

The technique of laser cooling is perhaps the 'magic bullet' which provided access to the ultracold temperature regime for the first time. The principle of laser cooling [66] is basically that a photon of light of wavelength λ absorbed by an atom will impart momentum $p = \hbar k$ upon the atom (where $\hbar$ is the reduced Planck's constant and $k = 2\pi/\lambda$ is the photons angular wavenumber). If the incident laser beam is 'red detuned' from an atomic resonance atoms moving towards the beam will 'see' the light Doppler shifted closer to resonance, whilst atoms moving away from the laser beam will see the light shifted further from resonance. Thus atoms moving towards the beam are more likely to absorb photons from it than those moving away. The amount of momentum which a single photon can impart on an atom moving at a

thermal velocity is relatively small in relation to the atom's momentum. For Doppler cooling to significantly reduce an atom's momentum, therefore a large number of photons must be scattered by the atom. Following absorption of a photon an atom promoted into the excited state will 'relax' back into a lower energy state through spontaneous emission of a photon. Alkali atomic species which are relatively easily laser cooled have atomic structure with 'closed' optical transitions *i.e.*, a laser frequency exists which for a fixed polarisation will promote atoms from a ground state sub-level into an excited state from which spontaneous emission can only lead to atom relaxation back into the initial state. Such cycling transitions allow multiple photon momentum transfer to take place. Atoms moving towards a laser beam will always receive momentum from the beam leading to a reduction in atom velocity, whilst over many successive cycles of laser cooling the net momentum change resulting from spontaneous emission of photons will on average be zero. Thus an atom moving towards a 'red detuned' laser is slowed down by it. When three orthogonal pairs of counterpropagating red detuned laser beams (with appropriate polarisations) are incident upon an atom the rate at which photons are scattered by the atom from the beams which it is moving towards is greater than that from the beams which it is moving away from. Thus whilst the atom's momentum remains significantly greater than that of a single photon, the net effect of multiple photon scattering is always to reduce the atom's net velocity.

2.1.1 Magneto-Optical Traps

Often referred to as 'the workhorse of atomic physics', the magneto-optical trap (MOT) acts to simultaneously confine and cool atoms falling within its capture range. The confinement arises through the application of a magnetic quadrupole field of a few G per cm in conjunction with a six laser beam Doppler cooling array as described above. The principle of magneto-optical confinement is shown for a simple 'model' atomic species in figure 2.1, whilst the required optical frequencies for ^{87}Rb and ^{133}Cs magneto-optical trapping are shown in figure 2.2. For ^{87}Rb (and similarly ^{133}Cs) the operation of a MOT requires additional laser frequencies to that of the simple model.
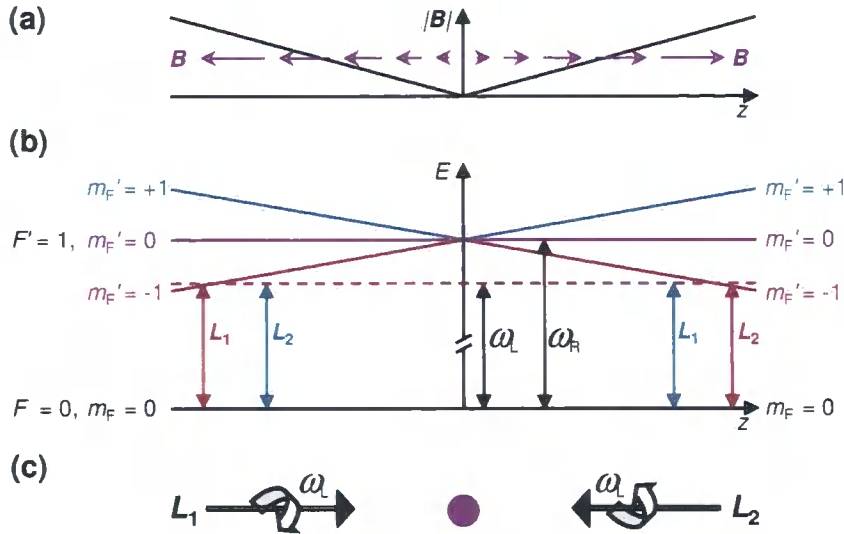
Figure 2.1: Schematic diagram to illustrate general principles of a magneto-optical trap in one dimension. For an atomic species with ground state $F = 0$ in the presence of a quadrupole magnetic field along the z axis (a), the energy of the $F' = 1$, $m_{\mathrm{F}}' = +1$ (blue line), 0 (black line), and -1 (red line) Zeeman sub-levels of the excited state is shown (b). Here the effective Landé g_{F} factor for the ground and excited states is equal to one. A pair of counterpropagating laser beams of equal angular frequency ω_{L} and same sense circular polarisation 'red' detuned from the resonant zero-field $F = 0$ to $F' = 1$ optical transition ω_{R} are incident upon the atomic sample (c). For atoms with negative position coordinate z laser beam L_1 will target $\Delta m_{\mathrm{F}} = -1$ transitions, whilst L_2 will target $\Delta m_{\mathrm{F}} = +1$ transitions. As the magnetic quadrupole field brings the $m_{\mathrm{F}}' = -1$ state closer to resonance than the $m_{\mathrm{F}}' = +1$ state, atoms with negative z coordinate will scatter more photons from laser L_1 than L_2, thus will experience a net momentum gain to the right (towards $z = 0$). Similarly atoms with positive z coordinate will scatter more photons from laser L_2 than L_1 and so will have a net momentum gain to the left (also towards $z = 0$). With three orthogonal pairs of laser beams and appropriate choice of polarisation atoms may be confined in this manner in all three dimensions.

The natural linewidth $\Gamma_{^{87}Rb} \simeq 2\pi \cdot 6$ MHz of the ^{87}Rb excited state is sufficiently broad in comparison to the excited state hyperfine splitting that approximately 1 in 10,000 photons absorbed from the 'cooling' laser beam close to resonance with $F = 2 \rightarrow F' = 3$ transition actually drives atoms into the $F' = 2$ state. From this excited state atoms may decay into the lower hyperfine ground state, effectively being removed from the laser cooling cycle altogether. Without the addition of a 'repumping' beam exciting atoms from the lower hyperfine ground state, effectively 'plugging' this loss channel, the lifetime of atoms in the MOT would be limited to $\simeq 1$ ms. The 'cooling' and 'repumping' laser frequencies required for magneto-optical trapping of ^{87}Rb and ^{133}Cs are shown in figure 2.2.
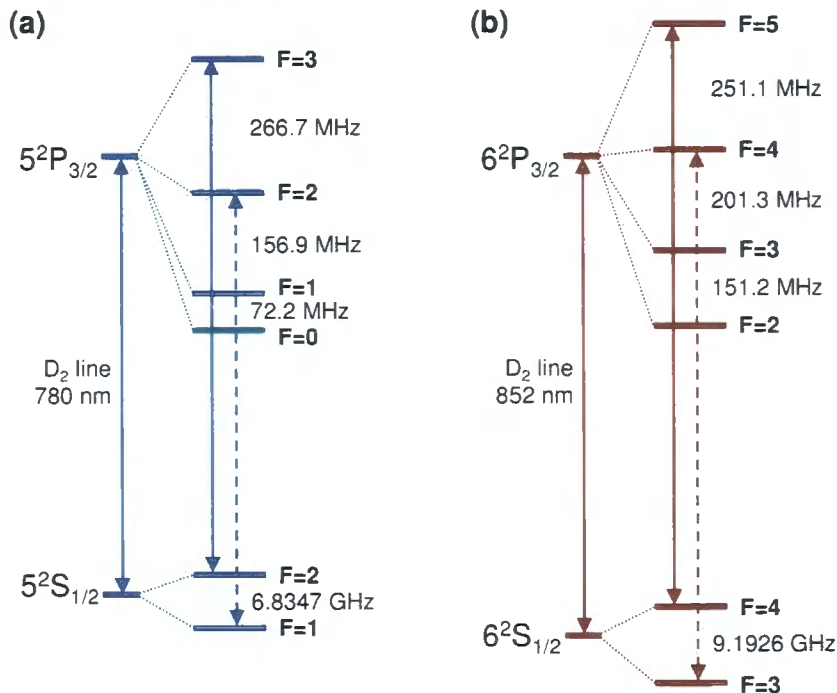
Figure 2.2: Simplified atomic level structure for ^{87}Rb (a) and ^{133}Cs (b) (the D_2-lines have been omitted). The laser cooling (solid arrows) and repumping (dashed arrows) transitions for both species are shown.

2.1.2 Sub-Doppler Cooling

The minimum temperature realisable in a MOT for an atomic excited state natural linewidth Γ was initially thought to be limited by the diffusion

heating of spontaneous emission to the so called Doppler limit [67]:

$$T_D = \frac{\hbar\Gamma}{2k_B} \quad . \tag{2.1}$$

For ^{87}Rb and ^{133}Cs the Doppler limits are 146 and 125 μK respectively. When MOT temperatures significantly below the Doppler limits began to be observed in MOTs it became clear that a far more subtle interaction than simply diffusive photon scattering was taking place. The explanation for this sub-Doppler cooling mechanism provided by Cohen-Tannoudji led to his Nobel prize award in 1997 [7]. The basic principle is that single frequency counterpropagating 'red' detuned laser beams with effectively orthogonal polarisations generate an optical field with a spatially varying polarisation which induces a spatially varying energy shift. Atoms in different Zeeman sublevels experience different energy shifts in a manner which results in a net optical pumping of atoms from the higher potential energy sub-level into lowest energy sublevels [33]. As an optically pumped atom propagates away from the region where its potential energy is a minimum, exchanging kinetic energy for potential energy, the probability of absorbing a photon increases. Effectively the atom is continuously climbing a potential 'hill' analogous to the Greek mythological figure Sisyphus, form which this process gets its name. The temperature limit for this 'Sisyphus cooling' process is limited to the recoil energy of an atom due to the emission of a single photon:

$$T_r = \frac{(\hbar k)^2}{2k_B m} \quad , \tag{2.2}$$

where $k = 2\pi/\lambda$ is the angular wavenumber of the absorbed laser light. For ^{87}Rb and ^{133}Cs the recoil limits are 361.96 and 180.05 nK respectively.

Optical Molasses

For the apparatus described in chapter 3 the Sisyphus cooling technique is optimised in a stage referred to as the optical molasses. Here the parameters of the MOT are altered to minimise the trapped atom ensemble temperature. First and foremost the Sisyphus cooling mechanism can only work effectively when the the polarisation gradient induced ac Stark shift contribution to the energy splitting for atoms in different ground state Zeeman sublevels

dominates the Zeeman energy splitting. This is achieved by switching the quadrupole coils off. For detuning from resonance δ (Hz) significantly greater than the natural transition line-width $|\delta| \gg \Gamma$ the equilibrium atomic cloud temperature T is given [46]:

$$k_B T \simeq \frac{\hbar \Omega^2}{8|2\pi\delta|} \quad , \tag{2.3}$$

where $\Omega = -2\mathbf{d} \cdot \mathcal{E}_0/\hbar$ is the Rabi frequency for each ground to excited state transition, where $\mathbf{d}$ is the transition dipole moment and $\mathcal{E}_0$ the incident laser electric field magnitude. Hence the temperature obtained in the optical molasses is reduced by reducing the laser intensity and increasing the magnitude of the laser detuning from resonance compared to that of the MOT. Close to the atomic recoil velocity the approximation of equation 2.3 breaks down, whilst at low intensity and large detuning from resonance the the optical molasses velocity capture range and the rate at which cooling proceeds are greatly reduced [68]. Hence optimal performance of the optical molasses is achieved at finite laser detuning and non-zero intensity.

Compressed MOT

When transferring atoms from a dissipative magneto-optical trap into a magnetic or other type of conservative trap, if the MOT density distribution is broad in comparison to the conservative trap geometry, there is the potential to pick up a significant amount of potential energy during the transfer. Following elastic collisions in the magnetic trap this potential energy will be converted to kinetic energy, hence increasing the ensemble temperature. To avoid this situation it is desirable to maximise the spatial atom number density prior to loading the magnetic trap. The main factor limiting the densities attainable in a 'standard' MOT is atomic absorption of light re-radiated by confined atoms [69]. Compression may therefore be achieved by reducing the rate at which photons are scattered by the atoms at the centre of the trap. There are two distinct approaches to achieving this, that of transient compression of a MOT [45] and that of engineering the MOT to confine atoms at the trap centre in a non-interacting optically 'dark' state [70]. The transient compression technique in which the cooling light intensity is temporally reduced (or the the laser frequency is further red detuned) tends to result

in a two-component Gaussian type distribution, with a high density central atom distribution and a broader, less dense distribution. For relatively small MOT loads of $\simeq 10^8$ atoms the transient compression technique is effective in retaining the majority of the atoms in the MOT in the high density region. As the atom number increases the two-distribution behavior becomes increasingly apparent, resulting in heating of the sample under compression. The 'dark' spontaneous-force optical trap (Dark SPOT) trap contains a region in the trap centre upon which there is no incident repumping light. Atoms remaining in this region following excitation into a state away from the cooling transition are susceptible to decay into a lower hyperfine ground state which is not subject to excitation from the incident cooling light. Thus the Dark SPOT greatly reduces the proportion of atoms liable to absorption of re-radiated light. For ^{87}Rb and ^{133}Cs the excited state hyperfine splittings are such that only approximately 1 in 10,000 photons of resonant cooling light will excite into a non-cooling transition. In order to rapidly populate the 'dark' state for these atomic species a forced dark SPOT MOT may be implemented in which atoms are actively depumped from the upper hyperfine ground state into a non-cooling state. Although the dark SPOT technique has several key advantages over temporal compression, for the apparatus described in chapter 3 the number of non anti-reflection (AR) coated surfaces in the science region of the apparatus in combination with the non-normal laser beam incidence to the science cell would make it extremely difficult to entirely eliminate repumping light from the atomic sample. For this reason a temporal compression is effected.

2.1.3 Spectroscopy

All of the laser frequencies required for laser cooling, optical pumping, and absorption imaging must be stabilised to specific absolute optical frequencies to within a few hundred kHz. Such laser stabilisation and reference for the apparatus described in chapter 3 is achieved using a combination of Doppler and sub-Doppler spectroscopic techniques.

Doppler Spectroscopy

The velocity of atoms of mass m in a thermal ensemble at temperature T follows a Maxwellian probability distribution, which in one dimension has the form:

$$P(v_z, v_z + dv_z) = \sqrt{\frac{m}{2\pi k_{\mathrm{B}} T}} \exp\left(\frac{m v_z^2}{2 k_{\mathrm{B}} T}\right) dv_z \quad , \qquad (2.4)$$

where $P(v_z, v_z + dv_z)$ is the probability of an individual atom having a component of velocity along the z axis between v_z and $v_z + dv_z$ [71]. A laser beam of frequency f_{laser} incident on an ensemble of such 'thermal' atoms will be Doppler shifted by a frequency Δf in the frame of reference of each individual atom as:

$$\frac{\Delta f}{f_0} = \frac{v}{c} \quad , \qquad (2.5)$$

where v is an individual atoms velocity towards the laser, and c is the speed of light. Substituting the full-width half-maximum of the velocity distribution in Equation 2.4 into Equation 2.5 the FWHM of the absorption spectrum of an ensemble of thermal atoms is given:

$$\Delta f_{\mathrm{FWHM}} = \frac{f_0}{c} \Delta v_{\mathrm{FWHM}} = \frac{2 f_0}{c} \sqrt{\frac{2 k_{\mathrm{B}} T \ln 2}{m}}. \qquad (2.6)$$

For dilute atomic vapors of ^{87}Rb and ^{133}Cs at 'room temperature' ($\simeq 20$ °C) this results in a Doppler broadening of the frequency distribution of light absorbed from a weak laser beam near-resonant with the D2 transition, to a FWHM frequency width of $\simeq 500$ MHz. This Doppler width is greater than the fine structure frequency splitting of the excited D2 line, hence the contributions to the Doppler absorption profile of individual transition components are difficult to isolate.

As the master cooling lasers for both atomic species need to be stabilised to frequencies within a few hundred kHz of the line centre of the 6.065(9) MHz and 5.2227(66) MHz wide D2 transitions in ^{87}Rb and ^{133}Cs respectively a form of spectroscopy free of Doppler broadening is used as a frequency reference.

Hyperfine Pumping Spectroscopy

Hyperfine pumping spectroscopy occurs when two counter-propagating laser beams target ground state atoms of the same velocity class. If there is a relative imbalance in intensity of the two beams, it is most probable for atoms to be excited by the more intense beam. As a result of the intense beam's promotion of atoms to an excited state, the number of ground state atoms available for promotion by the weaker beam is depleted, and hence the degree of atomic absorption of the weaker beam is greatly reduced. As hyperfine pumping spectroscopy occurs only for atoms of a velocity class for which both laser beams are resonant, the effect is free of Doppler-broadening. Hyperfine pumping spectroscopy is used in the apparatus described in chapter 3 to reference the lock point of the DAVLL stabilisation scheme (section 3.2.4) to an absolute atomic frequency.

2.2 Magnetic Trapping of Atoms

The energy of a neutral atom with magnetic moment $\vec{\mu}$ is shifted by the presence of a magnetic field $\vec{B}$:

$$E = \vec{\mu} \cdot \vec{B} \quad, \tag{2.7}$$

producing a resultant force on the atom of:

$$\vec{F} = \vec{\nabla} \left(\vec{\mu} \cdot \vec{B} \right) \quad. \tag{2.8}$$

This force may be used to confine atoms by constructing a spatially varying magnetic field such that the energy of an atom at the trap centre is a local minimum, hence the B-field at the trap centre must be antiparallel to the trapped atoms magnetic moment. It is not possible to create a local magnetic field maxima in all three dimensions, as Wing's theorem proves [47], hence atoms with negative magnetic moments (*i.e.,* those in high magnetic field seeking states) cannot be confined using magnetic fields alone. This limits the range of trappable states to low magnetic field seeking states (*i.e.,* those with positive magnetic moments).

2.2.1 Zeeman Effect

The nature of the coupling between total electronic and nuclear magnetic moments of an atom has a strong dependance on the magnitude of an applied magnetic field. Such an applied field lifts the degeneracy of atomic Zeeman sublevels, resulting in a field dependent splitting. At low fields the coupling between total electronic magnetic and nuclear magnetic moments dominates that between the individual magnetic moments and the applied B-field. Following the discussion in Ref [72] the $|IJFM_F\rangle$ representation of the atomic state gives the first order energy shift at low B-field:

$$\Delta E = g_F \mu_{\mathrm{B}} B M_F \quad , \tag{2.9}$$

where g_F is an effective g-value. Hence at 'low' bias fields the energy of each m_F state varies linearly with increasing B-field. Depending on the sign of g_F either all positive or all negative m_F states with the same F quantum number are magnetically trappable.

At 'high' bias fields the $|IJFM_F\rangle$ representation is no longer appropriate, as the coupling between the individual magnetic moments and the applied magnetic field dominates that between the total electronic magnetic and nuclear magnetic moments. Instead the $|IJM_IM_J\rangle$ coupling appropriately describes the atomic state, giving a first order energy shift at high B-field:

$$\Delta E = g_J \mu_{\mathrm{B}} B M_J - g_I \mu_{\mathrm{B}} B M_I \quad , \tag{2.10}$$

where the first term is dominant ($|g_J| \gg |g_I|$). Hence at 'high' bias fields depending on the sign of g_J either all positive or all negative m_J states with the same J quantum number are magnetically trappable. Atomic states which are magnetically trappable at low B-fields are not necessarily magnetically trappable at high B-fields and vice versa.

Zeeman Effect on Hyperfine Ground States

For the $^2S_{1/2}$ ground states of the alkalis the magnetic field dependent energy shift ΔE (J) in all magnetic field regions is described exactly by the Breit-Rabi formula:

$$\Delta E = -\frac{h\upsilon_{\mathrm{HFS}}}{2\left(2I+1\right)} - g_I \mu_{\mathrm{B}} B m_F \pm \tfrac{1}{2} h\upsilon_{\mathrm{HFS}} \left(1 + \frac{4m_F}{2I+1}x + x^2\right)^{1/2} \quad , \tag{2.11}$$

where v_{HFS} is the hyperfine splitting of the ground states at zero bias field and:

$$x = \frac{(g_J + g_I)\,\mu_B B}{h v_{HFS}} \quad . \tag{2.12}$$

Plots of Breit-Rabi calculations for the ground states of ^{87}Rb and ^{133}Cs (figures 2.3 and 2.4) show the B-field dependent energy shift for all Zeeman sub-levels of the two ground states in each atomic species. Note that the $|F = 1, m_F = -1\rangle$ state is the only magnetically trappable Zeeman sub-level of the ^{87}Rb lower hyperfine ground state at low bias fields, and becomes non-magnetically trappable at fields above $B = 1220.87(1)$ G, whilst for ^{133}Cs the $|F = 3, m_F = -3\rangle$ state ceases to be magnetically trappable at B-fields above $B = 2462.22(1)$ G, thus the maximum magnetic field range over which the ^{87}Rb -^{133}Cs mixture can be investigated in a purely magnetic trap in the lower hyperfine ground states is $0 < B < 1220.87$ G.

2.2.2 Magnetic Trap Geometry

Wing [47] describes two categories of magnetic trap which generate a local magnetic field minimum in three dimensions. The quadrupole trap, in which the field at the trap centre is zero, and the Ioffe-Pritchard trap, for which the magnetic field at the center is a non-zero local minimum in all three dimensions.

2.2.3 Quadrupole Traps

The simplest magnetic trap is a quadrupole trap, which has zero bias field at the trap centre, and B-field magnitude increasing with distance in all 3 dimensions. One method of producing a quadrupole gradient is at the centre of a pair of identical coils, axially separated and with currents running in the opposite sense (appendix C.1.3). As the magnitude of the magnetic trapping force is proportional to the B-field gradient, increasing the gradient increases trap depth and trap frequency. A full description of circular coil pair quadrupole trapping geometry can be found in appendix C.1.3.
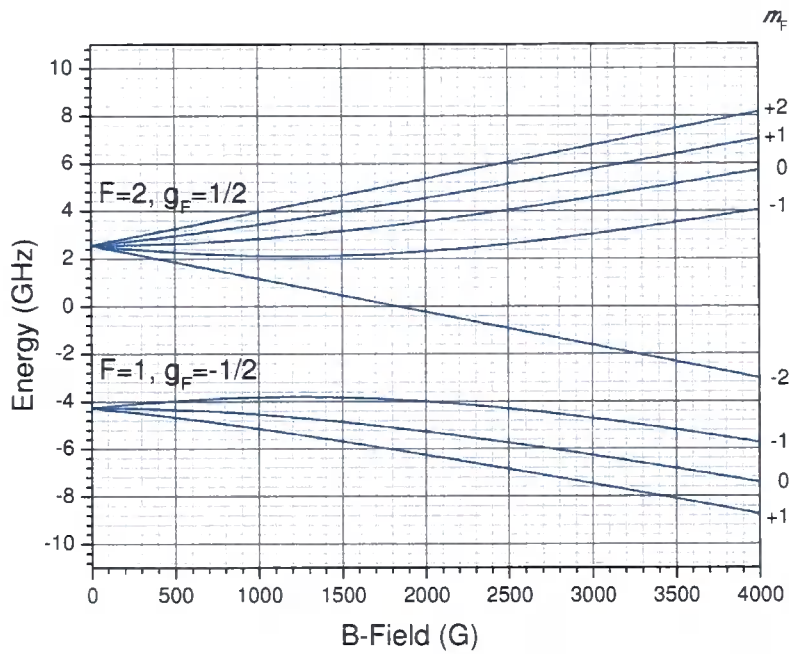
Figure 2.3: Breit-Rabi diagram showing the Zeeman effect on the hyperfine ground states of ^{87}Rb.
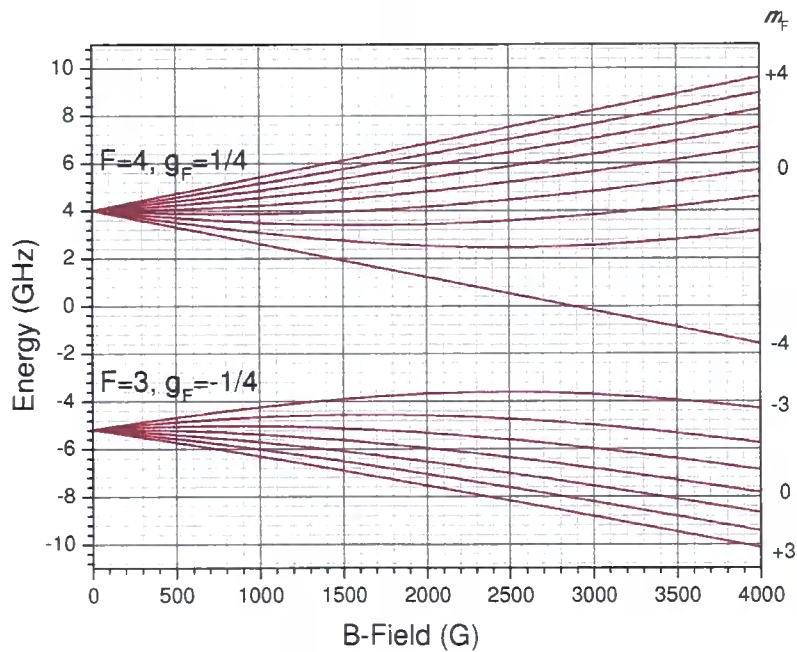
Figure 2.4: Breit-Rabi diagram showing the Zeeman effect on the hyperfine ground states of ^{133}Cs.
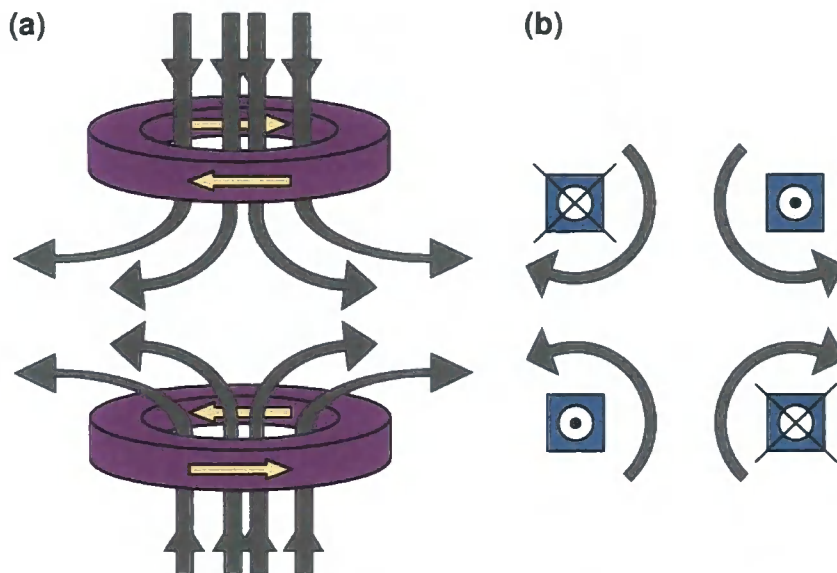
Figure 2.5: Magnetic trap configurations generating a quadrupole magnetic field (grey arrows). A pair of identical circular coils transmitting electrical currents (yellow arrows) in the opposite sense (a) or a set of four equally spaced bars with current configurations into (crosses) and out of (dots) the page (b) both generate quadrupole fields.

Majorana Transitions

The combined magnetic moment of an atom (μ) in a magnetic field of magnitude B precesses about the magnetic quantisation axis at the Larmor frequency:

$$\omega_{\text{Larmor}} = \frac{\mu B}{\hbar} \quad . \tag{2.13}$$

When the rate of change of magnetic field direction experienced by the atom becomes comparable to the Larmor frequency, the atom's magnetic moment can no longer adiabatically follow the magnetic field direction, hence the atom may undergo 'spin flips' into non magnetic trapping states. For a quadrupole trap with magnetic field gradient ∇B at the trap centre, such Majorana transitions are liable to occur at axial distances (z) from the centre of the trap:

$$z \leq \left(\frac{\hbar^2}{\mu m \nabla B} \right)^{1/3} \quad , \tag{2.14}$$

where m and μ are the atoms mass and combined magnetic moment respectively. This 'hole' at the trap centre results in loss of the coldest magnetically

trapped atoms, limiting the maximum achievable phase-space density.

2.2.4 Ioffe-Pritchard Traps

Ioffe-Pritchard traps are a category of magnetic traps in which an axial magnetic field is combined with a radial magnetic field gradient to produce quadrupole confinement in the radial direction, and a non-zero axial magnetic field at the trap centre. One method of implementing such a trap is to combine a set of quadrupole bars ('Ioffe-bars') with a pair of identical axially separated coils with currents running in the same sense (part (a) in figure 2.6). The magnetic field produced by the Ioffe-Pritchard trap varies as:

$$B(r, z) = B_0 + \frac{\gamma}{2}z^2 + \left(\frac{\beta^2}{2B_0} - \frac{\gamma}{4}\right)r^2 \quad , \tag{2.15}$$

where B_0 is the bias field at the centre of the trap and γ and β are constants of the traps geometry defined here.

Trap Frequencies

The positional dependence of B-field in the Ioffe-Pritchard trap leads to a positional dependence in atomic potential energy away from the B-field minimum, and hence harmonic trapping of low-field seeking atoms close to the centre of the trap. The potential energy of a trapped atom follows:

$$E = \mu B = \mu B_0 + \frac{\mu\gamma}{2}z^2 + \mu\left(\frac{\beta^2}{2B_0} - \frac{\gamma}{4}\right)r^2 \quad , \tag{2.16}$$

$$= E_0 + \frac{1}{2}m\left(\omega_z{}^2 z^2 + \omega_r{}^2 r^2\right) \quad , \tag{2.17}$$

where:

$$\omega_z = \sqrt{\frac{\mu\gamma}{m}} \quad , \omega_r = \sqrt{\frac{\mu}{m}\left(\frac{\beta^2}{B_0} - \frac{\gamma}{2}\right)} \quad , \tag{2.18}$$

are the axial and radial frequencies at which atoms oscillate in the magnetic trap (trap frequencies). Note the dependence of radial trap frequency on magnetic bias field. As the bias field is reduced the radial trap frequency increases, whilst there is no corresponding change in axial trapping frequency. This allows the geometry of the magnetically trapped cloud to be tuned by varying the applied bias field, a feature which is especially useful in 'mode

matching' the shape of an atom cloud in the MOT and the corresponding magnetic trapping potential. Increased radial trapping frequencies result in increased collision rates in the magnetic trap, and hence improve the efficiency of evaporative cooling.
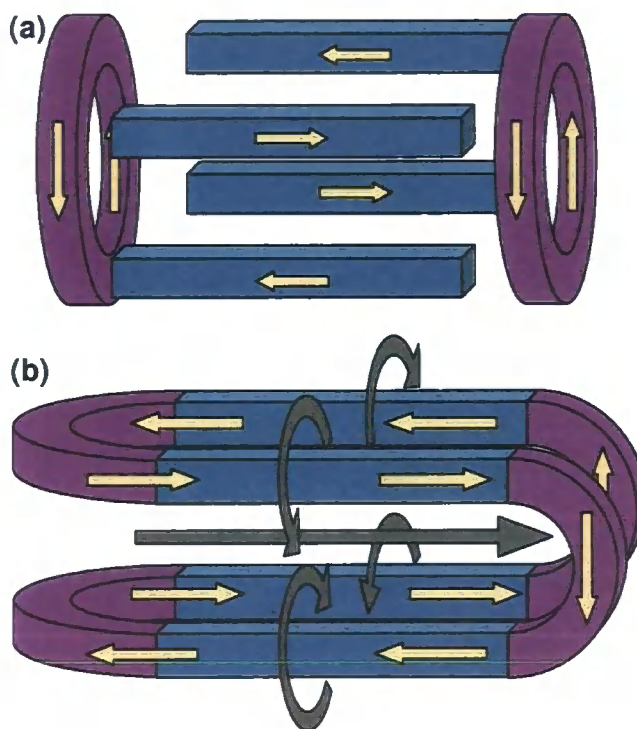
Figure 2.6: Ioffe-Pritchard trap configurations. A magnetic quadrupole field combined with a non-zero magnetic field at the trap centre constitutes an Ioffe-Pritchard magnetic trap. The magnetic field generated by a combination of quadrupole bars (blue) and circular coils (purple) transmitting electrical currents (yellow arrows) in the same sense (a) can be simulated with a single 'baseball coil' (b).

'Baseball' Trap

One implementation of the Ioffe-Pritchard trap is the 'baseball' trap, in which the Ioffe bars and axial 'pinch' coils are combined into a single magnetic trapping coil (figure 2.2.4). This configuration is advantageous in offering increased optical access compared to an Ioffe-Pritchard trap consisting of separate bars and coils. It is also possible to reduce the bias field at the trap

centre with an additional pair of bias offset coils.

Magnetic Levitation and Gravitational Sag

Atom trapping experiments are subject to the influence of gravity, hence free atoms accelerate relative to a 'fixed' experimental apparatus. With no trapping force to confine the atoms they would collide with the lower wall of the vacuum apparatus within $\simeq 45$ ms. This dramatically limits the interaction time of any atom trapping experiment. It is therefore desirable for a trapping force to compensate the force of gravity. The energy of a magnetically trapped atom in the presence of gravity is exactly compensated when:

$$F_k = \mu \frac{\partial B}{\partial k} - mg = 0 \quad , \tag{2.19}$$

where k is the axis on which gravity acts. For levitation of ^{87}Rb and ^{133}Cs ground state atoms at low bias fields the corresponding magnetic trap gradients along the k axis are shown in table 2.1. For a pair of quadrupole coils aligned with the cylindrically symmetric (z) axis of the trap parallel to the gravitational field, the gravitational force close to the centre of the trap (point P) is compensated by the β term of the trapping potential of equation C.11, where:

$$\beta = \left. \frac{\partial B_z}{\partial z} \right|_{\mathrm{P}} \quad . \tag{2.20}$$

The magnetic field gradient produced by an Ioffe-Pritchard trap with axial axis parallel to the gravitational field compensates the gravitational force when a trapped atom is sagged a distance z from the centre of the trap:

$$z = \frac{mg}{\mu \gamma} \quad , \tag{2.21}$$

whilst the corresponding radial sag of an atom in a Ioffe-Pritchard trap with the radial axis parallel to the gravitational field is:

$$r = \frac{mg}{\mu} \left(\frac{\beta^2}{B_0} - \frac{\gamma}{2} \right)^{-1} \quad . \tag{2.22}$$

At bias fields below $\simeq 86$ G the magnetic moment to mass ratios (μ/m), and hence gravitational displacements of ^{87}Rb and ^{133}Cs differ by less than 2 % leading to a high degree of spatial overlap in a magnetic trap of this form.

(a) ^{87}Rb

(b) ^{133}Cs

F	m_F	$\frac{\partial B}{\partial k}$ levitation (G cm^{-1})
2	± 2	15.26
	± 1	30.52
	0	N/A
1	± 1	30.52
	0	N/A

F	m_F	$\frac{\partial B}{\partial k}$ levitation (G cm^{-1})
4	± 4	23.34
	± 3	31.12
	± 2	46.67
	± 1	93.35
	0	N/A
3	± 3	31.12
	± 2	46.67
	± 1	93.35
	0	N/A

Table 2.1: Magnetic trap B-field gradients required to levitate ground state ^{87}Rb and ^{133}Cs atoms against gravity, where k is the axis on which gravity acts.

2.3 Cold Collisions

Cold collisions between atoms are fundamentally the reason for a quantum degenerate gas displaying superfluid behaviour. In addition to being the essence of many-body behavior in ultracold systems, cold collisions are also essential to the realisation of high phase-space densities via forced evaporative cooling and offer a means by which interatomic potentials may be probed and ultracold molecules created. Cold collisions may be broadly categorised into elastic and inelastic collisions. Elastic collisions allow ultra-cold temperatures of atomic ensembles to be realised via evaporative cooling processes, whilst inelastic collisions which are often associated with number loss and heating in atomic ensembles, may also be utilised in the creation of ultracold molecules. Both elastic and inelastic collisional properties may be affected by the application of magnetic and electric fields. This tunability of collisional behavior is highly desirable in ultracold systems, and has been harnessed in the realisation of Bose-Einstein condensation and the creation of pure samples of both homonuclear, and heteronuclear ultra-cold molecules.

The parameters governing single and two-species elastic and inelastic collisions are introduced below, including the most important factor at ultracold temperatures, the s-wave scattering length.

2.3.1   Origin of the Scattering Length

Two atoms colliding experience a potential, the shape of which is governed by a combination of the attractive Van der Waals potential and a repulsive contact potential. 'Free' atoms have a wave function which varies spatially with the de Broglie wavelength. When incident upon a potential, the energy of a colliding atom pair is increased by that of the potential. This results in a corresponding decrease in both the de Broglie wavelength, and the oscillation amplitude within the potential.
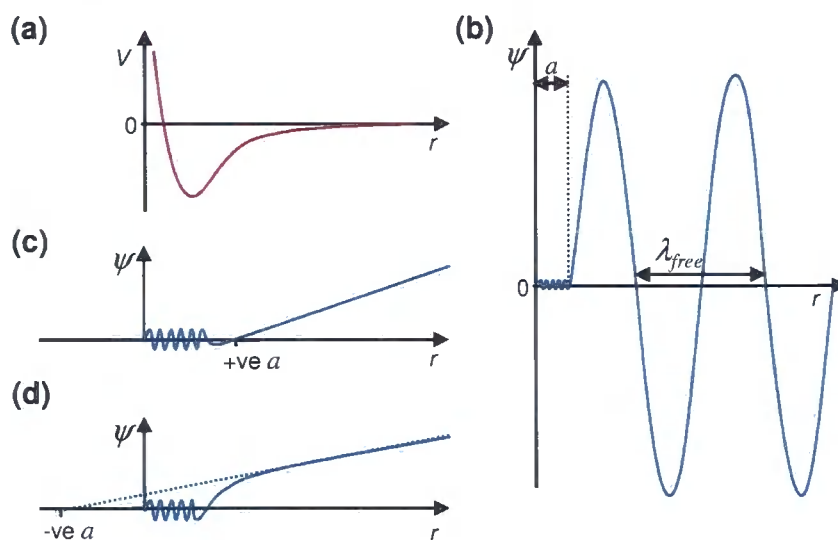
Figure 2.7: Schematic figure showing the potential energy V of a a pair of colliding atoms as a function of separation r (a). Short wavelength, low amplitude oscillations of the wavefunction $\psi(r)$ at short range (b), phase shift the origin of the 'free atom' de Broglie oscillations (wavelength λ_{free}), effectively shifting the atomic separation at which 'free atoms' interact by an amount a, referred to as the scattering length. The scattering length can be positive (c) or negative (d) depending upon the shape of the potential at short range, and is highly sensitive to the proximity of bound molecular states to the free atom continuum.

The presence of 'fast', low amplitude wavefunction oscillations within the interatomic potential (due to the reduced de Broglie wavelength), results in a phase shift of the 'free' atom de Broglie oscillations (figure 2.7). This can be understood by considering the oscillations within the potential as effectively reducing the extent to which the 'free atom' de Broglie oscillations can impinge upon the short range interatomic potential. The phase shift determines the effective atomic separation at which the 'free atom' de Broglie oscillations begin and hence the maximum distance at which 'free' atoms begin to interact with one another. This distance is described as the scattering length. For a positive wave vector phase shift, the scattering length is positive, hence atomic collisions are repulsive, whilst a negative scattering length is characteristic of attractive interactions.

The magnitude and sign of the scattering length is highly dependent upon the short range potential, which in turn is dependent upon the number of bound molecular states supported by it. Thus the value of the scattering length provides a means by which to probe the short-range wave function, which is impossible to measure directly due to the minuscule probability of atoms colliding at such close proximities. The addition of an extra molecular state in the short range potential, for example, results in a dramatic change in the scattering length: increasing as the energy of the 'free' molecular state is reduced, becoming infinite as the 'free' state becomes bound, and becoming negative before reducing in magnitude as the 'bound' molecular state becomes more deeply bound. An abrupt change in the scattering length as a function of an externally applied field is therefore indicative of the presence of a degeneracy between free atomic and bound molecular potentials. Such 'Feshbach' resonances can be used to create molecules, hence characterisation of the scattering length not only offers a means by which to probe molecular states, but also is a significant step towards the creation of ultra-cold molecules.

The scattering length so far described is that of atoms undergoing s-wave collisions, that is collisions which are described by the first spherical harmonic function of a partial wave expansion of the colliding atom wave function [11]. These are the lowest energy collision processes of Bosonic isotopes, and are the dominant collisional process in the low temperature limit. Bosonic

isotopes at higher temperatures may also have significant d-wave contributions to the wave function, a characteristic feature of which is a temperature dependence of the collision cross section.

2.3.2 Elastic Collisions

Single species elastic collisions are the mechanism by which atom clouds rethermalise following adiabatic processes such as evaporative cooling. For two component mixtures the efficiency of 'sympathetic cooling', in which a 'target' species is effectively cooled through thermalisation with a 'buffer' gas at a lower temperature, relies upon the interspecies elastic collision rate. This method can be especially useful in cooling Fermionic isotopes, which in the single species case rely upon p-wave collisions to exchange energy, hence the addition of a second atomic species allows inter-species s-wave collisions to mediate energy exchange between Fermionic atoms of the same species. For ^{133}Cs , which is yet to be condensed in a magnetic trap due to high inelastic loss rates, implementing sympathetic cooling with a ^{87}Rb buffer gas, which is readily cooled via forced evaporation, may offer an alternative route to quantum degeneracy of ^{133}Cs without the inherent losses of direct evaporative cooling. Efficient implementation of both evaporative and sympathetic cooling techniques requires a high ratio of elastic to inelastic collisions.

Single Species

The key parameter governing single species elastic collisions is the elastic collision cross section σ, which away from resonances to first order is approximated as:

$$\sigma = \frac{8\pi a^2}{1 + k^2 a^2} \quad , \qquad (2.23)$$

where a is the scattering length and k the mean de Broglie wave vector for the frame of reference in which the target atom is stationary, which depends upon the atomic mass m and ensemble temperature T as:

$$k = \sqrt{\frac{16 m k_{\mathrm{B}} T}{\pi \hbar^2}} \quad . \qquad (2.24)$$

The single species two-body elastic collision rate γ_c is proportional to the collision cross section σ as [73]:

$$\gamma_c = \langle n \rangle \langle v \rangle \sigma \quad , \tag{2.25}$$

where the mean number density $\langle n \rangle$ and relative collision velocity $\langle v \rangle$ in the trap are:

$$\langle n \rangle = \frac{1}{N} \int_V n^2(\mathbf{r}) \, \mathrm{d}^3\mathbf{r}, \quad \langle v \rangle = \sqrt{\frac{16 k_B T}{\pi m}} \quad , \tag{2.26}$$

for an ensemble of N atoms with mass m and position dependent density profile $n(\mathbf{r})$ at a temperature of T °K. For a Gaussian atom cloud with peak number density n_0, $\langle n \rangle = n_0 / (2\sqrt{2})$. Figure 2.8 shows the dependence of collision cross section on ensemble temperature for ^{87}Rb and ^{133}Cs atoms in a harmonic trap. At high temperatures the de Broglie wavelength:

$$\lambda_{dB} = \sqrt{\frac{h^2}{2\pi k_B T}} \quad , \tag{2.27}$$

is significantly lower than the scattering length, hence the collisional cross section of equation 2.23 is limited by the relative de Broglie wave vector to a value:

$$\sigma = \frac{8\pi}{k^2} \propto \frac{1}{T} \quad . \tag{2.28}$$

This is the unitarity limit. In the low temperature limit the de Broglie wavelength is significantly greater than the scattering length, hence the collisional cross section is dependent only on the scattering length, and the cross section saturates to a value of:

$$\sigma = 8\pi a^2 \quad , \tag{2.29}$$

where a is the background collision rate (away from interatomic resonances). For two-body elastic collisions between ^{133}Cs atoms in the $|F = 3, m_F = -3\rangle$ state the s-wave scattering length varies with magnetic field due to the presence of single-species Feshbach resonances, taking a value of $a_{133\text{Cs}} = 2250 \, a_0$ at a B-field of 165.50(6) G (where a_0 is the Bohr radius). In contrast the s-wave scattering length for two-body collisions between ^{87}Rb atoms in the $|F = 1, m_F = -1\rangle$ state remains at a constant value of $a_{87\text{Rb}} = 102(6) \, a_0$ over the B-field range probed in this experiment [74]. This difference in scattering length results in a difference in the variation of collision cross-section with temperature of the two atomic species (figure 2.8(a)). For both species at 'high' temperatures a reduction in temperature results in
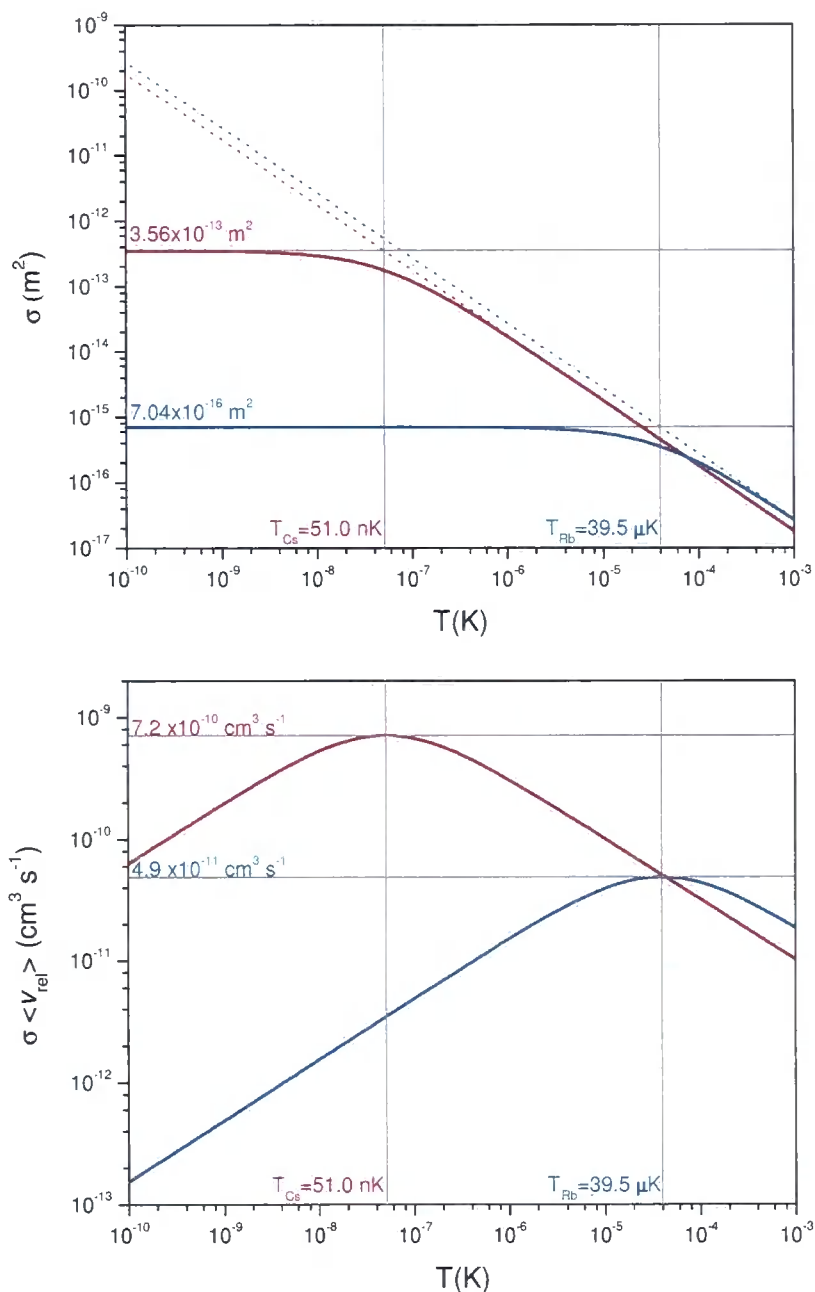
Figure 2.8: Variation in ^{87}Rb (blue solid line) and ^{133}Cs (red solid line) single species elastic collision cross sections (a) and rate coefficients (b) as a function of atom cloud temperature. At high temperatures the collision cross sections vary as $8\pi/k^2$ (dashed lines) where k is the mean de Broglie wave vector (see text). This is described as the 'unitarity limit'. In the low temperature limit, the collision cross sections saturate to be $\sigma = 8\pi a^2$, where a is the single-species scattering length. Below $T \simeq 39.5$ μK the cross section for ^{87}Rb saturates to a value of $\sigma_{^{87}\mathrm{Rb}\ ^{87}\mathrm{Rb}} = 7.04 \times 10^{-16}$ m^2, whilst that of ^{133}Cs increases until the the temperature falls below $T \simeq 51.0$ nK, at which it saturates to a value of $\sigma_{^{133}\mathrm{Cs}\ ^{133}\mathrm{Cs}} = 3.56 \times 10^{-13}$ m^2. The elastic collision rate coefficients (b) are maximised at these saturation temperatures.

an increase in collision cross-section. At low temperatures the collision cross sections for each atomic species saturate at values of $\sigma_{^{87}\text{Rb}^{87}\text{Rb}} = 7.04 \times 10^{-16}$ m^2 and $\sigma_{^{133}\text{Cs}^{133}\text{Cs}} = 3.56 \times 10^{-13}$ m^2 respectively. The saturation cross section for ^{87}Rb is three orders of magnitude lower than that for ^{133}Cs, whilst the onset of saturation for ^{87}Rb occurs at a temperature three orders of magnitude higher than for ^{133}Cs. Thus, in contrast to the case for ^{133}Cs, below $\simeq 40$ μK reducing the temperature of ^{87}Rb atoms will not result in a significant increase in the collision cross section. The corresponding dependence of the elastic collision rate coefficient ($\bar{v}\,\sigma$ from equation 2.25) upon temperature is shown in figure 2.8(b). Here the collision rate coefficients for each species increase with reduction in temperature until the corresponding collision cross section saturation temperatures are reached. Below the saturation temperatures the rate coefficients are reduced from the peak values. Clearly the degree to which evaporative cooling enhances the single species elastic collision rate for each species will be markedly different above and below the temperatures at which the collision cross sections begin to saturate.

Two Species

Interspecies two-body elastic collisions are governed by the two-species elastic collision cross section, which is to first order given (for collisions between species i and species j) by [75, 76]:

$$\sigma_{ij} = \frac{4\pi a_{ij}{}^2}{1 + k_{ij}{}^2 a_{ij}{}^2} \quad , \tag{2.30}$$

where a_{ij} is the interspecies scattering length and k_{ij} the mean de Broglie wave vector for collisions between two heteronuclear atoms, which depends upon the individual masses m_i and m_j, reduced mass $\mu = m_i m_j / (m_i + m_j)$, and single species ensemble temperatures T_i and T_j as:

$$k_{ij} = \mu \sqrt{\frac{8k_\text{B}}{\pi\hbar^2}\left(\frac{T_i}{m_i} + \frac{T_j}{m_j}\right)} \quad . \tag{2.31}$$

The factor of two discrepancy between the expression for the interspecies elastic cross section (equation 2.30) and that for single species collisions (equation 2.23) is due to the distinguishable nature of the particles in the two species case [11]. Following the discussion for single species elastic collisions,

the two species elastic collision rate for species i due to collisions with species j is given by:

$$\gamma_{ij} = \langle n_j \rangle_i \cdot \langle v_{ij} \rangle \cdot \sigma_{ij} \quad , \tag{2.32}$$

where $\langle n_j \rangle_i$, the mean density of atoms of species j experienced by atoms of species i, and $\langle v_{ij} \rangle$, the mean relative velocity of the two collisional partners are:

$$\langle n_j \rangle_i = \frac{1}{N_i} \int_V n_i(\mathbf{r}) n_j(\mathbf{r}) \, \mathrm{d}^3\mathbf{r}, \quad \langle v_{ij} \rangle = \sqrt{\frac{8k_{\mathrm{B}}}{\pi} \left(\frac{T_i}{m_i} + \frac{T_j}{m_j} \right)} \quad , \tag{2.33}$$

for an ensemble of N_i atoms of species i with position dependent density profile $n_i(\mathbf{r})$ in the presence of a number density profile $n_j(\mathbf{r})$ of species j. The interspecies elastic cross section in the unitarity limit becomes:

$$\sigma_{ij} = \frac{4\pi}{k_{ij}^2} \quad , \tag{2.34}$$

whilst in the 'low temperature limit' saturates to:

$$\sigma_{ij} = 4\pi a_{ij}^2 \quad . \tag{2.35}$$

2.3.3 Inelastic Collisions: Single Species Trap

Inelastic collisions change the total kinetic energy of an atomic system. Within a single-species trap atomic sample inelastic collisions can broadly be separated into three categories: Background collisions with residual gas molecules, two-body homonuclear collisions in which the electronic structure of the colliding partners is altered, and three body homonuclear collisions in which molecule formation with two colliding partners results in energy release. Inelastic processes are most easily identified experimentally by the loss of atoms from a conservative trap due to an above trap-depth increase in kinetic energy of one or more collisional partners. Although inelastic collisions are often identified as 'bad collisions' in terms of reducing the efficiency of evaporative cooling processes, the presence of such collisions can indicate molecule creation and prove vital in pinning down the shape of interatomic potentials.

Background Residual Gas Collisions

A molecule with 'thermal' velocity colliding with a trapped atom will with near certainty impart enough energy for the atom to escape the trapping potential altogether. Although not necessarily inelastic, such residual gas collisions result in a change in the total kinetic energy of the trapped atomic ensemble. At low densities, the lifetime of atoms confined within a magnetic trap is limited by this process. The rate of such collisions is independent of trapped atom ensemble density, hence although resulting in a reduction in atom number, residual gas collisions do not result in significant heating of the trapped atomic sample. Through careful design and construction of an ultra-high vacuum system in which ensembles are trapped, magnetic trap lifetimes in excess of 100 s can be achieved.

Two-Body Inelastic Collisions

For a single species atomic ensemble magnetically trapped in the lower hyperfine ground state, hyperfine-structure changing collisions resulting in transitions to the upper hyperfine ground state are energetically forbidden, thus the only remaining two-body inelastic processes to which the colliding atoms are susceptible are dipolar angular momentum changing collisions. Two mechanisms exist for such dipolar collisions in alkali atoms, the direct spin-spin coupling between colliding atoms and the second order spin-orbit interaction. The relative strength of these two coupling processes increases with alkali atom mass, due to a resultant reduction in the energy level spacing, whilst the spin-orbit interaction is significant in heavy atoms due to the effectively relativistic electron velocities, so significant in fact that the successful Bose-Einstein condensation of ^{87}Rb preceded that of ^{133}Cs by eight years. The spin-spin and second order spin-orbit interactions in all alkalis are opposite in sign, however for ^{87}Rb the two effects are nearly identical in magnitude, hence there is an anomalously low dipolar relaxation rate. For ^{133}Cs this is not the case, the magnitude of the second order spin-orbit interaction exceeds that of the spin-spin interaction, leading to dipolar relaxation rates $\simeq 50,000$ times greater than those for ^{87}Rb [77]. Thus in spite of the greater scattering length between ^{133}Cs atoms in the $|F = 3, m_F = -3\rangle$ state in comparison

to ^{87}Rb in the $|F = 1, m_F = -1\rangle$ state, the increased ratio of of elastic to inelastic collisions in ^{87}Rb in comparison to ^{133}Cs at increased atom number densities results in far more favorable conditions for evaporative cooling of ^{87}Rb . Thus the techniques required to produce Bose-Einstein condensates of ^{87}Rb are far less complex than is the case for ^{133}Cs , hence the delay between realisation of quantum degeneracy in the two atomic species.

Three-Body Inelastic Collisions

When three atoms are involved in a collision two of the colliding partners may form a molecule. In this case the molecular binding energy is released as the combined kinetic energy of the molecule and remaining atom. The energy released in most cases is significantly greater than the trap depth, hence both the molecule and remaining atom escape from the trap. As the three body loss rate scales with the square of atom number density, atoms participating in this loss process are predominantly those at the trap centre, with below average potential energy. Thus this process of three body recombination results in a net increase in the mean energy of atoms remaining in trap. It is effectively a heating process and is highly detrimental in high density atomic ensembles.

Inelastic Collision Rates

Incorporating all three loss mechanisms described above, the number of atoms trapped within a single species ensemble N_i evolves over time as:

$$\frac{\mathrm{d}N_i}{\mathrm{d}t} = -\gamma N_i - K_{2i} \int_V n_i{}^2(\mathbf{r}) \, \mathrm{d}^3\mathbf{r} - K_{3i} \int_V n_i{}^3(\mathbf{r}) \, \mathrm{d}^3\mathbf{r} \quad , \qquad (2.36)$$

where γ is the background collision rate with residual gas atoms, $n_i(\mathbf{r})$ is the position dependent density and K_{2i} and K_{3i} are the rate constants for two and three body single species inelastic collisions respectively. For a Gaussian distribution of atoms (appendix B.2.1), the mean number density experienced by a trapped atom is:

$$\langle n_i \rangle = \frac{1}{N_i} \int_V n_i{}^2(\mathbf{r}) \, \mathrm{d}^3\mathbf{r} = \frac{n_{\mathrm{pk}}}{2\sqrt{2}} \quad , \qquad (2.37)$$

where n_{pk} is the peak atom number density at the cloud centre. Similarly the mean number density squared experienced by an atom within the ensemble is:

$$\langle n_i{}^2 \rangle = \frac{1}{N_i} \int_V n_i{}^3(\mathbf{r}) \ \mathrm{d}^3\mathbf{r} = \frac{n_{i\mathrm{pk}}{}^2}{3\sqrt{3}} = \frac{8\langle n_i \rangle^2}{3\sqrt{3}} \quad . \tag{2.38}$$

Thus equation 2.36 can be expressed in the form:

$$\frac{\mathrm{d}N_i}{\mathrm{d}t} = -\gamma N_i - K_{2ii}\langle n_i \rangle N_i - K_{3i}\langle n_i{}^2 \rangle N_i \quad . \tag{2.39}$$

2.3.4 Inelastic Collisions: Two-Species Trap

For a two-component atomic mixture, the number of inelastic loss mechanisms is greatly increased from that of a single atomic species. In addition to the single species loss processes of both components, heteronuclear loss mechanisms must also be considered.

Inelastic Collision Rates

The addition of a second species results in three additional terms to the loss rate of equation 2.36. For two species i and j the number of atoms of species i evolves as:

$$\frac{\mathrm{d}N_i}{\mathrm{d}t} = - \gamma N_i - K_{2i} \int_V n_i{}^2(\mathbf{r}) \ \mathrm{d}^3\mathbf{r} \ - K_{3i} \int_V n_i{}^3(\mathbf{r}) \ \mathrm{d}^3\mathbf{r} \ - K_{2ij} \int_V n_i(\mathbf{r})n_j(\mathbf{r}) \ \mathrm{d}^3\mathbf{r}$$
$$- K_{3iij} \int_V n_i{}^2(\mathbf{r})n_j(\mathbf{r}) \ \mathrm{d}^3\mathbf{r} \ - K_{3ijj} \int_V n_i(\mathbf{r})n_j{}^2(\mathbf{r}) \ \mathrm{d}^3\mathbf{r} \quad , \tag{2.40}$$

where $n_i(\mathbf{r})$ and $n_j(\mathbf{r})$ are the position dependent densities of species i and j respectively. K_{2i} and K_{3i} are the rate constants for homonuclear two and three body inelastic collisions of species i, and K_{2ij}, K_{3iij} and K_{3ijj} are the rate constants for two and three body heteronuclear inelastic collisions. In each term the indices represent the number of atoms of each species involved in each category of collision. The single species collision integrals are evaluated in section 2.3.3, whilst the two-species collision terms are discussed in the following pages. The argument followed in this discussion is that presented by Anderlini *et al.* [75].

Heteronuclear Inelastic Collisions

For magnetically trapped atomic samples of species i and j, assuming that the trap frequencies of the two species ω_i and ω_j along each axis of the trap are related by the scaling factor β as:

$$m_j\omega_j{}^2 = \beta^2 m_i\omega_i{}^2 \quad , \tag{2.41}$$

where m_i and m_j are the atomic masses of species i and j respectively, the two-species collision terms of equation 2.40 neglecting the effect of gravity are evaluated. The mean density of atoms of species j with Gaussian density distribution at temperature T_j experienced by atoms of species i with Gaussian density distribution at temperature T_i is:

$$\langle n_j \rangle_i = \frac{1}{N_i} \int_V n_i(\mathbf{r}) n_j(\mathbf{r}) \, \mathrm{d}^3\mathbf{r} = n_{j\mathrm{pk}} \left(\frac{T_j}{T_j + \beta^2 T_i} \right)^{3/2} \quad , \tag{2.42}$$

where $n_{j\mathrm{pk}}$ is the density of species j at the trap centre. Accounting for the difference in gravitational sag Δz of the two atomic species along the vertical axis (here denoted the z axis) equation 2.42 is modified by a factor:

$$F_{j(i)} = \exp\left[-\frac{m_i\omega_{iz}{}^2}{2k_\mathrm{B}} \left(\frac{\beta^2}{T_j + \beta^2 T_i} \right) \Delta z^2 \right] \quad . \tag{2.43}$$

Again initially neglecting the difference in gravitational sag of the two atomic species, the mean number density product of species i and j experienced by an atom of species i within the ensemble is given by:

$$\langle n_i n_j \rangle_i = \frac{1}{N_i} \int_V n_i{}^2(\mathbf{r}) n_j(\mathbf{r}) \, \mathrm{d}^3\mathbf{r} = n_{i\mathrm{pk}} n_{j\mathrm{pk}} \left(\frac{T_j}{2T_j + \beta^2 T_i} \right)^{3/2} \quad . \tag{2.44}$$

Similarly the mean number density squared of species j experienced by an atom of species i is:

$$\langle n_j{}^2 \rangle_i = \frac{1}{N_i} \int_V n_i(\mathbf{r}) n_j{}^2(\mathbf{r}) \, \mathrm{d}^3\mathbf{r} = n_{j\mathrm{pk}}{}^2 \left(\frac{T_j}{T_j + 2\beta^2 T_i} \right)^{3/2} \quad . \tag{2.45}$$

The difference in gravitational sag of the two atomic species is accounted for by modifying equations 2.44 and 2.45 by the factors:

$$F_{ij(i)} = \exp\left[-\frac{m_i\omega_{iz}{}^2}{2k_\mathrm{B}} \left(\frac{2\beta^2}{2T_j + \beta^2 T_i} \right) \Delta z^2 \right] \quad , \tag{2.46}$$

and

$$F_{jj(i)} = \exp\left[-\frac{m_i\omega_{iz}^2}{2k_{\mathrm{B}}}\left(\frac{2\beta^2}{T_j + 2\beta^2 T_i}\right)\Delta z^2\right] \quad , \qquad (2.47)$$

respectively. By substituting equations 2.42 to 2.47 into equation 2.40, the total atom loss rate of species i in the presence of species j is expressed as:

$$\frac{\mathrm{d}N_i}{\mathrm{d}t} = -(\gamma + K_{2ii}\langle n_i\rangle + K_{3i}\langle n_i{}^2\rangle + K_{2ij}\langle n_j\rangle_i \; F_{j(i)}$$
$$+ K_{3iij}\langle n_i n_j\rangle_i \; F_{ij(i)} + K_{3ijj}\langle n_j{}^2\rangle_i \; F_{jj(i)})\; N_i \quad . \qquad (2.48)$$

This expression has many terms, but essentially describes an exponential loss in atom number with density dependent loss rate. The single species rate constants may be extracted from fits of loss rate as a function of peak number density in the single species magnetic trap. Repeating these measurements for varying number densities of a second atomic species in the two-species magnetic trap the values of the two and three body two-species inelastic collision rate constants may also be obtained. The two-species inelastic collision term which occurs at the lowest order of density is that for two-body collisions K_{2ij}. Thus of the two-species inelastic collision rate constants, it is the two-body rate constant for which the measurement sensitivity is greatest.

2.4 Feshbach Resonances

When the energy of a bound molecular state is close to that of two colliding atoms, a strong coupling between the molecular and atomic states arises. If the atomic magnetic moments are different to those of the corresponding molecule, the relative energies of the atomic and molecular states can be tuned through the application of a magnetic field, as shown in figure 2.9. As the molecular potential approaches the 'free atom' continuum, the scattering length is highly sensitive to the applied magnetic field (see section 2.3.1). This feature in the scattering length profile is described as a magnetic Feshbach resonance. In the region of such a resonance the scattering length a as a function of applied magnetic field B varies as [11]:

$$a = a_{\mathrm{bg}}\left(1 - \frac{\Delta}{B - B_0}\right) \quad , \qquad (2.49)$$

where a_{bg} is the background scattering length (the value taken away from the resonance), B_0 is resonance position (where the scattering length diverges to

$a = \pm\infty$) and Δ is the resonance width. Thus through ramping the magnetic field across a magnetic Feshbach resonance, the nature of interactions in the atomic ensemble can be tuned from attractive to repulsive. Through varying the magnetic field the interaction strength can be arbitrarily tuned, or even 'switched off' altogether.
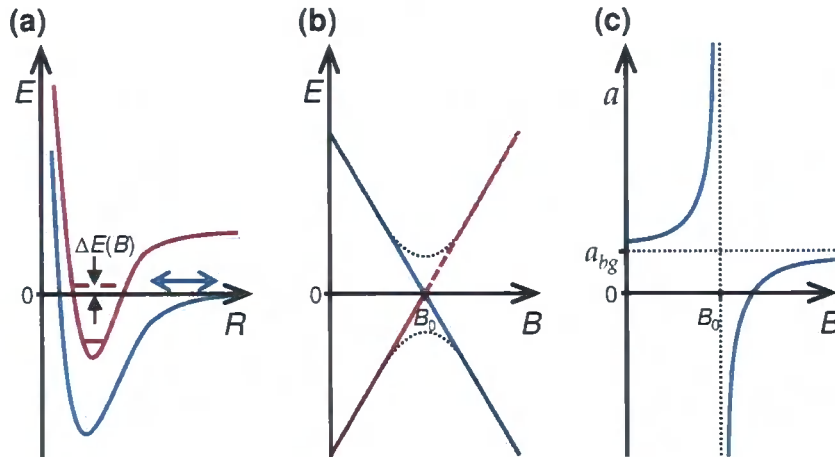
Figure 2.9: Feshbach resonance schematic. When the energy (E) of the 'least bound' state (red dashed line) of a molecular potential (red solid line) is close to that of two colliding free atoms (blue line) as shown in (a), and there is a difference between the atomic and molecular magnetic moments, the energy difference ΔE may be tuned through varying the applied magnetic field (B). The energy of the atomic continuum and bound molecular states as a function of applied magnetic field is shown in (b). At field B_0 the energies of the two states coincide, leading to a strong coupling between the open entrance channel (free atom potential; blue line) and the closed channel (the molecular potential; red line). This leads to an avoided crossing between the two channels (black dashed lines). When the difference of the two energies becomes zero, the molecular state is no longer bound (red dashed line). By adiabatically sweeping the magnetic field through the resonance 'free' atoms may be converted into bound molecules. In the region of a Feshbach resonance the scattering length of the collisional partners is greatly modified (c), becoming $\pm\infty$ at B_0.

2.4.1 Molecule Creation

As a Feshbach resonance is a feature of strong coupling between atomic and molecular potentials, atoms can be converted into molecules through ramping the magnetic field sufficiently slowly that the colliding partners adiabatically follow the avoided crossing [24]. Molecules created in this manner are referred to as 'Feshbach molecules'. The binding energy of these molecules, by virtue of the association mechanism is very low, and the molecules are extremely large (of the order of the scattering length). Bosonic Feshbach molecules are also highly susceptible to relaxation through inelastic atom-molecule and molecule-molecule collisions, limiting the trap lifetime to a few ms. Bosonic Feshbach molecules created in a three dimensional optical lattice [78] have greatly enhanced lifetimes due to isolation of individual Feshbach molecules in single lattice sites. The challenge to transfer such Feshbach molecules into more deeply bound states, and even ground states is being met 'head on' for both homonuclear and heteronuclear molecules. A cursory description of such techniques is given in chapter 1, whilst an in depth analysis of these methods is beyond the scope of this document.

2.4.2 Resonance Detection

The strong coupling between atomic and molecular states near a magnetic Feshbach resonance leads to a dramatic enhancement of three body recombination rates, and hence increased three body inelastic losses. Inelastic magnetic field dependent losses therefore clearly signify the presence of a Feshbach resonance. As the scattering length magnitude is enhanced close to the centre of a resonance, the thermalisation rates for radial and axial components of a trapped atomic ensemble are liable to increase close to a resonance, thus magnetic field dependent thermalisation rates are also a resonance signifier.

2.4.3 Other Coupling Mechanisms

Coupling between atomic and bound molecular states may also be achieved by optical means [79] (optical Feshbach resonances) or through the

application of radio-frequencies, or oscillating magnetic fields [11]. Coupling between molecular states via Feshbach resonances has also allowed detailed molecular spectra to be obtained, most notably in diatomic ^{133}Cs [16], whilst perhaps the most intriguing resonance observations have been those of resonance between free atomic and bound triatomic molecular states in ^{133}Cs [36], so called 'Efimov states'.

2.5 Forced Evaporative Cooling

Evaporative cooling of a single-species atomic ensemble is implemented in order to increase both the atom number density and the phase-space density. From a trapped ensemble with mean vertical energy component $\langle E_v \rangle = k_B T_v$ (where T_v is the width of the energy distribution along the vertical axis, analogous to the temperature but in a non-thermalised sample), atoms which have vertical components of energy above $\tilde{E}_v = \eta \langle E_v \rangle$ are removed from the trap through radio-frequency induced transfer into non-magnetically trappable states. This results in a reduction in the mean energy of the atoms remaining in the trap. The energy selectivity of this process arises through targeting atoms which oscillate to positions highly displaced from the magnetic trap centre, hence have a high combined kinetic and potential energy. Neglecting the effect of gravity, the B-field of the magnetic trap increases with displacement. Thus appropriate selection of radio frequency effectively places an 'RF knife' at a constant energy contour a fixed energy away from the trap centre. Atoms traversing this energy contour will be removed from the trap (assuming an infinitely 'sharp' RF knife).

2.5.1 Gravitational Sag

As atoms magnetically trapped in an Ioffe-Pritchard trap are gravitationally 'sagged' below the trap B-field minimum, atoms vertically below the centre of the trapped atom cloud are subject to higher B-fields than those vertically above the cloud centre. The atomic energy contour targeted by a single radio frequency is fundamentally a surface of constant magnetic field. Thus depending on the selected radio-frequency, an 'RF knife' will prefer-

entially remove atoms from either above or below the atom cloud centre. Effectively atoms with vertical energy component $\eta\langle E_\mathrm{v}\rangle$ may be removed from the magnetic trap by the absorption of one of two different radio-frequencies.

2.5.2 Cutting Surface

The frequency of the 'RF knife' used to evaporate atoms is maintained to cut away atoms with energy $\tilde{E}_\mathrm{v} = \eta k_\mathrm{B} T_\mathrm{v}$. Providing the atoms remaining after each evaporation stage fully thermalise prior to increasing the depth of the 'cut' maintaining evaporation at constant η ensures that the fraction of atoms removed from the trap at each 'cut' is the same, *i.e.* $\Delta N/N$ is constant. The fraction of the atom cloud's energy $\Delta E/E$ which is contained in the $\tilde{E}_\mathrm{v} \geq \eta k_\mathrm{B} T_\mathrm{v}$ tail of the Boltzmann energy distribution is also constant for constant η. As thermalisation of the atom cloud results in the energy removed during an RF cut ΔE being distributed between all of the remaining constituent atoms, the fractional drop in atom cloud temperature $(\Delta T/T)$ after each evaporation stage is also constant. This simple model, which considers only elastic collisions, demonstrates that for RF evaporation at a constant η the reduction in temperature ΔT achieved through loss in atom number ΔN is given by:

$$\frac{\Delta T}{T} = \alpha \, \frac{\Delta N}{N} \quad , \quad i.e:\ \ T \propto N^\alpha \quad . \tag{2.50}$$

where N and T are the number of trapped atoms and temperature of the atomic ensemble remaining in the magnetic trap. The value of α is dependent upon η and is characteristic of the evaporation efficiency. The rate at which evaporation may proceed depends upon the elastic and inelastic collision rates within the trap. For high elastic to inelastic collision ratios a higher value of η and longer evaporation duration will result in greater evaporation efficiency. The opposite is the case for low elastic to inelastic collision ratios. Thus the rate at which evaporation proceeds is best optimised experimentally, from which optimisation the efficiency α may be determined. In order to achieve Bose-Einstein condensation, the key parameter to maximise during evaporation is the phase-space density (PSD):

$$\mathrm{PSD} = n \, \lambda_{\mathrm{dB}}{}^3 \quad , \tag{2.51}$$

where n is the atom number density and λ_{dB} the de Broglie wavelength. Substituting the expressions for atom number density in a harmonic trap (equation B.27) and de Broglie wavelength (equation 1.3) into equation 2.51, the phase-space density is found to be proportional to the total atom number, and inverse cube of the ensemble temperature:

$$\text{PSD} \propto \frac{N}{T^3} \quad . \tag{2.52}$$

This leads to the relation between atom number and phase-space density of:

$$\text{PSD} \propto N^{-\gamma} \quad , \tag{2.53}$$

where $\gamma = 3\alpha - 1$ is the evaporation efficiency with which the phase-space density is increased. The constant of proportionality depends upon the parameters of the magnetically trapped atom cloud prior to evaporation. The optimised evaporation efficiencies for ^{87}Rb and ^{133}Cs in this experiment are contained in section 5.4.

Chapter 3

Experimental Apparatus

The two-species nature of the collisional studies described in chapters 5 necessitates the construction of an extensive apparatus, which is described fully in this chapter. From laser frequency generation, to the shape of the magnetic trap, every aspect of the apparatus is tailored for use with both ^{87}Rb and ^{133}Cs. This results in a far greater level of operational complexity than that required for a single atomic species, which in itself would prove a formidable task. Optimisation and characterisation of the apparatus performance also provides a significant challenge. A full description of this process is given in chapter 4.

3.1 Overview

The experimental apparatus consists of a two-species double MOT system from which an Ioffe-Pritchard type 'baseball' magnetic trap is loaded (see schematic figure 3.1). Alkali metal dispensers (AMDs) are the atom source for a two species cold atomic beam produced by the pyramid MOT (section 3.4). The cold atomic beam passes through the apex of the pyramid and a constriction in the vacuum system before being captured in two overlapped 6 beam MOTs in the science region of the apparatus (section 3.5). Two ion pumps and a non-evaporable getter (NEG) pump in conjunction with the constriction ensure the pyramid MOT and science regions of the vacuum chamber are differentially pumped (section 3.3). This allows the pyramid
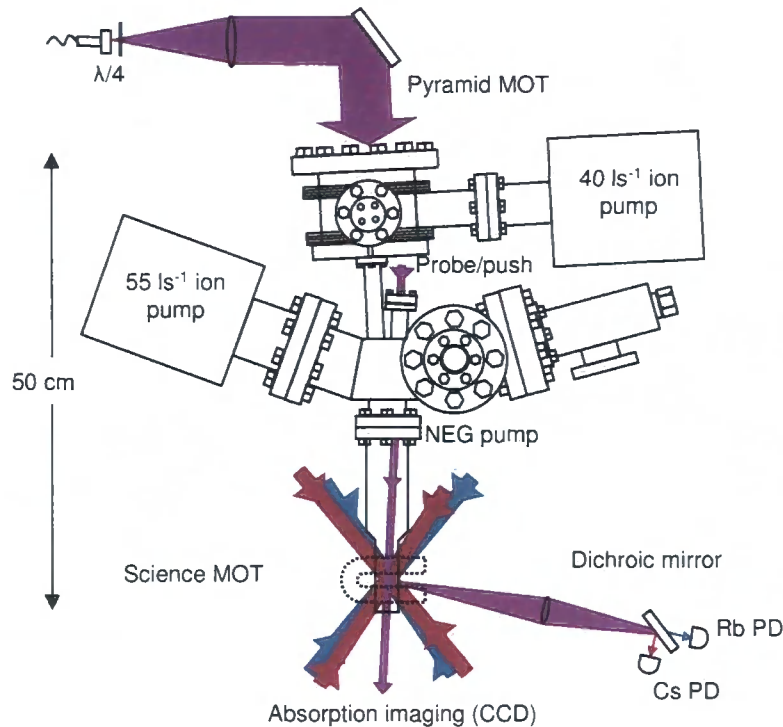
Figure 3.1: Schematic diagram of the two species double MOT apparatus. A pyramid MOT produces a two-species cold-atomic beam from a background vapour of Rb and Cs. This beam passes through a differential pumping tube, and into the science region of the apparatus, where it is captured in two overlapped six beam science MOTs. Atoms are then transferred into a Ioffe-Pritchard magnetic trap (dotted line) where collisional studies are carried out. The intensity and alignment of the four MOT beams in the plane of the table are controlled independently for each species. Each beam contains both cooling and repumping light. In the vertical direction, the cooling and repumping light for both ^{87}Rb and ^{133}Cs are aligned along a single beam path (not shown). The number of ^{87}Rb (^{133}Cs) atoms loaded into the science MOT is monitored by measuring the science MOT fluorescence transmitted (reflected) by a dichroic mirror and imaged onto a calibrated photodiode (PD). Imaging the atomic absorption of a probe beam onto a CCD camera provides numeric and spatial information about the trapped clouds.

MOT to provide a captured flux in excess of 1×10^7 atoms s^{-1} for each species in the science MOT, whilst maintaining a single species atom lifetime in the magnetic trap of 100 s. Atom ensembles from the science MOT are aligned with the centre of the magnetic trap in a compressed MOT stage (section 3.7.1) and pre-cooled in an optical molasses phase (section 3.7.2) prior to optical pumping into single Zeeman sublevels for each species (section 3.7.3). The magnetic trap is then switched on (section 3.6.3) to simultaneously capture ensembles of both atomic species. This provides the starting point for investigation of single species and interspecies cold collisions in a magnetic trap. Full spatial distributions of atoms released from the magnetic trap and MOT are obtained through absorption imaging (section 3.8.2), whilst calibrated dichroic fluorescence imaging (section 3.8.1) is used to monitor the number of atoms initially loaded into the MOT.

3.2 Laser System

The apparatus presented above requires several laser frequencies to operate. As part of this work we developed a reliable laser system incorporating several novel improvements to standard laser locking techniques.

3.2.1 Optical Frequencies

Both the MOTs require cooling and repumping light for each species, whilst transfer to the magnetic trap requires additional laser frequencies in order to polarise the atomic ensembles into single Zeeman sublevels of the lower hyperfine ground states (see figure 3.2). For two-species MOT operation, atom losses due to light-assisted interspecies cold collisions are eliminated by spatially displacing one of the science MOTs with a resonant laser beam (section 5.1.3). Absorption imaging of atoms also requires a beam resonant with the closed cooling transition for both species. A summary of the required laser frequencies can be found in table 3.1.
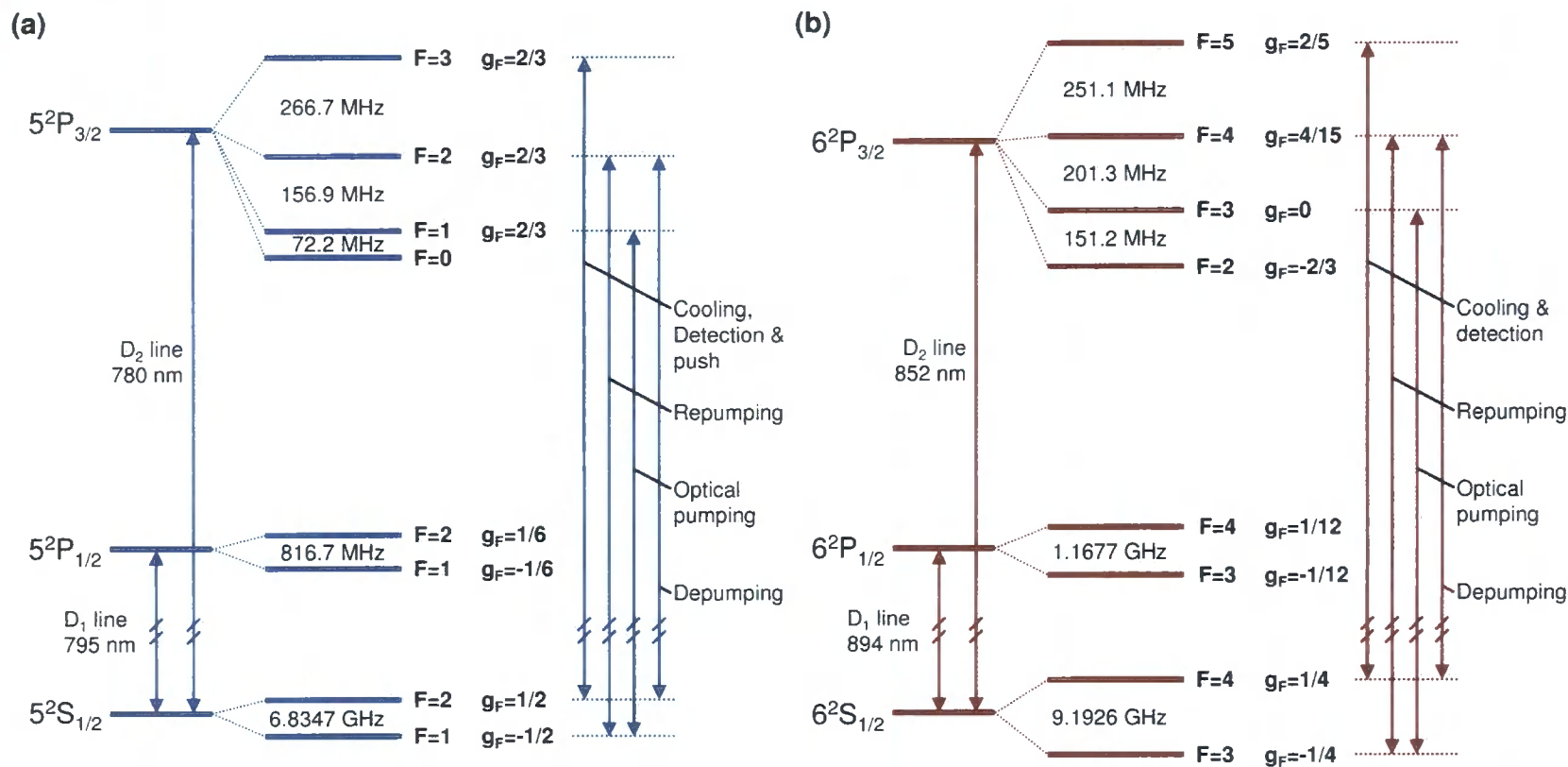
Figure 3.2: Hyperfine structure of ^{87}Rb (a) and ^{133}Cs (b) in the ground state and first electronic excited states. Optical transitions with which lasers from the apparatus described below are resonant/close to resonance are indicated.

	^{87}Rb		^{133}Cs	
	Transition	Detuning (MHz)	Transition	Detuning (MHz)
Pyramid	$F = 2 \rightarrow F' = 3$	-16.9(2)	$F = 4 \rightarrow F' = 5$	-16.1(2)
MOT	$F = 2 \rightarrow F' = 3$	-12.4(2)	$F = 4 \rightarrow F' = 5$	-10.3(2)
Push	$F = 2 \rightarrow F' = 3$	0.0(2)	$F = 4 \rightarrow F' = 5$	0.0(2)
CMOT	$F = 2 \rightarrow F' = 3$	-20.5(2)	$F = 4 \rightarrow F' = 5$	0.0(2)
Molasses	$F = 2 \rightarrow F' = 3$	-60.0(2)	$F = 4 \rightarrow F' = 5$	-60.0(2)
Depumping	$F = 2 \rightarrow F' = 2$	0.0(2)	$F = 4 \rightarrow F' = 4$	0.0(2)
Probing	$F = 2 \rightarrow F' = 3$	-0.5(2)	$F = 4 \rightarrow F' = 5$	-0.3(2)
Repumping	$F = 1 \rightarrow F' = 2$	0.0(2)	$F = 3 \rightarrow F' = 4$	0.0(2)
Optical pumping	$F = 1 \rightarrow F' = 1$	0.0(2)	$F = 3 \rightarrow F' = 3$	0.0(2)

Table 3.1: Breakdown of required laser frequencies for the experiment. Detunings and their errors show the measured values following optimisation.

3.2.2 Optical Layout

All of the required laser frequencies (table 3.1) are derived from six diode lasers and transferred from a separate laser table to the vacuum apparatus table using polarisation maintaining optical fibres. This de-couples the optical frequency stabilisation (section 3.2.1) from the MOT beam alignment. For each species a cooling (repumping) master laser frequency stabilised using the dichroic atomic vapour laser lock (DAVLL) (section 3.2.4) operates at the pyramid MOT cooling (repumping) frequency. All additional frequencies are derived using acousto-optic modulators (AOMs), with power for the science MOT cooling light generated through optical injection of a slave laser. The scheme used to derive these additional frequencies for ^{87}Rb is outlined in figure 3.3. The ^{133}Cs frequency derivation operates on the same principles. Light for the pyramid MOT, optical pumping, and imaging of both atomic species is combined using dichroic optics prior to coupling into single optical fibres. The full laser setup with which this scheme is implemented is shown in figure 3.4 and described in the following sub-sections.
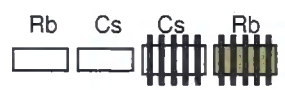
□ ■ ■	Raised 'Optical breadboard' at 152.4 mm; magnetic coil obstruction; general obstruction.	▬ ▬ ◤ ▬	25.4 mm ϕ optics: Mirror; 50:50 beam-splitter; uncoated wedged blank; dichroic beam-splitter.
—·—·— ▭	Trap centre; fused silica cell.	◣ ◢ ◥ ◥	Mirrors: 40 mm ϕ; 40 mm ϕ; 50 mm ϕ; 100 mm ϕ. (reflecting surface uppermost)
▬ ► ⋯►	^{133}Cs laser beams: cooling; repump; 21.8(2) mm ϕ cooling + repump.	— — Z — F — A	Quarter waveplate: Low order; cemented zero order; true zero order.
▬ ► ⋯►	^{87}Rb laser beams: cooling; repump; 21.8(2) mm ϕ cooling + repump.	— — Z — F — A	Half waveplate: Low order; cemented zero order; true zero order.
▬ —	Combined ^{133}Cs and ^{87}Rb light: 40.8(8) mm ϕ; 12.7 mm ϕ.	Pyramid ◿ Pyramid ◣	Optical fibre couplers (including fibre name): Input; output.
^{87}Rb Slave ⬜ CCD	Laser (including name); CCD camera (Andor iXon 885).	FR ➡ ⦚AOM5	Faraday rotator; optical isolator, acousto-optic modulator.
— ND ▬▬ ▬▬LA	Neutral density filter; shutter 2 mm ϕ; shutter 6mm ϕ.	⊠ ⊠ ⊠b ⊠50:50	Beam-splitters: Narrowband polarising; rotatable narrowband polarising; broadband polarising; 50:50 beam-splitting (all polarisations).
⬭f100 ⬭f100d ⊠	Singlet lenses; doublet lens; anamorphic prism pair (lenses with focal length in mm).	Rb Cs Cs Rb ▭ ▭ ||||| |||||	Rb 7 cm vapour cell; Cs 5 cm vapour cell; Cs 5 cm DAVLL cell; Rb 5 cm heated DAVLL cell.
⊙ ⦃⊙ ⊙LA ⦃⊙	Photodiodes: Single 1 mm^2; differencing pair 1mm^2; single large area 100 mm^2.		

Table 3.2: Optics key.
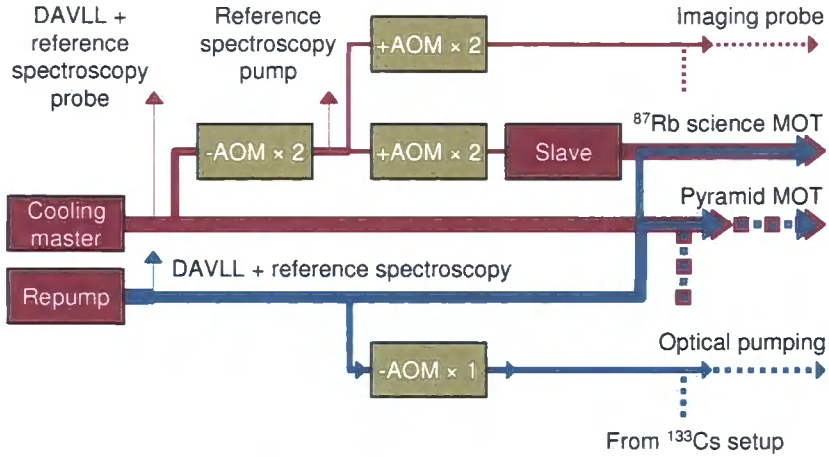
Figure 3.3: Schematic diagram of the optical layout for ^{87}Rb. Three lasers provide light for cooling, repumping, imaging and optical pumping in the double-MOT system. The ^{133}Cs layout is similar. Line thickness indicates relative beam power. Acousto-optic modulators (AOMs) upshifting (+) and downshifting (-) the laser frequency in double-pass ($\times 2$) and single-pass ($\times 1$) configurations allow independent control of all frequency detunings. Larger shifts in frequency required for optical pumping and depumping stages are obtained by additionally applying a DC voltage offset to the dichroic atomic vapour laser lock (DAVLL) signal in order to offset the laser lock point. All light is transferred from the laser table to the experiment via polarisation-maintaining optical fibres. For the pyramid MOT, optical pumping, and imaging light, dichroic beam-splitters are used to combine 780 nm (solid lines) and 852 nm (dashed lines) beams before transmitting both wavelengths down single fibres.

3.2.3 Lasers

The six diode-lasers from which all of the required optical frequencies are derived consist of one commercial 'master' laser, one 'home-built' master laser and one 'home-built' slave laser for each atomic species.

Commercial Master Lasers

The frequency of all cooling, depumping, and probing light used in this apparatus is derived from two commercially purchased grating stabilised extended
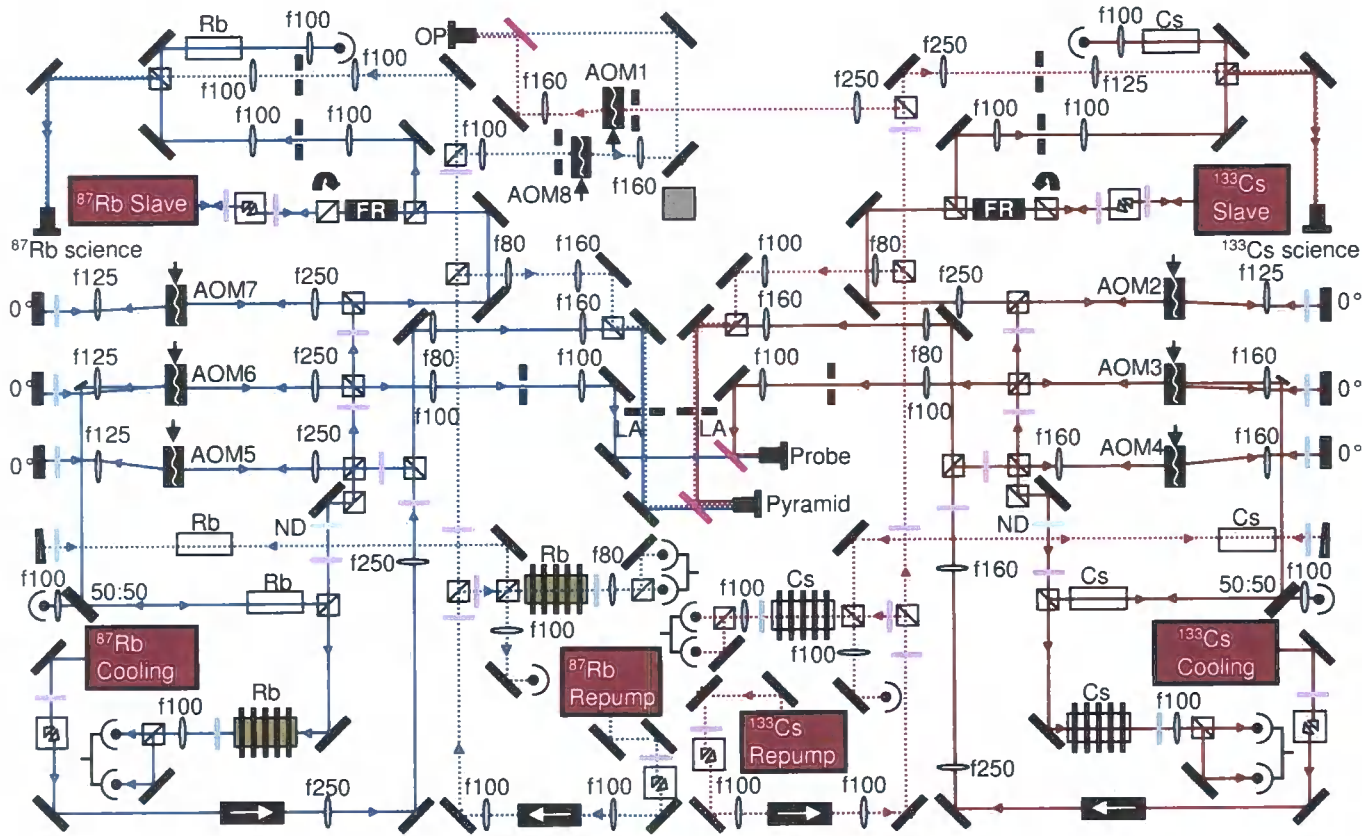
Figure 3.4: Laser table optical setup. Beam-paths of laser light close to resonance with the cooling (solid lines) and repumping (dashed lines) transitions in ^{87}Rb (Blue) and ^{133}Cs (Red) are shown. All required laser frequencies are transferred to the vacuum apparatus table using polarisation-maintaining optical fibres. The key to the symbols used in this figure is contained in table 3.2.

cavity diode 'master' lasers (a Toptica DL100 and a Sacher Lasertechnik Lynx
TEC 120 providing $\simeq$ 220 mW of light at 780 nm and 150 mW of light at 852
nm respectively). Both laser systems employ piezoelectric actuators to con-
trol the angle of a diffraction grating which, in conjunction with one facet of
the laser diode, comprises the extended laser cavity. Laser frequency control
over ranges > 20 GHz is achieved by increasing the current through the laser
diode in proportion to the voltage applied to the piezoelectric actuator. In
addition to grating stabilisation, both laser systems incorporate temperature
stabilisation of laser diodes through feedback control of Peltier coolers.

Home-built Lasers

All 'home-built' diode lasers [80] are temperature stabilised using feedback
controlled Peltier coolers (Wavelength electronics MPT 2500). In both laser
designs the ^{87}Rb (^{133}Cs) diodes are driven using positive (negative) cur-
rent driver EW1291 (EW1206) developed by the Oxford University central
electronics workshop.

Repumping Master Lasers

One 'Littrow' configuration home-built grating stabilised extended cavity
diode laser [81, 82] provides repumping and optical pumping light for each
atomic species. Each laser is built to the 'compact mirror mount' design
developed by K. J. Weatherill *et al.* [83]. In this design the laser diode
is mounted in a collimation tube package (Thorlabs LT240P-B), with the
whole assembly mounted in an internally bored cuboidal aluminium block of
$l \times w \times h = 80.0 \times 38.0 \times 38.0$ mm such that the laser output is towards the
centre of the block. On the opposite face of this block, an ultra-stable kinetic
0.5 inch mirror mount (Thorlabs KS05) is mounted, upon which a piezoelec-
tric actuator is fixed using epoxy. On the opposite side of the piezoelectric
actuator, the laser diffraction grating is similarly fixed. The aluminium block
is screwed onto a solid-aluminium base of $l \times w \times h = 50.0 \times 38.0 \times 67.0$ mm
using nylon screws, with a Peltier cooler sandwiched between the two alu-
minium blocks. This allows a sufficient rate of thermal transfer for effective
temperature stabilisation of the laser diode using the Peltier cooler.

Collimated laser light from the diode output facet is reflected from the diffraction grating out of the aluminium block, whilst the mirror mount is adjusted such that the first diffracted order of the grating is injected back into the facet. The ^{87}Rb (^{133}Cs) laser uses a 120 mW 780 nm Sharp GH0781 (50 mW, 852 nm SDL-5401-G1) laser diode . The voltage applied to the piezoelectric actuator on which each laser diffraction grating is mounted, and hence the optical frequency of each laser, is controlled using Oxford University Piezo driver EW1145. Laser frequency drifts induced by lab-temperature fluctuations are minimised through encasing the laser unit in an aluminium box, with a 10×14 mm anti-reflection window allowing transmission of the laser output beam.

Slave Lasers

The slave laser design consists simply of a laser diode in a collimation tube package (Thorlabs LT240P-B), mounted in a temperature stabilised aluminium block. The ^{87}Rb (^{133}Cs) slave laser incorporates an 80 mW Sanyo 780nm DL-7140-2015 (100 mW SDL 5411) laser diode.

3.2.4 Laser Frequency Stabilisation: The Dichroic Atomic Vapour Laser Lock (DAVLL)

The lasers used in this apparatus must operate reliably at absolute frequencies less than a natural linewidth ($\simeq 6$ MHz) away from atomic cooling and repumping transitions. Considering these transitions occur at optical frequencies of several hundred THz, simultaneously achieving the required frequency stability in all six laser systems used in this apparatus provides a significant challenge. Many different approaches are taken to achieving laser stabilities at this level. The method used in this apparatus is that of the dichroic atomic vapour laser lock (DAVLL) [84, 85]. This scheme does not require 'dithering' of the laser frequency [86], or the use of expensive electro-optical modulators (EOMs) necessary in external radio-frequency phase modulation schemes [87, 88]. Compared to other dither-free techniques, the DAVLL locking scheme offers an extremely large capture range (typically several GHz).

This feature is utilised here to rapidly switch the stabilised laser frequencies over several hundred MHz, allowing optical pumping and depumping transitions to be accessed using the repumping and cooling laser systems respectively.

Principles

Dichroic atomic vapour spectroscopy utilises the Zeeman effect in introducing a dichroism between the optical frequencies at which the absorption of light of different circular polarisations by an atomic vapour is maximised. The medium for spectroscopy is an atomic vapour cell in a region of an applied magnetic field. A linearly polarised laser beam at an optical frequency close to that of the centre of a manifold of Doppler broadened atomic transitions (f_c) passing through the vapour cell with wave vector parallel to the applied B-field is used to probe the atomic sample. With the Zeeman degeneracy lifted, transitions from an $|\bar{F}, m_F\rangle$ ground state to an $|F', m_F' = m_F + 1\rangle$ excited state occur at higher resonant optical frequencies than those to an $|F', m_F' = m_F - 1\rangle$ excited state. A linearly polarised laser beam can be decomposed into two laser beams of equal optical power and opposite circular polarisations σ^+ and σ^-, driving optical transitions where $\Delta m_F = +1$ and $\Delta m_F = -1$ respectively. The line centres of the absorption profiles for the σ^+ and σ^- components of such a laser beam are displaced to higher and lower frequencies respectively in the presence of an applied B-field compared to the Zeeman degenerate case where they are coincident (this affect can be seen in figure 3.5 (b)). The degree of frequency separation depends upon the magnitude of the applied B-field and also on the relative Zeeman shifts of individual hyperfine atomic states. Frequency shifts comparable to the thermal Doppler width are generated in ^{87}Rb and ^{133}Cs through the application of B-fields < 100 G.

Implementation

The circular polarisation components of an incident linearly polarised probe beam which are transmitted through an atomic vapour cell are separated using a zero order quarter waveplate and PBS cube (figure 3.5). Each
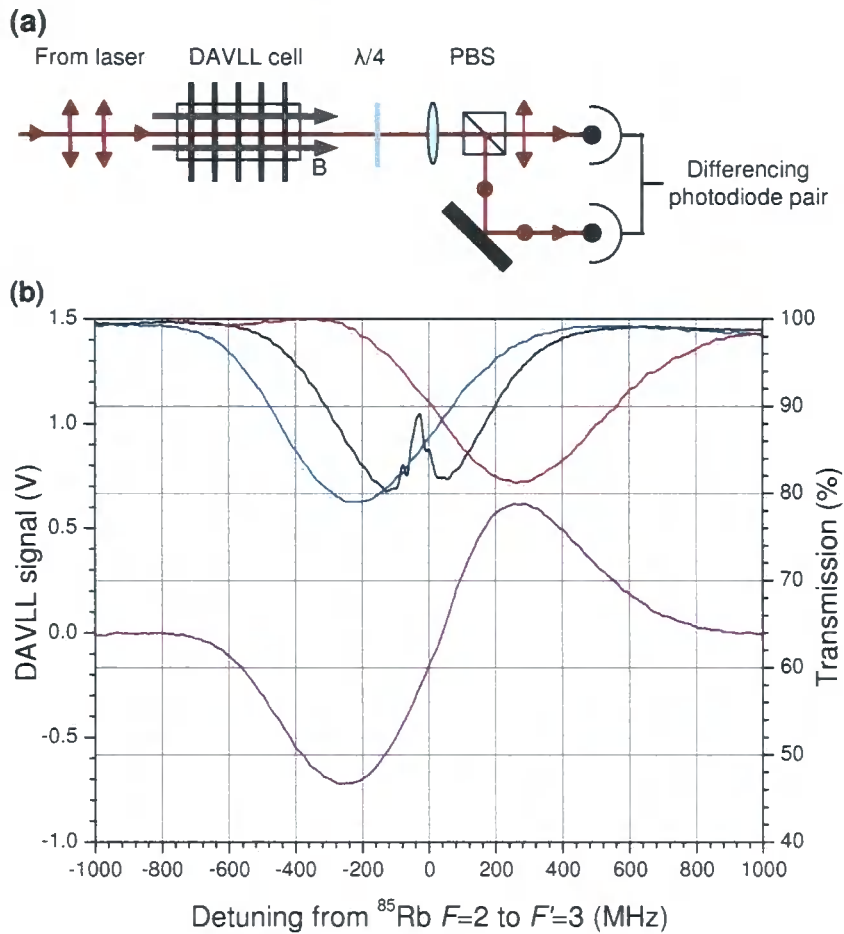
Figure 3.5: (a) A schematic diagram of optics used to generate a dispersion signal for the dichroic atomic vapour laser locking scheme. After transmission through the vapour cell, a quarter waveplate ($\lambda/4$) converts the two orthogonal circular laser beam components of which the incident linearly polarised laser beam is composed into two orthogonal linear polarisations. After separation using a polarising beam-splitting cube (PBS) the optical power of each polarisation component is measured using a photodiode. The difference between the two signals results in a dispersion signal similar to that shown in (b). (b) DAVLL on the ^{85}Rb $F = 2 \rightarrow F'$ transition, taken from [63]. The left hand scale shows the DAVLL signal (purple); the right hand scale shows the transmission through the cell. The intensity of the two circularly polarised beam components is shown (blue and red) together with the reference sub-Doppler spectrum (black) recorded in a separate cell for calibration.

component is then focused onto one photodiode of a differencing photodiode pair. The photodiode unit outputs a voltage which is proportional to the difference in optical power incident on the two photodiodes (the resulting signal is similar to that of the ^{85}Rb $F = 2 \rightarrow F'$ transition shown in figure 3.5 (b)). When scanning the laser frequency across a Doppler broadened optical transition the photodiode amplification is set to generate a voltage output range of $-10\,\text{V} < V_{\text{PD}} < +10\,\text{V}$. Implementing feedback control of the laser frequency, the laser output is stabilised at a frequency which produces a resultant feedback control input voltage of 0 V. Key features of any laser locking signal are the gradient, expressed in V of response per MHz frequency excursion, capture range (*i.e.* the maximum frequency deviation from which the laser can automatically re-stabilise to the lock-point), and the absolute frequency of the laser lock-point.

Lock-Point

The frequency to which the laser is stabilised can be tuned by either altering the angle of the quarter waveplate (hence applying a bias to one of the photodiodes) or directly applying an electronic voltage offset to the photodiode voltage input of the feedback circuit. The waveplate rotation method is largely independent of fluctuations in the laser intensity, but depending on the lock-point can be highly sensitive to temperature induced polarisation fluctuations [64]. The voltage offset method allows the waveplate angle to be fixed at a position where this effect is minimised, but results in a lock-point susceptible to laser intensity fluctuations. As each master laser setup utilises the application of such a voltage offset to rapidly switch the laser between two frequencies, at least one of the frequency lock-points is susceptible to such intensity fluctuation sensitivity.

The absolute frequency to which the laser is locked is determined by calibrating the DAVLL spectrum against the sub-Doppler absorption features of a hyperfine pumping spectroscopy reference. The combined method for setting the DAVLL lockpoint of each master laser is to first set the quarter waveplate at an angle of $\simeq 45°$ relative to the axis of polarisation of the laser beam incident on the vapour cell. Any adjustments made about this angle are to

compensate for the birefringence of the cell windows. This waveplate angle is found to give the lowest angular dependence on position of zero crossing [64]. With the laser scanning, an electronic voltage offset is then applied to the photodiode voltage input of the feedback control circuit, such that the DAVLL zero-crossing coincides with a peak in the hyperfine pumping spectroscopy signal determined to correspond to the desired locking frequency. The scan range is then reduced, and the DAVLL offset voltage manually tuned until the spectroscopy signal reaches the local maximum corresponding to the peak centre. The use of cemented/true zero order waveplates (rather than low order), in conjunction with high quality PBS cubes is essential in maximising lock-point stability.

Capture Range

The DAVLL locking scheme offers a capture range comparable with the Doppler width *i.e.* several hundred MHz. This allows the stabilised laser frequency to be rapidly changed over this range purely by switching the voltage offset added to the photodiode input signal. This offers much increased frequency switching range compared to that accessible by a single AOM in the double pass configuration, with none of the associated optical power loss. Increasing the applied B-field results in an increased capture range, although increasing the B-fields above $\simeq 125$ G results in an undesirable reduction in the dispersion signal gradient.

Gradient

The gradient of the DAVLL dispersion signal in the region of the lock point determines the laser lock sensitivity. This is expressed as the change in DAVLL signal per MHz frequency deviation. This increases with applied B-field until the Zeeman splitting of the σ^+ and σ^- absorption peaks (which is of the order $\simeq 1.4$ MHz G^{-1}) exceeds the Doppler width. For ^{87}Rb at 20°C the gradient is optimised at a B-field of $\simeq 100$ G. The DAVLL signal gradient for ^{87}Rb can be further increased either by increasing the gain of the photodiode detector pair, or increasing the on-resonance vapour cell absorption. As any electronic amplification of photodiode signal is accompanied

by a comparable amplification of electronic noise, it is most desirable from
a signal-to-noise perspective to increase the raw signal, *i.e.* the on-resonant
vapour cell absorption. As the DAVLL signal is composed of two Doppler absorption profiles, the maximum signal amplitude is given for an on resonance
vapour cell absorption of 100 % of incident laser light. The gradient however
depends on the signal amplitude variation per unit frequency deviation of the
DAVLL signal. The peak gradient for ^{87}Rb is experimentally found to occur
when the on-resonance Doppler absorption is $\simeq 75$ % [63]. At 20°C, the
on-resonance Doppler absorption of the ^{87}Rb $F = 1 \rightarrow F' = 0, 1, 2$ transition
in a 4.5 cm vapour cell is only 7(1) % (figure 3.6). Even using a 7 cm vapour
cell, the absorption is only increased to $\simeq 12$ %. Rather than increasing the
vapour cell length (and making the apparatus more cumbersome), the ^{87}Rb
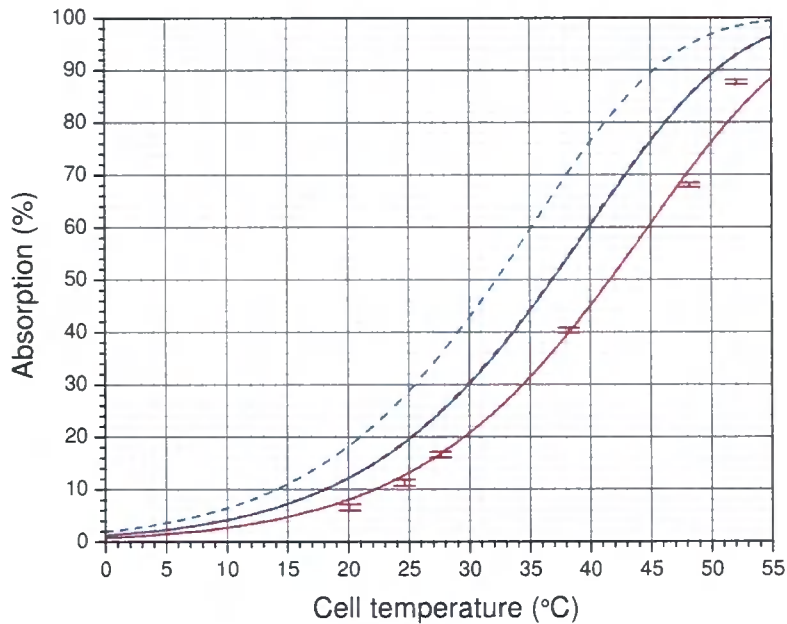
Figure 3.6: Temperature dependence of peak absorption through a Rb vapour
cell of a laser beam resonant with ^{87}Rb optical transitions. Blue (Red) solid
line is theoretical absorption of light resonant with the $F = 2 \rightarrow F' = 1, 2, 3$
($F = 1 \rightarrow F' = 0, 1, 2$) transition in a 4.5 cm long cell. Dashed lines show
corresponding absorption through a 7.0 cm long cell. Red data points are
experimentally measured absorption of light resonant with the $F = 1 \rightarrow$
$F' = 0, 1, 2$ transition in a 4.5 cm long cell.
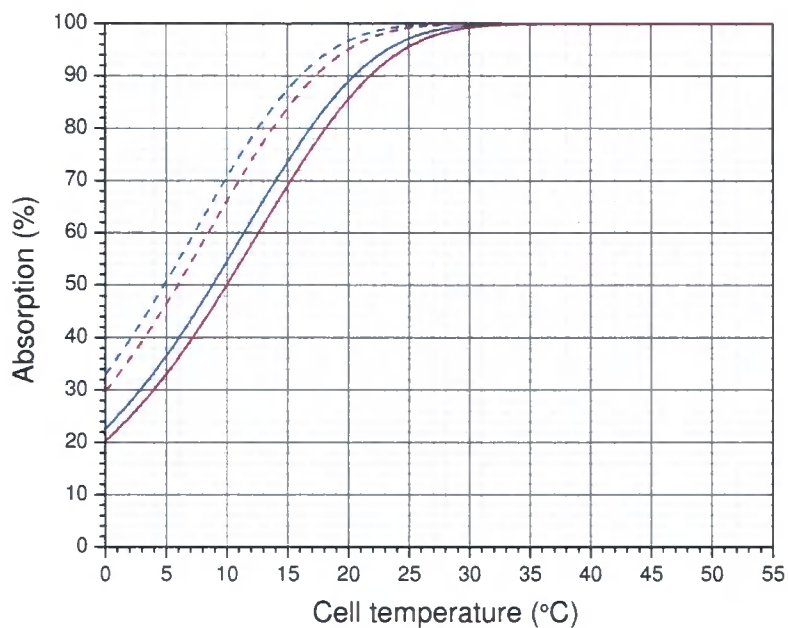
Figure 3.7: Temperature dependence of peak absorption through a Cs vapour cell of a laser beam resonant with ^{133}Cs optical transitions. Blue (Red) solid line is theoretical absorption of light resonant with the $F = 4 \rightarrow F' = 3, 4, 5$ $(F = 3 \rightarrow F' = 2, 3, 4)$ transition in a 4.5 cm long cell. Dashed lines show corresponding absorption through a 7.0 cm long cell.

vapour pressure, and hence the vapour cell absorption is increased by heating the Rb DAVLL cell. The ^{133}Cs DAVLL cell is constructed from annular magnets pressed out of permanently magnetic material ('refrigerator magnet') to tightly house a 4.5 cm vapour cell. The magnets are spaced using copper gaskets to optimise the magnetic field, and the whole unit is enclosed in a die-cast box. The ^{133}Cs peak Doppler absorption at 20°C for a 4.5 cm vapour cell is in excess of 85 % (figure 3.7). This could be optimised by cooling the cell, or using a shorter cell, but the gradient of the present DAVLL signal provides a suitable level of discrimination to maintain the laser-lock for the ^{133}Cs master cooling and repumping lasers.

Heated DAVLL

The first heated Rb DAVLL cell design implemented on this apparatus used annular magnets pressed out of permanently magnetic material ('refrigerator magnet') to produce the axial magnetic field and house the central region of a 4.5 cm vapour cell. Both ends of the vapour cell were housed in brass end-caps, each heated with a Peltier element. This unit was successful in allowing access to cell temperatures $17 < T < 50$ °C [64], but was limited in performance by poor thermal stability of the permanent magnets. These stability issues have been largely eliminated through the development of a solenoid DAVLL cell unit. Passing a 4.0 A current through a solenoid coil in which a 4.5 cm vapour cell is housed simultaneously provides near optimum B-field and (through Joule heating) cell absorption with which the DAVLL signal amplitude is maximised [63]. Implementation of this solenoid DAVLL cell has ensured that the long-term stability of the ^{87}Rb master cooling and repumping lasers does not limit the apparatus operation.

3.2.5   Cooling Laser System

The commercial master lasers are operated at the pyramid MOT cooling light frequencies. This allows light from the cooling master lasers to be transferred directly to the pyramid MOT without the $\simeq 15(30)$ % power loss which would result from a single (double) pass through an acousto-optic modulator (AOM). The derivation of optical frequencies required for: laser spectroscopy; absorption imaging probe light; slave injection; and pyramid MOT cooling light from the ^{87}Rb and ^{133}Cs master cooling lasers can be seen in schematic figures 3.8 and 3.9 respectively. This arrangement provides $\simeq 110$ mW (54.0 mW) of power from the ^{87}Rb (^{133}Cs) master laser at an optimised detuning of -17.0(2) MHz (-16.1(2) MHz) for injection into the pyramid MOT fibre. The remaining $\simeq 30$ mW of power from each laser provides all of the light required for laser spectroscopy, probing of atoms in the science cell, and injection of the science MOT slave lasers. The majority of the ^{87}Rb (^{133}Cs) laser power diverted from the pyramid fibre is coupled into 110 MHz centre frequency 'spectroscopy' AOM5 (AOM4) operating at 115.7(2) MHz (110.2(2) MHz) in a double pass configuration. The AOM
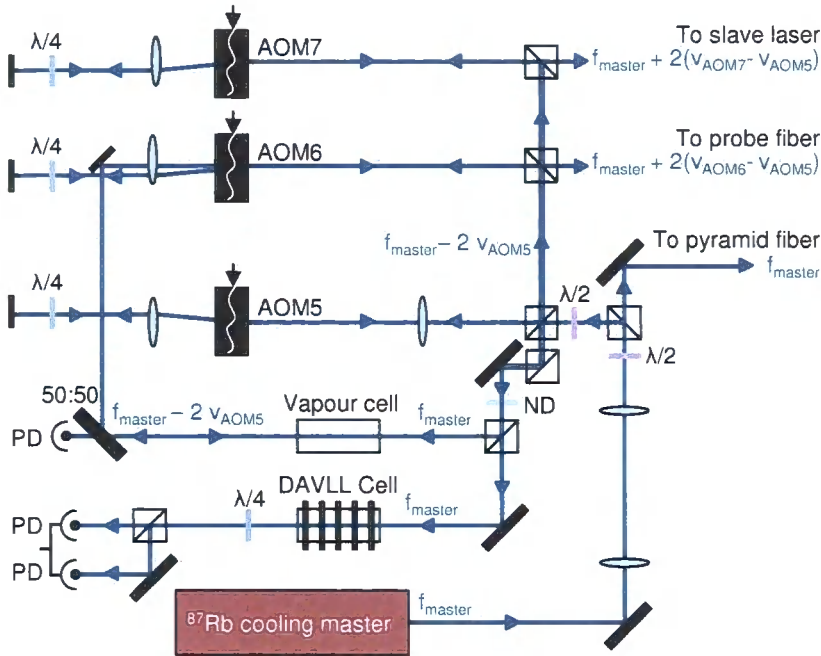
Figure 3.8: Schematic diagram illustrating derivation of spectroscopy, probing, and slave laser injection beams from the [87]Rb master cooling laser optical output. Note the frequency difference between hyperfine pumping spectroscopy pump and probe beams transmitted through the vapour cell. The key to the symbols used in this figure is contained in table 3.2.

is aligned to optimise the proportion of incident light down-shifted into the first order of the diffraction profile, resulting in a $\simeq$ 6.7 mW [87]Rb (9.6 mW) [133]Cs) laser beam at a frequency -248.4(2) MHz (236.5(2) MHz) detuned from resonance with the cooling transition. The rest of the diverted power is polarisation purified using a polarising beam-splitting cube (PBS) before separation into two probing beams. One 103 μW [87]Rb (46.3 μW [133]Cs) beam is directed into a DAVLL vapour cell in order to generate a laser locking signal. The other 9.3 μW beam is directed into a 7.0 cm [87]Rb (5.5 cm [133]Cs) atomic vapour cell. The laser light from this 'probe beam' which is transmitted through the vapour cell is focussed onto an amplified BPX65 photodiode. Counter-propagated with this probe beam is a 160 μW 'pump' beam, derived from light double passed by the 'spectroscopy' AOM. These beams generate a Doppler free hyperfine pumping spectroscopy signal to which the cooling master laser lock-point is referenced (section 3.2.5). The remaining opti-
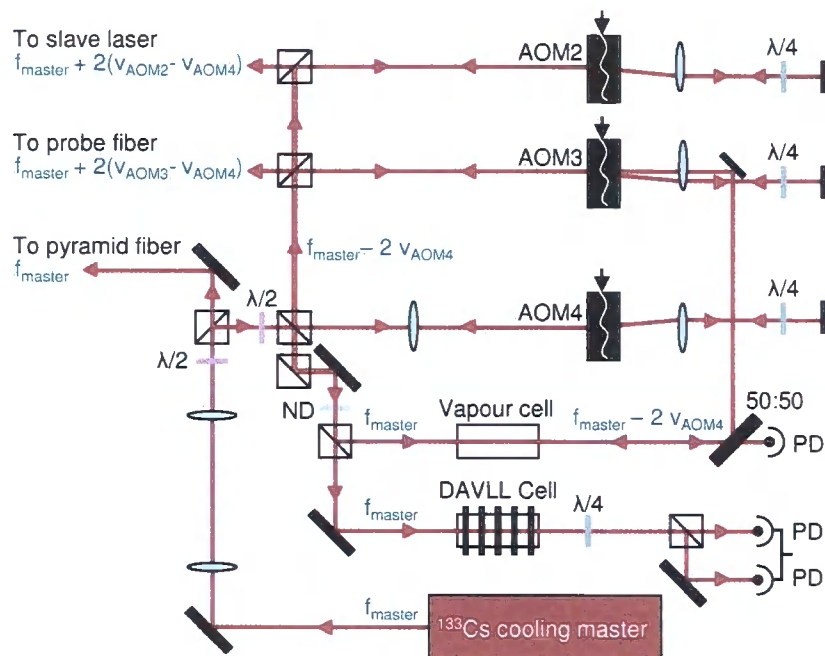
Figure 3.9: Schematic diagram illustrating derivation of spectroscopy, probing, and slave laser injection beams from the ^{133}Cs master cooling laser optical output. Note the frequency difference between hyperfine pumping spectroscopy pump and probe beams transmitted through the vapour cell. The key to the symbols used in this figure is contained in table 3.2.

cal power transmitted by the 'spectroscopy' AOM is distributed between two AOMs aligned in double pass configurations to maximise the power upshifted into the first order of their respective diffraction profiles. The double-pass output of AOM6 (AOM3) is resonant with the cooling transitions of magnetically trapped atoms in the vacuum apparatus. This light is injected into the 'probe' optical fibre, the output of which is used to probe atoms in the magnetic trap (section 3.8.2). The double pass output of AOM7 (AOM2) is used to inject a slave laser which provides cooling and depumping light for the science MOT.

Hyperfine Pumping Spectroscopy

Hyperfine pumping spectroscopy is used to reference the lock point of the DAVLL stabilisation scheme to an absolute atomic frequency. The optimum

detuning from resonance with the $F = 2 \rightarrow F' = 3$ ($F = 4 \rightarrow F' = 5$) transition in ^{87}Rb (^{133}Cs) for the pyramid MOT cooling light is estimated to be: $0 \text{ MHz} < \Delta f_{\text{Laser}} < 20 \text{ MHz}$ for both species. The laser frequency at which sub-Doppler peaks occur in the spectroscopy signal is tuned by altering the operating frequency of the downshifting AOM from which the spectroscopy pump beam is derived for each species (AOMs 5 and 4 for ^{87}Rb and ^{133}Cs respectively). The ^{87}Rb (^{133}Cs) spectroscopy crossover peak $F = 2 \rightarrow F' = 2,3$ ($F = 4 \rightarrow F' = 4,5$) is used as the frequency reference for the cooling master laser lockpoint. The master laser detunings from resonance with the cooling transitions for ^{87}Rb and ^{133}Cs as a function of AOM frequency are:

$$\Delta f(^{87}\text{Rb }) = f_{\text{AOM5}} - 132.7(2) \text{ MHz} \quad \text{and} \qquad (3.1)$$

$$\Delta f(^{133}\text{Cs }) = f_{\text{AOM4}} - 126.3(2) \text{ MHz} \quad \text{respectively.} \qquad (3.2)$$

The frequency offsets used in equations 3.1 and 3.2 are the frequency separation of the laser crossover peaks from the cooling transitions as measured in the Durham laboratory (table 3.3). With AOM5 and AOM4 (section

	Peak separation	Steck (MHz)	Durham (MHz)
^{87}Rb	$(F = 2 \rightarrow F' = 3) - (F = 2 \rightarrow F' = 2,3)$	133.325(5)	132.7(2)
^{133}Cs	$(F = 4 \rightarrow F' = 5) - (F = 4 \rightarrow F' = 4,5)$	125.50(1)	126.3(2)

Table 3.3: Spectroscopy frequency calibrations. A comparison between the calibrations from the work of D. Steck et al. [89, 90] and those measured using the experimental apparatus at Durham (Although less precise, the Durham measurements are used in detuning calculations for the Durham apparatus).

A.2) aligned at central operating frequencies of 120.7 MHz and 114.3 MHz respectively, tuning the AOM frequencies over a range of ± 12 MHz allows the pyramid MOT cooling light detuning from resonance for both species $\Delta f_{\text{pyramid}}$ to be independently varied from $0 < \Delta f_{\text{pyramid}} < 24$ MHz.

Slave Lasers

Home-built, temperature stabilised diode slave lasers are used to provide all optical power for the science MOT cooling light, in addition to depumping light for optimal transfer of atoms into the magnetic trap (section 3.7.3). Each slave laser is injected with $\simeq 200$ μW of light derived from the master cooling laser. Optical isolation of the slave laser diodes from back-reflection is achieved using a 45° Faraday rotator in combination with a pair of PBS cubes (appendix A.3). Light derived from the master laser is injected into the rejection port of the PBS cube at the isolator output (relative to the slave laser beam path). This light is transmitted by the PBS cube at the isolator input and hence focused by the diodes collimation lens into the slave laser diode facet. As the beam used to inject the slave laser is first double-passed through an AOM, the optical frequency at which the slave is injected can be optimised independently of that of the cooling master laser. This also allows the slave laser frequency to be quickly switched by changing the AOM operating frequency, a feature which is utilised in the compressed MOT, optical molasses, and optical pumping stages of each experiment.

3.2.6 Repumping Laser System

Both repumping lasers used in this apparatus are frequency referenced using a counter-propagating pump-probe scheme. After transmission through a 7 cm Rb (5 cm Cs) atomic vapour cell 5 % of the 150 μW pump beam (a reflection from a single face of a non AR coated wedged glass blank) is retro-reflected into the vapour cell as the counter-propagating probe beam (figure 3.4). As the pump and probe beam are identical in laser frequency, a hyperfine pumping spectroscopy peak occurs when the frequency output of the repumping laser is resonant with the $F = 1 \rightarrow F' = 2$ ($F = 3 \rightarrow F' = 4$) repumping transition in ^{87}Rb (^{133}Cs). These peaks are used as absolute frequency references with which to monitor the locking point of the repump laser DAVLL frequency stabilisation schemes (section 3.2.4). The optical output power of each repump laser is separated into three main beams providing: Repumping light for the pyramid MOT, repumping light for the science MOT, and light for optically pumping atoms into the lower hyperfine

ground states (section 3.7.3). The pyramid and second MOT light are at the frequency of the repumping transitions, whilst light for optical pumping must be close to resonance with the $F = 1 \rightarrow F' = 1$ and $F = 3 \rightarrow F' = 3$ transitions in ^{87}Rb and ^{133}Cs respectively. This frequency shift is achieved using a combination of an AOM aligned to optimise light downshifted into the first diffraction order, and directly applying a voltage offset to the voltage lock-point of the DAVLL spectroscopy locking electronics. Light diffracted into the first downshifted order by each optical pumping AOM (AOM 8 and 1 for ^{87}Rb and ^{133}Cs respectively) is combined at identical linear polarisations using a dichroic mirror. Both beams are then coupled into a single optical fibre (the OP fibre in figure 3.4). The downshifting AOMs are used in combination with the DAVLL lock-point offset to allow fast optical power switching times ($<< 1\mu$s) for each optical pumping beam.

3.2.7 Optical Coupling to Vaccum Chamber Table

All of the laser light required to trap and cool atoms is transferred from the laser table onto the vacuum chamber table using polarisation maintaining single mode optical fibres (appendix A.4). Each laser beam is coupled into a fibre's collimation lens via a telescope comprising of a pair of AR coated singlet lenses. The focal lengths of each lens pair are experimentally selected to provide the optimum coupling efficiency for that beam. Multiple laser beams for a single atomic species (in the case of the pyramid fibre and the science MOT fibres) are coupled into a single fibre at perpendicular linear polarisations after combination using a PBS cube. Laser beams for different species (in the case of the pyramid, optical pumping, and probe fibres) are combined at identical linear polarisations using dichroic beam splitters (appendix A.5).

3.3 Vacuum Apparatus

In order to trap and cool atoms at sub millikelvin temperatures it is essential to isolate them from thermal atoms at atmospheric pressures and temperatures. This isolation is achieved through trapping atoms in a region
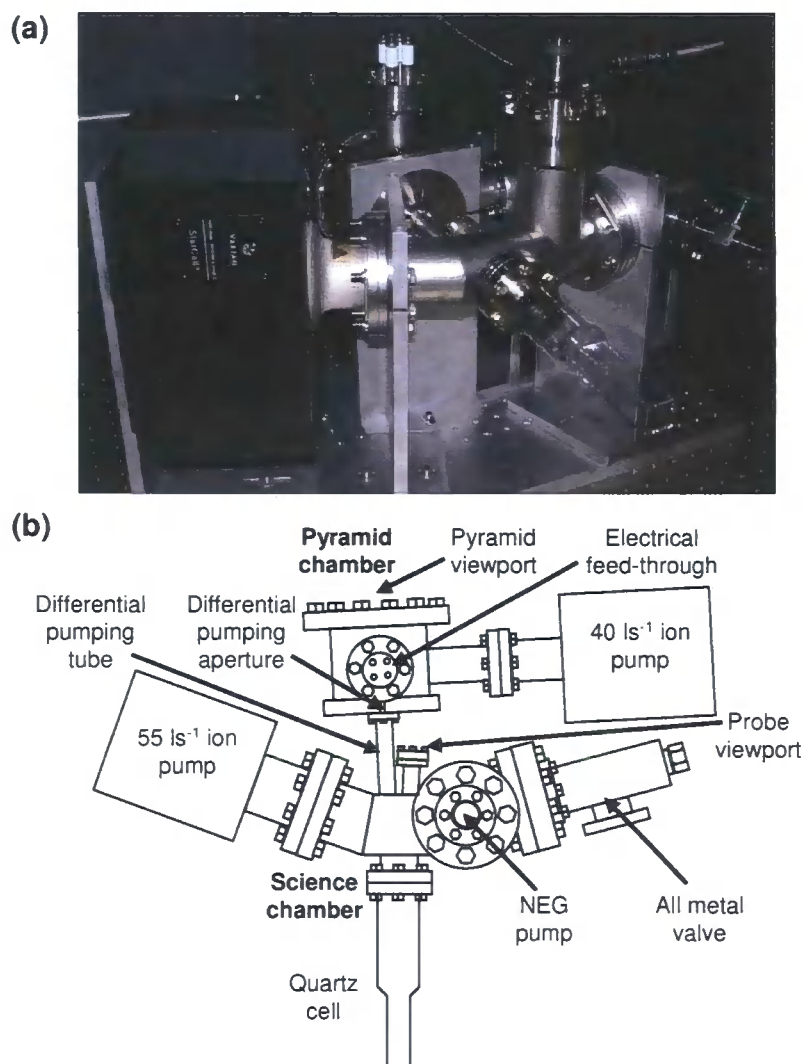
Figure 3.10: The assembled vacuum system seen in situ (a) is also shown as a schematic from above (b). Note how the science chamber vacuum pumps and all metal valve are swept back towards the pyramid chamber in order to maximise optical access to the protruding quartz science cell. The plate on which the chamber is mounted (a) also incorporates tapped holes from which optics are mounted to give access to the probe viewport, allowing probing along the axis of the science cell.

evacuated to pressures below 6×10^{-10} Torr. The vacuum system used in this apparatus (figure 3.10) is designed to achieve such low pressures whilst incorporating a 'high pressure' region ($p \simeq 10^{-8}$ Torr) in which ^{87}Rb and ^{133}Cs atoms are initially captured. The region in which atoms are initially captured is described as the pyramid chamber, whilst the region in which magnetic trapping occurs is described as the 'science chamber'. A series of constrictions between the two chambers results in the desired pressure differential between the apparatus regions. Laser beams are transmitted into the vacuum system through glass viewports and a quartz science cell, whilst all other components of the vacuum system are constructed from non-magnetic stainless steel. Connections between all vacuum chamber components are via copper gasket sealed CF flanges.

3.3.1 Pyramid Chamber

The pyramid chamber contains the pyramidal optic mirror and alkali-metal dispensers for ^{87}Rb and ^{133}Cs . Two sets of 4 pin electrical feedthroughs (VG Scientia ZEFT34A) transmit the currents required to operate the dispensers into the vacuum chamber (section 3.3.1), whilst the mounted pyramid optics are fixed in place by screwing a pair of internally bored hex-head screws into blind tapped holes inside the vacuum chamber. The pyramid optics are enclosed with a 90 mm clear-diameter view-port. One port of the chamber is pumped with a 40 ls^{-1} ion pump (Varian Starcell), whilst the final port incorporates a DN16CF blind tapped flange with a clear diameter of 5 mm bored through the 17 mm thick stainless steel face.

3.3.2 Science Chamber

The science chamber is primarily constructed of 58.9 mm inner diameter (ID) tubing, and pumped using both a 55 ls^{-1} Varian Starcell ion pump and a SAES non-evaporable getter (NEG) pump with effective pumping speed for hydrogen of 400 ls^{-1}. In addition to the 80 mm long differential pumping tube connecting the pyramid chamber, a 30 mm long tube terminated with a 16 mm clear diameter view-port provides optical access for the absorption

imaging probe beam (section 3.8.2). Both of these tubes have inner diameters of 15.7 mm. An all-metal valve allows initial system pump-out using an external pump-out rig (section 3.3.4). Once in-situ the air-side flange of the all-metal valve is terminated with an up-to air valve, through which the connecting cavity is evacuated to $\simeq 10^{-2}$ Torr using a roughing pump. The final port connection is to the science cell in which interspecies experiments are carried out.

Science Cell

The science cell is custom made from 2 mm thick fused silica (quartz) by Optiglass Limited. It consists of a length of square cross section tubing with internal dimensions of $20 \times 20 \times 83$ mm terminated with a square end. The cell is manufactured using an 'optical contacting' technique to maintain the uniformity of the flat faces during the manufacturing process. This cuboidal section is attached to a 70 mm OD 316LN stainless steel CF flange via a cylindrical glass tube. The tube is made from a series of different glasses with graded thermal expansion coefficients to ensure thermal stability of the glass-to-metal seal.

3.3.3   Differential Pumping

The 5 mm diameter, 17 mm long tube of the pyramid chamber and the 15.7 mm diameter, 80 mm long tube of the science chamber have conductances for air of $\simeq 0.9 \, \mathrm{ls^{-1}}$ and $\simeq 5.3 \, \mathrm{ls^{-1}}$ respectively. The combined series conductance of these two tubes is $\simeq 0.8 \, \mathrm{ls^{-1}}$. This is almost two orders of magnitude below the pumping speed of the science chamber ion pump, hence a factor of $\simeq 100$ in pressure differential between the two chambers can be maintained.

3.3.4   Pumping and Bake-out

The vacuum system is initially pumped out using a rouging pump backed turbo-molecular pump system developed by Paul Griffin *et al.* [91]. This brings the vacuum system to a low base pressure prior to activation of the NEG and ION sorption pumps, which have a limited capacity, though offer

increased pumping speeds for noble gases and hydrogen respectively. The pump-out rig is fitted with a residual-gas analyser (RGA) and an ion gauge. This allows detection of 'virtual leaks' due to contaminants and actual leaks through helium leak detection. The pump-out rig also incorporates a temperature stabilised oven, which is operated at temperature ramps of $\pm$ 1°C minute^{-1}. Through baking the system within this oven the rate of molecular desorption from the chamber walls is accelerated. This results in a reduction in post-bake room temperature system pressure. After testing the pyramid chamber for leaks without connection to the science chamber, the whole vacuum system is assembled without ion-pump magnets and connected to the pump-out rig. After initial leak-testing of the fully assembled system, the pump-out procedure described in table 3.4 is followed. The change in net system pressure during the bake-out procedure, and also the contributions of individual molecular vapour pressures can be seen in figure 3.11. After disconnection from the pump-out rig, and with all permanent vacuum pumps operating, a system pressure below 1×10^{-10} Torr is achieved. The corresponding background-collision limited magnetic trap lifetimes are in excess of 100 s.

Stage	Action
1	Rough out system through turbo-pump.
2	Switch on turbo-pump.
3	Helium leak-test system.
4	Bake system to 200 °C .
5	De-gas ion gauge.
6	De-gas each dispenser at 5 A for 90 s.
7	Bake for 4 days.
8	Return system to room temperature.
9	Activate NEG pump (apply 16 V for 1 hour).
10	Degas each dispenser at 5 A for 30 s.
11	Bake for 10 days at 215 °C .
12	Degas dispensers at 3 A for 1 day.
13	Switch off RGA.
14	Attach magnets and switch on ion pumps.
15	Pump for 1 day.
16	Close all-metal valve finger tight.
17	Bake for 3 days at 175 °C .
18	Close all-metal valve using 12 Nm torque.
19	Pump for 12 days at room temperature.
20	Disconnect mixture system from pump-out rig.
21	Attach up-to air valve.
22	Rough out all-metal valve through up-to air valve.
23	Close up-to air valve.

Table 3.4: Vacuum pump-out procedure.
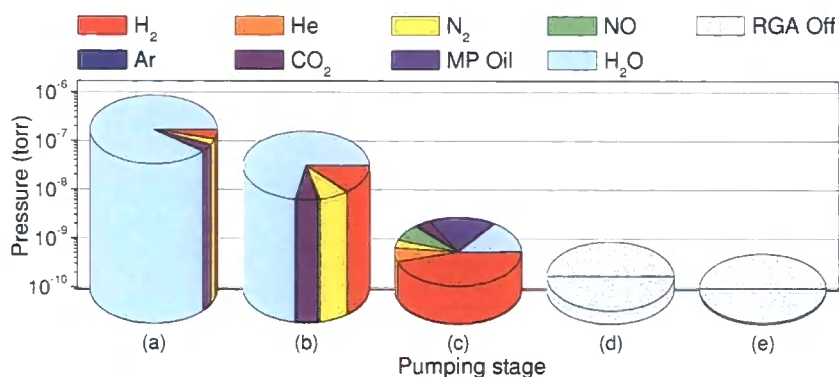
Figure 3.11: Vacuum system pressure after each sequential stage of pumping. The column height gives the total pressure in the system measured using an ion gauge. The relative molecular partial pressures seen in the composition of each column are measured using a residual gas analyser. Note: As there is no helium naturally present in the earth's atmosphere, any measure of helium is anomalous, hence the maximum measured helium content gives an indication of the minimum resolvable partial pressure using the residual gas analyser. Initially the system is pumped with a turbomolecular pump backed by a roughing pump. (a) After pumping for 1 hour at 20 °C. Water vapor constitutes 89 % of the residual gas pressure. (b) After 45 hours pumping at 20 °C. The system pressure has dropped by an order of magnitude, with water remaining the dominant contaminant. (c) Returning the system to 20 °C after baking at 200 °C for 90 hours. The increase in degassing rate due to the baking process has allowed the turbomolecular pump to efficiently reduce the total pressure of the system by a further 2 orders of magnitude. As this pump is relatively inefficient at removing small molecules, hydrogen is now the dominant contaminant, with only pump oil and water also remaining in significant quantities. (d) After an 11 day bakeout at 215 °C with the nonevaporable getter pump activated. It was necessary to switch off the residual gas analyser as its operation was causing a significant contribution to the systems total pressure. (e) After a final 3 day bake out at 175 °C followed by 23 days pumping at 20 °C with the two ion pumps operating. The measured system pressure has dropped below 1×10^{-10} Torr (section 3.3).

3.4   The Pyramid MOT

The pyramid MOT consists of six counter-propagating laser beams in conjunction with a magnetic quadrupole field produced by a pair of identical magnetic coils operating in an anti-Helmholtz configuration (appendix C.1.3). Comparable apparatus are described for single, and two species operation in [41] and [92] respectively. The six laser beams are derived from the output of the pyramid optical fibre, which is collimated using a 250 mm focal length lens to a $1/e^2$ radius of 20.4(4) mm after transmission through an achromatic quarter waveplate (figure 3.14). The collimated beam is then
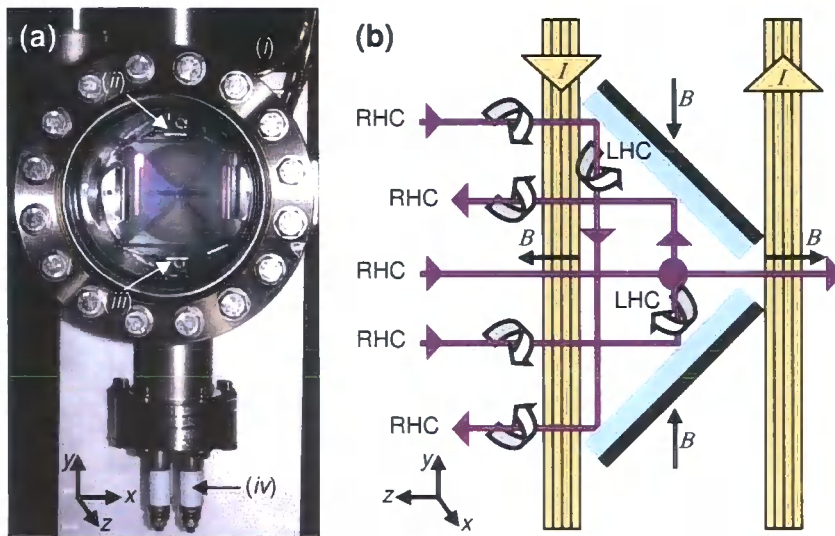
Figure 3.12: Pyramid optics mounted in vacuum chamber (a). Rb and Cs atoms are released from alkali-metal dispensers (*iii*) and (*ii*) respectively when an electrical current is transmitted through them. The current enters the vacuum system through electrical feedthroughs (*iv*) mounted above and below the pyramid optics. A pair of coils wound directly onto the vacuum chamber in the anti-Helmholtz configuration (*i*) produces a magnetic quadrupole field. Cooling and repumping light for both species are combined in a single laser beam incident on the pyramid optics. The incident circularly polarised cooling light (b) is transmitted along the axis of the quadrupole coils. Following reflection from the pyramidal mirror, the single incident laser beam generates all six beams required for magneto-optical trapping in this configuration.

reflected by a 100 mm diameter mirror through an AR coated vacuum window to be incident upon a pyramidal mirror arrangement contained within the vacuum apparatus pyramid chamber (see figure 3.12 (a)).

3.4.1   Pyramidal Mirror

The pyramidal mirror is constructed from two planer chisel prism mirrors and two tetrahedral prism mirrors, held in place by a pair of stainless steel clips (figure 3.13). Each single reflection of the incident beam produces a perpendicular reflected beam with opposite circular polarisation. With the axis of the coil pair parallel to the incident laser beams wave vector, a single reflection from all four constituent optics of the pyramidal mirror produces two counter-propagating pairs of reflected laser beams along the radial axes of the coil pair with opposite handedness to the incident axial beam (figure 3.12 (b)). A second reflection of any of these four beams produces an axial doubly reflected beam of identical polarisation to, and counter-propagating with, the incident axial beam. Thus six beams of the required polarisations for a MOT are produced using a single in-vacuo optical element.
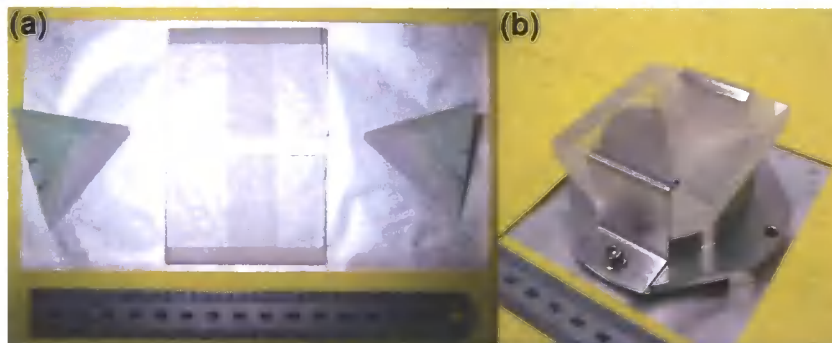
Figure 3.13: Pyramid optics consisting of two chisel prisms, and two tetrahedral prisms with highly reflective broadband mirror coatings (a). Images are of optics identical to those used in this apparatus. The optics are assembled in a 304 stainless steel mount (b) to produce an inverted pyramid with 60 mm × 60 mm square base, and 30 mm height. The optics do not intersect at the pyramid apex, leaving a square aperture of $\simeq 2.4 \times 3.0$ mm.

3.4.2 Alkali-metal Dispensers (AMDs)

The atom source for this apparatus is a set of three ^{87}Rb (^{133}Cs) alkali-metal dispensers (AMDs) mounted below (above) the pyramid optics (figure 3.12(a)). The AMDs are electrically connected by spot-welding of the 0.14 mm thick stainless steel dispenser tabs to 1 mm stainless steel rods. The rods are each screwed onto a separate internal terminal of a UHV vacuum feedthrough (section 3.3.1). Each array is connected via four rods such that a voltage can be applied across each dispenser individually. During operation, a single dispenser of each species is operated continuously at $3.0 < I < 3.3$ A, with higher currents of 5 A applied to all dispensers only during 30 second de-gassing periods in the vacuum construction phase (section 3.3.4). This low current operation ensures longevity of the AMD contents.

3.4.3 Magnetic coils

The pyramid MOT magnetic field is controlled by a pair of quadrupole 'MOT' coils in an anti-Helmholtz configuration and two circular 'shim' coils.

Pyramid MOT Coils

The water-cooled quadrupole pyramid MOT coils are wound directly onto the vacuum chamber in the manner described in table C.7. The coils produce a linear B-field gradient of 0.55 G A^{-1} and are powered using a 32 A DC power supply, feedback controlled by a bank of field effect transistors (FETS).

Pyramid Shim Coils

In addition to the water-cooled quadrupole coils, two shim coils are used to adjust the position of the B-field zero, and hence the centre, of the pyramid MOT. Using the orientations of figure 3.14, these two shim coils are mounted to the north of the pyramid chamber centre around the outside of the chamber window (Pyramid N-S shim), and against the east side of the chamber (Pyramid E-W shim). The shim coil parameters and dimensions can be found in tables 3.5 and C.7 respectively. With the pyramid MOT

running at a gradient of 8.5(1) G cm^{-1}, a current of $-2 < I < 2$ A applied to the appropriate shim coil is sufficient to move the position of the magnetic field zero, and hence the trap centre, across the full 6 cm width and 3 cm depth of the pyramidal mirror. The shim coil currents are adjusted to position the MOT centre directly over the hole in the pyramid apex. The optical pressure imbalance caused by the absence of a retro-reflecting axial MOT beam in this case causes atoms to be optically 'pushed' from the pyramid chamber into the science region of the vacuum apparatus.

3.5 The Science MOT

Atoms pushed through the apex of the pyramid MOT are captured in the two species science MOT. The horizontal trapping light is provided by 4 independent counter-propagating horizontal MOT beams for each species (figure 3.14). Vertical trapping light for both species is combined in a single pair of counter-propagating beams (figure 3.16). The magnetic field gradient required for magneto-optical trapping is produced from a pair of identical coils operating in an anti-Helmholtz configuration (appendix C.1.3).

3.5.1 MOT Beams

The outputs of the ^{133}Cs and ^{87}Rb optical fibres are both collimated to $1/e^2$ radii of 10.9(1) mm (figure 3.15). The laser beams are then split using 25.4 mm diameter species specific cemented zero order half waveplates in combination with 20 mm side-length broadband polarising beam-splitting cubes. One third of the cooling laser power from each fibre output is combined on a single non-polarising beam-splitting cube to produce a pair of linearly polarised two-species laser beams (see figure 3.16). The required circular polarisations of the vertical MOT beams are achieved using a ^{87}Rb (^{133}Cs) specific true zero-order quarter wave-plate for the combined up (down) beam. The remaining two thirds of the optical power from each fibre output is split into two pairs of counter-propagating beams for each species. The ^{87}Rb (^{133}Cs) horizontal MOT beams are aligned relative to the N-S axis of figure 3.14 at angles of -34.1(1)° and +40.1(1)° (-40.3(1)° and +33.5(1)°) respectively.
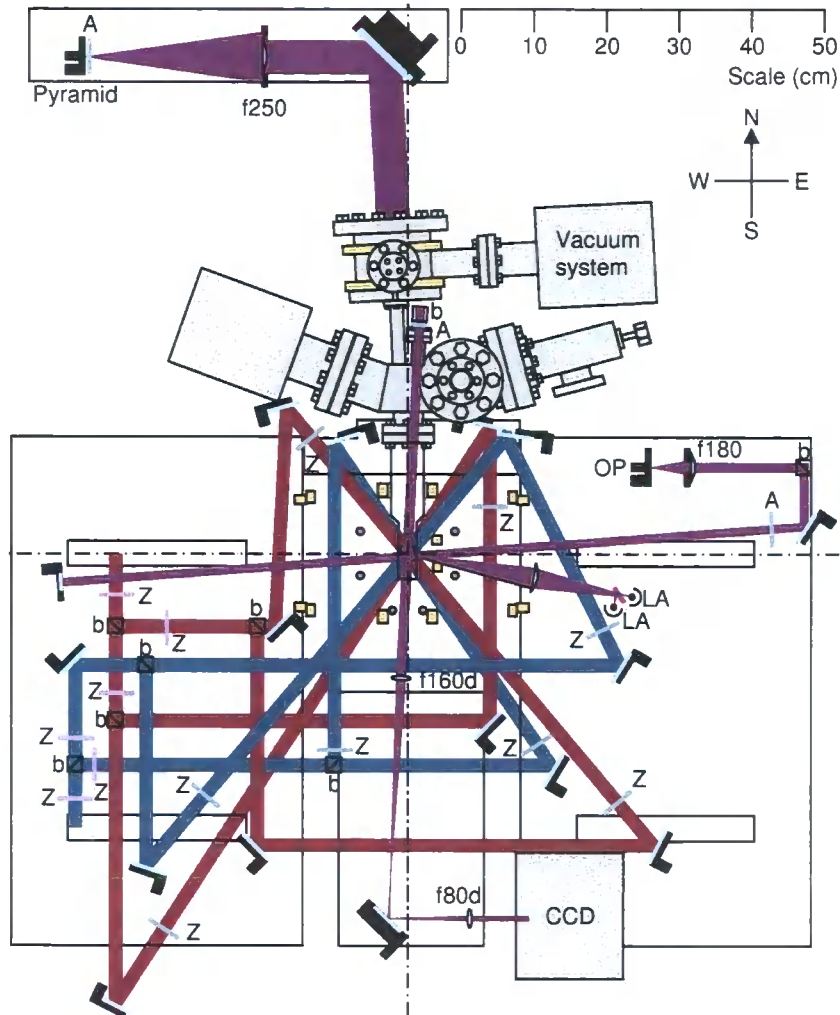
Figure 3.14: Schematic view of vacuum chamber table in plane 254 mm above optical bench. All laser frequencies are transmitted from the laser table using optical fibres. Cooling and repumping light for both atomic species combined in the output of the pyramid MOT fibre is used to produce a two-species cold-atomic beam for capture in the science MOT. Species specific combined cooling and repumping beams for ^{87}Rb (blue) and ^{133}Cs (red) are brought from optical fibre outputs below this plane via periscopes, as is the combined two-species probe beam. The probe, pyramid, and optical pumping fibre outputs (purple) contain combined light for both atomic species. Parameters of trapped atoms are calculated from MOT fluorescence imaged onto separate calibrated large area (LA) photodiodes for each species, and imaged atomic absorption of each probe beam frequency onto a CCD camera (see text). See figure key in table 3.2.
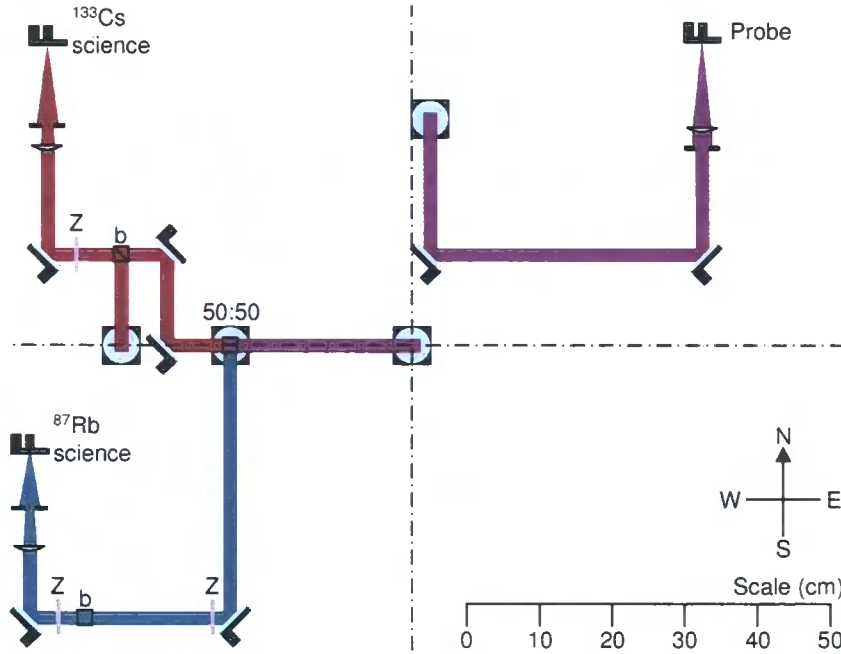
Figure 3.15: Schematic view of vacuum chamber table optics mounted directly to the optical bench. All laser frequencies are transmitted from the laser table using optical fibres. Combined cooling and repumping light for ^{87}Rb (blue) (^{133}Cs (red)) is collimated from an optical fibre output 70 mm (89 mm) above the optical bench. One third of the cooling laser power for each species is combined on a single non-polarising beam-splitting cube to produce the up/down MOT beam pair (purple). The remaining cooling laser power is transmitted to the plane 254 mm above the optical bench using a periscope for each species. After collimation from the probe fibre output, combined probing light for both species (purple) is transmitted to the 254 mm plane using a periscope. See figure key in table 3.2.
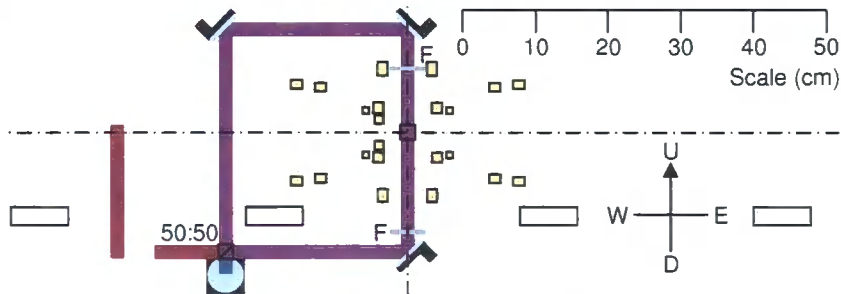
Figure 3.16: Schematic view of vacuum chamber table optics in the N-S, E-W plane. Species specific combined cooling and repumping beams for ^{87}Rb (blue) and ^{133}Cs (red) are incident on adjacent faces of a single non-polarising beam-splitting cube. One combined two-species output of this cube is transmitted through a ^{87}Rb (^{133}Cs) true zero order quarter waveplate to form the up (down) vertical MOT beam, shown in purple. See figure key in table 3.2.

3.5.2 MOT Coils

The MOT coils described in table C.7 are operated in an anti-Helmholtz configuration (appendix C.1.3) to produce a B-field gradient of 0.78(1) G A^{-1} of transmitted current. The current through the coils is supplied and controlled using a Xantrex XPD 7.5-67 DC programmable power supply, switched via a DC voltage multiplexer (section 3.9.1). In addition to operating at a current of 12.2(1) A for the MOT phase of the experiment, the MOT coil/supply combination is selected to allow magnetic levitation of ^{87}Rb and ^{133}Cs in the $|F = 1, m_F = \pm 1\rangle$ and $|F = 3, m_F = \pm 3\rangle$ states respectively (table 2.1). For this task the maximum supply operation current of 67 A is more than sufficient.

3.6 Magnetic Trapping

Atoms of both species loaded into the science MOT are are simultaneously transferred into an Ioffe-Pritchard magnetic trap (section 2.2.4) in which they are cooled through simultaneous radio-frequency evaporation.

3.6.1 The Magnetic Trap

The magnetic trap is composed of a series of magnetic coils (see figure 3.17). The primary trapping 'baseball' produces an Ioffe-Pritchard trap geometry, whilst providing excellent optical access for the eight science MOT beams in the horizontal plane. Additional Helmholtz configuration (appendix C.1.2) bias coils are used to enhance the bias field produced by the baseball coil. The bias field can also be reduced by operating a pair of Helmholtz configuration cancellation coils to produce a bias field in opposition to that of the baseball coil. Future experiments may involve optical dipole trapping in a levitation trap (a configuration in which ^{133}Cs has been successfully condensed [13]). For this configuration the MOT coils would be used to magnetically levitate both atomic species, whilst bias fields can be tuned using the additional vertical bias Helmholtz coil pair. Fine tuning of the magnetic bias field, and hence the position of the magnetic trap centre, in all three dimensions is

achieved using four pairs of shim coils. Details of coil construction and water cooling can be found in appendix C.2, whilst coil dimensions are contained in table C.7.
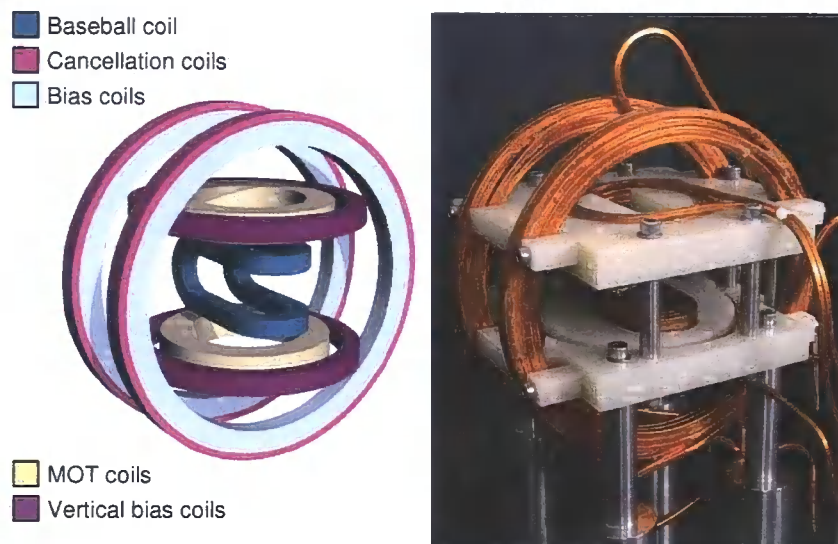
Figure 3.17: The magnetic trap. The colour coded schematic on the left highlights the different coils in the final assembly shown on the right.

Coil Parameters

The magnetic field produced as a function of axial distance z in cm from the centre of a pair of identical circular coils can be approximated to second order by the expansion:

$$B(z) = B_0 + \beta z + \frac{\gamma}{2}z^2 \quad , \tag{3.3}$$

where B_0 is the bias field at the centre of the coil pair in G, and β and γ are the B-field gradient and curvature expressed in G cm^{-1} and G cm^{-2} respectively. Each of these parameters is proportional to the current transmitted through the coil pair. Hence the bias field, gradient, and curvature of a coil pair is more generally parameterised in units G A^{-1}, G cm^{-1} A^{-1}, and G cm^{-2} A^{-1} respectively. For coil pairs with the current operating in the opposite sense (*i.e.* MOT and pyramid MOT coils), symmetry considerations give $B_0 = 0$ and $\gamma = 0$. In contrast, coil pairs with the current operating in the same sense (*i.e.* cancellation, bias, grey bias and vertical bias coils), symmetry

considerations give $\beta = 0$. The remaining B-field expansion parameters for each circular coil pair (table 3.5) are obtained by fitting the B-field due to a 100 A coil current as a function of position (measured by axially translating a calibrated Hall probe) with equation 3.3.

The baseball coil B-field as a function of radial (r) and axial (z) position in cm is approximated using the Ioffe-Pritchard expansion (section 2.2.4):

$$B(r,z) = B_0 + \frac{\gamma}{2}z^2 + \left(\frac{\beta^2}{2B_0} - \frac{\gamma}{4}\right)r^2 \quad , \tag{3.4}$$

where B_0 is the axial magnetic bias field at the centre of the coil in G, and β and γ are the radial B-field gradient and axial curvature expressed in G cm^{-1} and G cm^{-2} respectively. Again, as the bias field, gradient,

Baseball	B_0	0.3410(3)	G A^{-1}
	β	1.087(4)	G cm^{-1} A^{-1}
	γ	0.154(2)	G cm^{-2} A^{-1}
Cancellation	B_0	0.3487(2)	G A^{-1}
	γ	-0.00486(5)	G cm^{-2} A^{-1}
Bias	B_0	1.085(1)	G A^{-1}
	γ	-0.0164(1)	G cm^{-2} A^{-1}
Grey bias	B_0	2.59(2)	G A^{-1}
Vertical Bias	B_0	0.6011(2)	G A^{-1}
	γ	-0.0000(3)	G cm^{-2} A^{-1}
MOT	β	0.78(1)	G cm^{-1} A^{-1}
Pyramid MOT	β	0.55(2)	G cm^{-1} A^{-1}
Pyramid shim N-S	B_0	3.6(4)	G A^{-1}
Pyramid shim E-W	B_0	1.5(1)	G A^{-1}
Science shim S	B_0	1.22(2)	G A^{-1}

Table 3.5: B-field expansion parameters for all coils used in the atom trapping apparatus. Note the pyramid E-W (N-S) shim consists of a single coil producing a gradient of 10.4(3) G A^{-1} placed at at distances of 110(2) mm West (60(2) mm North) of the pyramid MOT coil centre. The quoted B-field values for these coils are those at the centre of the pyramid MOT coil pair.

and curvature of the coil is proportional to the transmitted current, these parameters are more generally expressed in units $G\ A^{-1}$, $G\ cm^{-1}\ A^{-1}$, and $G\ cm^{-2}\ A^{-1}$ respectively. For the baseball coil these parameters (see table 3.5) are obtained by measuring the B-field due to a 100 A coil current as a function of position by translating a calibrated Hall probe along both the axial and radial directions. The resulting data is fitted with equation 3.4.

3.6.2 B-Field Dependance of Trap Geometry

The axial and radial components of the Ioffe-Pritchard expansion (equation 3.4) determine the axial and radial frequencies respectively at which atoms harmonically oscillate within the magnetic trap. As shown in section 2.2.4, the resulting axial and radial trap frequencies expressed in radians per second are:

$$\omega_z = \sqrt{\frac{\mu\gamma}{m}} \quad \text{and} \tag{3.5}$$

$$\omega_r = \sqrt{\frac{\mu}{m}\left(\frac{\beta^2}{B_0} - \frac{\gamma}{2}\right)} \quad \text{respectively.} \tag{3.6}$$

By operating coil pairs in conjunction with the baseball coil, the parameters used in the Ioffe-Pritchard expansion are modified to be the sum of those from all contributing coils. By varying the relative contribution of each coil to the magnetic bias field, the relative magnitude of the axial and radial frequencies at which atoms oscillate in the trap can be adjusted without changing the B-field at the trap centre, as shown in figure 3.18. The absolute magnitude of the axial and radial trapping frequencies is affected by changing the trap geometry in this manner, and also by varying the magnetic bias field. This second effect is due to the variation in magnetic moment of ^{87}Rb and ^{133}Cs with applied magnetic field (figure 3.19), a consequence of the second-order Zeeman splitting. For a single species the magnetic moment variation affects both axial and radial trapping frequencies equally. As the relative change in the magnetic moments of ^{87}Rb and ^{133}Cs with B-field are different, so to are the relative changes in trap frequencies. When operating the baseball coil at a fixed current, and tuning the magnetic field with an additional bias coil pair, both of these effects can be significant in changing the absolute, and relative trap frequencies for the two atomic species (figure 3.20).
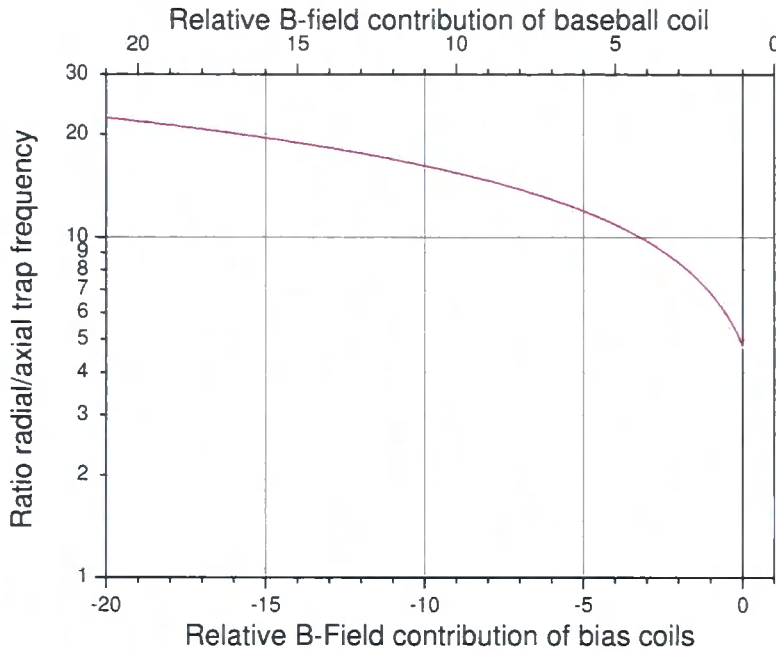
Figure 3.18: Theoretical ratio of trap frequencies at a fixed net magnetic field as a function of the relative contributions of the baseball coils (top axis) and a pair of Helmholtz coils (bottom axis). For B-field contributions enhancing (opposing) that of the baseball coil, the parameters of the bias (cancellation) coil pair are used. The magnitude of the radial trapping frequency is greatly increased by canceling the majority of the baseball coil field.
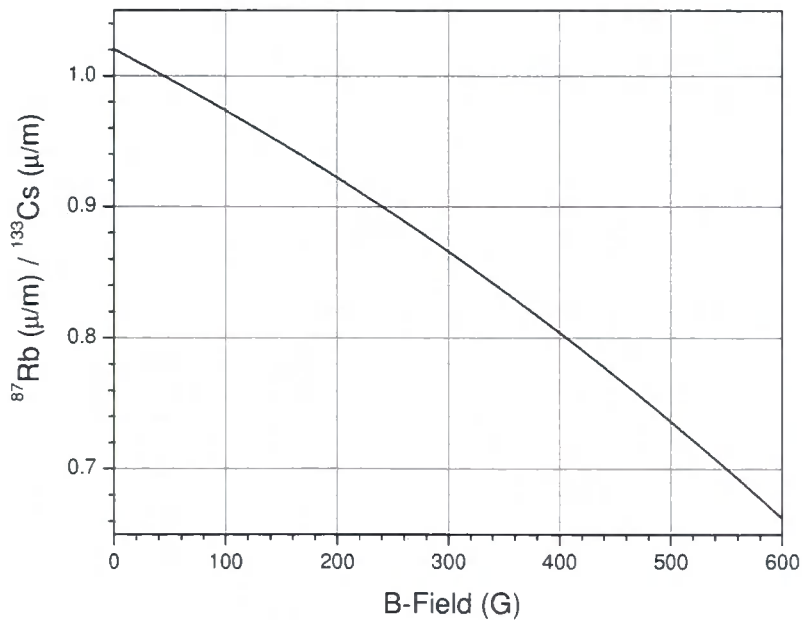
Figure 3.19: The relative magnetic moment to mass ratios for ^{87}Rb and ^{133}Cs as a function of magnetic field. At a B-field of $\simeq 45$ G ^{87}Rb and ^{133}Cs have identical magnetic moment to mass ratios and hence identical trap frequencies.
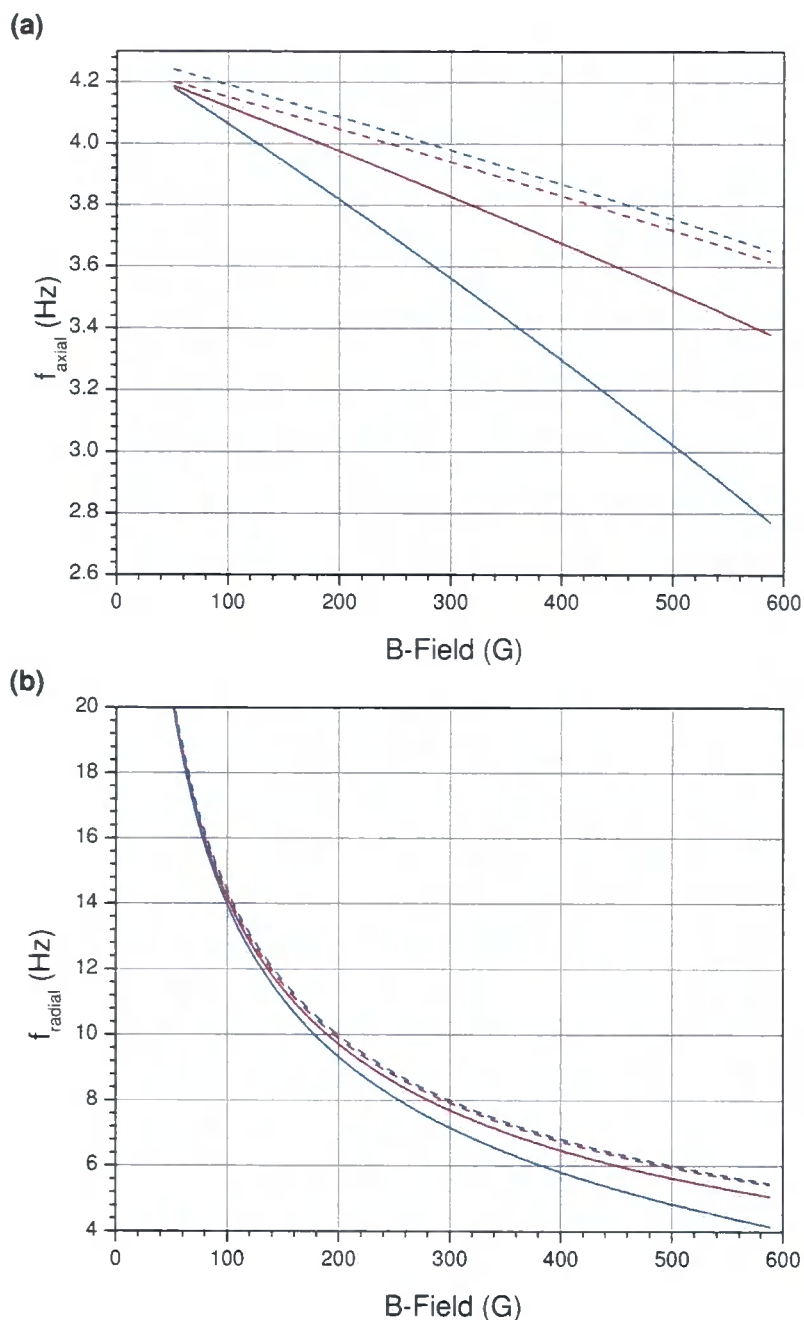
Figure 3.20: Theoretical magnetic trap frequencies for ^{87}Rb (blue) and ^{133}Cs (red) in the $|F = 1, m_F = -1\rangle$ and $|F = 3, m_F = -3\rangle$ states respectively as a function of B-field at the trap centre. Data assumes a constant baseball coil current of 150 A, contributing 51.2 G to the B-field, with the remaining B-field supplied by the bias coil pair. Dashed lines show the trap frequency variation due to the change in Ioffe-Pritchard expansion coefficients for an assumed fixed ^{87}Rb (^{133}Cs) magnetic moment of 0.5 μ_B (0.75 μ_B). Solid lines also take into account the change in magnetic moment due to the second order Zeeman splitting. The axial trap frequency change (a) due to each of these effects is on the same scale, whilst the radial trap frequency (b) is predominantly affected by the expansion coefficient change.

Gravitational Sag

The magnetic trap frequencies determine not only atomic collision rates, but also the distance to which magnetically trapped atoms sag under the influence of gravity. Taking gravity to act along the radial axis of the Ioffe-Pritchard trap, the radial sag r as a function of radial trap frequency ω_r is:

$$r = \frac{g}{\omega_r{}^2} \quad , \tag{3.7}$$

where g is the acceleration due to gravity.
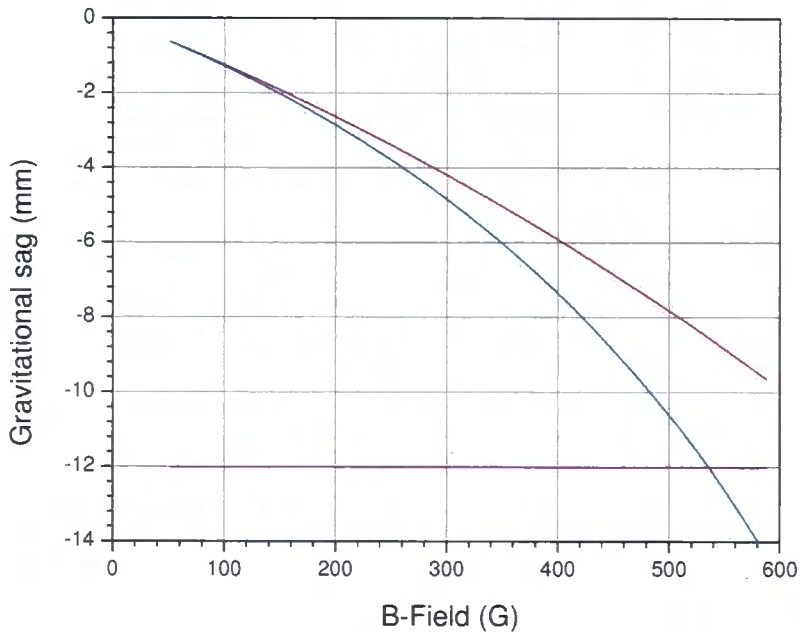
Figure 3.21: The gravitational sag of ^{87}Rb (blue) and ^{133}Cs (red) as a function of magnetic field. Data assumes a constant baseball coil current of 150 A, contributing 51.2 G to the B-field, with the remaining B-field supplied by the bias coil pair. At a B-field of $\simeq 45$ G the gravitational sag of ^{87}Rb and ^{133}Cs is identical. Above this B-field the relative sag between the two components increases. At $\simeq 538$ G the centre of the sagged ^{87}Rb cloud will intersect the cell wall (purple).

At magnetic fields above $\simeq 45$ G (where the magnetic moment to mass ratios of ^{87}Rb and ^{133}Cs are equal) increasing the magnetic field causes an increase in the relative sag of the mixtures components, reducing the cloud overlap

to zero when the relative sag becomes greater than the cloud size. Figure 3.21 shows the theoretical gravitational sag for ^{87}Rb and ^{133}Cs as a function of B-field for a constant baseball coil current of 150 A (contributing 51.2 G to the B-field) with the additional B-field supplied by the bias coils. At $\simeq$ 530 G the absolute gravitational sag of trapped ^{87}Rb atoms will cause the cloud centre to coincide with the lower face of the glass cell, resulting in complete loss of ^{87}Rb atoms from the trap. This limits the magnetic field range for magnetic trapping of the mixture in this apparatus to $B \leq 530$ G. The absolute limit for experiments employing magnetic trapping of ^{87}Rb in this state is $B \leq 1220(1)$ G. Above this field the magnetic moment for ^{87}Rb is negative (the turning point in figure 2.3), hence atoms are no-longer in magnetically trappable low-field seeking states [47].

The 'Weak' Trap

Initial experiments take place in the weak trap, in which the baseball coil is operated in conjunction with the bias coil pair. The weak trap geometry is suitable for loading of the magnetic trap as atoms spatially distributed in the MOT will pick up little potential energy through the magnetic trap loading process. Through tuning the magnetic field generated by the bias coil pair preliminary searches for Feshbach resonances are made.

The 'Tight' Trap

The cancellation coils are configured such that when operated in series with the baseball coil, the net bias field is close to zero. At low bias fields the radial trapping frequencies for both atomic species are significantly enhanced (section 2.2.4). As ^{87}Rb is most readily condensed in such a 'tight' magnetic trapping geometry this coil configuration is promising for studies of sympathetic cooling. Series operation of baseball and cancellation coils also offers the advantage of reducing bias field fluctuations through cancellation of the majority of current noise.
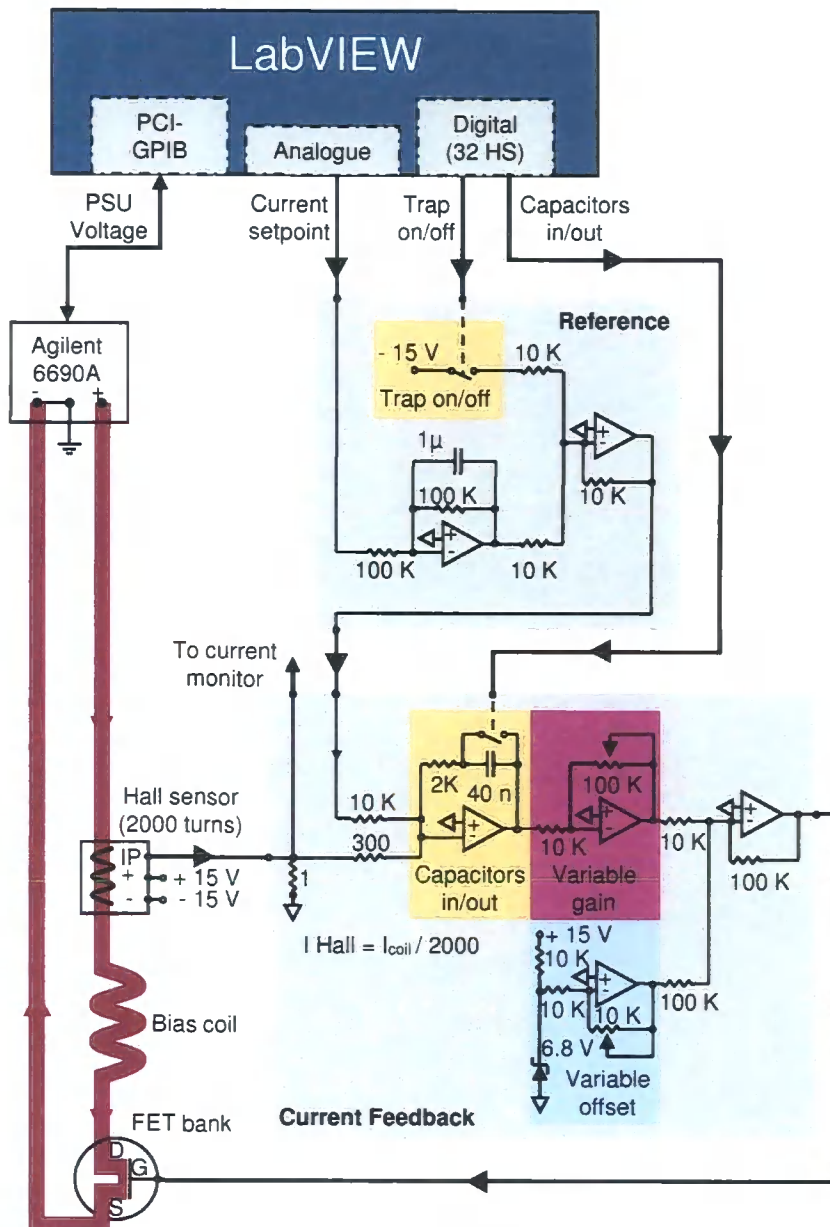
Figure 3.22: The current passing through each coil is supplied by an Agilent power supply operating in a 'constant voltage' mode, and regulated using a field-effect transistor (FET) bank. The FET bank gate voltage is set by the 'current feedback' circuit board in which a control voltage from the 'reference' circuit board is compared to the coil current measured with a Hall-effect current sensor. Additional LabVIEW digital outputs to the feedback and reference boards allow stabilising capacitors to be switched in/out of the feedback control loop, and 15 V to be added to the feedback board control input respectively (reducing trap turn on/off times). During operation the bias coil current supply voltage is externally switched through a general-purposed interface bus (GPIB).

(a)

Agilent 6681A

− +

8V, 580 A power supply

Hall sensor ▼

BBall coil

G D
S
Baseball FET

Hall sensor ▼

Cancellation coil

G D
S
Baseball + cancel FET

From magnetic trap controller

(b)

Agilent 6690A

− +

15V, 440 A power supply

Hall sensor ▼

Bias coil

G D
S
Bias FET

Hall sensor ▼

Vertical bias coil

G D
S
Vertical bias FET

From magnetic trap controller
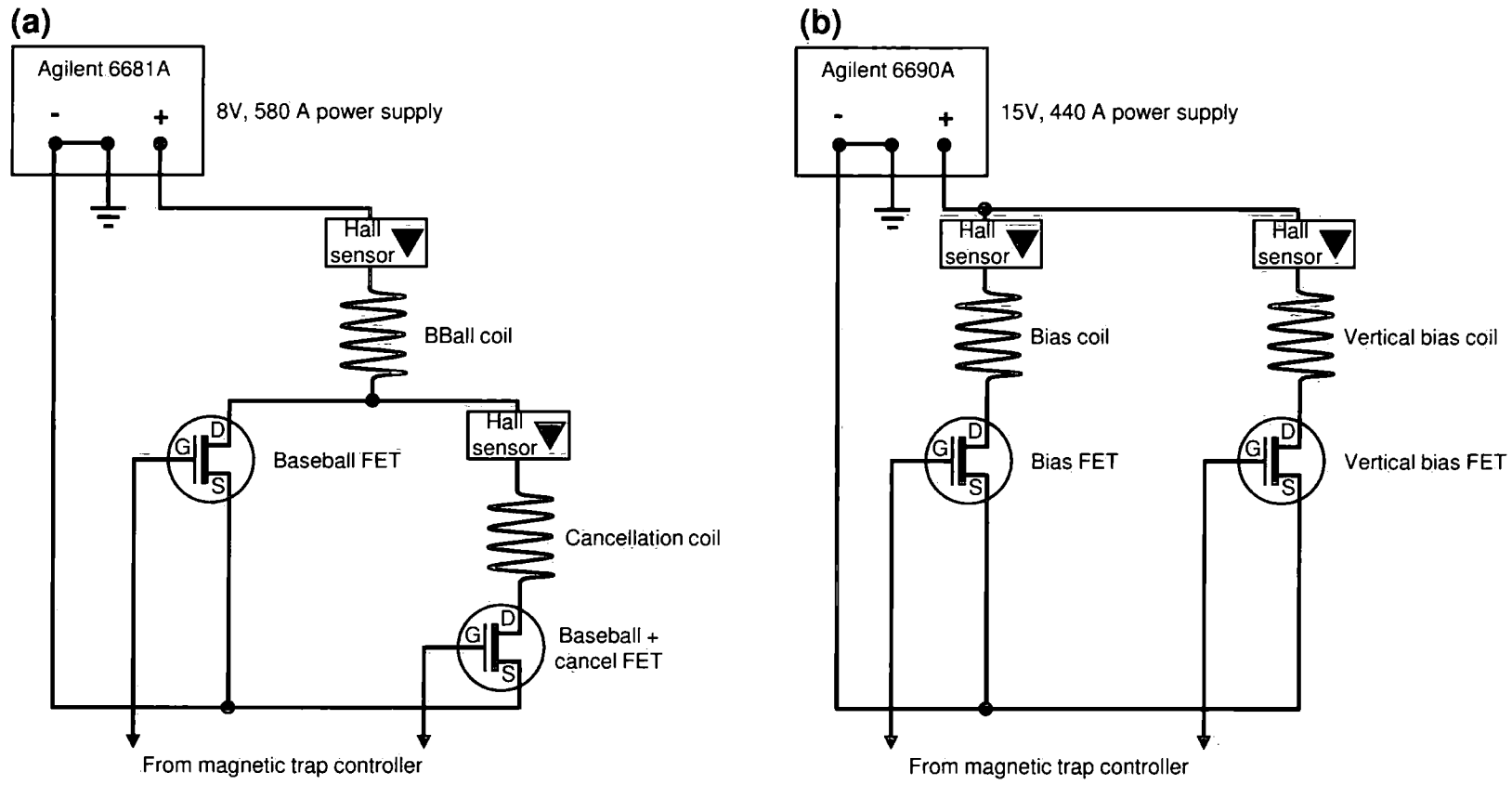
Figure 3.23: Circuit (a) is configured to allow the baseball (BB) coil to be operated alone, or in series with the cancellation coils. For the former (later) case the current is regulated using the baseball (baseball + cancel) field-effect transistor (FET) bank, with the gate of the baseball + cancel (baseball) FET bank grounded. The bias coils (b) are independently regulated using separate FET banks.

3.6.3 Magnetic Trap Control

The current passing through the magnetic trapping coils is supplied via two power supplies providing up to 580 A at 8 V (Agilent 6681A) and 440 A at 15 V (Agilent 6690A). The current drawn from each supply is regulated using a series of feedback controlled banks of field-effect transistors (figure 3.23). The current set-point, trap operational state and power supply voltage are controlled via a 'LabVIEW' computer control system (figure 3.22). All of the high current electrical connections are made using 50 mm^2 diameter insulated welding cable and appropriate cable lugs.

FET Banks

The FET banks consist of a length of rectangular cross section copper tubing (microwave guide tubing) on the upper surface of which four transistors (ST Microelectronics STE180NE10) are clamped. The field-effect transistors (FETs) are electronically connected in parallel to have a common source, drain and ground. Water is pumped through the tubing in order to dissipate power generated by the transistors (appendix C.5).

Hall-Effect Current Sensors

Each Hall-effect sensor (Honeywell CSNL181) comprises of a soft 'c' shaped iron core through which a cable transmitting current to the magnetic trap is passed. Wound around this core is a 2000 turn toroidal coil. A Hall-effect sensor which intersects the core regulates the current through the toroidal coil to null the magnetic field which it detects. This results in the Hall sensor drawing a current which is 2000 times lower than that of the regulated magnetic trap coil.

Feedback Electronics

The feedback electronics (figure 3.22) are split across two circuit boards: The current feedback board and the reference board (Boards EW1282 and EW1285 produced by Central Electronics, Oxford). The current feedback board compares a voltage output from the reference board with the voltage dropped across a 1 Ω sense resistor due the current drawn by the Hall-effect current sensor. The difference between these signals is amplified in two stages prior to summing with a tunable voltage offset and transmission to the FET bank gates. Fast magnetic trap turn on/off times are achieved by transiently by-passing the capacitors in the first amplification stage through switching a digital LabVIEW output channel. For ultimate trap frequency stability the capacitors are switched into the circuit after trap turn-on. The second amplification stage gain is increased to achieve minimum trap turn on time without runaway trap oscillations. The tunable offset is adjusted such that transient current oscillations during trap turn on are centred about the stabilised current set-point (*i.e.* the current due to the contribution of the voltage offset alone is equal to the current set-point).

GPIB Control

Most efficient operation of FETs is achieved when either fully open (dropping no voltage) or fully closed (drawing no current). In order to avoid operating in between these extremes ('throttling' the FETs) the high current power supply voltage for the bias coils is switched before trap ramps to ensure that any voltage drop across the FET banks whilst current is flowing is kept to a minimum.

3.7 Loading the Magnetic Trap

After loading the science MOT, the cold atomic beam from the pyramid MOT is removed by closing the pyramid shutters for both species, and also switching off the pyramid MOT coils. Transfer of atoms from the science MOT into the magnetic trap then proceeds through three stages. The objectives

for transfer are to:

- Minimise energy picked up by atoms during the magnetic trap capture.

- Increase the atom density through transient compression of the atom cloud.

- Cool the sample through an optical molasses phase.

- Polarise the states in which atoms are magnetically trapped.

3.7.1 Compressed Magneto-optical Trap (CMOT)

The compressed MOT stage of transfer has two objectives: Increasing the atom density through transient compression of the cloud and minimising the potential energy picked up by atoms during loading into the magnetic trap. During the CMOT phase the detuning of cooling light for both species is increased to reduce the rate at which cooling light is scattered, and hence cloud heating due to re-absorption of scattered photons. Simultaneously increasing the MOT coil gradient increases the trap 'spring constant'. Petrich *et al.* demonstrated a more than tenfold transient increase in atom density using this method [44]. During the CMOT phase, the position of the B-field minimum, and hence the atom cloud centre, is adjusted using the science MOT shim coils to be aligned with that of the magnetic trap (by minimising the amplitude of atom cloud oscillations in the magnetic trap). This minimises the potential energy gained by the atom cloud during the magnetic trap loading phase.

3.7.2 Optical Molasses

The polarisation gradient cooling mechanism is employed in a 15 ms optical molasses. During this phase the MOT coils are switched off and science MOT shim coils are switched to zero the magnetic field at the centre of the trap. Simultaneously the detuning from resonance of the cooling light for both species is increased to -60 MHz, proportionally increasing the strength of the sub-Doppler frictional force and reducing the minimum equilibrium cloud temperature (equation 2.3).

3.7.3 Optical Pumping

After sub-Doppler cooling in the optical molasses, ^{87}Rb (^{133}Cs) atoms are polarised into the magnetically trappable $|F = 1, m_F = -1\rangle$ ($|F = 3, m_F = -3\rangle$) states. This is achieved using two different laser frequencies for each species: Circularly polarised optical pumping light (section 3.2.6), and depumping light (table 3.1). The optical pumping light drives σ^- transitions from the $F = 1$ to the $F' = 1$ ($F = 3$ to the $F' = 3$) manifold in ^{87}Rb (^{133}Cs) (see figure 3.24). Excited ^{87}Rb (^{133}Cs) atoms undergoing spontaneous emission into the upper hyperfine ground states are depumped into the $F' = 2$ ($F' = 4$) excited state manifold. This combination of frequencies and polarisations pumps atoms into states with increasingly negative magnetic quantum numbers. ^{87}Rb (^{133}Cs) atoms in the $|F = 1, m_F = -1\rangle$ ($|F = 3, m_F = -3\rangle$) state are not subject to excitation by the optical pumping beam, hence this is a dark state in which atoms accumulate. The optical pumping fibre output is circularly polarised using an achromatic quarter waveplate (figure 3.14) and aligned with the centre of the magnetically trapped atom cloud. After transmission through the science cell the optical pumping beam is retro-reflected. This reduces the net increase in atomic momentum due to the optical pumping process. Depumping light is generated through increasing the detuning of light from both science MOT slave lasers by two methods simultaneously: Increasing the the operational frequency of the slave injecting AOM and adding a voltage offset to the lock-point of the master cooling laser DAVLL spectroscopy electronics.

3.8 Diagnostics

Two different methods are used to measure the properties of atoms in this experiment: Fluorescence imaging with which the number of atoms in the MOT can be calculated; and absorption imaging which in addition to atom number also provides detailed spatial information about each trapped atom sample. The apparatus for both imaging systems is described below, along with a discussion of the relative merits of each technique.
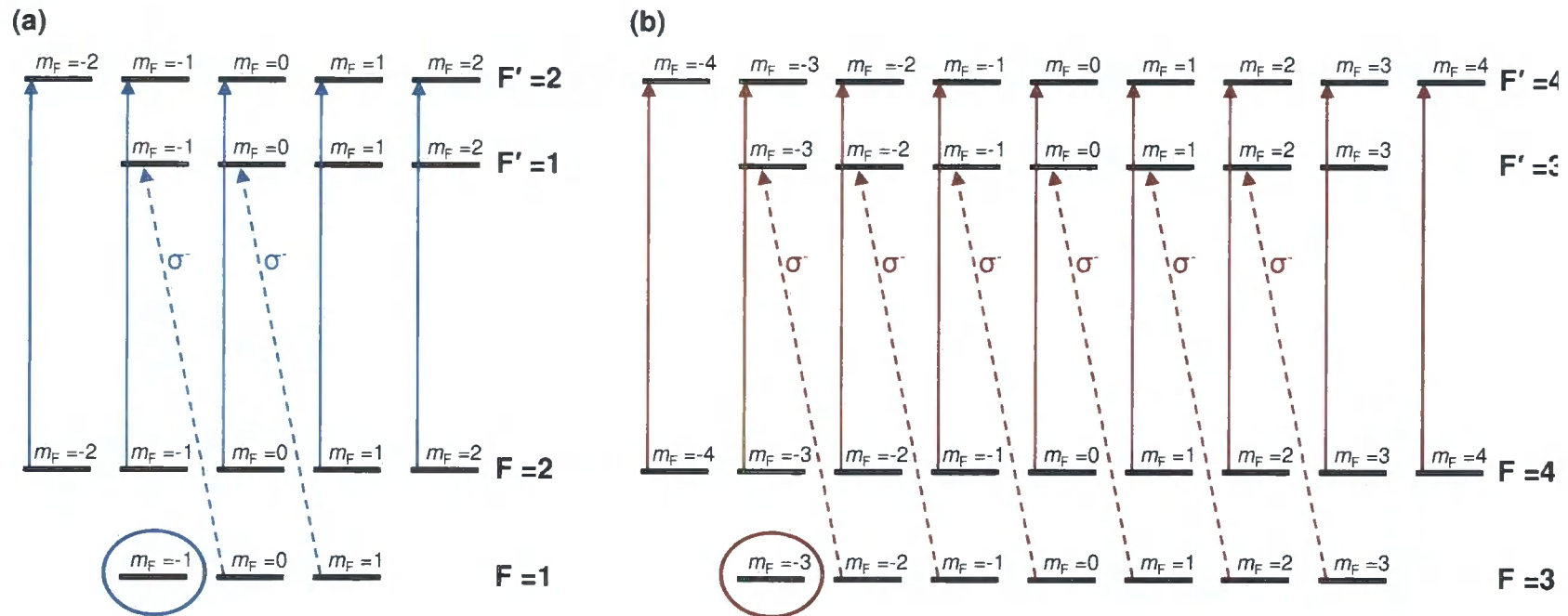
Figure 3.24: Optical pumping scheme for ^{87}Rb (a) and ^{133}Cs (b). The circularly polarised optical pumping beams (dashed arrows) drive σ^- transitions from the $F = 1$ to the $F' = 1$ ($F = 3$ to the $F' = 3$) manifold in ^{87}Rb (^{133}Cs). Depumping light (solid arrows) ensures atoms do not accumulate in the upper hyperfine ground state. Under this combination of optical frequencies ^{87}Rb (^{133}Cs) atoms are optically pumped towards and accumulate in the $|F = 1, m_F = -1\rangle$ ($|F = 3, m_F = -3\rangle$) dark state (circled).

3.8.1 Fluorescence Imaging

Imaging the optical fluorescence of atoms in a MOT (figure 3.25) allows the number of trapped atoms present to be calculated. This aids both in optimisation of consistent trap loading, and monitoring of apparatus performance. A fraction of the solid angle of MOT fluorescence captured within the central 28 mm diameter of an 80 mm focal length single lens, is focused onto a pair of large area photodiodes (Thorlabs DET36A). The transverse magnification of this system is calculated:

$$M_{\mathrm{T}} = -\frac{s_i}{s_o} = -0.78(1) \quad .$$ (3.8)

Hence the maximum diameter of spherical atom cloud which can be imaged onto each photodiode (producing an image diameter of 3.6 mm) is:

$$D_{max} = \frac{3.6}{|M|} = 4.6(1)\,\mathrm{mm} \quad .$$ (3.9)

This is greater than the visually estimated maximum trapped cloud size diameter of 4.2 mm, allowing fluorescence from the whole cloud to be captured. The use of a dichroic beam-splitter (appendix A.5) allows the fluorescence due to ^{87}Rb and ^{133}Cs atoms to be measured individually on separate photodiodes. Both photodiodes produce a current proportional to the optical power incident upon them, with responsivities $\mathcal{R}(780\text{ nm}) = 0.49(1)$ and $\mathcal{R}(852\text{ nm}) = 0.55(1)$ A W^{-1}. This current produces a voltage across a 1
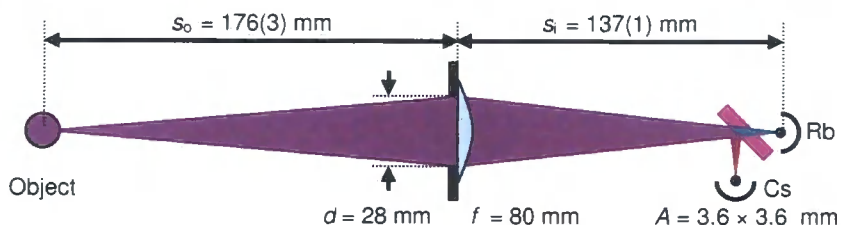
Figure 3.25: Two species fluorescence imaging. The acceptance diameter of the 80 mm focal length lens (and hence the imaging solid angle) is limited by a 28 mm diameter aperture. The MOT fluorescence from ^{87}Rb and ^{133}Cs atoms is measured separately using a pair of large area photodiodes in combination with a dichroic beam-splitter. See key in table 3.2.

MΩ oscilloscope input resistance which is directly proportional to atom number, with constant of proportionality calculated as outlined in appendix B. The 28 mm diameter aperture limiting the fluorescence imaging solid angle (equation B.3) is the maximum aperture diameter for which the measured fluorescence intensity variation from a fixed atom number with respect to change in aperture area remains linear (figure 3.26).
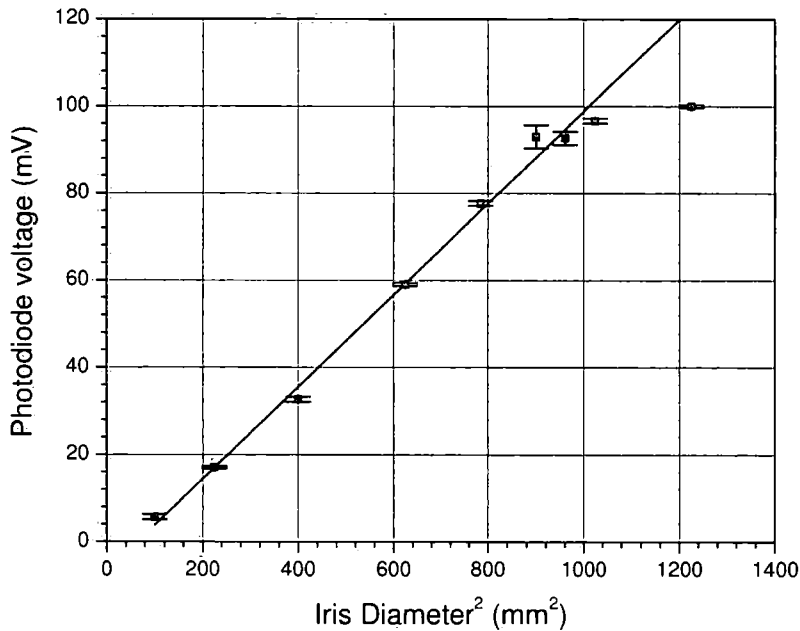
Figure 3.26: Photodiode voltage due to fluorescence from $5.7(1) \times 10^8$ ^{133}Cs atoms as a function of lens collection diameter squared. The black line is a linear fit of the first six data points. Above 900 mm^2 (30 mm diameter) the baseball coil limits the collection solid angle, indicated by deviation of data points from the linear fit. To ensure accurate calculations of atom number the collection solid angle is limited by a 28 mm diameter aperture.

MOT Recapture

The number of atoms loaded into the science MOT is measured by imaging the atom cloud fluorescence in the manner described above. Once loaded into the magnetic trap the atoms emit no fluorescence, hence continuous monitoring of the atom number via fluorescence imaging is no longer possible. It is a

simple matter however to release the atom cloud from the magnetic trap and immediately recapture into the science MOT (without the pyramid MOT source in operation). Although the absolute atom number is difficult to obtain directly with fluorescence imaging (due in part to the uncertainty of the branching ratios within the six beam MOT), the fraction of atoms initially loaded into the science MOT which are subsequently recaptured provides an excellent diagnostic when optimising and monitoring the apparatus performance.

3.8.2 Absorption Imaging

Detailed properties of atom clouds are obtained through absorption imaging (see figure 3.27), where the profile of light from a 10 μs probe laser beam transmitted through an atomic sample is imaged onto a frame transfer CCD camera (Andor iXon 885) .
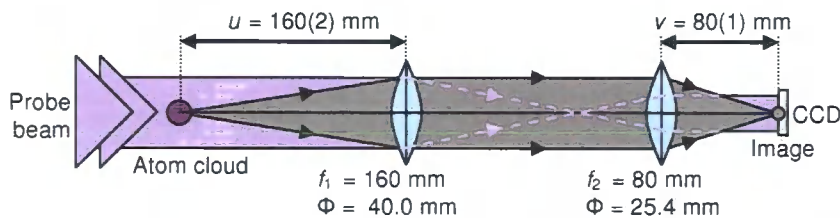
Figure 3.27: Absorption imaging schematic. The absorption profile of a probe beam collimated to a $1/e^2$ radius $w = 7.48(2)$ mm incident upon an atom cloud is imaged onto an 8×8 mm CCD. Two diffraction limited achromatic doublet lenses are used to produce an image with magnification $M = 0.46(5)$ (section 4.8.2). The in-situ imaging system can be seen in figure 3.14.

Principles

An applied B-field of 1.99(3) G from the science MOT south shim coil ensures that light from the circularly polarised probe beam drives σ^- transitions, optically pumping atoms into the $|F' = 3, m'_F = -3\rangle$ and $|F' = 5, m'_F = -5\rangle$ states of ^{87}Rb and ^{133}Cs respectively. In addition to the probe beam,

repumping light is incident on the atomic samples, pumping atoms out of the lower hyperfine ground states. This selection of laser frequencies and probe beam helicity ensures that atoms are pumped from the magnetically trapped states into the closed stretched states with the minimum number of optical transitions. Once in the stretched states atoms continuously absorb light from the probe laser beam, producing a shadow in the imaged laser beam profile from which properties including atom number, cloud temperature, and number density are calculated. The probe beam intensities of $I_{probe} \simeq 0.1 \, I_s$ for both species ensure low sensitivity of peak absorption to fluctuations in probe beam intensity.

Single Species Imaging

Atom cloud properties of a single species are extracted from the intensity profiles of three separate images as described in appendix B.2:

$$I_1 = \text{Probe beam} + \text{Atoms} + \text{Background}, \tag{3.10}$$

$$I_2 = \text{Probe beam} + \text{Background}, \tag{3.11}$$

$$I_3 = \text{Background only}. \tag{3.12}$$

For each 'shot' all three images are used to calculate the optical depth (OD) measured on each camera pixel as:

$$\text{OD} = \ln\left(\frac{I_2 - I_3}{I_1 - I_3}\right) \quad . \tag{3.13}$$

The limitations in accuracy of optical depths extracted in this manner are investigated in section 4.8.2.

Probe Beam Switching

The individual species specific laser beams of which the probe beam is composed are switched using separate AOMs and shutters. This ensures 30 dB extinction within the 1 μs LabVIEW switching time and also total probe beam extinction within 20 μs.

Two Species Imaging

Operating the CCD camera in a 'fast kinetics' frame transfer mode allows two images to be captured within 4.92(1) ms of each other. This delay is sufficiently short to allow properties of both atomic species to be determined within a single experimental 'shot'. The camera CCD array is split vertically into two halves, the first of which is permanently exposed to incident light whilst the second is permanently masked. After exposing the camera CCD to a 10 μs probe pulse of 852 nm ^{133}Cs light, the array of accumulated charges in the exposed section of the CCD is shifted vertically into the masked section. Once the information contained within the first image is stored in this manner, the CCD is then exposed to a 10 μs probe pulse of 780 nm ^{87}Rb light. Three pairs of images are obtained in this manner, corresponding to the three single images described in section 3.10.

3.8.3 Imaging Discussion

Both absorption and fluorescence imaging techniques are used in this apparatus, as the two techniques complement each other greatly. The number of atoms loaded into the MOT is monitored through imaging the MOT fluorescence, which also proves an excellent tool in measuring the relative change in atom number between experimental stages. Both ^{87}Rb and ^{133}Cs can be simultaneously imaged in this manner through the use of dichroic optics. Absorption imaging is fundamentally a far more complex process, especially when operating with two different atomic species simultaneously. The ability to spatially image atom clouds allows properties including cloud temperature, density and phase space density to be easily obtained from a single experimental 'shot', whilst the probing of each atomic cloud on closed cooling transitions eliminates much of the uncertainty in absolute atom numbers associated with fluorescence estimates (due to uncertainty in branching ratios). The best imaging system for this apparatus is to combine both methods to best effect. For example the accuracy of atom numbers obtained by fluorescence imaging is easily improved through directly calibrating the fluorescence photodiode signal against the number of atoms measured via absorption imaging. Similarly, any laser frequency drifts which would result

in inaccurate absorption images can easily be detected through comparison with atom recapture ratios.

3.9 Experimental Control

The operational state of all aspects of the experimental apparatus is determined by the value of:

- Analogue voltage inputs to variable device drivers (*e.g.* shim coil current drivers).

- Digital switching of discrete electronic devices (*e.g.* shutters).

- Direct programming of a small number of devices via a general-purpose interface bus (GPIB).

All constant analogue voltages are set by trimming potentiometers on internal/external voltage reference boards. Whilst all apparatus switching and GPIB programming is controlled from a 'LabVIEW' computer program via three National Instruments interface boards:

- High speed (2 MHz) 32 channel digital TTL input/output board (PCI-DIO-32-HS).

- Combined 8 digital TTL, 8 analogue, channel input/output data acquisition (DAQ) board (PCI-6713).

- GPIB board for direct communication with external devices (PCI-GPIB).

3.9.1 Analogue to Digital

Where switching of a device driver set-point between two or more discrete analogue voltages is required (*i.e.* it is not necessary to continuously vary the analogue voltage), a digital signal is used to switch between discrete potentiometer set analogue levels. Electronic units developed by the Central

Electronics Workshop at the Oxford University Physics Department are used to implement such switching:

- Switching between two analogue levels using a single TTL control input is achieved with the 'Voltage Reference Switching Unit' EW1288.

- Switching between four analogue levels with binary input bits provided by two TTL control inputs of the 'Voltage Level Multiplexer'.

These devices effectively allow TTL signals from 'LabVIEW' digital outputs to control analogue switching operations.

3.9.2 Analogue Control

With all discrete analogue voltages switched digitally (section 3.9.1) the only analogue voltage set-points which are not digitised in this manner are those used to control the current set-points in the magnetic trap baseball, bias, cancellation, and vertical bias coils respectively (figure 3.22). These 'current set-point' voltages are generated at the first four analogue output channels A0 to A3 respectively of PCI-6713. These currents are switched prior to magnetic trap turn on, after magnetic trap turn off, and during magnetic trap ramps only.

3.9.3 Digital Control

All digital switching operations are triggered by the channels from PCI-DIO-32-HS (labeled A0-D8) and the first four digital channels on PCI-6713 (DIO0-DIO3), all of which are initialised as output channels. The timing sequence for loading the magnetic trap from the MOT, conducting an experiment, and imaging both atomic species can be seen in tables 3.6 and 3.7. This timing sequence is triggered at the beginning of each experimental shot. The only additional input required is a digital TTL signal from the camera after each pair of images is taken, indicating that the CCD is ready to capture a subsequent pair of images.

Channel			Loading MOT	MOT	CMOT	MOL	OP	MT	MT ramp	MT hold	Image 1	Image 2	Image 3
A	0	BB on/off											
A	1	Bias on/off											
A	2	BB cap's in/out											
A	3	Bias cap's in/out											
A	6	Grey shims 1											
A	7	Grey shims 2											
B	0	MOT shims 1											
B	1	MOT shims 2											
B	2	MOT coils 1											
B	3	MOT coils 2											
B	5	Camera fire											
C	0	Cs MOT shutter											
C	1	Cs rep. shutter											
C	2	Cs probe shutter											
C	3	Cs OP shutter											

Continued on next page

Table 3.6: Idealised timing diagram showing TTL high and low (0 and 1) states of LabVIEW digital experimental outputs during a typical experiment. Black (gold) lines show outputs (inputs). Sequences shaded in lilac (white) occur on a timescale of tens of ms (seconds), with microsecond (tens of ms) accuracy. This table is split across two pages.

Channel			Loading MOT	MOT	CMOT	MOL	OP	MT	MT ramp	MT hold	Image 1	Image 2	Image 3
C	4	Rb MOT shutter											
C	5	Rb rep. shutter											
C	6	Rb probe shutter											
C	7	Rb OP shutter											
D	0	Cs MOT det. 1											
D	1	Cs MOT det. 2											
D	2	Rb MOT det. 1											
D	3	Rb MOT det. 2											
D	4	Cs Op/probe pulse											
D	5	Rb Op/probe pulse											
D	6	OP det.											
DIO 0		Cs pyramid shutter											
DIO 1		Rb pyramid shutter											
DIO 2		Pyramid coils											
DIO 3		Pyramid shims											
DIO 4		Andor response											

Continued from previous page

Table 3.7: Idealised timing diagram *continued* showing TTL high and low (0 and 1) states of LabVIEW digital experimental outputs during a typical experiment. Black (gold) lines show outputs (inputs). Sequences shaded in lilac (white) occur on a timescale of tens of ms (seconds), with microsecond (tens of ms) accuracy. This table is split across two pages.

3.9.4 GPIB Control

Operation of the magnetic trap bias coil current supply (section 3.6.3), and two RF signal generators (Agilent E4400B) used to generate radio-frequency evaporation ramps, is achieved by directly programming these devices through the GPIB interface board.

3.9.5 LabVIEW Control Programme

The programme used to control the outputs of all three National Instruments boards is developed from that described in [93] to be suitable for two species experiments.

Timing Hierarchy

Two different levels of timing are utilised in this experiment; microsecond accuracy for aspects where coincidence of events/reproducability is time-critical (*e.g.* transfer of atoms into the magnetic trap, absorption imaging of atoms), and low-level accuracy within a few tens of milliseconds for operations which occur over a longer timescale (*e.g.* MOT loading, magnetic trap hold times).

- Microsecond timing is achieved by loading the states to which all of the digital output channels must be set at each microsecond interval into an electronic buffer. The electronic buffer is then triggered to output this data to the interface boards at a 1 MHz clock frequency. The use of a buffer eliminates the variability of output times induced by dependence on software command execution times.

- Low-level timing accuracy is determined using software 'hold' commands prior to directly addressing channel outputs through software controls. These timings are dependent on software command execution times.

Device Delays

Known device delays (*e.g.* coil/shutter switching times) are entered into the LabVIEW control programme. The programme then incorporates these delays into calculations used to evaluate device switching times, ensuring the *experimental parameters* are switched at the times outlined in tables 3.6 and 3.7.

Chapter 4

Results: Optimisation and Characterisation

This chapter describes the optimisation of all stages of the experiment required to obtain a magnetically trapped, cold atomic mixture, along with characterisation of the operational parameters and diagnostics. As a first iteration the apparatus is optimised for both species individually. This inherently assumes the behavior of both species to be independent. Where this assumption is found wanting the results of optimisation are indicative of novel inter-species collisional behavior, hence are presented in the experimental results chapter.

4.1 Pyramid MOT Optimisation

The role of the pyramid MOT (section 3.4) is to provide a source of cold atoms for investigation in the UHV science region of the vacuum apparatus. Thus the objective of pyramid MOT optimisation is to provide the maximum rate of atomic flux capture for fixed parameters of the science MOT. The pyramid and science MOT parameters are broadly optimised prior to rigorous optimisation of the pyramid MOT with the science MOT fixed. This ensures the consecutive optimisation of both MOT stages results in a globally optimal apparatus performance. Key parameters affecting the pyramid MOT performance for each species include: magnetic field (gradient and position of

zero), cooling light (detuning and intensity), repumping light (intensity) and atomic vapour pressure (dispenser current). Not all of these parameters are independent from each other for the single species case. Also, optimum magnetic field characteristics for one species may not match those obtained for the second species, and so in some cases a compromise may be required. Initial optimisation is carried out for ^{133}Cs, exploring the full parameter space. After this all independent ^{87}Rb parameters are optimised. In both cases the optimisation is performed by measuring the atom number captured in the science MOT after 10 s while varying the parameters of the pyramid MOT. The relative captured atom number after 10 s is measured by imaging the science MOT fluorescence onto a calibrated photodiode.

4.1.1 Single Species Operation

Initially atomic dispenser currents of 3.00(1) A are selected for both species. The captured flux is highly sensitive to the dispenser current, *e.g.* increasing to 4.00(1) A results in an order of magnitude increase in the captured atomic flux over a 10 s period. Ultimately both the lifetime of atoms in the magnetic trap, and the operational lifetime of the dispensers will be adversely affected by operating at unnecessarily high currents. The 51.6(2) mW (53.9(2) mW) maximum ^{87}Rb (^{133}Cs) cooling light output of the pyramid fibre, provides a peak laser beam intensity of 9.1(2) mW cm^{-2} (9.3(2) mW cm^{-2}) incident upon the pyramid optics (section 3.4). This maximum available cooling light intensity is used during the optimisation process for both species, with the effective total pyramid MOT cooling light intensity having approximately six times this value. The ^{87}Rb (^{133}Cs) repumping light combined into the pyramid beam provides 0.39(1) mW cm^{-2} (0.37(1) mW cm^{-2}) of intensity incident upon the pyramidal mirror. This is sufficient to ensure atoms remain in the cycling cooling transitions.

Pyramid Alignment

Whether the pyramid MOT acts as a static MOT or a cold-atomic beam source depends on the alignment of the MOT centre. Although the direction of the cold-atomic beam is not strongly dependent on the pyramid laser

beam alignment (due to the divergence of the atomic beam), it is essential for the laser beam not to contribute optical pressure to the science MOT trapping region. This is achieved by positioning the laser beam transmitted through the pyramid apex $\simeq 5$ mm above the science MOT centre. Two shim coils (section 3.4.3) mounted to generate B-fields in the E-W and N-S direction (using the orientation definition of figure 3.14) allow separate adjustment of the transverse (horizontal) and axial position of the B-field zero respectively. This allows the MOT to be horizontally centred upon the aperture at the pyramid apex and vertically positioned at the centre of the pyramid optics capture volume. The degree of movement of the MOT
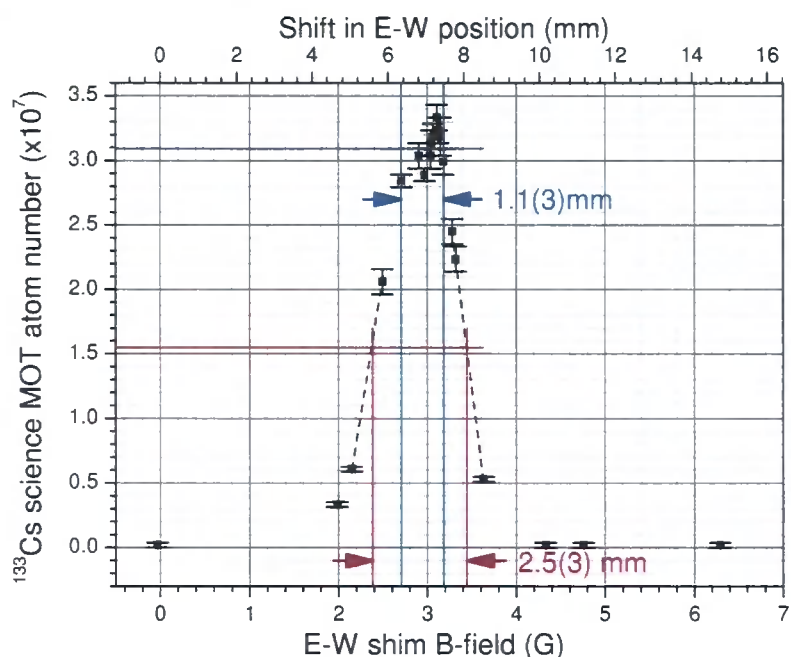
Figure 4.1: Pyramid east-west shim magnetic field optimisation for an axial (N-S) MOT coil gradient of 8.5(3) G cm^{-1}. Varying the magnetic field produced by the pyramid E-W shim coil (bottom axis), results in a positional shift (top axis) of the B-field zero. The ^{133}Cs atom number captured in the science MOT after 10 s (y axis) is measured by imaging the science MOT fluorescence onto a calibrated photodiode. The captured atom number reaches a maximum of $3.09(5) \times 10^7$ atoms, over a B-field zero position range of 1.1(3) mm. The data is consistent with a horizontal aperture size of 2.5(3) mm and a MOT cloud size of 1.4(4) mm (see text for details).

centre is proportional to the applied B-field, with constant of proportionality dependent on the pyramid MOT coil B-field gradient. The dependence of the captured ^{133}Cs pyramid MOT flux on transverse position of B-field centre at a MOT coil gradient of 8.5(3) G cm^{-1} is shown in figure 4.1. Note the distinct region over which the captured flux is a maximum. The uniformity of this maximum indicates that within this 1.1(3) mm region the captured atom cloud is entirely over the aperture at the pyramid apex. When the captured flux drops to half this maximum value, only half of the pyramid MOT cloud is over the pyramid apex. The two E-W B-field zero positions at which this occurs are separated by 2.5(3) mm. This indicates the width of the pyramid apex in the E-W direction is 2.5(3) mm. This is consistent with
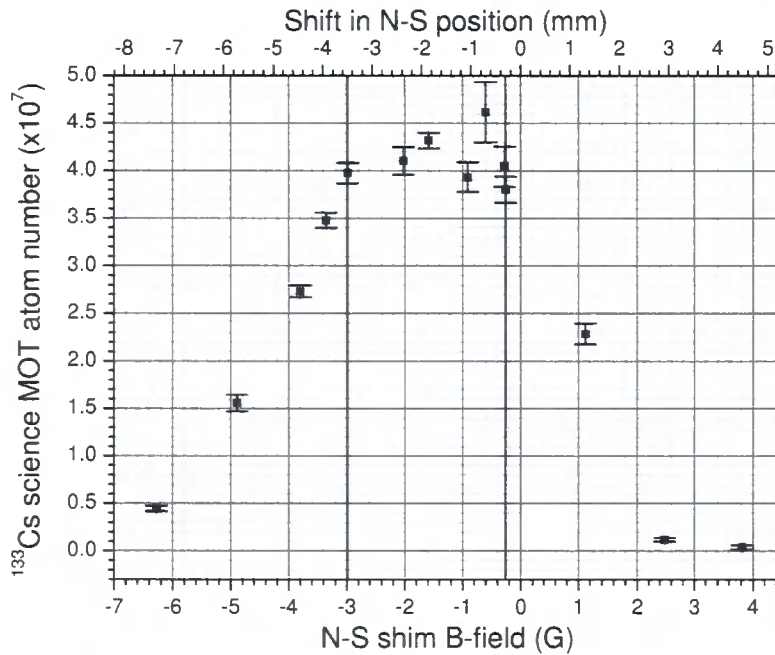
Figure 4.2: Pyramid north-south magnetic field optimisation for an axial (N-S) MOT coil gradient of 8.5(3) G cm^{-1}. Varying the magnetic field produced by the pyramid N-S shim coil (bottom axis), results in a positional shift (top axis) of the B-field zero. The ^{133}Cs atom number captured in the science MOT after 10 s (y axis) is measured by imaging the science MOT fluorescence onto a calibrated photodiode. During science MOT loading the N-S B-field is set to 1.3(1) G. At this field the ^{133}Cs atom number captured over a 10 s period is maximised.

the visually estimated apex width of $\simeq 3$ mm. Subtracting the width of the maximum region from that of the half-maximum, the pyramid atom cloud width is calculated to be 1.4(4) mm. During loading of the science MOT the B-field zero is positioned at the centre of the maximum flux region (applied E-W B-field of 2.7(2) G). The corresponding captured flux dependence on applied axial B-field (figure 4.2) displays a clear maximum at an applied N-S magnetic field of 1.3(1) G. The N-S coils are subsequently operated at this B-field during science MOT loading.

Detuning and Intensity

The ^{133}Cs pyramid MOT cooling light detuning at which the maximum ^{133}Cs flux is captured in the science MOT is measured for a range of magnetic field gradients (figure 4.3(a)). As the B-field gradient is increased, the magnitude of the zero-field laser detuning from resonance at which the captured flux is maximised shows a corresponding increase (figure 4.3(b)). This ensures the Zeeman-shifted cooling light detuning from resonance observed by atoms at the edge of the pyramid MOT capture volume remains negative at the increased gradient. The 1.00(3) MHz cm G^{-1} gradient of a linear fit to this data when divided by the linear Zeeman shift of $\simeq 1.4$ MHz G^{-1} is equivalent to an axial distance from the MOT centre to the edge of the trapping region of 7.1(2) mm (this is comparable to the axial mirror dimension of 42.4 mm). The maximum captured ^{133}Cs flux occurs within a B-field gradient range $5.0 < \frac{\partial B}{\partial z} < 11.0$ G cm^{-1}. At a fixed gradient of 8.5(3) G cm^{-1} the optimum detuning for maximum captured ^{133}Cs flux is -16.1(2) MHz. Repeating this measurement for ^{87}Rb gives an optimum cooling light detuning from resonance of -17.0(2) MHz.

Figure 4.3: ^{133}Cs pyramid MOT detuning optimisation. The cooling light detuning (a) is varied for magnetic field gradients of: 5.0(2)(Blue), 8.5(3) (Purple), 11.0(4) (Black) and 13.8(5) G cm^{-1} (Red). The ^{133}Cs atom number captured in the science MOT after 10 s (y axis) is measured by imaging the science MOT fluorescence onto a calibrated photodiode. At each B-field gradient the B-fields produced by the E-W and N-S pyramid MOT shim coils are adjusted to maximise this captured atom number. Of the measured B-field gradients the maximum flux is obtained at 8.5(3) G cm^{-1}, with a cooling light detuning of -16.1(2) MHz. As the B-field gradient is increased, the magnitude of the laser detuning from resonance at which the captured flux is maximised shows a corresponding increase (b).

4.1.2 Two Species Operation

The captured atom flux in a single species science MOT is not affected by the presence of a second species in the pyramid MOT (figure 4.4). This demonstrates that the atomic densities in the cold-atomic beam are too low for two species collisions to be a significant source of atom loss. Thus the pyramid MOT provides an excellent atom source for two-species cold atom experiments.
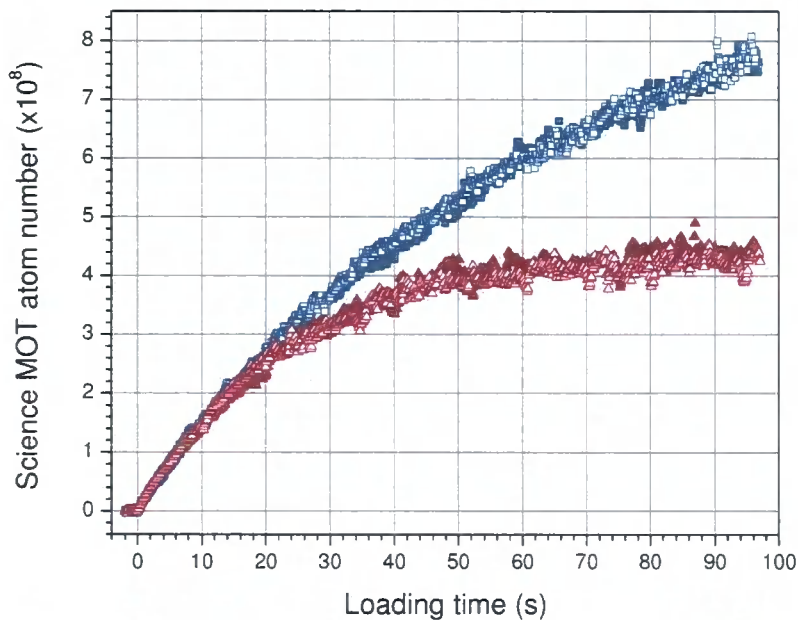
Figure 4.4: Single species science MOT loading for various configurations of the pyramid MOT: ^{87}Rb alone (solid blue), ^{87}Rb with ^{133}Cs (open blue), ^{133}Cs alone (solid red), and ^{133}Cs with ^{87}Rb (open red). Each data point is a 10 point moving average of the atom number measured from the science MOT fluorescence imaged onto a calibrated photodiode. The data demonstrate that the atomic flux from the pyramid MOT is not affected by the presence of a second species.

4.2 Science MOT Optimisation

The parameters of the science MOT are optimised to capture the maximum number of atoms for collective transfer into the magnetic trap. The number of atoms captured in the science MOT will reach a maximum when the rate of atom loss due to light-assisted cold collisions and background collisions with residual gas molecules becomes equal to the loading rate from the pyramid MOT. With the pyramid MOT parameters fixed to produce a continuous single species cold-atomic beam (section 4.1) the balance between loading and loss rates for each species is governed by many parameters, including: magnetic field (gradient and position of zero), cooling light (detuning and intensity), repumping light (intensity), laser beam alignment and atom flux from the pyramid MOT. As is the case for the pyramid MOT, not all of these parameters are independent from each other for the single species case. Initial optimisation is carried out for ^{133}Cs alone, exploring the full parameter space to give the maximum total number of ^{133}Cs atoms trapped in the science MOT (not the maximum number of atoms captured within 10 s). After this all independent ^{87}Rb parameters are optimised for the single species case to maximise the number of trapped ^{87}Rb atoms. Initially the centres of the science MOT beams for both species are aligned to intersect within $\simeq 1$ mm of the geometrical centre of the magnetic trapping coils. It is at this position which the pyramid MOT was optimised. The maximum cooling light power output from the ^{87}Rb (^{133}Cs) science MOT optical fibre of 55.0(1) mW (41.5(1) mW) is used during optimisation, providing six laser beams with identical intensities of 2.28(7) mW cm^{-2} (2.06(4) mW cm^{-2}). Repumping light of 86(3) μW cm^{-2} and 97(2) μW cm^{-2} for ^{87}Rb and ^{133}Cs respectively is sufficient to ensure all atoms remain in the cycling cooling transitions.

4.2.1 Single Species Operation

The dependence of the equilibrium atom number loaded from the ^{133}Cs cold-atomic beam into the ^{133}Cs science MOT as a function of cooling light detuning for a range of science MOT coil gradients is investigated (figure 4.5) with all beam intensities fixed as described in section 4.2. The number of ^{133}Cs

atoms loaded into the science MOT is maximised at a B-field gradient of 13.0(2) G cm^{-1} at a cooling light detuning of -10.5(2) MHz. Repeating this measurement for ^{87}Rb gives an optimal cooling light detuning from resonance of -12.2(2) MHz.

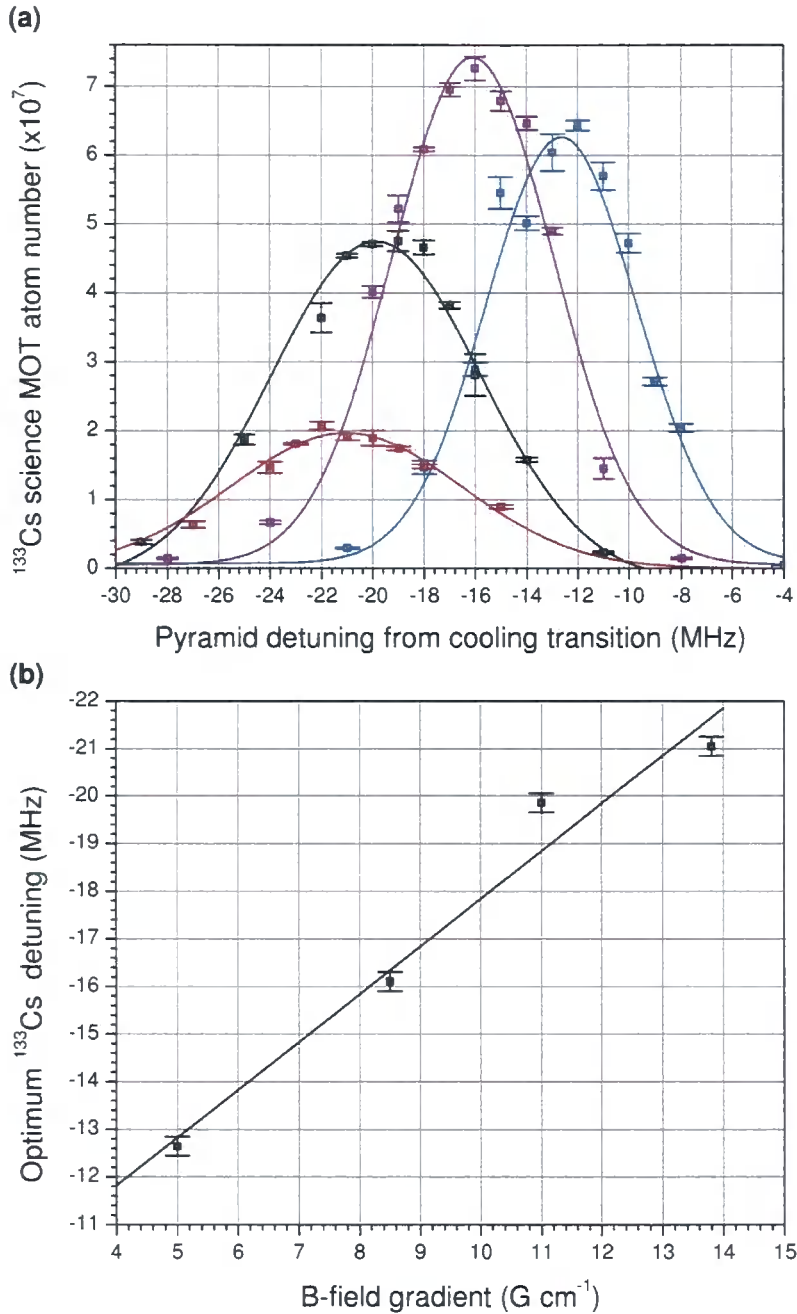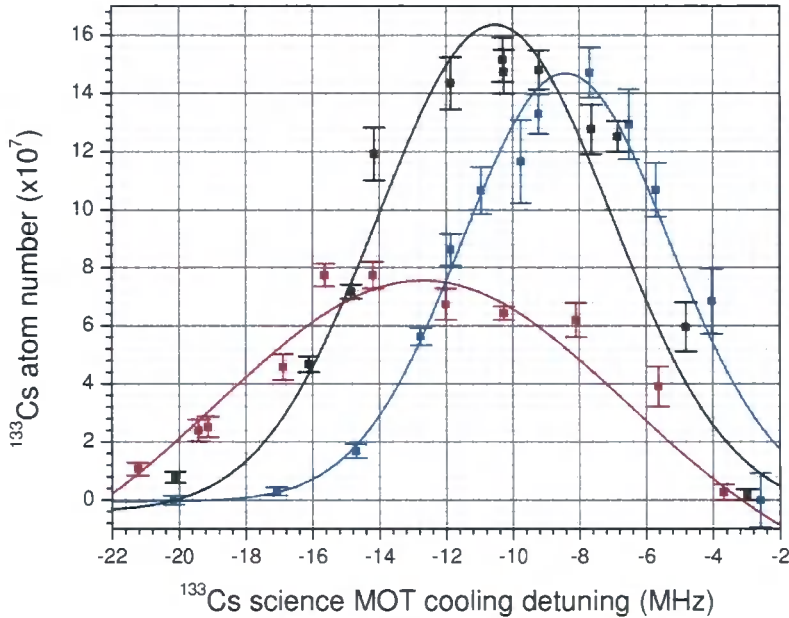Figure 4.5: Science MOT cooling detuning optimisation. The ^{133}Cs cooling light detuning is varied for magnetic field gradients of: 5.13(7)(Blue), 13.0(2) (Black) and 15.0(2) G cm^{-1} (Red). Lines shown are to guide the eye. The equilibrium ^{133}Cs atom number captured in the fully loaded science MOT (y axis) is measured by imaging the science MOT fluorescence onto a calibrated photodiode. At each B-field gradient the B-fields produced by the science MOT shim coils are adjusted to align the B-field zero with the geometrical centre of the baseball coil. Of the measured B-field gradients the maximum flux is obtained at 13.0(2) G cm^{-1}, with a cooling light detuning of -10.5(2) MHz. As the B-field gradient is increased, the magnitude of the laser detuning from resonance at which the captured flux is maximised shows a corresponding increase.

4.3 Compressed MOT Optimisation

The CMOT stage allows a transient change in MOT parameters from those used to maximise the number of atoms captured in the MOT to those most favourable for loading into the magnetic trap, as described in section 3.7.1. As the potential energy of magnetically trapped atoms is dependent on their position in the magnetic trap, it is favorable to load them directly into the position at which the sum of magnetic and gravitational potential energy is minimised, described hereafter as the magnetic trap centre (not to be confused with the geometrical coil centre). The gravitational sag, and hence the centre of oscillation, is different for atoms trapped in each Zeeman sub-level, hence it is necessary to ensure the CMOT parameters are optimised for the $|F = 1, m_F = -1\rangle$ and $|F = 3, m_F = -3\rangle$ states of ^{87}Rb and ^{133}Cs respectively. With depumping light for each species ensuring only the lower hyperfine ground states are populated, even without optical pumping, only atoms in the desired ^{87}Rb Zeeman sub-level are magnetically trapped (this is not the case for ^{133}Cs). For this reason, optimisation of the cloud position during the CMOT stage is carried out using ^{87}Rb atoms. The further from the potential minimum atoms are loaded, the greater their gain in potential energy due to the magnetic trap loading process. Atoms loaded away from the trap centre will oscillate harmonically within the trap. Interatomic collisions eventually redistribute this energy throughout the atomic ensemble, resulting in a net gain in temperature of the trapped atom cloud (and loss of phase-space density). If the atom cloud centre of the CMOT is offset from the magnetic trap centre, the entire ensemble of trapped atoms will oscillate with a significant amplitude at the corresponding radial/axial magnetic trap frequencies (as can be seen in figure 4.6). This process is described as 'sloshing'. If the magnetic trap shape is not matched to that of the atom cloud prior to loading, the magnetically trapped cloud will alternately expand and contract at the corresponding radial and axial trap frequencies. This process is described as 'breathing'. Preliminary investigation of the effect of varying the B-field gradient, cooling light detuning, and duration of the ^{87}Rb CMOT phase showed little variation in the peak optical depth of the atom cloud following loading into the magnetic trap (as measured through absorption imaging), indicating little variation in atom number density. Fixing the

CMOT B-field gradient and detuning at 20.2(3) G cm^{-1} and -28.7(3) MHz respectively, the optimum cloud position for loading the magnetic trap (in terms of minimising the potential energy picked up by the atomic ensemble) is obtained using the method described below.
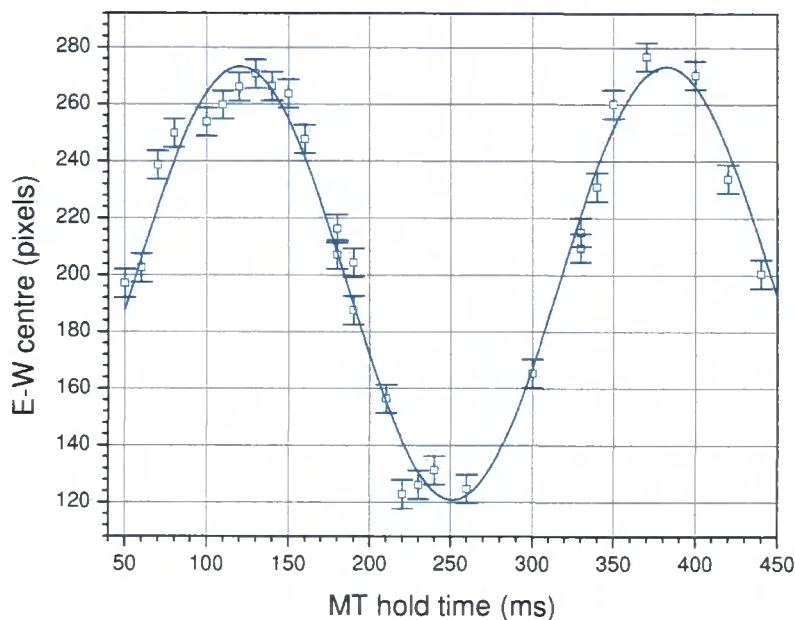
Figure 4.6: Imaged E-W (axial) centre of ^{87}Rb atom cloud as a function of hold time in the magnetic trap (blue data points). This data is typical of atoms 'sloshing' in the trap. Blue line shows a sinusoidal fit to the data.

4.3.1 Slosh Amplitude Minimisation

In order to minimise the amplitude at which atoms loaded into the magnetic trap oscillate, the position of B-field zero during the CMOT phase must be tuned to coincide with the centre of oscillation in the magnetic trap. This is achieved by measuring the slosh amplitude in the magnetic trap as a function of applied magnetic field along the N-S, E-W and U-D axes during the CMOT phase, before setting these parameters to those of the fitted minimum value. It is not necessary to repeatedly characterise a full trap oscillation in the manner of figure 4.6 in order to obtain the oscillation amplitude at each value of applied shim-coil field. The method described below allows the

oscillation amplitude along each axis of the trap to be obtained from three images, providing the corresponding trap frequency is known.

Method

As the oscillation of atoms along one axis of the Ioffe-Pritchard trap is to first order harmonic with a trap frequency ω, the position of the atom cloud centre u at any time t will satisfy the equation:

$$\frac{\mathrm{d}^2 u}{\mathrm{d}t^2} = -\omega^2 \left(u - c_0\right) \quad , \tag{4.1}$$

where c_0 is the position of the magnetic trap centre of oscillation. Solving this equation for an atom cloud with position and velocity of the cloud centre at time $t = 0$ of $u(0) = a + c_0$ and $\dot{u}(0) = v$ respectively gives:

$$u(t) = A \sin\left(\omega t + \phi\right) + c_0 \quad , \tag{4.2}$$

where the slosh amplitude A and phase ϕ are:

$$A = \left(a^2 + \frac{v^2}{\omega^2}\right)^{\frac{1}{2}} \quad \text{and} \tag{4.3}$$

$$\phi = \tan^{-1}\left(\frac{a\omega}{v}\right) \quad . \tag{4.4}$$

Taking images at times $t = 0$, $t = \frac{T}{4}$ and $t = \frac{T}{2}$ (where $T = \frac{2\pi}{\omega}$ is the trap oscillation period) the positions of the atom cloud centre are:

$$u(t = 0) = c_1 = A \sin\phi + c_0 \quad , \tag{4.5}$$

$$u(t = \tfrac{T}{4}) = c_2 = A \cos\phi + c_0 \quad \text{and} \tag{4.6}$$

$$u(t = \tfrac{T}{2}) = c_3 = -A \sin\phi + c_0 \quad . \tag{4.7}$$

From these three measurements the centre of oscillation in the magnetic trap, slosh amplitude, and phase introduced in equation 4.2 are extracted as:

$$c_0 = \frac{c_1 + c_3}{2} \quad , \tag{4.8}$$

$$A = \left[(c_1 - c_0)^2 + (c_2 - c_0)^2\right]^{\frac{1}{2}} \quad \text{and} \tag{4.9}$$

$$\phi = \tan^{-1}\left(\frac{c_1 - c_0}{c_2 - c_0}\right) \quad . \tag{4.10}$$

The slosh amplitude is minimised by varying the magnetic field applied along the investigated axis until the a minimum value of A is found. The magnitude of this minimum (A_{min}) corresponds to the mean velocity of the atomic ensemble along the axis when the magnetic trap is initially loaded:

$$v_{\mathrm{load}} = \omega A_{\mathrm{min}} \quad . \tag{4.11}$$

Minimising Slosh Amplitude In Image Plane

The slosh amplitude along the two axes of the imaged plane (U-D and E-W axes of figure 3.14) as a function of applied magnetic field from the U-D and E-W shim coil pairs respectively is shown in figure 4.7. The images analysed to produce these figures are of atoms released from the magnetic trap after varying hold times. Prior to loading into the magnetic trap the atomic ensemble is subject to a 15 ms optical molasses and 1.40 ms optical pumping phase. Through tuning the magnetic fields provided by the U-D and E-W shim coil pairs, the oscillation amplitudes in the U-D and E-W directions are reduced to 0.20(7) mm and 1.6(2) mm respectively (figure 4.7). Eliminating the optical pumping phase results in a further reduction in oscillation amplitude along the E-W direction to 0.61(2) mm. This indicates the net velocity imparted upon the atom cloud by the optical pumping beam. This effect is fully investigated in section 4.5, but to simplify matters the optical pumping phase is eliminated during further optimisation of the CMOT phase.

Minimising Slosh Amplitude in Non-Imaged (N-S) Direction

Although the amplitude of oscillations along the N-S direction cannot be monitored directly in the imaged plane, such oscillations result in heating of the atomic ensemble. Figure 4.8 shows the axial temperature (that along the E-W axis) of the atomic cloud after 10 s as a function of control voltage applied to the south shim coil (which the magnetic field applied along the N-S axis is proportional to). The resulting data (figure 4.8) show a clear minimum temperature (with no optical pumping) of 52.7(6) μK at a south shim control voltage of 0.491(5) V.
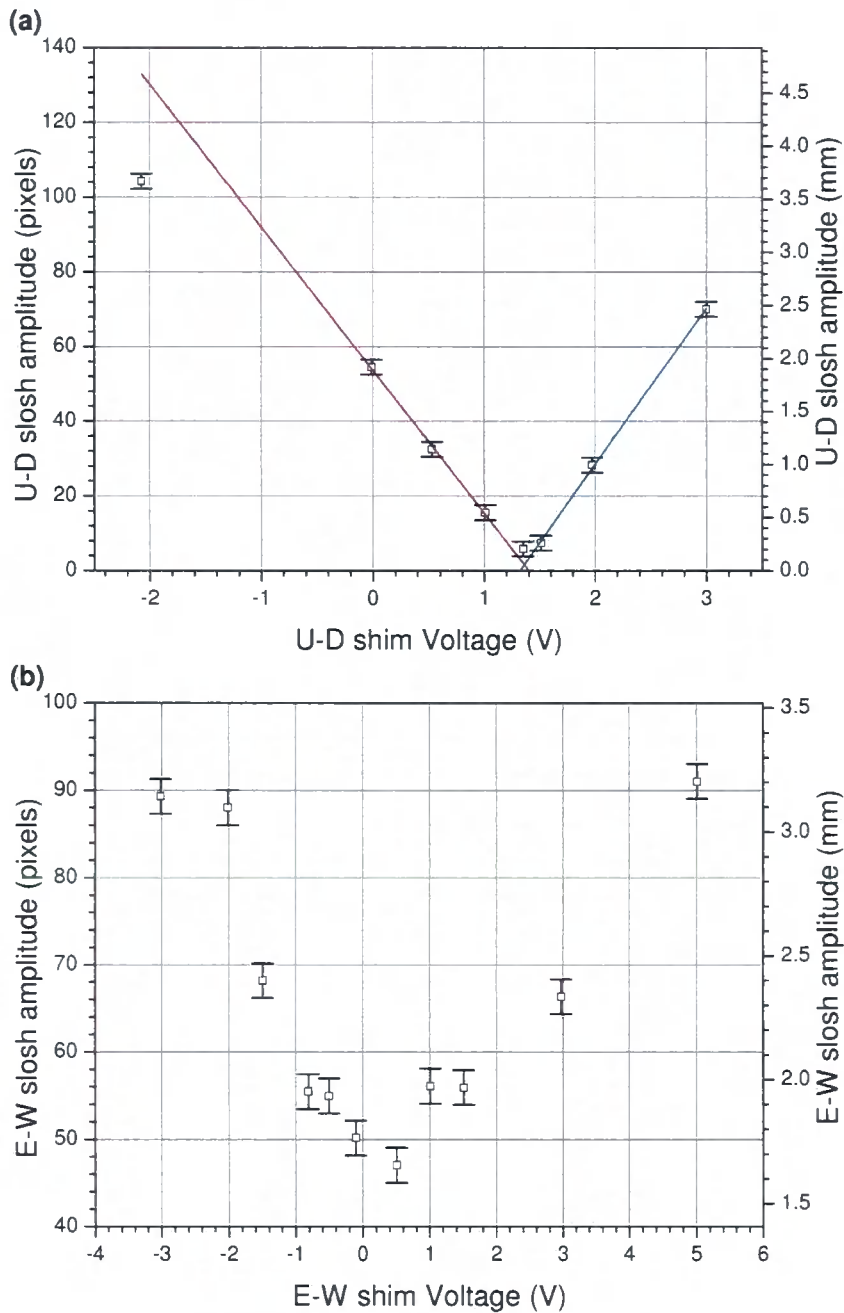
Figure 4.7: ^{87}Rb oscillation amplitude in the E-W and N-S direction as a function of control voltage applied to the corresponding shim coil pairs during the CMOT experimental phase (which the magnetic field is proportional to) is shown in figures (a) and (b) respectively. The CMOT phase is immediately followed by an optical molasses and an optical pumping phase before loading the atomic ensemble into the magnetic trap. In both cases the oscillation amplitude is measured using the three-point method described in section 4.3.1. The U-D (E-W) oscillation amplitude is reduced to 0.20(7) mm (1.6(2) mm) at an U-D (E-W) control voltage of 1.350(5) V (0.506(5) V).
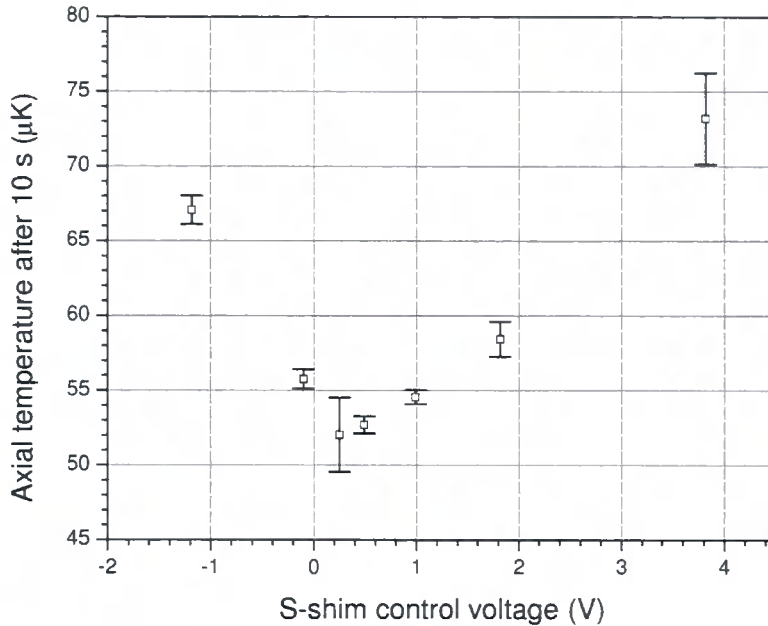
Figure 4.8: ^{87}Rb axial (E-W) temperature after a 10 s hold in the magnetic trap as a function of south shim control voltage during compressed MOT phase (which the magnetic field applied along N-S axis is proportional to). At 0.491(5) V the atom cloud temperature is reduced to 52.7(6) μK.

4.4   Optical Molasses Optimisation

With the position of the ^{87}Rb cloud centre during the CMOT stage optimised in all three directions, attention is focussed on reducing the temperature at which atoms are loaded into the magnetic trap. The objective of the optical molasses optimisation is to minimise this loading temperature without significantly increasing the cloud size from that obtained at the end of the CMOT stage. The molasses is implemented by simultaneously increasing the ^{133}Cs (^{87}Rb) cooling light detuning to -59.9(8) MHz (60.1(3) MHz) and switching off the science MOT coils. The magnetic field contributions from each of the science cell shim coils are set to null the B-field at the CMOT centre, by adjusting the B-field along the N-S, E-W and U-D axes to minimise any cloud drift when the quadrupole field is removed. Varying the length of the optical molasses phase, the proportion of atoms successfully transferred into the magnetic trap is monitored through MOT recapture (see figure 4.9).
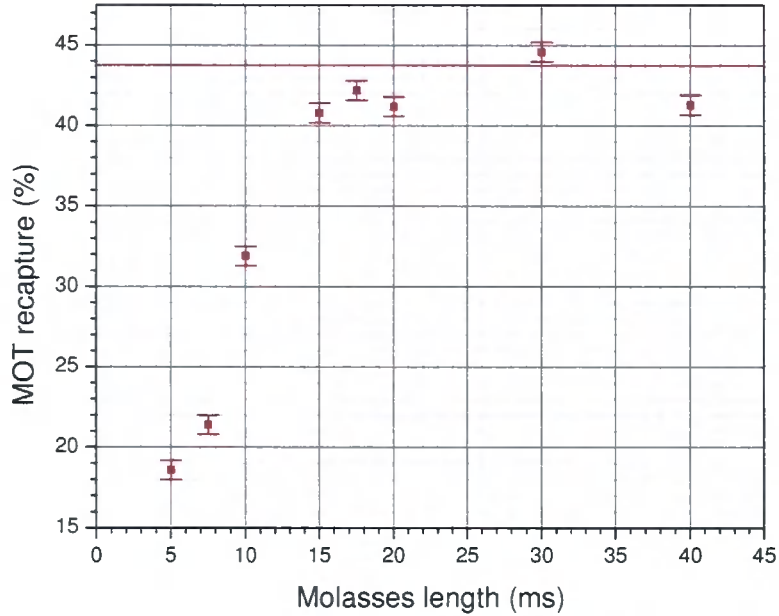
Figure 4.9: Percentage of atoms from a 10 s ^{133}Cs science MOT load recaptured in the MOT after a 1 s hold in the magnetic trap as a function of optical molasses duration. During the molasses phase the ^{133}Cs cooling light is detuned -59.9(8) MHz from the $F = 4 \rightarrow F' = 5$ transition. Note no optical pumping or depumping is implemented for this data, hence the maximum expected recapture proportion is $\simeq 44\%$ (red line). Increasing the optical molasses duration above $\simeq 15$ ms does not significantly increase the recapture percentage, hence the duration is set to be 15 ms.

For an optical molasses duration of 15 ms, 41.0(5) % of atoms loaded into the ^{133}Cs science MOT are successfully transferred into the magnetic trap. As the data of figure 4.9 are taken without optical pumping or depumping, the maximum proportion of atoms expected to be transferred into the magnetic trap is $\simeq 44$ % (only seven of the sixteen Zeeman sub-levels are magnetically trappable). This indicates that, in terms of number transfer, there is little to be gained in further adjusting the ^{133}Cs optical molasses parameters. The temperature of a cloud of ^{87}Rb atoms after the 15 ms optical molasses phase is measured to be 8(1) μK (figure 4.10). This demonstrates how effective the optical molasses is in cooling small atom clouds prior to transfer into the magnetic trap.
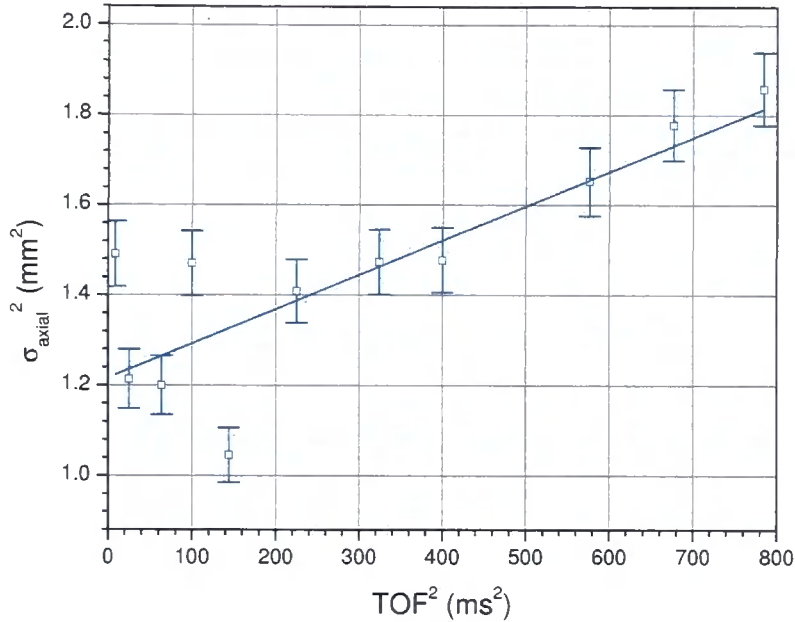
Figure 4.10: The squared axial $e^{-1/2}$ radius ($\sigma_{\mathrm{ax}}{}^2$) of a cloud of $3.6(3) \times 10^7$ ^{87}Rb atoms as a function of squared time of flight (TOF) following a 15 ms optical molasses is shown (blue symbols). The axial temperature of the cloud is calculated by fitting: $\sigma_{\mathrm{ax}}{}^2(t) = \sigma_0{}^2 + (k_{\mathrm{B}}T_{\mathrm{ax}}/m_{\mathrm{Rb}})\, t^2$ to the data (blue line), from which the axial temperature $T_{\mathrm{ax}} = 8(1)\ \mu$K is obtained. The axial atom cloud radius is measured from absorption images taken at varying times after release from the optical molasses.

4.5 Optical Pumping Optimisation

The objective of the optical pumping stage is to polarise the entire ^{87}Rb (^{133}Cs) ensemble into the single $|F = 1,\, m_F = -1\rangle$ ($|F = 3,\, m_F = -3\rangle$) atomic state without significantly heating the atomic ensemble. Parameters affecting the optical pumping performance for each species include: optical pumping beam (intensity, duration and polarisation), depumping light (intensity and duration) and the magnitude of the applied magnetic quantization field. Initially the optical pumping and depumping light for each species is set to be simultaneously incident on a ^{87}Rb atomic ensemble for 1.50 ms, and resonant with the respective transitions in table 3.1. The quantisation field along the axis of the optical pumping beam is set using the grey

shim coils to be 2.00(4) G. Hyperfine state selective images of ^{87}Rb (^{133}Cs)
ensembles after release from the magnetic trap with depumping light present
(section 3.7.3) show a complete absence of atoms in the upper-hyperfine state
(contrary to the case when depumping light is not present). With effective
depumping in place, optimisation of the optical pumping beam parameters
may be carried out.

4.5.1 Polarisation and Detuning

The first parameter to be optimised is the optical pumping beam polarisa-
tion, which is set for both atomic species using a single achromatic quarter
waveplate. The proportion of ^{87}Rb atoms loaded into the MOT which are
subsequently recaptured after a 2s hold in the magnetic trap as a function of
angle of the achromatic waveplate used to circularly polarise the 0.96(2) mW
optical pumping beam is shown in figure 4.11. The waveplate angle is sub-
sequently set to -60.2(2) ° relative to the arbitrary angle at which it is fixed
into a rotatable mount. At this angle the proportion of recaptured atoms
is maximised to be 50.8(3) %. For this waveplate angle, the ^{87}Rb recapture
proportion is not sensitive to a $\simeq \pm 10$ MHz shift in optical pumping beam
detuning from the $F = 1 \rightarrow F' = 1$ transition, thus the detuning of 0(1) MHz
for both atomic species entirely suitable. The data shown in figure 4.11 is
taken using MOTs significantly larger in diameter than the optical pumping
beam. For smaller MOTs, setting the waveplate angle 90 ° away from that
at which recapture is maximised results in no atoms being recaptured.

4.5.2 Intensity and Duration

Once the atomic ensemble is polarised into the desired state there is nothing
to be gained from continuing to expose the atoms to optical pumping light, as
this can lead to heating of the ensemble (as can excessive beam intensities).
A prolonged optical pumping stage would also allow the unconfined ensemble
to expand unnecessarily prior to loading into the magnetic trap. Figure 4.13
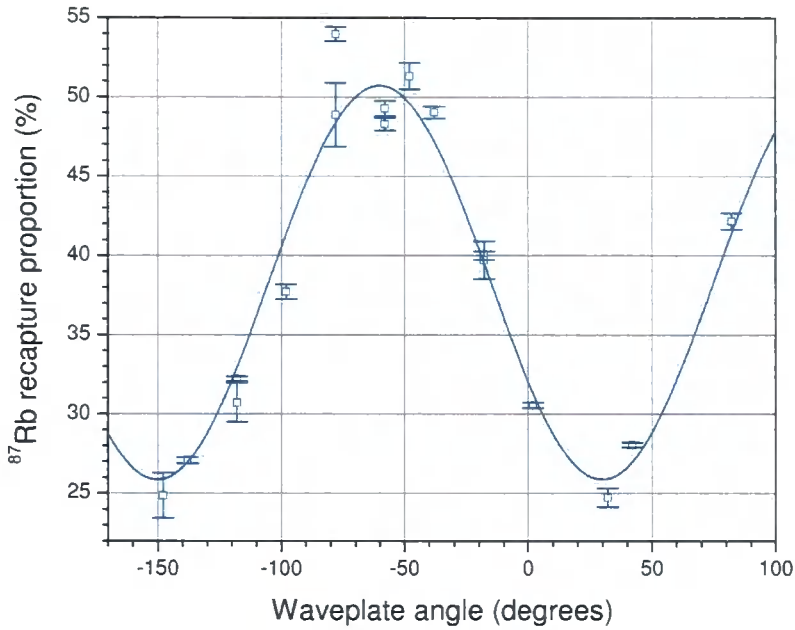
Figure 4.11: Proportion of atoms loaded into the ^{87}Rb MOT recaptured after a 2 s hold in the magnetic trap as a function of optical pumping quarter waveplate angle θ (blue data points). The position of this angular scale relative to the waveplate axis is subject to an arbitrary offset. From the recapture $= A + B \cdot \sin^2(\theta - \phi)$ fit (blue line), the waveplate angles at which this proportion is maximised to 50.8(3) % are θ=-60.2(2) and θ=119.8(2) °.
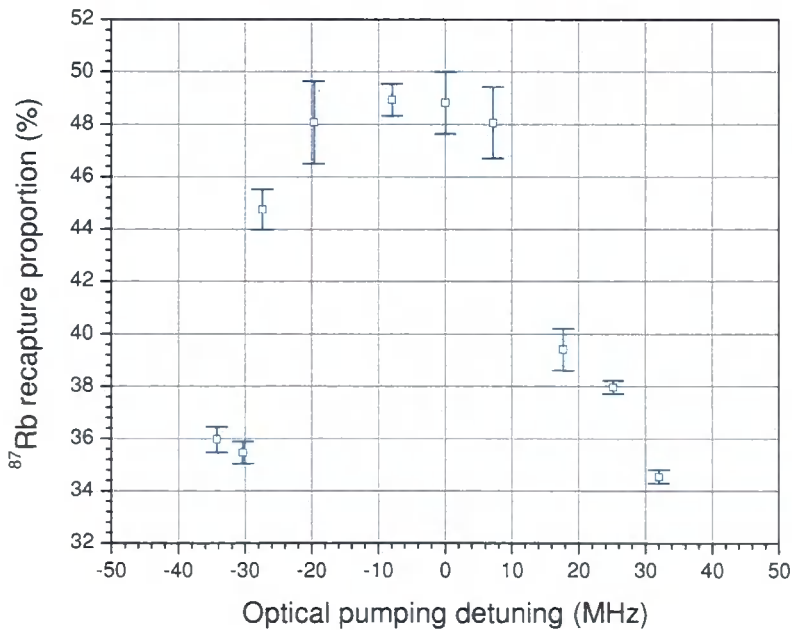
Figure 4.12: Proportion of atoms loaded into the ^{87}Rb MOT recaptured after a 2 s hold in the magnetic trap as a function of 0.96(2) mW optical pumping beam detuning from resonance with $F = 1 \rightarrow F' = 1$ transition. The recapture proportion varies little over the detuning range $-20 < \Delta < +10$.

shows the proportion of atoms loaded into the ^{87}Rb MOT recaptured after a 2 s hold in the magnetic trap as a function of optical pumping duration for various beam intensities. Clearly for the present experimental parameters the the optimum optical pumping duration for ^{87}Rb is $\simeq 1.40$ ms, whilst setting the beam power to $0.22(1)$ mW ($I \simeq 0.17$ mW cm^{-2}) provides sufficient intensity to optically pump the ^{87}Rb ensemble (providing a recapture proportion of $\simeq 62$ %). Similarly optimising these parameters for ^{133}Cs gives a recapture proportion of $\simeq 60$ % for an optical pumping duration of 1.40 ms and beam power of $0.10(1)$ mW ($I \simeq 0.08$ mW cm^{-2}).
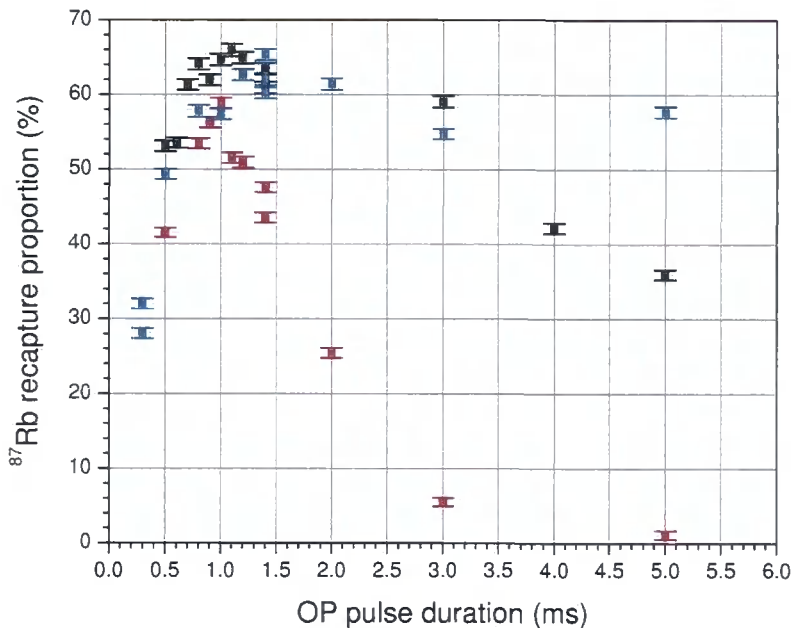
Figure 4.13: Proportion of atoms loaded into the ^{87}Rb MOT recaptured after a 2 s hold in the magnetic trap as a function of optical pumping duration for beam powers of: $0.22(1)$(Blue), $1.12(2)$ (Black) and $4.51(2)$ mW (Red). The recapture proportion increases with duration up to $\simeq 1.4$ ms. Further increasing the duration results in a decrease in the recapture proportion for higher beam powers, possibly due to heating of the atomic ensemble. Thus the duration is set to 1.40 ms and beam power $0.22(1)$ mW, at which the maximum recapture proportion is $\simeq 62$ %.

4.5.3 Heating Due to Optical Pumping

Optical pumping of atoms necessitates scattering of photons, and hence can lead to heating of the atomic sample. This effect can clearly be seen in figure 4.14, where the peak-to-peak axial oscillation amplitude is significantly increased (from 1.6(2) mm to 3.7(4) mm) through the addition of a single optical pumping (OP) beam. From the relative phase shift of the sinusoidal oscillations, the difference in mean initial velocity of the ensemble due to the presence of the single OP beam is calculated using equation 4.4 to be 12(3) mm s^{-1}. This is equivalent to a mean of 2.0(5) photons from the optical pumping beam being scattered by each atom. Adding a second OP beam (by
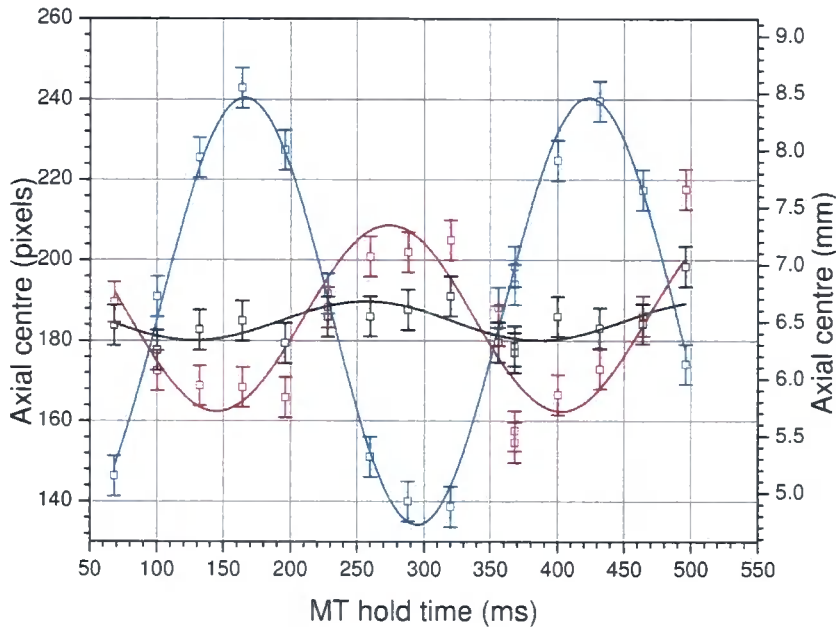
Figure 4.14: ^{87}Rb atom cloud axial position as a function of hold time in the magnetic trap (data points) with: no optical pumping (red), optical pumping from a single beam (blue) and two beams (black), where the second beam is a retro-reflection of the first. Sinusoidal fits to each data set at the measured trap frequency (solid lines) reveal the amplitude and relative phases of oscillation in each case. Clearly the single optical pumping (OP) beam increases the oscillation amplitude relative to the case of no OP whilst for the counter propagating OP beams the amplitude is reduced.

retro-reflecting the first beam after transmission through the science cell) the peak-to-peak oscillation amplitude is reduced to 0.3(3) mm, less even than the amplitude with no OP beam. The addition of the retro-reflection of the OP beam significantly reduces any ensemble centre of mass motion due to the optical pumping process.

4.6 Magnetic Trap Optimisation

The key parameters for turn on of the magnetic trap with regard to atomic properties are the B-field and trap frequencies at which the trap is initially loaded. Additional technical factors which must be considered regard minimising the trap turn-on and turn-off times, as well as achieving a suitable level of B-field stability and avoiding over-heating of the apparatus.

4.6.1 B-Field Selection

Over the B-field range attainable with this apparatus, two regions of magnetic field contain known ^{133}Cs Feshbach resonances ($25 < B < 40$ G and $80 < B < 135$). Although access to these resonances proves incredibly useful in testing the apparatus sensitivity with known Feshbach resonances, it is important to avoid these B-field regions when switching on the trap. Avoiding these regions during initial searches for interspecies resonances also greatly simplifies the interpretation of interspecies collisional behavior. Of the accessible regions in which no ^{133}Cs resonances are present, selecting a turn-on field $B > 135$ G offers the largest range over which the B-field can be tuned without encountering a ^{133}Cs resonance.

4.6.2 Trap Turn-On Parameters

In order to allow access to the maximum range of B-fields the 'weak trap' (section 3.6.2) configuration is used. After switching on the magnetic trap, all B-field ramps are carried out through tuning the current in the bias coil pair. This is conservatively limited to a maximum of 300 A to avoid overheating of the coils (see appendix C.3.2). The magnetic trap is initially loaded at

baseball and bias coil currents of $\simeq$150 A and $\simeq$100 A respectively, producing an axial B-field at the trap centre of 166.0(3) G, hence avoiding the ^{133}Cs Feshbach resonances described above. The axial and radial trap frequencies for both species in this case of $\simeq$ 4 Hz and $\simeq$ 11 Hz respectively are sufficiently low to avoid significant potential energy pick-up during trap loading (as described in section 4.3). With the initial magnetic trap parameters fixed, implementation of the magnetic trap turn on is optimised.

4.6.3 Implementing Trap Turn-On

The trap turn on is a balance between minimising the turn on time and avoiding overheating of the field-effect transistor (FET) banks. Despite being water-cooled, there is a limit as to how much power can be dissipated from each FET bank. When this limit is exceeded the temperature of the FETs increases with time until one FET ultimately fails. During trap turn on
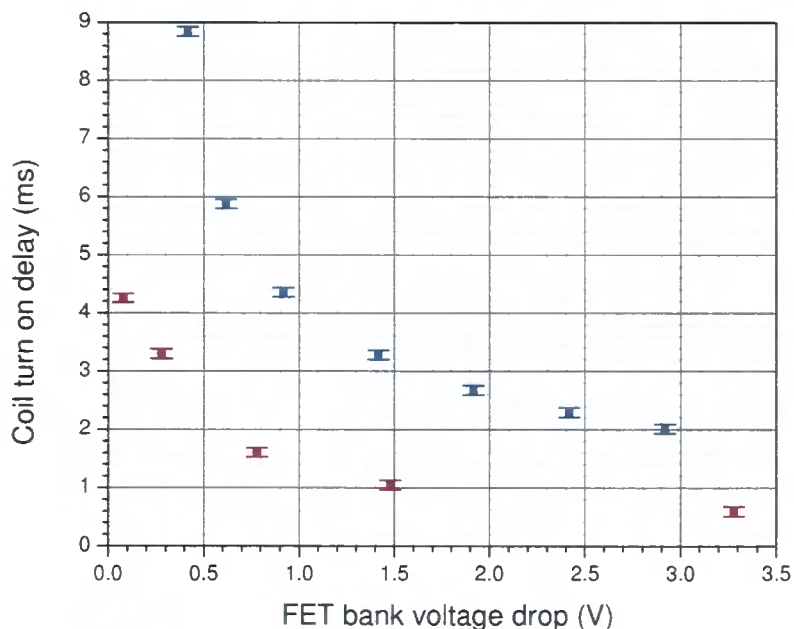
Figure 4.15: Time taken for current in baseball coil (bias coil pair) to be switched from zero to 150 (120) A as a function of voltage dropped between FET bank source and drain is shown in red (blue). Clearly increasing the voltage drop across a FET bank reduces the coil turn-on time.

the voltage supplied by each high current power supply is split between the trapping coil/coil pair and corresponding FET bank. In order to protect a FET bank from overheating, the voltage dropped across it when transmitting current should be minimised. However, reducing the voltage drop in this way dramatically increases the coil turn-on time, as shown in figure 4.15. This problem may be circumvented by switching the power supply output voltage once the trap is turned on, as described below for the bias coils.

Baseball Coil

The baseball FET bank operates without runaway heating at 150 A with a voltage drop of $\simeq 3.28(1)$ V (at a supply voltage of 5.00(1) V). This results in a baseball coil turn on time of 0.58(1) ms and required FET bank power dissipation of $\simeq 490$ W.

Bias Coils

Initial operation of the bias coil pair through FET bank control of a power supply operating at a constant voltage (figure 3.23(b)) resulted in repeated transistor failures. Such failures occurred for FET bank power dissipation in excess of 390 W over periods of several minutes. The bias coil control was subsequently modified to switch the trap on at a power supply voltage of 5.00(1) V. The corresponding FET bank voltage drop of $\simeq 2.8$ V results in a 1.68(1) ms turn-on time. Following trap turn on, the power supply voltage is immediately switched over GPIB (section 3.6.3) to reduce the FET bank voltage drop to $\simeq 0.8$ V. Prior to magnetic trap ramps, the power supply voltage is again switched to give a FET bank voltage drop of $\simeq 0.8$ V at the maximum ramp current. The value of 0.8 V corresponds to a FET bank power dissipation at 300 A of 240 W, significantly below the Bias FET bank failure power of 390 W. Switching the power supply voltage in this way avoids transistor failure without compromising trap turn-on time.

4.7 Absorption Imaging Optimisation

Parameters affecting the accuracy of measured atom cloud properties include: Probe beam (intensity, detuning, polarisation and duration), magnetic quantisation field, atomic cloud optical depth, duration of exposure to repumping light, camera (exposure time, gain and read-out parameters). The objective of absorption imaging optimisation is to maximise the accuracy of extracted atom cloud properties for both atomic species. This is achieved through setting probe beam parameters which are consistent with the assumptions of image analysis calculations, and operating the CCD camera in a mode for which the image resolution is maximised.

4.7.1 Probe Beam Properties

At probe beam intensities significantly below the atom's saturation intensity ($I << I_S$), the calculations with which atom numbers are extracted from absorption images (see appendix B.2) are to first order independent of beam intensity. For this reason probe intensities for each species are set to be $I_{probe} \simeq 0.1\ I_s$. Photon scattering during exposure to the probe beam is assumed to be a two-level process. For this to be a fair assumption it it is important to probe atoms on a closed transition. Ensuring the time taken to transfer trapped atoms into a stretched atomic state (on which they are probed) is small in comparison to the probe exposure time improves the accuracy of the two-level model. Trapped ^{87}Rb (^{133}Cs) atoms should be in the $|F = 1, m_F = -1\rangle$ ($|F = 3, m_F = -3\rangle$) atomic states prior to release from the magnetic trap. Applying a probe beam quantisation field eliminates the possibility of the magnetic field magnitude becoming zero, hence ensuring the atoms remain in these states upon release from the magnetic trap. By applying ^{87}Rb (^{133}Cs) repumping light for a period of 150 μs prior to the probe beam pulse (and throughout the pulse duration), all of the trapped ^{87}Rb (^{133}Cs) atoms are transferred into the upper hyperfine state. Once the probe beam is incident upon the atom cloud, the closest closed transitions
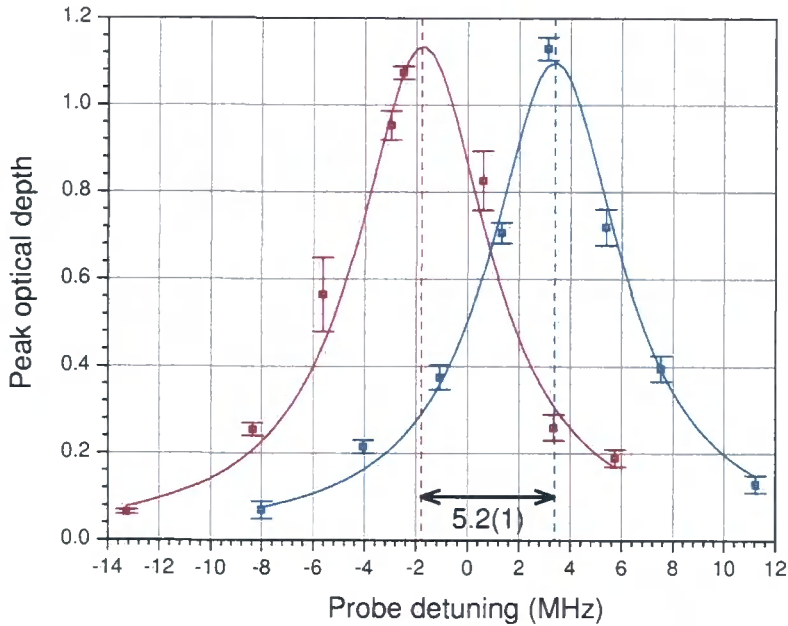
Figure 4.16: Optical depth of a cloud of $3.2(2) \times 10^8$ ^{87}Rb atoms directly after release from the science MOT as a function of probe beam detuning from resonance with the zero bias field $F = 2 \rightarrow F' = 3$ transition. An applied B-field of 1.99(3) G causes the peak absorption of a σ^+ probe beam to occur at a higher optical frequency (Blue line). Similarly the peak absorption of a σ^- probe beam is shifted to a lower optical frequency (Red line). The 5.2(1) MHz frequency separation of the two circular components gives a measured fine structure Zeeman splitting of 1.31(6) MHz G^{-1}. This is in close agreement with the theoretical value of 1.40 MHz G^{-1}. The asymmetry of the frequency shifts for the two polarisations may be attributed to the atom cloud population within the MOT being distributed across multiple m_F states prior to imaging (unlike the case for imaging spin polarised atoms from the magnetic trap which is closer to a two-level system).

(in terms of required number of photons scattered) are the:

$$|F = 2, m_F = -2\rangle \rightarrow |F' = 3, m_F' = -3\rangle \quad \text{and}$$

$$|F = 4, m_F = -4\rangle \rightarrow |F' = 5, m_F' = -5\rangle$$

transitions for ^{87}Rb and ^{133}Cs respectively. Optical pumping of ^{87}Rb (^{133}Cs) into the $|F = 2, m_F = -2\rangle$ ($|F = 4, m_F = -4\rangle$) state is achieved by setting the probe beam polarisation to drive σ^- transitions. Setting the probe beam polarisation to be circular is simply a case of rotating the achromatic probe beam quarter-waveplate to an angle of ± 45 ° relative to its polarisation axis. Which of these orientations drives σ^- transitions is identified by measuring (in the case of ^{87}Rb) the frequency detuning from resonance with the zero bias field $F = 2 \rightarrow F' = 3$ transition at which the peak optical depth (OD) of a ^{87}Rb atom cloud is maximised. Figure 4.16 shows the measured OD of a cloud of $3.2(2) \times 10^8$ ^{87}Rb atoms directly after release from the science MOT as a function of probe detuning for each circularly polarising orientation of the probe beam quarter waveplate. The orientation at which the peak OD is measured at a lower frequency than in the zero-field case (the red line in figure 4.16) is identified as driving σ^- transitions (through reference to figure 2.3). Spin polarised atoms released from the magnetic trap probed with this helicity of circularly polarised light will undergo fewer optical transitions before entering the closed transition, hence this probe beam polarisation will result in the most accurate measurement of atom cloud parameters.

4.7.2 Timing and Camera Parameters

After preliminarily imaging using single species imaging routines, two species imaging using the frame transfer feature of the Andor iXon CCD camera is used exclusively. This has the tremendous benefit of allowing near-simultaneous images of both atomic species to be taken in a single experimental 'shot'. The timings for the frame transfer imaging routine are displayed in table 4.1, whilst the corresponding camera parameters are shown in table 4.2. The selected parameters result in reliable camera and software operation in conjunction with the 'LabVIEW' interface software, whilst minimising the duration between capturing images of ^{133}Cs and ^{87}Rb atoms.

Camera exposure duration	3	**ms**
Duration probe shutter open	2	**ms**
Repump time	150	μs
Probe pulse duration	10	μs
Delay between ^{133}Cs and ^{87}Rb images	4.92	**ms**
Delay between image pairs	400	**ms**

Table 4.1: Timing settings relating to two species absorption imaging of atoms released from the magnetic trap. All durations are centred around each individual probe pulse. The 'repump time' is the duration for which repumping light is incident on the atom cloud prior to the probe pulse. Delays between ^{87}Rb and ^{133}Cs images, and delays between image pairs are a limited by the camera shift speed and Andor software processing time respectively.

CCD rows per image	1002 $\times$	
Camera shift speed	1.9176	μs **row**$^{-1}$
Binning	2 $\times$ 2	**pixels**
Resolution	14	**bit**
Read-out rate	27	**MHz**
Amplifier gain	4	

Table 4.2: Camera parameters for two-species frame-transfer imaging. Parameters are selected to provide the maximum accuracy in individual pixel intensity read-out, whilst minimising the delay between obtaining the first and second image due to the frame transfer process.

4.8 Characterisation

Alongside optimisation of the apparatus performance, precise characterisation of key experimental parameters is required to carry out experiments and obtain useful quantitative results from experimental data. For example: precise measurement of magnetic fields allows the B-field position of Feshbach resonances to be precisely identified. Similarly the accuracy of atom cloud properties obtained from absorption images relies on characterisation of magnetic trap frequencies and also the imaging system magnification.

4.8.1 Magnetic Trap

The properties of the magnetic trap field which have the greatest impact on the atom's behavior, in terms affecting elastic and inelastic collision rates are the magnetic bias field and the trapping frequencies for each atomic species. The measurement of these properties is described below.

Trap Frequency

The magnetic trap frequencies for each atomic species shown in table 4.3 are measured by imaging the position of the centre of trapped atom clouds as a function of hold time in the magnetic trap.

This can be seen for ^{87}Rb and ^{133}Cs in figures 4.17 and 4.18 respectively. The axial (z axis) trapping frequencies are obtained by fitting the axial cloud positions for each species with exponentially decaying sinusoids. Coupling between oscillations along the two radial axes of the trap results in the imaged (y axis) radial cloud centre oscillating at the mean radial trap frequency, with oscillation amplitude modulated at the difference between the radial trap frequencies along the imaged (y) and non-imaged (x) axes. The y axis scales of figures 4.17 and 4.18 are not common due to imaging system re-alignment between acquisition of the two data sets. The high level of precision in these measurements is achieved through acquiring data in clusters separated by many oscillation periods.
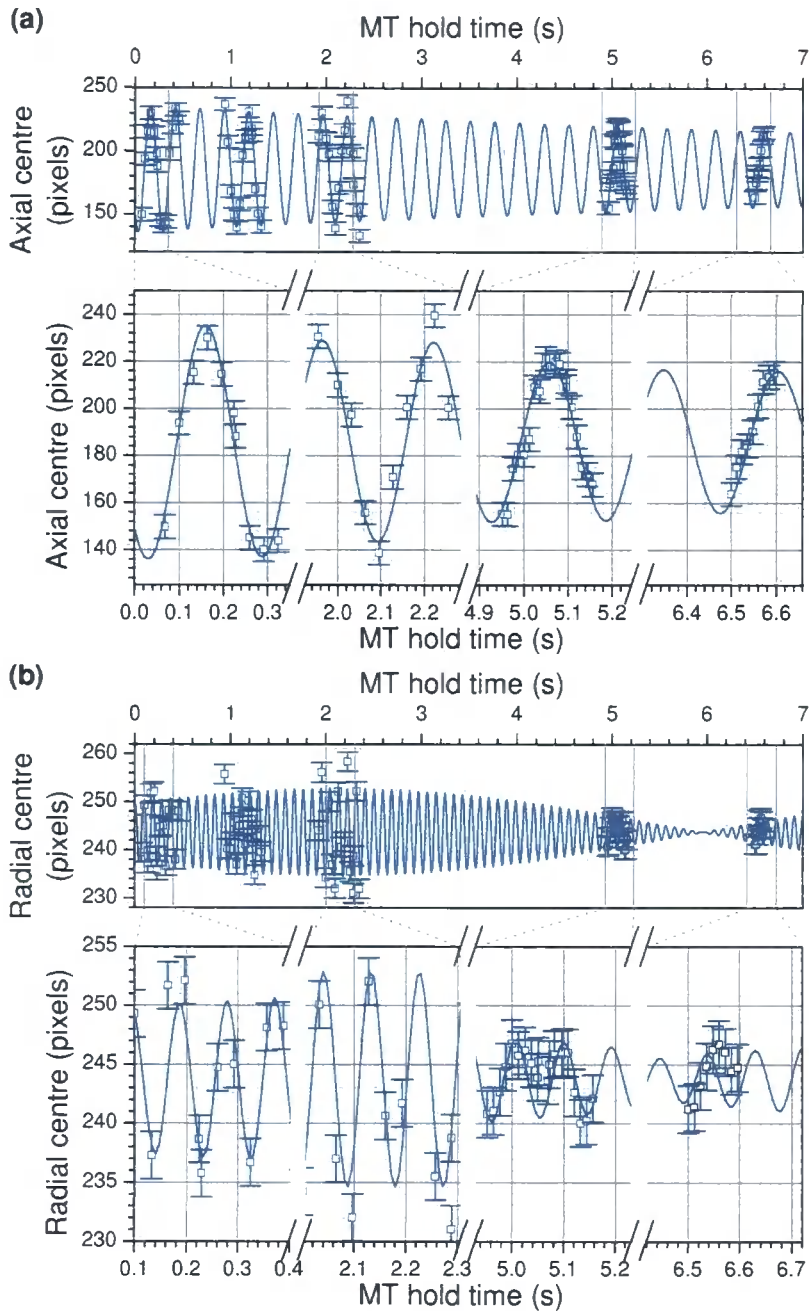
Figure 4.17: Positions of imaged ^{87}Rb atom cloud centre along the y (radial) and z (axial) axes of the magnetic trap as a function of magnetic trap hold time are shown in (a) and (b) respectively (blue symbols). Fitting (a) with an exponentially decaying sinusoid (blue line) the axial harmonic trapping frequency is found to be 3.879(2) Hz. Coupling between oscillations in the imaged (y) and non-imaged (x) radial directions leads to modulation of the oscillation amplitude along the imaged radial direction. Fitting (b) with the product of two sinusoids (blue line), the oscillation and modulation frequencies are extracted, from which the radial trap frequencies are found to be 10.721(8) and 10.851(8) Hz. The enlarged sections of each figure demonstrate how closely the fitted lines match the data across many trap oscillations.
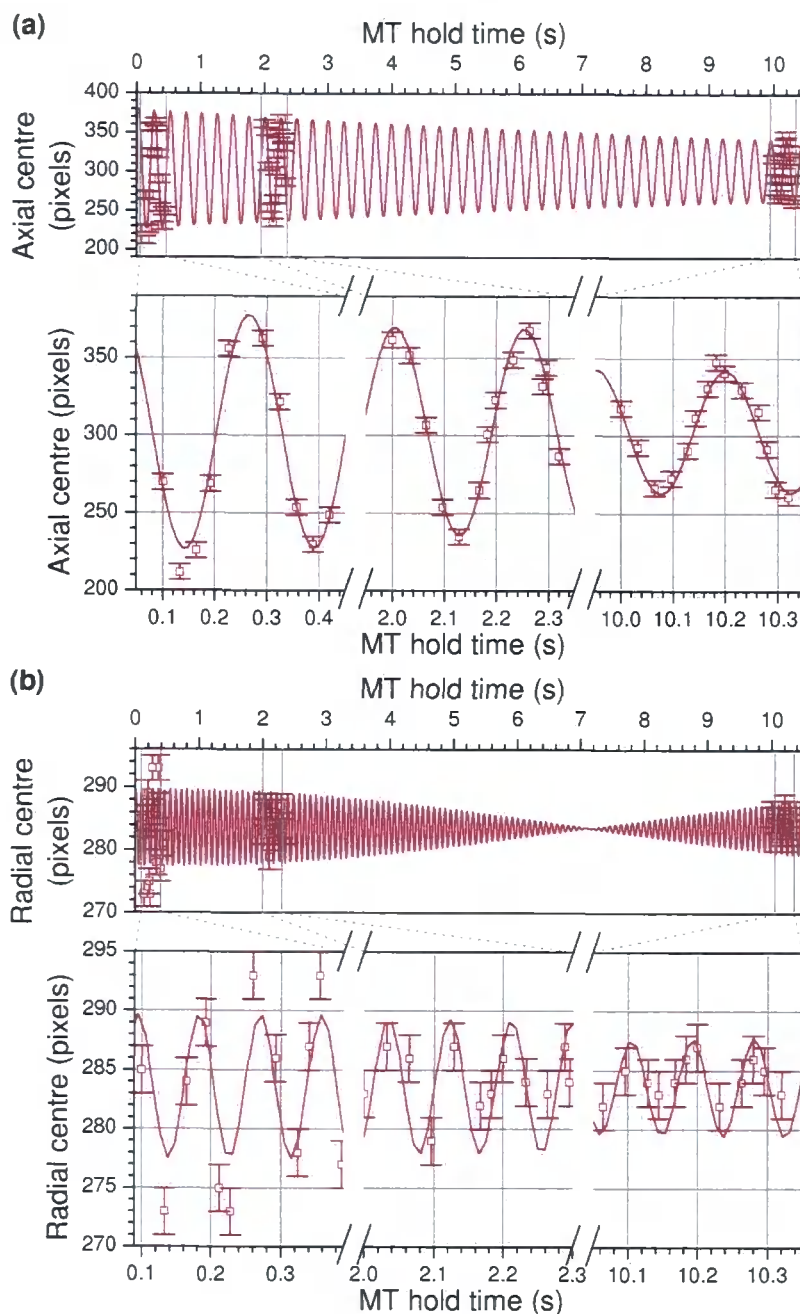
Figure 4.18: Positions of imaged ^{133}Cs atom cloud centre along the y (radial) and z (axial) axes of the magnetic trap as a function of magnetic trap hold time are shown in (a) and (b) respectively (blue symbols). Fitting (a) with an exponentially decaying sinusoid (blue line) the axial harmonic trapping frequency is found to be 4.027(1) Hz. Coupling between oscillations in the imaged (y) and non-imaged (x) radial directions leads to modulation of the oscillation amplitude along the imaged radial direction. Fitting (b) with the product of two sinusoids (blue line), the oscillation and modulation frequencies are extracted, from which the radial trap frequencies are found to be 11.30(1) and 11.38(1) Hz. The enlarged sections of each figure demonstrate how closely the fitted lines match the data across many trap oscillations.

	Measured		Modelled		
	Axial	Radial	Axial	Radial	Units
^{87}Rb	3.879(2)	10.721(8), 10.851(8)	3.91	10.74	**Hz**
^{133}Cs	4.027(1)	11.30(1), 11.38(1)	4.04	11.07	**Hz**

Table 4.3: Magnetic trap frequencies for ^{87}Rb and ^{133}Cs with the baseball coil (bias coils) transmitting a current of 150 (100) A. The measured trap frequencies along the axial(z) and both radial trap directions are shown, along with those calculated from the B-field expansion parameters (table 3.5) at the geometrical trap centre. These modelled values take the variation of atom magnetic moment with B-field into account, but neglect gravity.

Magnetic Field Calibration

Each trapped atom oscillates about the trap centre with an energy dependent amplitude along each of the three axes, hence every trapped atom probes the trap centre B-field. For this reason a radio-frequency equal to the Zeeman splitting between adjacent magnetic sub-levels of the lower hyperfine ground state at the trap centre causes all atoms to be ejected from the magnetic trap. From a measurement of this frequency the magnetic field at the trap centre is ascertained using the Breit-Rabi formula (equation 2.11). For trapped atom clouds with width small in comparison to the gravitational sag from the B-field minimum, atoms vertically below the cloud centre probe higher magnetic fields than those above. As a result, the radio-frequencies required to remove atoms from the upper and lower edges of such an atom cloud differ, allowing the vertical surface from which atoms undergo forced evaporation to be selected through choice of radio-frequency. Figure 4.19 shows the number of ^{87}Rb atoms remaining in the magnetic trap following radio-frequency ramps from either above or below the frequency of the trap centre Zeeman splitting. The x axis intercepts of linear fits to the data 'cutting' from vertically above and below the atom cloud are 118.77(8) and 118.97(2) MHz respectively.
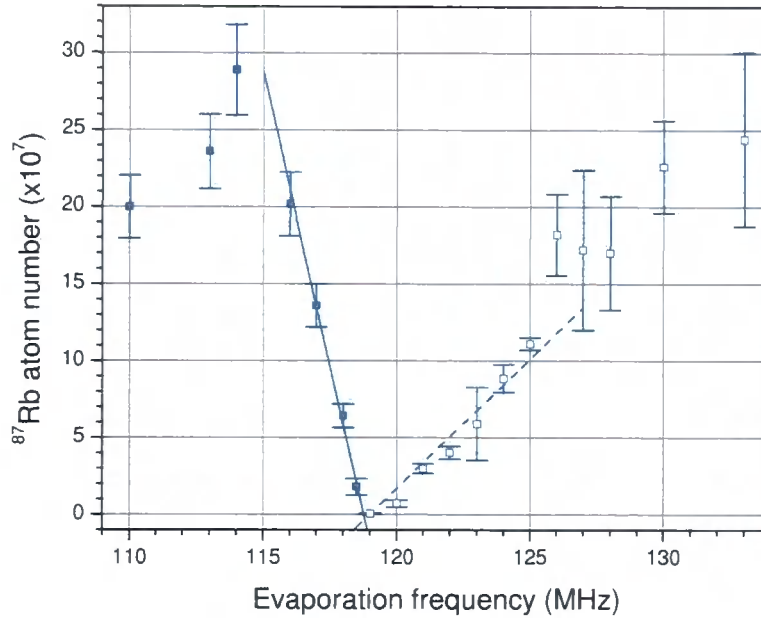
Figure 4.19: Number of magnetically trapped ^{87}Rb atoms after a 60 s, -15 dBm radio frequency ramp as a function of ramp final frequency. Solid (hollow) data points correspond to frequency ramps beginning at 101 MHz (140 MHz) and increasing (decreasing) to the final frequency. The x axis intercepts of linear fits to the data 'cutting' from vertically above (solid line) and below (dashed line) the atom cloud are 118.77(8) and 118.97(2) MHz respectively. The mean of these radio frequencies (118.87(4) MHz) is the Zeeman splitting at the trap centre, corresponding to a trap centre B-field of 166.70(6) G (calculated using equation 2.11).

The mean of these frequencies is the Zeeman splitting at the trap centre, from which the B-field is calculated, whilst the frequency difference indicates the width of the RF 'knife'. The frequency values measured from figure 4.19 along with corresponding measurements taken for a ^{133}Cs atom cloud are shown alongside the respective B-field values in table 4.4. The measured B-field for ^{87}Rb is 1.20(8) G greater than that for ^{133}Cs. This is consistent with ^{87}Rb having a lower radial trap frequency than ^{133}Cs (see table 4.3), resulting in an increased gravitational sag, hence an increase in the magnetic field at the trap centre. This reduction in overlap of the two atomic species may lead to a significant reduction in the sensitivity to interspecies resonances, especially

at low temperatures where the size of the atom clouds becomes comparable with the sag (section 5.3.2). For both species the B-field is greater than the 159.7(2) G calculated at the geometrical centre of the magnetic trap from the measured trapping coil parameters, consistent with atom cloud gravitational sag.

	Centre frequency (MHz)	'Knife width' (MHz)	B-field (G)
^{87}Rb	118.87(4)	0.20(8)	166.70(6)
^{133}Cs	59.92(2)	0.12(4)	165.50(6)

Table 4.4: Measured radio-frequencies of ^{87}Rb and ^{133}Cs Zeeman splittings between adjacent magnetic sub-levels of the lower hyperfine ground states at the magnetic trap centre and corresponding B-fields calculated from the Breit-Rabi formula (equation 2.11). For both species the B-field is greater than the 159.7(2) G estimated at the geometrical centre of the magnetic trap. The effective width of radio-frequency 'knife' in each case is also shown.

4.8.2 Imaging

The precision of absolute measurements of atom cloud parameters from absorption images (*i.e.*, atom cloud numbers, densities and temperatures) is limited by both the accuracy of optical depth measurements and the precision with which the imaging system magnification is known. Similarly, the accuracy of atom numbers extracted through fluorescence imaging is limited by many factors, including the uncertainty in effective Clebsch-Gordan coefficients for atoms in this apparatus. Characterisation of the absorption imaging system magnification and uncertainty in measured optical depths, along with calibration of measured fluorescence signals is detailed below.

Absorption Imaging Magnification

Here the absorption imaging system magnification ($M_{\text{absorption}}$) is measured by comparing the acceleration due to gravity of the atom cloud image (g'),

with that of the atom cloud due to gravity (g). The ratio of these two values yields the magnification:

$$M_{\text{absorption}} = \frac{g'}{g} \quad .$$

<div align="right">(4.12)</div>
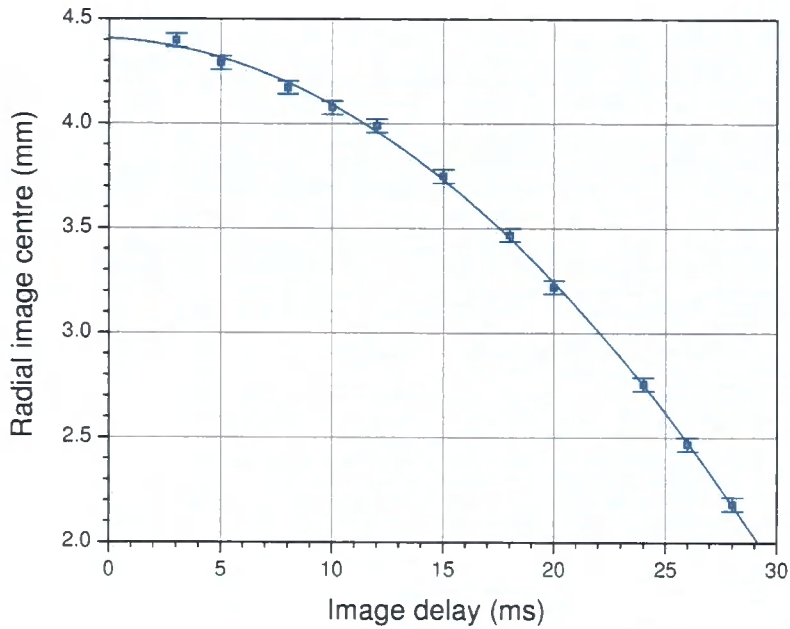
Figure 4.20: ^{87}Rb cloud image radial (vertical) position as a function of time after release from the magneto-optical trap, including data points (blue squares) and a quadratic fit to the data (blue line). The absorption imaging system magnification is calibrated from this data (section 4.8.2).

The acceleration of the atom cloud image is obtained by measuring the position of the imaged atom cloud centre as a function of time-of-flight following release from the science MOT (as shown in figure 4.8.2). Fitting the imaged atom cloud centre s' at varying times t after release from the MOT as:

$$s' = s + ut + \frac{1}{2}g't^2 \quad , \tag{4.13}$$

where s is the cloud position at $t = 0$ and u is the initial cloud velocity, gives an image acceleration $g' = 5.3(2)$ m s^{-2}. This measurement corresponds to a magnification $M_{\mathrm{absorption}} = 0.54(2)$. After subsequent adjustment of the imaging optics, the magnification was re-calibrated to be $M_{\mathrm{absorption}} = 0.46(5)$.

Optical Depth Uncertainty

The accuracy of absorption imaging measurements of atom number and all other properties calculated from the atom number depends primarily on the degree of certainty attainable in peak optical depth measurements. This is dependent on both the measured optical depth, and the shot-to shot variation in the three images (section 3.10) from which the OD profile is obtained. The mean N_c and standard deviation σ_c of the peak number of counts recorded on the CCD camera for each of the three images (with no atoms present) is shown in table 4.5 for two species imaging of ^{87}Rb and ^{133}Cs .

(a) ^{87}Rb			(b) ^{133}Cs		
Image	Mean counts	Standard deviation	Image	Mean counts	Standard deviation
I_1	2450	30	I_1	1260	30
I_2	2450	30	I_2	1260	30
I_3	380	7	I_3	380	7

Table 4.5: Variation in two-species absorption imaging peak counts for the three images required to obtain an optical depth profile for ^{87}Rb (a) and ^{133}Cs (b) when no atoms are present.

These statistical fluctuations lead to an uncertainty in measured optical depth of:

$$\sigma_{\text{OD}} = \frac{\sqrt{2\sigma_3{}^2 + (\sigma_1{}^2 + \sigma_3{}^2)\, e^{-2\text{OD}}}}{N_2 - N_3} \quad , \tag{4.14}$$

where σ_1, σ_2 and σ_3 are the uncertainties in number of counts N_1, N_2 and N_3 for images I_1, I_2 and I_3 respectively.

For ^{87}Rb atoms the fractional error in optical depth due to recorded image count uncertainty remains below 10 % for measured optical depths in excess of $\simeq 4.5$ (the corresponding limit for ^{133}Cs is $\simeq 3.5$).

Fluorescence Imaging Calibration

Although there is much value in using fluorescence imaging to measure the number of atoms loaded into the magnetic trap, the accuracy of absolute atom numbers extracted using the calculations presented in appendix B.1 is limited by many parameters, including the fact that the effective Clebsch-Gordan coefficients for atoms in this apparatus are unknown. By comparing the fluorescence imaging signal in mV to the atom number obtained from from absorption images taken immediately after the MOT is loaded, a true calibration of the atom number per mV signal is obtained. Figure 4.21 gives calibrations of the mV signal due to atom fluorescence incident on the ^{87}Rb large area photodiode described in section 3.8.1 using two different methods of analysis of absorption images. By fitting Gian profiles to the imaged optical depth distributions, a calibration of $1.13(5) \times 10^6$ ^{87}Rb atoms per mV is obtained. Summing the measured optical depths of each pixel within the CCD array gives an alternative calibration of $1.42(5) \times 10^6$ ^{87}Rb atoms per mV. This is in excellent agreement with the calibration calculated in appendix B.1 of $1.5(2) \times 10^6$ ^{87}Rb atoms per mV. Such close agreement between atom numbers calculated using entirely different methods instills a tremendous degree of confidence in the diagnostics used in this apparatus. It is also worth noting that the calculated MOT fluorescence atom number calibration uses the saturation intensity for isotropic polarisation of light close to the $F = 2 \rightarrow F' = 3$ transition [89]. Using instead the saturation intensity for the cycling transition $|F = 2,\, m_F = \pm 2\rangle \rightarrow |F' = 3,\, m_F{}' = \pm 3\rangle$ results in an under-estimate of the calibration by approximately a factor

of two. This demonstrates the validity of using the isotropic polarisation saturation intensity.
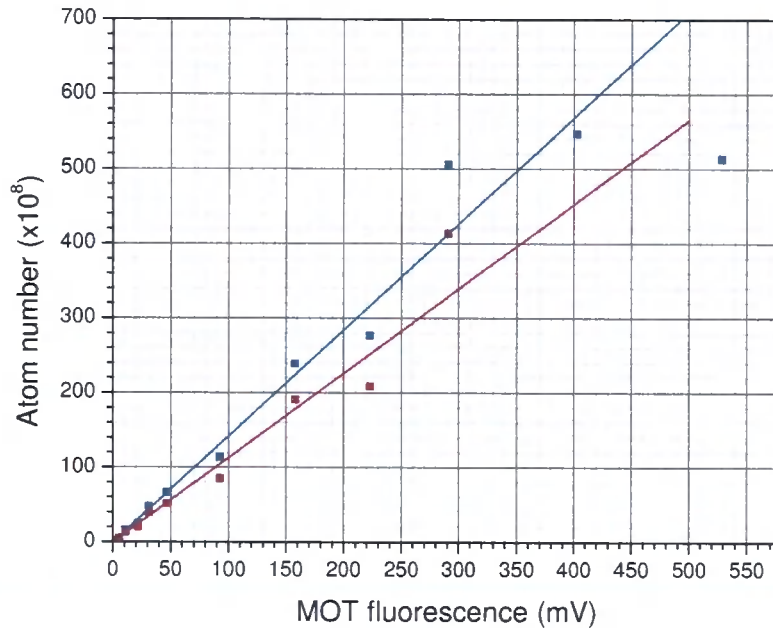
Figure 4.21: The number of ^{87}Rb atoms loaded into the MOT measured through absorption imaging as a function of the mV signal due to atom fluorescence incident on a large area photodiode. The red data-points are the atom numbers obtained from Gaussian fits to the imaged optical depth distributions. The blue-data points are the atom numbers obtained by summing the measured optical depths of each pixel within the CCD array. Linear fits to the Gaussian fit data (red line) and summed optical depth data (blue line) give ^{87}Rb fluorescence calibrations of $1.13(5) \times 10^6$ and $1.42(5) \times 10^6$ atoms per mV fluorescence signal respectively.

Chapter 5

Results: Magnetic Trapping and Loss Measurements

This chapter describes results on magnetic trapping of an ultracold atomic mixture using the apparatus described in chapter 3. Characterisation of the performance of the apparatus for the two-species mixture is presented, along with novel techniques implemented to improve this two-species operation. The sensitivity of the apparatus to interspecies Feshbach resonances is also calculated, whilst the single-species sensitivity is tested through the measurements of ^{133}Cs Feshbach resonances. Improvements to the sensitivity are made through optimisation of single and simultaneous two-species radiofrequency evaporation. Finally a search for Feshbach resonances over the B-field range $168 \leq B \leq 350$ G is made.

5.1 Two Species Science MOT Performance

Ideal performance of a two-species atom source for the magnetic trap would allow independent loading of arbitrary numbers of ^{87}Rb and ^{133}Cs atoms, with no reduction in atom number or loaded phase-space density when compared with single species operation. The presence of a second species in the science MOT however, has an extremely detrimental affect on the number of atoms of either species which can be loaded into the science MOT. This is primarily due to light assisted interspecies collisions. A substantial investigation

148

of such collisions has been carried out using this apparatus, and is rigorously analysed by Margaret Harris in her PhD thesis [94]. The key results of this analysis are included below to aid understanding of both the effect of such collisions in limiting magnetic trap loading, and also the mechanism by which the 'push' technique described below inhibits such collisions.

5.1.1 Loading of the Two-Species MOT

In contrast to the two-species pyramid MOT, for which there is no detectable difference in performance when operating with a second species present (section 4.1.2), the higher atom number densities in the science MOT lead to significant losses due to light assisted interspecies inelastic collisions. This is illustrated in figure 5.1. Here the science MOT parameters are modified to ensure the trapped ^{133}Cs atom cloud remains entirely within the much larger ^{87}Rb cloud, as this greatly aids analysis of atom losses due to interspecies collisions. After fully loading the modified ^{133}Cs MOT for $\simeq 45$ s with ^{87}Rb cooling light incident upon the atomic ensemble, ^{87}Rb repumping light is introduced. The subsequent loading of ^{87}Rb atoms into the trap results in a rapid reduction in the number of ^{133}Cs atoms present in the MOT to $\simeq 25$ % of the fully loaded value. At $t \simeq 300$ s the loading sequence is reversed, with a reduction in ^{87}Rb atom number to $\simeq 30$ % of the fully loaded value due to the introduction of ^{133}Cs atoms.

5.1.2 Light Assisted MOT Collisions

The loss processes involved in the two species MOT are highly complex, and there is much to be gained by carrying out detailed investigations of the loss rate dependence on MOT parameters. Through characterising the atom number and density dependence of single species MOT losses the relative contributions of collisions with trapped and thermal 'background' gas atoms can be isolated [95]. Extending these studies to investigate loss rate dependence on optical intensity allows single species losses due to hyperfine structure changing collisions between ground state atoms to be measured [69]. Further analysis of optical detuning dependence can also prove instructive

in separating loss rate contributions due to fine structure changing excited state collisions and radiative escape processes. Investigations of single-species MOTs in this manner have greatly aided the development of single species models of ground and excited state trap loss [96]. For the two-species MOT, the wealth of information which can be extracted from such measurements is greatly increased. Comparisons of the intensity dependence of the inter-
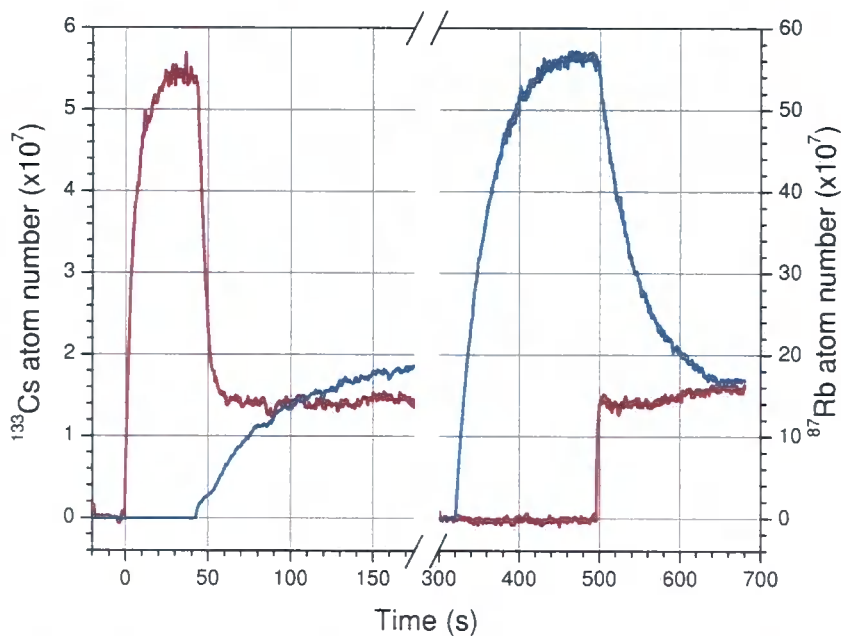
Figure 5.1: Loading and loss of ^{87}Rb (blue line) and ^{133}Cs (red line) atoms in the science MOT. Initially, only ^{133}Cs atoms are trapped. Unblocking the ^{87}Rb repumping beam after $\simeq 45$ s leads to rapid losses of $\simeq 75$ % of the ^{133}Cs cloud. At $t \simeq 300$ s the loading sequence is reversed. Note that the ^{133}Cs MOT reaches its two-species equilibrium value within 10 s after the ^{133}Cs repumping beam is unblocked, while the ^{87}Rb cloud decays much more slowly due to the reduced overlap with the ^{133}Cs cloud. These data are taken with a science MOT B-field gradient of 20.8(2) G and ^{133}Cs cooling light detuning of -18.2(2) MHz in order to ensure the trapped ^{133}Cs atom cloud remains entirely within the much larger ^{87}Rb cloud. These data are published in [65].

species collisional loss rates for each constituent species allow the identifica-
tion of the species which is predominantly in the excited state during loss
inducing collisions. Additionally, the dependence of loss rates on detuning
allows collisions in which both partners are initially in the excited state to
be characterised [97]. Analysis of these interspecies collisional losses offers a
window on the creation of heteronuclear polar molecules via photoassociation
[98].

As the science MOT in this apparatus is predominantly a tool with which
^{87}Rb and ^{133}Cs atoms are loaded into the magnetic trap, the primary concern
of the two-species MOT studies described below is to understand the inter-
species loss processes in the MOT to the extent that they may be managed.
The following sections therefore pay only brief attention to the measurement
of loss parameters before focusing on the techniques by which interspecies
MOT losses are managed in this apparatus.

Single Species MOT Loss Rate Calculations

For a single species MOT with an incident atomic flux capture rate L and
spatially varying atom number density n_i, the loading rate as a function of
loaded atom number N_i is given by [95]:

$$\frac{\mathrm{d}N_i}{\mathrm{d}t} = L - \gamma N_i - \beta_i \int_V n_i{}^2 \mathrm{d}^3r \quad , \tag{5.1}$$

where γ is the loss rate due to collisions with background gas atoms and β_i
is the loss rate coefficient for light-assisted inelastic collisions between cold
atoms of the same species. After loading a single species ^{133}Cs MOT, re-
moving the atom source eliminates the loading term from equation 5.1. The
resulting single species decay curve (red data points of figure 5.2) has two
characteristic time scales: An initial 'fast' density dependent decay dom-
inated by inelastic collisions with trapped atoms and a later 'slow' decay
where collisions with background gas atoms are the dominant loss mecha-
nism. Initially the MOT decays in size whilst the number density remains
uniform. In this circumstance the integral in equation 5.1 becomes:

$$\beta_i \int_V n_i{}^2 \mathrm{d}^3r = \beta_i \langle n_i \rangle N_i \quad , \tag{5.2}$$

where $\langle n_i \rangle$ is the mean number density. This 'density limited' regime is characterised by an exponential decay in the number of trapped [133]Cs atoms of the form:

$$N_i(t) = N_0 \exp\left[-\left(\gamma + \beta_i \langle n_i \rangle\right)t\right] \quad , \tag{5.3}$$

where N_0 is the number of atoms at time $t = 0$. As the number of trapped atoms decreases, the spatial cloud profile leaves the 'density limited' regime and the atom number density, along with the atom loss rate, decreases. As
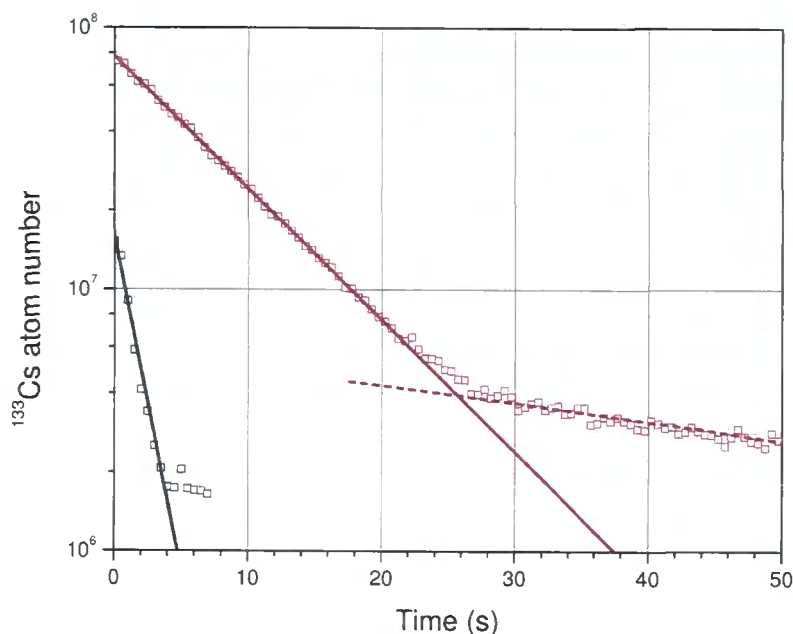
Figure 5.2: Decay of the [133]Cs MOT with (black symbols) and without (red symbols) [87]Rb present. The single species data exhibits two regions of exponential decay: An initial 'fast' decay dominated by inelastic collisions with trapped [133]Cs atoms, and a later 'slow' decay where collisions with background gas atoms are dominant. Exponential fits to these two regions (red solid and dashed lines respectively) give 1/e lifetimes of 9.8(7) s and 150(30) s respectively, from which the single species loss rate parameters for [133]Cs are found to be $1/\gamma_{133\text{Cs}} = 150(30)$ s and $\beta_{133\text{Cs}} = 2.1(1) \times 10^{-11}$ cm^3 s^{-1} (see text). The decay with [87]Rb atoms present has 'fast' decay 1/e lifetime of 1.73(8) s, five times greater than the corresponding single species decay. The corresponding two-species loss rate parameter $\beta_{133\text{Cs}\,87\text{Rb}} = 1.0(6) \times 10^{-10}$ cm^3 s^{-1}. These data are published in [65].

the atom number density decreases, the integral in equation 5.1 tends to zero and the collision rate with background gas atoms becomes dominant, hence the trapped atom number decays as:

$$N_i(t) = N_0 \exp\left[-\gamma t\right] \quad . \tag{5.4}$$

By fitting the 'fast' and 'slow' decay regimes of the ^{133}Cs single species (red symbols) data-set of figure 5.2 with equations 5.2 and 5.4 (red solid and dashed lines respectively) and using mean densities from absorption images, the single species loss rate parameters for ^{133}Cs are found to be $1/\gamma_{133}{}_{\rm Cs} = 150(30)$ s and $\beta_{133}{}_{\rm Cs} = 2.1(1) \times 10^{-11}$ cm^3 s^{-1}. Repeating this analysis for the ^{87}Rb single species MOT gives a value of $\beta_{87}{}_{\rm Rb} = 1.5(2) \times 10^{-11}$ cm^3 s^{-1}.

Two Species MOT Loss Rate Calculations

The loading rate of species i in the two-species MOT is found by adding an interspecies loss term to equation 5.1 [95]:

$$\frac{\mathrm{d}N_i}{\mathrm{d}t} = L - \gamma N_i - \beta_i \int_V n_i{}^2 \mathrm{d}^3 r - \beta_{ij} \int_V n_i n_j \mathrm{d}^3 r \quad , \tag{5.5}$$

where N_i is the number of atoms of species i, $n_{i,j}$ are the density profiles for each species in the science MOT and β_{ij} is the loss rate coefficient for loss of species i due to collisions with species j. The loss rate coefficient $\beta_{133}{}_{\rm Cs}{}^{87}{}_{\rm Rb}$ is measured here from the two-species data (black data points) presented in figure 5.2. Here both ^{87}Rb and ^{133}Cs are loaded into the science MOT until equilibrium values of each species are reached. At time $t = 0$ the ^{133}Cs pyramid MOT light is removed, eliminating the loading term from equation 5.5. As the ^{133}Cs atom cloud remains entirely within the 'density limited' region of the ^{87}Rb atom cloud, equation 5.5 has the form:

$$\frac{\mathrm{d}N_{133}{}_{\rm Cs}}{\mathrm{d}t} = -\left(\gamma + \beta_{133}{}_{\rm Cs} \langle n_{133}{}_{\rm Cs}\rangle + \beta_{133}{}_{\rm Cs}{}^{87}{}_{\rm Rb} \langle n_{87}{}_{\rm Rb}\rangle F_{133}{}_{\rm Cs}{}^{87}{}_{\rm Rb}\right) N_{133}{}_{\rm Cs} \quad , \tag{5.6}$$

where $F_{133}{}_{\rm Cs}{}^{87}{}_{\rm Rb}$ represents the (normalised) density of ^{133}Cs weighted by the probability distribution of ^{87}Rb. Thus whilst the ^{133}Cs atom cloud remains in the density limited regime, the ^{133}Cs atom number decays as:

$$N_{133}{}_{\rm Cs}(t) = N_0 \exp\left[-\left(\gamma + \beta_{133}{}_{\rm Cs} \langle n_{133}{}_{\rm Cs}\rangle + \beta_{133}{}_{\rm Cs}{}^{87}{}_{\rm Rb} \langle n_{87}{}_{\rm Rb}\rangle F_{133}{}_{\rm Cs}{}^{87}{}_{\rm Rb}\right) t\right] \quad . \tag{5.7}$$

Fitting an exponential decay to the region of two species data of figure 5.2 for which there is a 'fast' decay, gives a $1/e$ lifetime of $1.73(8)$ s, which is the exponent of equation 5.7. Substituting the values of γ_{133Cs}, β_{133Cs} and β_{87Rb} obtained from single species decay fits, and $\langle n_{133Cs} \rangle$, $\langle n_{87Rb} \rangle$ and $F_{133Cs\,87Rb}$ from absorption images of density limited two species clouds into equation 5.7, the loss rate coefficient is measured to be:

$$\beta_{133Cs\,87Rb} = 1.0(6) \times 10^{-10} \quad \mathrm{cm^3\,s^{-1}} \quad .$$

Repeating this measurement for ^{87}Rb in the two-species MOT gives:

$$\beta_{87Rb\,133Cs} = 1.6(4) \times 10^{-10} \quad \mathrm{cm^3\,s^{-1}} \quad .$$

An alternative method by which the interspecies term can be measured is through direct comparison of absorption images of each atomic species in single and two species MOTs loaded to their equilibrium states [99]. A typical loading sequence from which such a comparison may be made is shown in figure 5.1. Here the ^{87}Rb MOT is initially loaded to its equilibrium value with no ^{133}Cs atoms present (the ^{133}Cs repumping light is blocked). An absorption image at this equilibrium level is used to extract the ^{87}Rb atom number and number density distribution. Once the ^{87}Rb MOT has reached the single species equilibrium, the ^{133}Cs MOT is loaded (the ^{133}Cs repumping light is unblocked). The subsequent interspecies collisions lead to an imbalance in loading and loss rates until the ^{87}Rb MOT settles to a new (lower) equilibrium. Images of each species atom distribution at the new equilibrium are used to extract the atom number and density distribution of each species in the two-species MOT. At equilibrium MOT loads for the single and two-species cases, the loading and loss rates of equation 5.5 are equal, *i.e.* :

$$L = \gamma \tilde{N}_i + \beta_i \int_V \tilde{n}_i^2 \mathrm{d}^3 r \quad , \tag{5.8}$$

and

$$L = \gamma N_i + \beta_i \int_V n_i^2 \mathrm{d}^3 r + \beta_{ij} \int_V n_i n_j \mathrm{d}^3 r \quad , \tag{5.9}$$

for the single and two-species MOT equilibria respectively. Here the loaded atom number and density of the single species MOT are denoted $\tilde{N}_i$ and $\tilde{n}_i$. As the loading rate (L) is independent of the presence of a second species,

the loading rate from equation 5.8 is substituted into equation 5.9, which after rearrangement gives:

$$\beta_{ij} = \frac{\gamma \left(\tilde{N}_i - N_i \right) + \beta_i \left(\int_V \tilde{n}_i^2 d^3r - \int_V n_i^2 d^3r \right)}{\int_V n_i n_j d^3r} \quad .$$ (5.10)

By substituting the atom number and density profiles obtained for the single species and two-species MOT equilibrium loads, into equation 5.10, along with the value of β_i obtained from single species atom decay curves 5.1.2 the interspecies loss rate coefficients are obtained. Using this 'remaining number' method, values of the interspecies loss rate coefficients in this apparatus are measured to be:

$$\beta_{^{133}Cs\,^{87}Rb} = 9(2) \times 10^{-11} \quad cm^3 \; s^{-1} \quad and$$

$$\beta_{^{87}Rb\,^{133}Cs} = 2.1(3) \times 10^{-10} \quad cm^3 \; s^{-1} \quad .$$

These values are in good agreement with those obtained through measuring the MOT decay rates.

Clearly the fact that these two-species inelastic loss rate coefficients are an order of magnitude greater than the single species coefficients results in the dramatic reduction in the equilibrium atom numbers loaded into the two-species MOT. The value of each interspecies loss rate coefficient could be altered through changing the MOT beam intensities [95], or implementing a dark SPOT MOT [70]. A simpler method by which the two-species collisional losses can be effectively eliminated is to eliminate the spatial overlap of the two atomic species during the MOT loading phase, hence setting the interspecies loss term of equation 5.5 equal to zero:

$$\int_V n_i n_j d^3r = 0 \quad ,$$ (5.11)

In this case the loss rate for species i in the two-species MOT (equation 5.5) simplifies to that of the single species MOT (equation 5.1).

5.1.3 'Push Beam' Loading Method

One means by which to spatial separate the MOT loading regions for ^{87}Rb and ^{133}Cs is to displace one of the MOTs with an additional inhomogeneous optical pressure contribution from an additional laser beam near-resonant with the 'cooling transition' for one of the mixture components.

During two-species MOT loading an additional contribution to the optical pressure on the ^{87}Rb atom cloud is made by applying light resonant with the the ^{87}Rb cooling transition along the path of the absorption imaging probe beam. A peak optical intensity for this 'push beam' of 0.48(2) mW cm^{-2} is sufficient to physically displace the ^{87}Rb science MOT centre to several mm south of that of the ^{133}Cs science MOT (using the orientations of figure 3.14). Figure 5.3 shows the atom number obtained by imaging MOT fluorescence when loading the two-species MOT with and without the ^{87}Rb push beam. Initially the ^{87}Rb science MOT is loaded to $\simeq$ 50% of its maximum single species level before the ^{133}Cs MOT is turned on at $t = 40$ s. Without the push beam present the introduction of ^{133}Cs atoms causes a dramatic loss in the number of trapped ^{87}Rb atoms, whilst the ^{133}Cs MOT loads to only $\simeq$ 14 % of it's maximum single species level. When the push beam is present however, the ^{87}Rb MOT continues to load unaffected by the introduction of ^{133}Cs atoms, whilst the ^{133}Cs MOT loads to $\simeq$ 70 % of its maximum single species level before the two atom clouds overlap and interspecies inelastic collisions suppress further loading of the ^{133}Cs MOT. Clearly the addition of the push beam is highly successful in suppressing atom losses due to two-species light assisted inelastic collisions, allowing large numbers of atoms of both species to be simultaneously loaded into the science MOT.

(a)
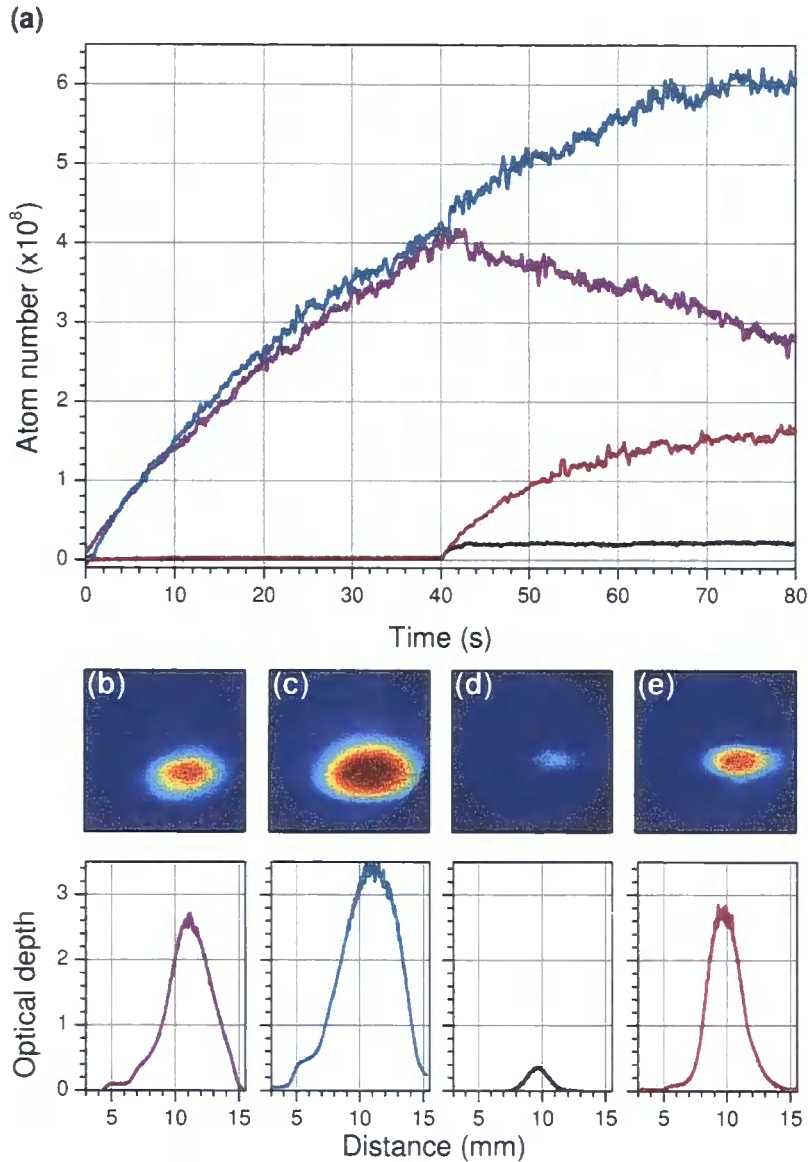
Figure 5.3: The ^{133}Cs MOT is switched on after 40 s of loading ^{87}Rb alone (a). Without the ^{87}Rb push beam atoms are lost from the ^{87}Rb MOT (purple line), and loading of the ^{133}Cs MOT is greatly impaired (black line). Adding the 'push' beam displaces the ^{87}Rb MOT from the ^{133}Cs MOT loading region, resulting in enhanced loading of ^{87}Rb (blue line) and ^{133}Cs (red line). Absorption images of magnetically trapped ^{87}Rb clouds loaded from unperturbed and displaced two species MOTs are shown in (b) and (c) respectively. The corresponding images for ^{133}Cs are (d) and (e). Cross-sections of the clouds in the vertical direction show increases in optical depth and size of both species with the push beam present. The optical depths scale on which images (b), (c) and (e) are displayed is 0-3, whilst image (d) is displayed on a 0-1 optical depth scale. The cross-sections are shown on a common 0-3.5 optical depth scale. These data are published in [65].

5.2   Two Species Magnetic Trapping

Moving forwards from magnetically trapping ^{87}Rb and ^{133}Cs single species atom clouds to simultaneously magnetically trapping both atomic species proves challenging due to the dominance of two-species light assisted inelastic collisions in the MOT, as described above. After loading the science MOT using the 'push beam' technique, the 'push beam' is removed at the start of the CMOT phase such that the ^{87}Rb and ^{133}Cs atom clouds are not displaced during magnetic trap loading. The loading of single and two species atom clouds into the magnetic trap using this technique is investigated below. Prior to characterisation of the dependence of interspecies loss rates on magnetic field or atom number, the lifetimes of simultaneously trapped ^{87}Rb and ^{133}Cs atom clouds at the loaded magnetic field are measured and compared to the corresponding single species lifetimes.

5.2.1   Pushed Loading of The Magnetic Trap

After simultaneously loading the science MOT with both atomic species with the ^{87}Rb 'push' beam present, magnetic trap loading is implemented. At the start of the CMOT phase the 'push' beam is removed, hence the once displaced ^{87}Rb atom cloud is shifted to be coincident with the ^{133}Cs atom cloud at the magnetic trap centre for the remaining duration of the loading process. The total time period for which the two atom clouds are overlapped prior to their being magnetically trapped is 26.4 ms, approximately two orders of magnitude less than the lifetime of either species in the non-pushed two species MOT in the density limited regime. Hence losses due to light-assisted inelastic collisions during the relatively short duration of species overlap should have little effect on the loaded numbers of atoms of either species in the magnetic trap. To test this hypothesis ^{87}Rb atoms are loaded into the magnetic trap from the 'pushed' single species science MOT and the 'pushed' two-species science MOT. Figure 5.4(b) shows the numbers of ^{87}Rb atoms transferred into the magnetic trap as a function of the number of ^{87}Rb atoms originally loaded into the 'pushed' science MOT, both with no ^{133}Cs atoms (hollow blue data) and with $3.0(6) \times 10^8$ ^{133}Cs atoms (solid blue data).
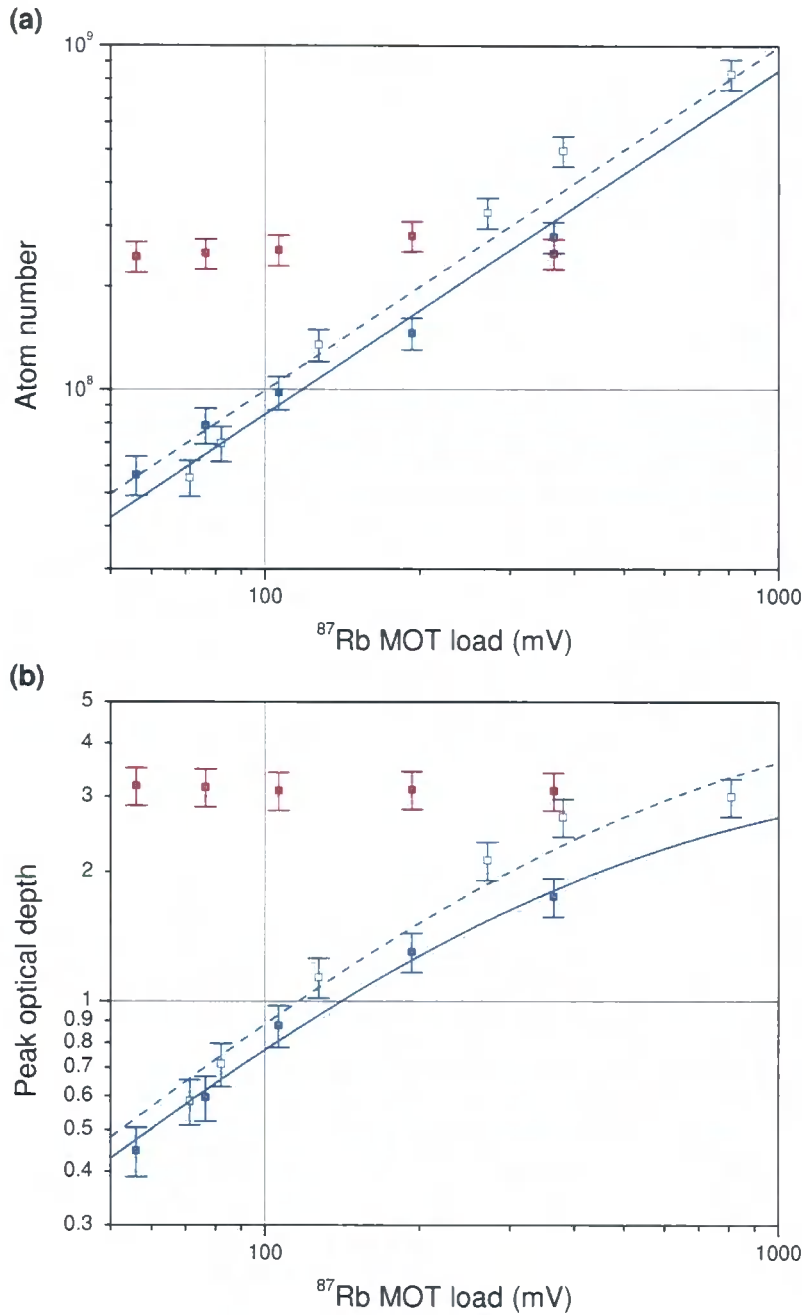
Figure 5.4: The number of ^{87}Rb atoms loaded into the single-species (two-species) magnetic trap from the single species (two-species) science MOT (a), and the corresponding atom cloud optical depth (b) as a function of ^{87}Rb MOT fluorescence photodiode signal are shown in the blue hollow (solid) data sets. For both single and two-species MOT loading the ^{87}Rb 'push' beam is present. During two species loading the ^{133}Cs MOT is initially loaded to its single species equilibrium before the ^{87}Rb science MOT is loaded for varying durations. The number of ^{133}Cs atoms loaded into the magnetic trap for each ^{87}Rb MOT load is also shown (red solid data points). Within errors the magnetic trap loading efficiencies for each species are seen to be independent of the presence of the second species in either MOT or magnetic trap.

The numbers of ^{133}Cs atoms transferred into the magnetic trap from the two-species MOT are also shown. The corresponding optical depths of atom clouds transferred into the magnetic trap are shown in figure 5.4(b). Linear fits to the number of ^{87}Rb atoms transferred as a function of MOT load with and without ^{133}Cs present have gradients of $0.85(4) \times 10^6$ and $1.00(5) \times 10^6$ atoms per mV respectively. This corresponds to a reduction in the number of ^{87}Rb atoms loaded into the magnetic trap of 15(6) % due to the presence of ^{133}Cs. As there are approximately an order of magnitude more ^{133}Cs atoms loaded for these data compared with the data of figure 5.2, the density of ^{87}Rb weighted by the probability distribution of ^{133}Cs atom presence will be approximately an order of magnitude greater. This increased species overlap is expected to result in a comparable increase in the rate of interspecies inelastic collisions, hence a corresponding reduction of the ^{87}Rb lifetime with ^{133}Cs present to (*i.e.* to $\simeq$ 200 ms). Thus the relative drop in ^{87}Rb atom number during the period of atom cloud overlap prior to magnetic trap loading is expected to be $\simeq 1 - \exp\left(-26.4/200\right) = 12.4$ %. This is consistent with the observed 15(6) % reduction, and significantly better than the reduction of $\simeq$ 70 % in atom number loaded into the science MOT without the push-beam technique (figure 5.1). The apparent lack of a corresponding reduction in ^{133}Cs atom number is due to the increased two-species lifetime of 9.8(7) s compared to the $\simeq$ 200 ms two-species lifetime of ^{87}Rb . The net effect of the science MOT 'push' technique on the maximum number of atoms loaded into the two-species magnetic trap is approximately a three fold increase for both atomic species. Calculation of these increases takes into account the interspecies collisional losses during both science MOT loading and transfer into the magnetic trap.

5.2.2 Atom Lifetime in the Magnetic Trap

With single and two-species magnetic trap loading optimised the obvious first step is to characterise the magnetic trap lifetimes for both species. The lifetime due to collisions with residual gases should be the same for both atomic species and will determine the maximum timescale over which experiments can take place.
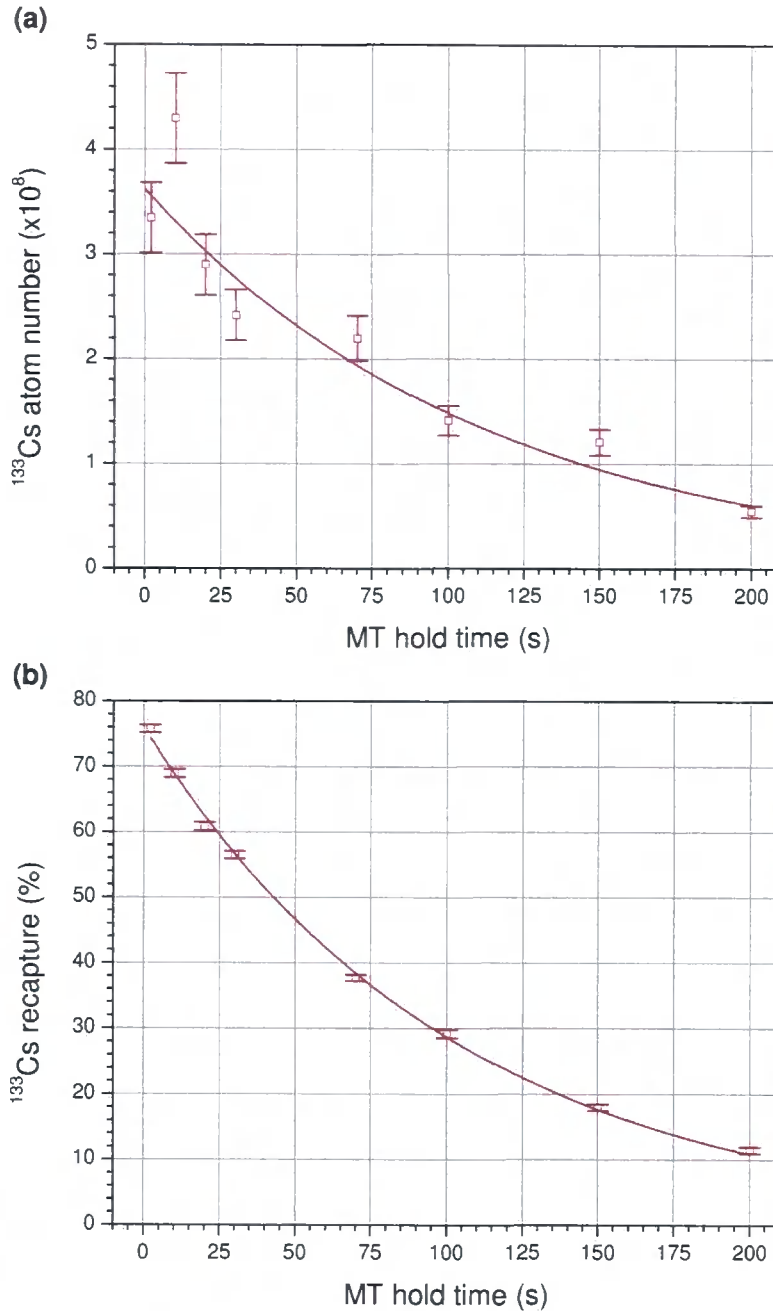
Figure 5.5: The number of ^{133}Cs atoms remaining in the single-species magnetic trap (measured from absorption images) as a function of trapping duration (a) is fitted with an exponential decay (solid line) from which the $1/e$ lifetime in the magnetic trap is determined to be 112(6) s. An independent measurement of the $1/e$ lifetime is obtained by fitting an exponential decay (solid line) to the imaged fluorescence of ^{133}Cs atoms recaptured in the science MOT following magnetic trapping, relative to the initial science MOT fluorescence (b). The $1/e$ lifetime in the magnetic trap from the recapture data is 103(1) s.

The number and percentage of loaded ^{133}Cs atoms remaining in the single-species magnetic trap as a function of trapping duration is shown in figure 5.5. Exponential fits to these data give $1/e$ lifetimes of ^{133}Cs atoms in the magnetic trap of $112(6)$ s from the atom number (obtained from absorption images) and $103(1)$ s from the recapture percentage (obtained from MOT fluorescence imaging)[1] The $1/e$ lifetime of ^{87}Rb atoms in the magnetic trap obtained from MOT recapture is $86(9)$ s. Comparison of recapture measurements of atomic lifetime in the magnetic trap made over several months show a significant variation over the range $80 \leq \tau_B \leq 400$ s. This is possibly due to a residual gas pressure dependence upon the number of consecutive days for which the atomic dispensers are operated prior to a lifetime measurement being made. The lifetime due to residual gas collisions is comparable to that measured in a similar apparatus [93], whilst the apparent background variation has no effect on comparative number measurements made on a single day, and is taken into account when comparing data sets measured on different occasions.

5.3 Initial Feshbach Search

With the lifetimes of each atomic species in the single-species magnetic trap characterised to be of the order $\simeq 100$ s, any decay occurring on a shorter timescale (for the same number and density parameters) with both species in the magnetic trap may be attributed to inelastic two species collisional losses. Any magnetic field dependence of the number of atoms remaining after a fixed duration in the magnetic trap (for B-fields outside of the regions of single species ^{87}Rb and ^{133}Cs Feshbach resonances) will be indicative of the presence of an interspecies Feshbach resonance.

---

[1]The increased precision of the recapture data highlights the value of imaging atomic fluorescence to make comparative measurements, as these are less sensitive to atom load and laser detuning fluctuations than absolute measurements from absorption images.

5.3.1   Two Species Magnetic Trap Loss Measurements

After loading the magnetic trap with both atomic species from the 'pushed' science MOT, the number of atoms of each species remaining as a function of the magnetic trap B-field at the end of a series of two B-field ramps for magnetic fields in the range $166 < B < 370$ G is shown in figure 5.6. Here
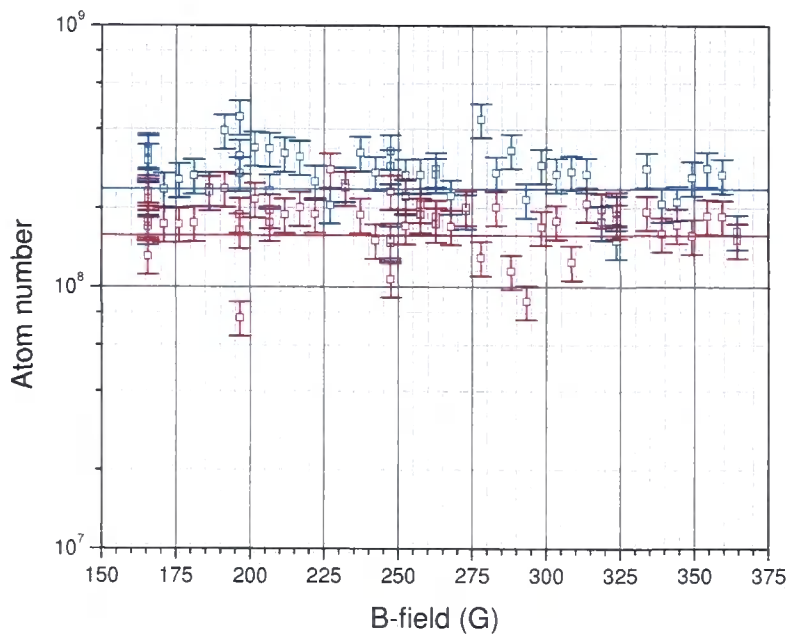
Figure 5.6: Number of ^{87}Rb (blue) and ^{133}Cs (red) atoms in the two-species magnetic trap as a function of trap B-field at the end of two B-field ramps. Initially the trap is simultaneously loaded from the 'pushed' science MOT (see text) to have $3.2(5) \times 10^8$ ^{87}Rb and $2.7(4) \times 10^8$ ^{133}Cs atoms at a temperature of $\simeq 100$ μK after a 2 s hold. The magnetic trap is switched on at a B-field (at the ^{133}Cs cloud centre) of 165.50(6) G at which it remains for 2 s. The B-field is then ramped over a 10 s period to be 5 G away from that of the plotted B-field end point. A 20 s ramp across the 5 G interrogation field range then takes place before atom release and subsequent absorption imaging. Fitting the number of atoms of each species at the end of the B-field ramp to a constant value gives $2.35(5) \times 10^8$ ^{87}Rb (blue line) and $1.57(3) \times 10^8$ ^{133}Cs (red line) atoms respectively.

the 'pushed' science MOT is loaded for 20 s with only ^{87}Rb trapping light present, and for a further 30 s with trapping light for both atomic species prior to atom transfer into the magnetic trap. Figure 5.6 does not show any dependence of the number of atoms remaining in the magnetic trap on the B-field at the end of the second (5 G wide) ramp. The mean reduction in the number of ^{87}Rb (^{133}Cs) atoms during the ramping period is consistent with a residual gas limited decay rate of 100(30) s (60(40) s), in agreement with the measured lifetimes of single species atom clouds in the magnetic trap. The extent to which the lack of observation of two-species B-field dependent losses in these data constrains the magnitude of any Feshbach resonances present over this B-field range can only be established through characterisation of the measurement sensitivity.

5.3.2 Feshbach Resonance Sensitivity

The sensitivity to detect interspecies Feshbach resonances depends upon many factors including: atom number density, cloud temperature, gravitational sag, trap frequencies, interrogation time magnetic trap lifetime and experimental reproducibility for both atomic species. Many of these parameters are not independent, hence characterising the sensitivity is non-trivial.

Density Dependence

The contribution of two-body inelastic collisions with ^{133}Cs atoms to rate of loss of ^{87}Rb atoms from the magnetic trap is given by:

$$\left.\frac{\mathrm{d}N_{^{87}\mathrm{Rb}}}{\mathrm{d}t}\right|_{^{87}\mathrm{Rb}\,^{133}\mathrm{Cs}} = -K_{2^{87}\mathrm{Rb}\,^{133}\mathrm{Cs}}\,\langle n_{^{133}\mathrm{Cs}}\rangle_{^{87}\mathrm{Rb}}\,F_{^{133}\mathrm{Cs}\,(^{87}\mathrm{Rb})}N_{^{87}\mathrm{Rb}} \quad,$$

(5.12)

where $\langle n_{^{133}\mathrm{Cs}}\rangle_{^{87}\mathrm{Rb}}$ is the mean density of ^{133}Cs atoms experienced by ^{87}Rb atoms in the magnetic trap, $N_{^{87}\mathrm{Rb}}$ is the number of trapped ^{87}Rb atoms and $F_{^{133}\mathrm{Cs}\,(^{87}\mathrm{Rb})}$ is the factor by which the rate at which ^{87}Rb atoms undergo inelastic two-body collisions with ^{133}Cs atoms is altered by the difference in gravitational sag of the two species (see section 2.3.4). The rate constant $K_{2^{87}\mathrm{Rb}\,^{133}\mathrm{Cs}}$ is characteristic of the two-species two-body inelastic collision rate. Similarly the contribution of two-body inelastic collisions with ^{87}Rb

atoms to the atom loss rate of ^{133}Cs atoms in the magnetic trap is given by:

$$\left. \frac{dN_{^{133}\text{Cs}}}{dt} \right|_{^{133}\text{Cs}\ ^{87}\text{Rb}} = -K_{2^{133}\text{Cs}\ ^{87}\text{Rb}} \left\langle n_{^{87}\text{Rb}} \right\rangle_{^{133}\text{Cs}} F_{^{87}\text{Rb}\ (^{133}\text{Cs})} N_{^{133}\text{Cs}} \quad ,$$

(5.13)

where the parameters correspond to those of equation 5.12 with species assignations reversed. The following discussion uses the term 'target species' to mean the species whose inelastic loss rate is being considered, and terms the species with which the 'target species' undergoes such collisions the 'partner species'. The density overlap factors of equations 5.12 and 5.13 are:

$$\left\langle n_{^{133}\text{Cs}} \right\rangle_{^{87}\text{Rb}} = n_{^{133}\text{Cs pk}} \left(\frac{T_{^{133}\text{Cs}}}{T_{^{133}\text{Cs}} + \beta^2 T_{^{87}\text{Rb}}} \right)^{3/2} \quad \text{and} \quad (5.14)$$

$$\left\langle n_{^{87}\text{Rb}} \right\rangle_{^{133}\text{Cs}} = n_{^{87}\text{Rb pk}} \left(\frac{\beta^2 T_{^{87}\text{Rb}}}{\beta^2 T_{^{87}\text{Rb}} + T_{^{133}\text{Cs}}} \right)^{3/2} \quad , \quad (5.15)$$

where:

$$m_{^{133}\text{Cs}} \omega_{^{133}\text{Cs}}^2 = \beta^2 m_{^{87}\text{Rb}} \omega_{^{87}\text{Rb}}^2 \quad , \quad (5.16)$$

for ^{87}Rb and ^{133}Cs trap frequencies $\omega_{^{87}\text{Rb}}$ and $\omega_{^{133}\text{Cs}}$ and masses $m_{^{87}\text{Rb}}$ and $m_{^{133}\text{Cs}}$ respectively (see section 2.3.4). Thus the exponential rate of atom loss for each atomic species due to two-species two-body inelastic collisions is proportional to the number density of the partner species and also a Gaussian overlap factor. Clearly the collision rate for each atomic species is most readily enhanced by increasing the atom number density of the partner species, whilst reducing the target species temperature also increases the Gaussian overlap factor towards a maximum value of one. However the effect which varying the temperature of either atomic species has on the two species inelastic collision rate sensitivity may only be determined after considering the effect of such a change on all parameters of equations 5.12 and 5.13.

Gravitational Sag

As the magnetic moments of ^{87}Rb and ^{133}Cs vary with applied magnetic field so too does the gravitational sag for each atomic species (section 3.6.2) leading to a reduction in overlap of the Gaussian density distributions of the two species within the magnetic trap. The extent to which the gravitational sag reduces the sensitivity to Feshbach resonances depends upon the magnitude

of the difference in sag compared to the atom cloud width for each species (see section 2.3.4). The measured difference in gravitational sag of ^{87}Rb and ^{133}Cs atom clouds during the interspecies Feshbach resonance search at 100 μK is shown in figure 5.7, along with the predicted difference derived from the measured parameters of the magnetic coils. The blue (red) data points of figure 5.8 show the corresponding reduction in the mean rate at which each trapped ^{87}Rb (^{133}Cs) atom is subject to a two-body inelastic collision with a trapped ^{133}Cs (^{87}Rb) atom due to the difference in sag of the two components during the 100 μK interspecies Feshbach resonance search. For temperatures of $\simeq$100 μK for ^{87}Rb and ^{133}Cs loaded atom clouds, the
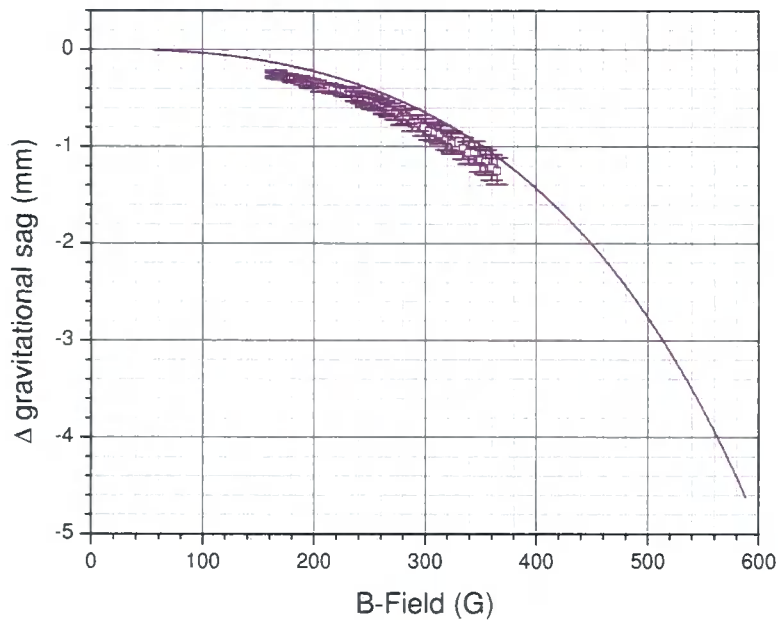
Figure 5.7: Measured difference in gravitational sag of ^{87}Rb and ^{133}Cs as a function of B-field applied during the interspecies Feshbach search at 100 μK (purple data points). For this data the position of each species prior to release from the magnetic trap is calculated from the imaged position of the atom cloud centres for ^{133}Cs (^{87}Rb) atoms 10 ms (14.92 ms) after release from the magnetic trap assuming constant acceleration under gravity. Also shown is the theoretical difference in gravitational sag of the two atomic species (purple line) calculated from the measured magnetic trap parameters and calculated magnetic moments of each species.

reduction in two-species, two-body inelastic collision rates for each species due to difference in gravitational sag across the B-field interrogation range is $\simeq 15$ %. Reduction in the temperature of both atomic species leads to a significant decrease in the gravitational overlap factor. Hence the extent to which inelastic collision rate sensitivity may be increased through number density gain via atomic evaporation must be tempered by the corresponding reduction in sensitivity due to the temperature dependence of the gravitational overlap factor.
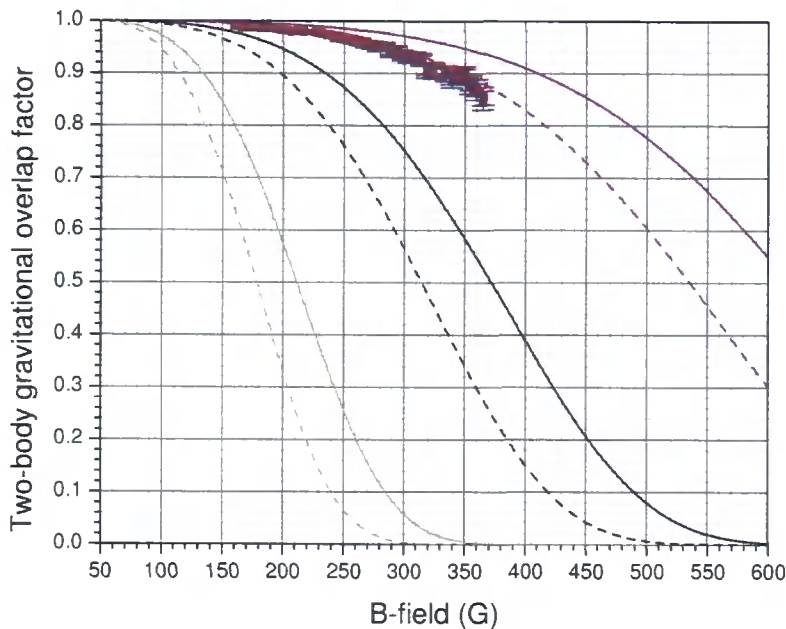
Figure 5.8: Gravitational overlap factor as a function of applied magnetic field during the interspecies Feshbach resonance search in the 'weak' magnetic trap. Blue (red) data points show that the factor by which the rate at which ^{87}Rb (^{133}Cs) atoms undergo two-body inelastic collisions with ^{133}Cs (^{87}Rb) atoms is altered due to the difference in gravitational sag of the two species. The empirical data is at a loaded trap temperature of $\simeq 100$ μK. Lines shown are the modeled gravitational overlap factors at constant mean temperatures (for both atomic species) of 100 (purple solid), 50 (purple dashed), 10 (black solid), 5 (black dashed), 1 (gold solid) and 0.5 (gold dashed) μK for the trap geometry used during the Feshbach resonance search.

Magnetic Field Localisation

As the atom number density for a single species atomic ensemble has a Gaussian distribution dependent upon ensemble temperature and position in the magnetic trap, the B-field probed by such an ensemble is distributed over a temperature dependent range. Assuming a uniform temperature T along all axes of the trapped atom cloud, the width B_w of the magnetic field range over which a proportion P of the trapped atoms are distributed is given by:

$$B_{\mathrm{w}} = -\frac{2K_{\mathrm{B}}T}{\mu} \ln\left(1 - P^2\right) \quad , \tag{5.17}$$

where μ is the magnetic moment of the atomic species in the trapped state. Assuming constant magnetic moments for ^{87}Rb and ^{133}Cs of $0.5\mu_{\mathrm{B}}$ and $0.75\mu_{\mathrm{B}}$
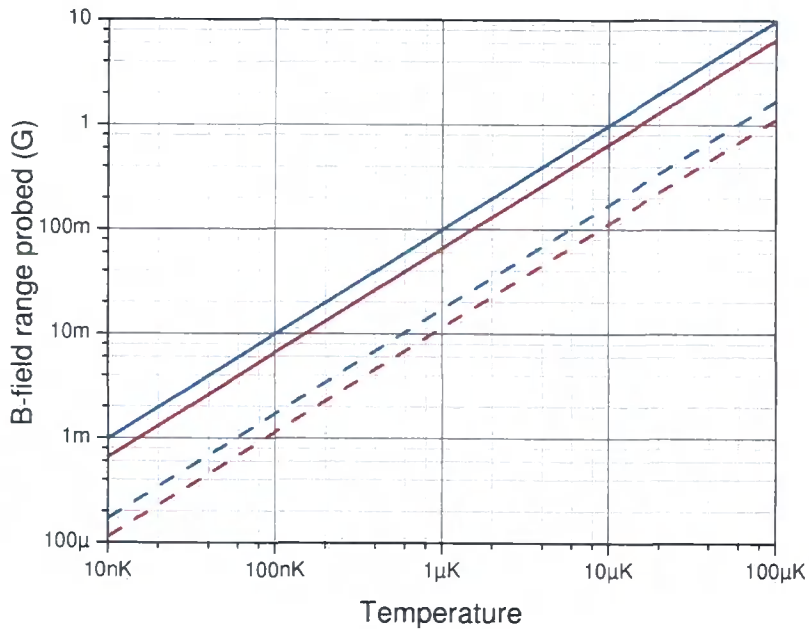
Figure 5.9: Width of B-field range probed by Gaussian distributions of ^{87}Rb (blue lines) and ^{133}Cs (red lines) atoms as a function of cloud temperatures. The solid (dashed) lines show the width of B-field range over which 90 % (50 %) of the atoms within each Gaussian cloud are distributed. These data are calculated assuming constant values for the magnetic moments of ^{87}Rb and ^{133}Cs of $0.5\mu_{\mathrm{B}}$ and $0.75\mu_{\mathrm{B}}$ respectively.

respectively, figure 5.9 shows the calculated B-field width probed by 50 % and 90 % of the atoms contained in ensembles of ^{87}Rb and ^{133}Cs atoms as a function temperature. At a temperature of $\simeq 100$ μK only $\simeq 50$ % of the trapped ^{133}Cs atoms are within a B-field range of 1 G, thus the sensitivity to resonances $\simeq 1$ G wide is immediately reduced by a factor of two compared with that achievable at temperatures several orders of magnitude lower.

Present Resonance Sensitivity

All of the factors discussed above are combined to estimate the minimum changes in two-body inelastic interspecies collision rate constants to which the Feshbach resonance search of figure 5.6 is sensitive:

$$K_{2^{87}\text{Rb}\ ^{133}\text{Cs}} \geq \frac{L_{^{87}\text{Rb}}}{\langle n_{^{133}\text{Cs}} \rangle_{^{87}\text{Rb}} F_{^{133}\text{Cs}(^{87}\text{Rb})} T_{\text{ramp}}} \cdot \frac{\sqrt{(B_{\text{res}})^2 + (B_{\text{ramp}} + B_{\text{w}})^2}}{B_{\text{res}}} \quad , \tag{5.18}$$

and:

$$K_{2^{133}\text{Cs}\ ^{87}\text{Rb}} \geq \frac{L_{^{133}\text{Cs}}}{\langle n_{^{87}\text{Rb}} \rangle_{^{133}\text{Cs}} F_{^{87}\text{Rb}(^{133}\text{Cs})} T_{\text{ramp}}} \cdot \frac{\sqrt{(B_{\text{res}})^2 + (B_{\text{ramp}} + B_{\text{w}})^2}}{B_{\text{res}}} \quad , \tag{5.19}$$

where $L_{^{87}\text{Rb}}$ and $L_{^{133}\text{Cs}}$ are the minimum detectable loss fractions of ^{87}Rb and ^{133}Cs respectively, B_{ramp} and T_{ramp} the width and duration of the B-field ramp at each datum point, B_{w} is the B-field range probed by 90 % of the atoms of the species with the narrowest Gaussian distribution and B_{res} is the full B-field width at which the interspecies rate constant takes half its maximum value. The ensemble parameters for both species during the interspecies Feshbach resonance search are shown in table 5.1.

Assuming sensitivity to loss fractions $L_{^{87}\text{Rb}}$, $L_{^{133}\text{Cs}} \geq 50$ %, equations 5.18 and 5.19 show that Feshbach resonances with $B_{\text{res}} = 1$ G would be detected during the resonance search if the peak rate constants:

$$K_{2^{87}\text{Rb}\ ^{133}\text{Cs}} \geq 6(1) \times 10^{-10} \text{cm}^3\text{s}^{-1} \quad \text{and}$$

$$K_{2^{133}\text{Cs}\ ^{87}\text{Rb}} \geq 5(1) \times 10^{-10} \text{cm}^3\text{s}^{-1} \quad .$$

These sensitivity limits are an order of magnitude above the single species two-body inelastic collision rate constants measured for ^{133}Cs Feshbach reso-

nances in the $|F = 3, m_F = -3\rangle$ state [93] and also two orders of magnitude above the upper limit placed on the inelastic two-body interspecies collision rate between ^{87}Rb atoms in the $|F = 2, m_F = 2\rangle$ and ^{133}Cs atoms in the $|F = 4, m_F = 4\rangle$ states over the B-field range $4 \leq B \leq 40$ G [75]. One means by which to increase the measurement sensitivity is to increase the atom number density for each atomic species (hence increase the density overlap). The ^{87}Rb and ^{133}Cs atom number densities of $\simeq 5 \times 10^{11}$ cm^{-3} at which interspecies Feshbach resonances between ^{87}Rb atoms in the $|F = 1, m_F = 1\rangle$ and ^{133}Cs atoms in the $|F = 3, m_F = 3\rangle$ states have been detected [100] are approximately two orders of magnitude greater than those at which the Feshbach search shown in figure 5.13 took place.

(a) Single species ensemble properties

$N_{^{87}\text{Rb}} =$	$3.5(5) \times 10^8$		$N_{^{133}\text{Cs}} =$	$2.7(4) \times 10^8$
$n_{^{87}\text{Rb pk}} =$	$1.78(6) \times 10^9$ **cm**$^{-3}$		$n_{^{133}\text{Cs pk}} =$	$2.53(6) \times 10^9$ **cm**$^{-3}$
$T_{^{87}\text{Rb}} \simeq$	100 μ**K**		$T_{^{133}\text{Cs}} \simeq$	100 μ**K**

(b) Two-species properties

$\langle n_{^{133}\text{Cs}} \rangle_{^{87}\text{Rb}} =$	$6(1) \times 10^8$ cm^{-3}		$\langle n_{^{87}\text{Rb}} \rangle_{^{133}\text{Cs}} =$	$7(2) \times 10^8$ cm^{-3}
$F_{^{133}\text{Cs}(^{87}\text{Rb})} \simeq$	0.85(2)		$F_{^{87}\text{Rb}(^{133}\text{Cs})} \simeq$	0.86(2)
$B_{\text{w}^{87}\text{Rb}} =$	9.9 G		$B_{\text{w}^{133}\text{Cs}} =$	6.6 G

(c) Estimated maximum rate constants

$K_{2^{87}\text{Rb}\,^{133}\text{Cs}} \leq 6(1) \times 10^{-10}$ cm^3 s^{-1}	$K_{2^{133}\text{Cs}\,^{87}\text{Rb}} \leq 5(1) \times 10^{-10}$ cm^3 s^{-1}

Table 5.1: Interspecies Feshbach resonance search at 100 μK measurement summary. The measured parameters of ^{87}Rb and ^{133}Cs atomic ensembles during the interspecies Feshbach resonance search of section 5.3.1 are shown (a) together with the calculated two-species density, gravitational overlap, and full B-field width over which 90 % of each atomic ensemble is distributed (b). From these data the sensitivity of the interspecies Feshbach search (comprising of a series of 20 s duration B-field ramps over 5 G intervals) is calculated (c).

Resonance Sensitivity Enhancement Strategies

The most significant factors limiting the Feshbach resonance sensitivity are the low number densities and the relatively large range of magnetic fields sampled by each trapped atomic species. The atom number density of each atomic species n_{pk} as a function of total atom number N and cloud temperature T is (see appendix B.2.1):

$$n_{\text{pk}} = N\omega_r{}^2\omega_z \left(\frac{m}{2\pi k_{\text{B}}T} \right)^{\frac{3}{2}} , \tag{5.20}$$

where m is the atomic mass and ω_r and ω_z are the radial and axial trapping frequencies respectively (section 2.2.4 and 4.8.1). Thus for the same atom number operating the magnetic trap at higher trap frequencies (*i.e.* the 'tight' trapping regime) or at lower temperatures will lead to density enhancement. As the parameters of equation 5.20 are not independent, increasing the number density is not simply a case of turning a single knob. Similarly the magnetic field range sampled by the atomic mixture during interspecies collisions is limited by the width of atom cloud with the narrowest Gaussian distribution. This can be reduced by reducing the temperature of either component of the atomic mixture, however reducing the temperature of either atomic species may result in a reduction in the fractional overlap of the ^{87}Rb and ^{133}Cs atom clouds due to the differential gravitational sag. Clearly the change in sensitivity to interspecies Feshbach resonances resulting from manipulation of the density or temperature of either atomic species is difficult to predict. It may however be evaluated through implementing such changes and measuring the resulting effects.

5.4 Single Species Evaporative Cooling

One means by which to simultaneously increase the atomic number density and reduce the range of B-fields probed by a trapped atomic ensemble is to implement evaporative cooling (section 2.5). The results of evaporatively cooling single species magnetically trapped clouds of ^{133}Cs and ^{87}Rb are shown in the following sections.

5.4.1 Evaporation Trajectories

Radio-frequency (RF) evaporative cooling is optimised separately for each atomic species in the corresponding single species magnetic trap. Eight stages of evaporative cooling are optimised for each species. For ^{133}Cs each evaporation stage reduces the temperature of the trapped atom cloud by a factor of two. During each evaporation stage of duration t_{stage} the frequency of the RF source is exponentially ramped as a function of time t between initial and final radio frequencies f_{start} and f_{stop} as:

$$f(t) = f_{\text{base}} + (f_{\text{start}} - f_{\text{base}}) \times \exp \frac{-t}{T} \quad , \tag{5.21}$$

where the characteristic timescale T of the exponential ramp is derived from the base frequency f_{base} to be:

$$T = \frac{-t_{\text{stage}}}{\ln \left(\frac{f_{\text{stop}} - f_{\text{base}}}{f_{\text{start}} - f_{\text{base}}} \right)} \quad . \tag{5.22}$$

Here f_{base} is initially set to be close to resonance with the transition frequency for atoms at the very centre of the atomic ensemble, satisfying the requirement to maintain the evaporation constant η (see section 2.5.2). After optimising the parameters of equation 5.21 for all eight stages of ^{133}Cs evaporation in the single species magnetic trap, evaporation of ^{87}Rb is optimised. Initial investigations of ^{87}Rb evaporation showed relatively long timescales were required to efficiently reduce the temperature by a factor of two at each evaporation stage. In order to progress towards evaporating simultaneously with both atomic species the total ^{87}Rb evaporation duration is fixed to equal that to which the ^{133}Cs evaporation is optimised. This requires the ^{87}Rb evaporation trajectory to be truncated such that following optimisation of all evaporation parameters with the exception of total evaporation duration, the ^{87}Rb ensemble temperature is 7.63 μK, far higher than that of ^{133}Cs (522 nK). The optimised eight-stage evaporation trajectories for single species magnetically trapped clouds of ^{133}Cs and ^{87}Rb atoms at atom-cloud centre B-fields of 166.70(6) and 165.50(6) G respectively are shown in table 5.2.

(a) Common parameters.			(b) ^{133}Cs single species evaporation trajectory.					(c) ^{87}Rb single species evaporation trajectory.				
Stage	t_{stage} (s)	t_{total} (s)	f_{start} (MHz)	f_{stop} (MHz)	f_{base} (MHz)	RF amp (dBm)	Temp (μK)	f_{start} (MHz)	f_{stop} (MHz)	f_{base} (MHz)	RF amp (dBm)	Temp (μK)
1	15	15	65.000	62.200	60.100	-10	64.1	140.000	125.800	118.900	-10	56.9
2	30	45	62.200	61.610	60.100	-10	27.9	125.800	123.300	118.900	-5	28.6
3	30	75	61.610	61.090	60.100	-15	15.2	123.300	121.300	120.000	-5	18.8
4	15	90	61.090	60.680	60.100	-10	8.24	121.300	120.200	118.900	-10	15.4
5	15	105	60.680	60.380	60.100	-15	3.96	120.200	119.455	40.000	-10	12.1
6	8	113	60.380	60.270	60.100	-15	2.03	119.455	119.050	118.900	-5	10.6
7	8	121	60.270	60.102	60.100	-10	1.04	119.050	118.700	118.500	-5	9.07
8	8	129	60.102	59.995	59.500	-5	0.522	118.700	118.535	118.500	-5	7.63

Table 5.2: Optimised evaporation trajectories for atomic species in the single species magnetic trap. The durations of each evaporation stage (a) are fixed to be equal for both species. The remaining evaporation parameters for ^{133}Cs (b) and ^{87}Rb (c) are optimised to give the greatest gain in ensemble phase-space density per atom removed from the magnetic trap. Here RF amp is the amplified amplitude of the radio-frequency source and Temp is the temperature at the end of each evaporation ramp. All other values are the parameters of equation 5.21. The magnetic trap coils are operated at the same current in both cases, however the centre of the magnetically trapped ^{133}Cs (^{87}Rb) cloud gravitationally sags to a B-field of 165.50(6) G (166.70(6) G). The difference between the temperatures of the ^{87}Rb and ^{133}Cs atom clouds after the eighth evaporation stage are due to the reduced rate of interatomic collisions in ^{87}Rb compared to ^{133}Cs during evaporation.

5.4.2 Radio-Frequency Shift With Magnetic Field

The degree to which altering the initial magnetic field at which the magnetic trap is turned on affects the evaporation parameters for each atomic species in the single species magnetic trap was characterised to aid in identifying whether loading of the two-species magnetic trap occurs at the position of an interspecies Feshbach resonance. By changing the magnetic field of single species trap loading the RF frequencies required to cool each atomic sample to the temperatures in table 5.2 are also altered. For each atomic species a constant radio-frequency offset is added to all of the frequencies in table 5.2 for each value of magnetic field at which the atom clouds are evaporated. The measured RF shifts are shown in table 5.3.

(a) ^{87}Rb RF shift

B-field (G)	RF shift (kHz)
156.7(1)	-6700
166.70(6)	0
176.7(1)	7600

(b) ^{133}Cs RF shift

B-field (G)	RF shift (kHz)
155.5(1)	-3444
160.5(1)	-1654
165.50(6)	5
170.5(1)	2029
175.5(1)	3941

Table 5.3: Shift in evaporation radio-frequencies as a function of trap turn-on magnetic field in the single species magnetic trap.

5.4.3 Evaporation Results

The number of ^{133}Cs and ^{87}Rb atoms remaining in the single species magnetic trap as a function of temperature and the atom cloud phase-space density as a function of atom number after each evaporation stage are shown in figures 5.10 and 5.11 respectively. Here the evaporation trajectories are optimised to give the maximum evaporation efficiency in terms of fractional gain in phase space density per fraction of atoms removed from the trap, *i.e.*, the

parameter γ in the equation:

$$\text{PSD} \propto N^{-\gamma} \quad , \tag{5.23}$$

is maximised (see section 2.5.2). The equivalent evaporation efficiency in terms of fractional reduction in temperature per fraction of atoms removed from the trap is the α parameter in the equation:

$$T \propto N^{\alpha} \quad , \tag{5.24}$$

where $\gamma = 3\alpha - 1$ (see section 2.5.2). The trajectories for ^{133}Cs (^{87}Rb) evaporation at five (three) different magnetic trap turn-on B-fields are shown in figure 5.10 (figure 5.11), where the frequencies of RF cut for each trajectory are adjusted by the values in table 5.3 to ensure the temperature of the atom cloud after each 'cut' is reduced to the corresponding level in table 5.2. For each B-field value the evaporation efficiency equations 5.24 and 5.23 are fitted to the evaporation data for each atomic species. The constants of proportionality for each fit vary with trap turn-on B-field due to trap loading parameters being fixed to those optimised for B=165.50(6) G and B=166.70(6) G for ^{133}Cs and ^{87}Rb respectively. The evaporation efficiency terms for each individual species show little dependence on trap turn-on B-field, thus any evaporation dependence on magnetic field within the two-species magnetic trap may be attributed to the presence of a two-species inelastic collisional resonance in the region of the magnetic trap loading field. The measured evaporation efficiencies for ^{87}Rb and ^{133}Cs in the single species magnetic trap are shown in table 5.4. The single species densities and elastic collision rates as a function of temperature using the evaporation efficiencies α from table 5.4, temperature dependent rate coefficients of figure 2.8(b) and mean initial temperature and numbers parameters for ^{87}Rb and ^{133}Cs are shown in (a) and (b) of figure 5.12 respectively. Clearly evaporating ^{133}Cs atoms after trap loading is highly beneficial in increasing both the elastic collision rate and the atom number density, enhancing both the apparatus sensitivity to inelastic collisions and providing favorable evaporative cooling efficiencies down to nK temperatures. For ^{87}Rb evaporative cooling through seven orders of magnitude only enhances the atom number density (hence the sensitivity to inelastic collisions) by a factor of two. Reducing the ^{87}Rb ensemble temperature from that at which the trap is loaded rapidly results in a drop in

(a)

(b)
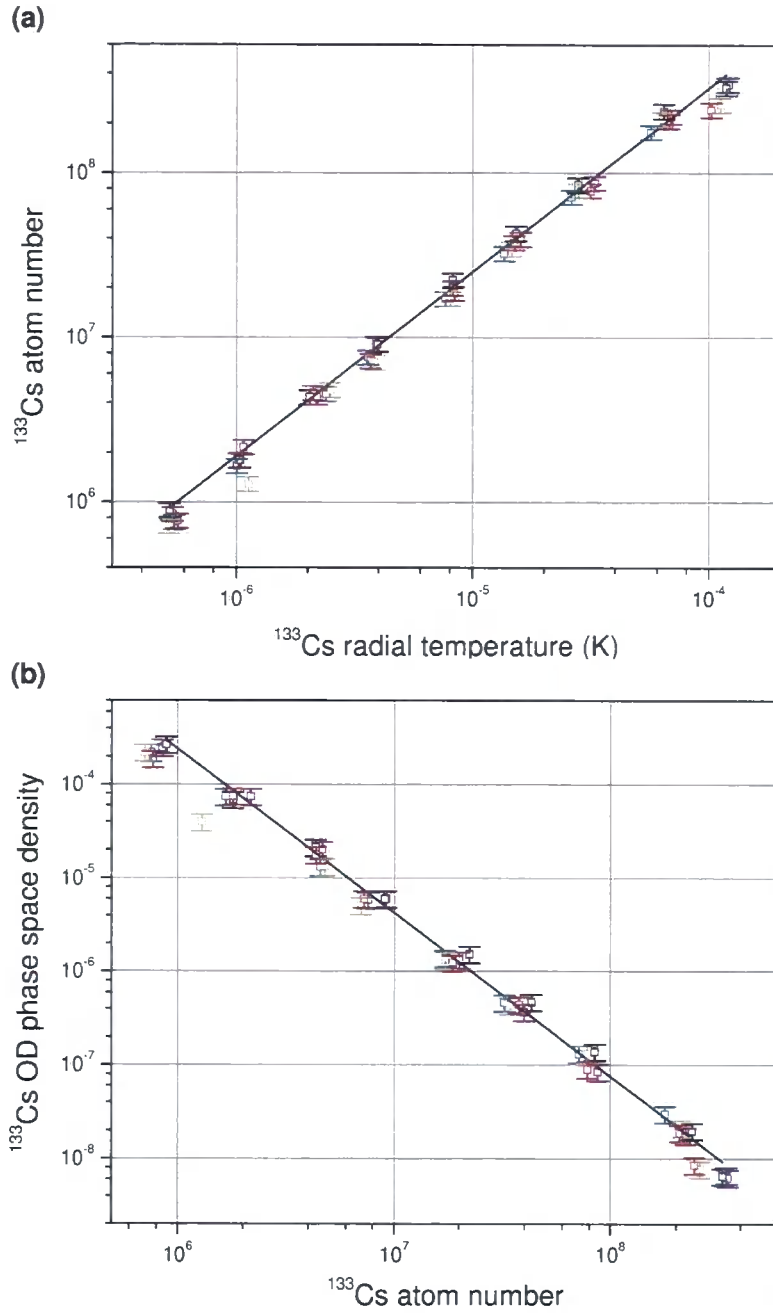
Figure 5.10: Atom number as a function of atom cloud temperature (a) and cloud phase-space density as a function of atom number (b) after each stage of radio-frequency evaporative cooling of ^{133}Cs in the single-species magnetic trap. Evaporation trajectories (hollow data) at 155.5(1) (Blue), 160.5(1) (Purple), 165.50(6) (Black), 170.5(1) (Red) and 175.5(1) (Gold) G are shown. Fitting the power law $N = C_1(B) \cdot T^{1/\alpha}$ to each data set of (a) gives a common evaporation efficiency value $\alpha = 0.887(7)$. Fitting power laws PSD $= C_2(B) \cdot T^{-\gamma}$ to each data set of (b) gives values of γ ranging from 1.62(3) to 1.78(3). The variation in γ is due to variation in the initial cloud parameters when loading at different B-fields. The displayed fits in (a) and (b) (black lines) are those for evaporation at 165.50(6) G.

(a)

(b)
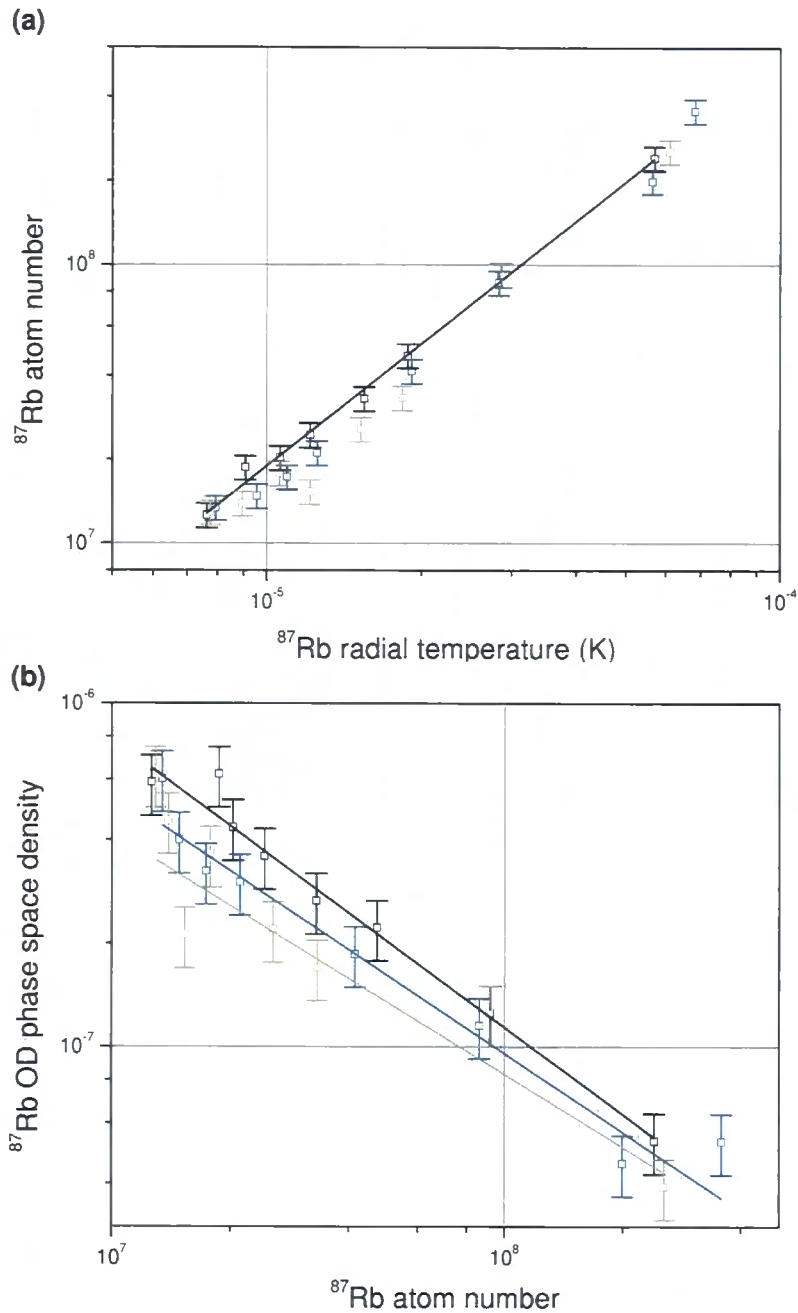
Figure 5.11: Atom number as a function of atom cloud temperature (a) and cloud phase-space density as a function of atom number (b) after each stage of radio-frequency evaporative cooling of ^{87}Rb in the single-species magnetic trap. Evaporation trajectories (hollow data) at 156.7(1) (Blue), 161.7(1) (Purple), 166.70(6) (Black), 171.7(1) (Red) and 176.7(1) (Gold) G are shown. Fitting the power law $N = C_1(B) \cdot T^{1/\alpha}$ to each data set of (a) gives a common evaporation efficiency value $\alpha = 0.66(1)$. Fitting power laws $\mathrm{PSD} = C_2(B) \cdot T^{-\gamma}$ to each data set of (b) gives a common value of $\gamma = 0.76(4)$. The colour of each fit in (a) and (b) (solid lines) corresponds to that of that of the fitted data set.
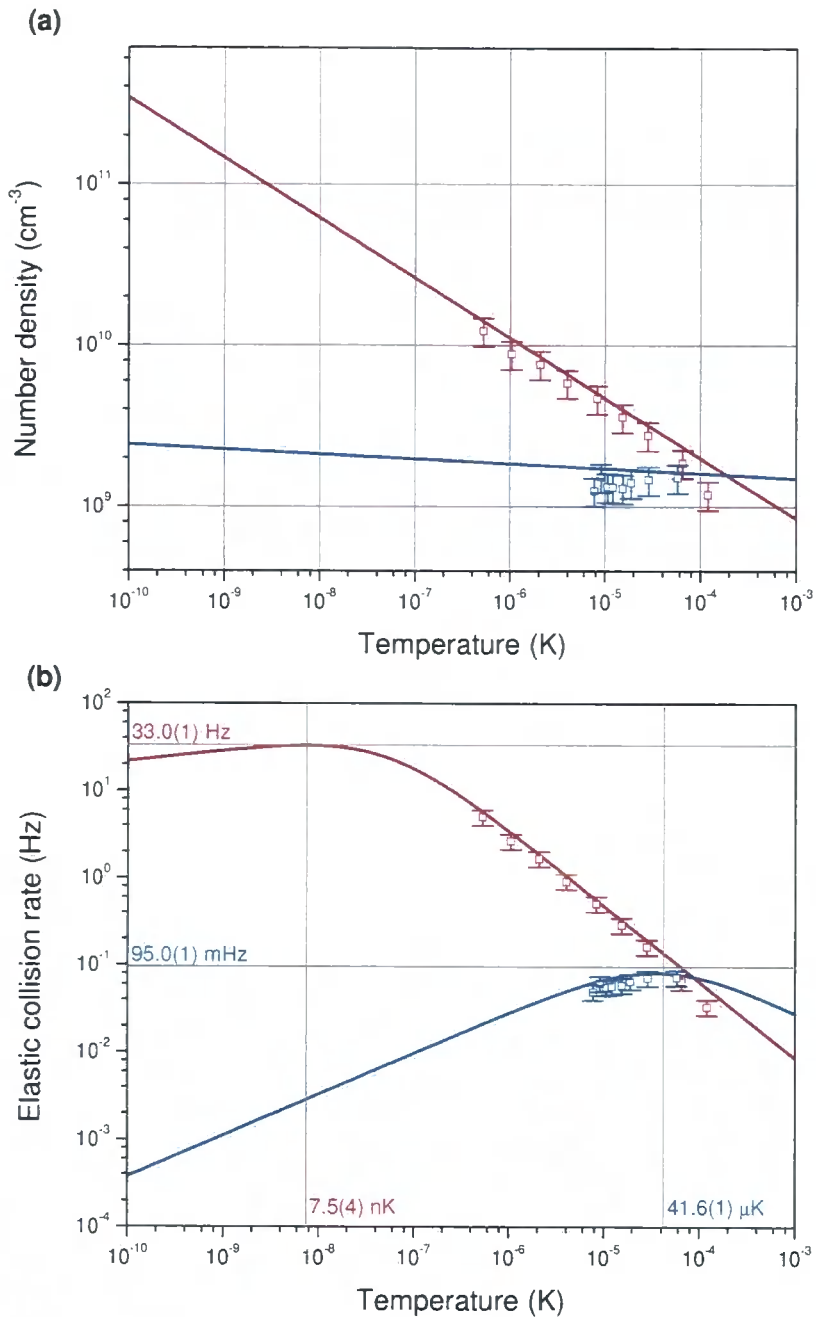
Figure 5.12: Atom number density (a) and elastic collision rate (b) as a function of temperature for ^{87}Rb (blue data points) and ^{133}Cs (red data points) in the single species magnetic trap. Also shown are the fitted density and collision rates for each species based on the measured evaporation efficiencies for the data shown. The extrapolated atom number densities increase with reduction in temperature, whilst the elastic collision rates for ^{87}Rb and ^{133}Cs peak at temperatures of 41.6(1) μK and 7.5(4) nK respectively.

the elastic collision rate, hence reducing the ^{87}Rb cloud temperature has a negative effect on the evaporative cooling rate. The most favorable elastic collision rates achievable for each atomic species in the current apparatus configuration appear to be of the order $\simeq$ 10 Hz for ^{133}Cs and $\simeq$ 0.1 Hz for ^{87}Rb.

Species	γ	α	$\gamma - 3\alpha + 1$
^{87}Rb	0.76(4)	0.66(1)	-0.22(5)
^{133}Cs	1.78(3)	0.887(7)	0.12(4)

Table 5.4: Evaporation efficiencies for ^{87}Rb and ^{133}Cs in the single species magnetic trap at a B-field at atom cloud centre of B=165.50(6) and B=166.70(6) G for ^{133}Cs and ^{87}Rb respectively. Efficiencies in terms of fractional gain in phase-space density per fraction of atoms removed from the trap (γ) and fractional reduction in temperature per fraction of atoms removed from the trap (α) are shown. These two evaporation efficiencies are expected to obey the relation $\gamma - 3\alpha + 1 = 0$.

5.5 ^{133}Cs Feshbach Resonances

In order to test the experimental sensitivity to Feshbach resonances following evaporation, and also confirm the B-field calibration, a cloud of ^{133}Cs atoms evaporatively cooled to a temperature of 3.6(6) μK is used to probe the known single species ^{133}Cs Feshbach resonances at $\simeq$ 118 and $\simeq$ 134 G. Figure 5.13 shows the number of ^{133}Cs atoms remaining in the magnetic trap after evaporation, a 10 s B-field ramp, and a 20s hold, as a function of the B-field at which the hold takes place. Two loss features are clearly visible, corresponding to the known Feshbach resonances. The centres and widths of these resonances are measured by fitting two Lorentzian profiles to the data of figure 5.13, superimposed upon a sloping background. The fit is of the form:

$$N = (N_0 + mB) \cdot \left(1 - \frac{L_1}{\left(1 + \frac{4(B-B_1)^2}{\gamma_1^2}\right)} - \frac{L_2}{\left(1 + \frac{4(B-B_2)^2}{\gamma_2^2}\right)} \right) \quad , \quad (5.25)$$

where N_0 and m are the y intercept and gradient of the sloping background, B_1 and B_2 are the centres of the two resonances and γ_1 and γ_2 are the corresponding peak widths. The constants L_1 and L_2 are the peak proportions of atoms lost due to each resonance. The measured resonance parameters are shown in table 5.5 alongside corresponding measurements and theoretical predictions of the B-field centres of the same two resonances obtained by other research groups [93, 101].
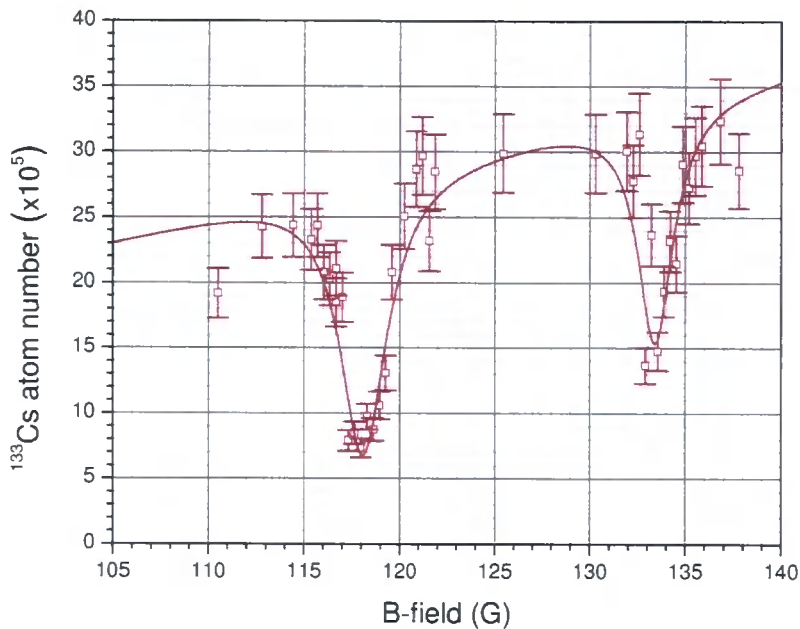
Figure 5.13: Number of ^{133}Cs atoms remaining in the magnetic trap following 105 s of evaporation to $\simeq 4$ μK as a function of magnetic field (red data points). The plotted magnetic field is that at which the cloud centre is situated for 20 s following a 10 s B-field ramp from the 166.50(6) G field at which evaporation takes place. The two loss features are fitted with Lorentzian profiles on a linear background (red line). The fitted line centres and widths (full-width at half maximum) of the two resonances are 118.06(5) and 133.4(1) G, and 3.0(3) and 2.3(5) G respectively.

(a) Durham measurements			(b) Comparison of resonance positions		
B (G)	γ (G)	Loss (%)	B_{Oxford}	B_{Stanford}	B_{Theory}
118.06(8)	2.9(3)	75(2)	118.46(3)	118.05(20)	118.57(2)
133.4(1)	2.2(5)	53(4)	133.52(3)	133.14(20)	133.48(2)

Table 5.5: Values for two ^{133}Cs inelastic Feshbach resonance B-field centres, B-field full-widths at half maximum loss, and maximum loss proportions due to resonances measured in the Durham apparatus (a). Also shown for comparison (b) are the B-field centres of the same two resonances measured in units of G at Oxford [93] (first column) and Stanford [101] (second column) along with theoretical values taken from reference [62] (third column).

5.5.1 ^{133}Cs Inelastic Collision Rate Coefficient

Assuming the dominant loss mechanism to be two-body inelastic collisions, and considering also the loss rate γ due to background collisions with residual gas molecules, the data of figure 5.13 is used to extract a value for the two-body inelastic collision rate coefficient $K_{2^{133}\text{Cs}^{133}\text{Cs}}$ in the expression:

$$\frac{\mathrm{d}N_{^{133}\text{Cs}}}{\mathrm{d}t} = -\gamma N_{^{133}\text{Cs}} - K_{2^{133}\text{Cs}^{133}\text{Cs}}\langle n_{^{133}\text{Cs}}\rangle N_{^{133}\text{Cs}} - \dots \quad , \qquad (5.26)$$

where $N_{^{133}\text{Cs}}$ and $\langle n_{^{133}\text{Cs}}\rangle$ are the number and mean number density of trapped ^{133}Cs atoms, both of which vary with time (see section 2.3.3). A small period of time δt after loading N_{on} atoms into the magnetic trap at a B-field centred upon a Feshbach resonance, the number of atoms remaining in the trap is:

$$N_{\text{on}}\left(t + \delta t\right) = N_{\text{on}}\left(t\right) \cdot \left(1 - \gamma\delta t - K_{2^{133}\text{Cs}^{133}\text{Cs}}\langle n_{^{133}\text{Cs}}\left(t\right)\rangle\delta t\right) \quad . \qquad (5.27)$$

In the absence of such a Feshbach resonance, the number of atoms remaining after a period δt is:

$$N_{\text{off}}\left(t + \delta t\right) = N_{\text{off}}\left(t\right) \cdot \left(1 - \gamma\delta t\right) \quad . \qquad (5.28)$$

In both cases the time period δt is assumed small in comparison to the 1/e atom lifetime in the magnetic trap. The ratio of equations 5.27 and 5.28:

$$\frac{N_{\text{on}}\left(t + \delta t\right)}{N_{\text{off}}\left(t + \delta t\right)} = \frac{N_{\text{on}}\left(t\right)}{N_{\text{off}}\left(t\right)}\left(1 - \frac{K_{2^{133}\text{Cs}^{133}\text{Cs}}\langle n_{^{133}\text{Cs}}\left(t\right)\rangle\delta t}{1 - \gamma\delta t}\right) \quad , \qquad (5.29)$$

gives the proportional loss of atoms during the period δt due to presence of the Feshbach resonance. After a total time T, the total proportional loss of atoms due to the Feshbach resonance is:

$$\frac{N_{\text{on}}(T)}{N_{\text{off}}(T)} = \frac{N_{\text{on}}(0)}{N_{\text{off}}(0)} \prod_{i=0}^{T/\delta t} \left(1 - \frac{K_{2^{133}\text{Cs}^{133}\text{Cs}} \langle n_{133\text{Cs}}(i\delta t)\rangle \delta t}{1 - \gamma\delta t}\right) \quad . \tag{5.30}$$

As $N_{\text{on}}(0) = N_{\text{off}}(0)$, and substituting the loss proportion $L = \frac{N_{\text{on}}(T)}{N_{\text{off}}(T)}$ into equation 5.30 gives:

$$L = \prod_{i=0}^{T/\delta t} \left(1 - \frac{K_{2^{133}\text{Cs}^{133}\text{Cs}} \langle n_{133\text{Cs}}(i\delta t)\rangle \delta t}{1 - \gamma\delta t}\right) \quad . \tag{5.31}$$

The value of the mean density term for each component of the product is approximated using the expression for number density in equation B.27 as:

$$\langle n_{133\text{Cs}}(i\delta t)\rangle \simeq \frac{\omega_r^2 \omega_z}{2\sqrt{2}} \left(\frac{m}{2\pi k_B T}\right)^{\frac{3}{2}} N_{\text{off}}(i\delta t) \cdot \left(\frac{N_{\text{on}}((i-1)\delta t)}{N_{\text{off}}((i-1)\delta t)}\right) \quad . \tag{5.32}$$

$$= \frac{\omega_r^2 \omega_z}{2\sqrt{2}} \left(\frac{m}{2\pi k_B T}\right)^{\frac{3}{2}} N_{\text{off}}(T) e^{\gamma(T-i\delta t)} \prod_{j=0}^{i-1} \left(1 - \frac{K_{2^{133}\text{Cs}^{133}\text{Cs}} \langle n_{133\text{Cs}}(j\delta t)\rangle \delta t}{1 - \gamma\delta t}\right) \quad . \tag{5.33}$$

For the two resonances identified in figure 5.13 taking $\gamma = 100$ s^{-1}, the values N_{off} from the linear background of the Lorentzian fit, temperatures T interpolated from data either side of each resonance and ω_r and ω_z calculated at the measured resonance B-field centres, the loss rate as a function of $K_{2^{133}\text{Cs}^{133}\text{Cs}}$ is evaluated. Setting the interval $\delta t = 0.5$ s, the loss proportions calculated from equation 5.31 are equal to those measured for the resonances at 118.06(5) and 133.4(1) G when the corresponding two-body inelastic collision rate coefficients are $1.1(1) \times 10^{-10}$ and $2.1(3) \times 10^{-11}$ cm^3 s^{-1} respectively. These estimates compare favorably with the rigourously measured values obtained in reference [93]. The reduction in sensitivity of the measured loss rates presented here due to the B-field width probed by the atoms ($\simeq 0.4$ G) is estimated to be $\leq 1\%$.

5.6 Two-Species Evaporation

Implementing evaporative cooling of ^{133}Cs in the single species magnetic trap increased the density by a factor of 10, allowing identification of two single

species ^{133}Cs Feshbach resonances. The density enhancement offered by the single species evaporation scheme for ^{87}Rb (table 5.2) results in only a very modest factor of two increase in the density, and hence sensitivity to single species resonances. Ideally simultaneous evaporation of both species could be implemented to produce a comparable enhancement in the ^{87}Rb atom number density to that of ^{133}Cs in the single species case, whilst maintaining the density gain achievable for ^{133}Cs alone. However, the sensitivity to interspecies resonances is dependent on many more parameters than just the individual species atom number densities (section 5.3.2). Hence the best way to test whether simultaneous evaporation will improve the experimental sensitivity to interspecies Feshbach resonances is to implement the scheme and measure the resulting sensitivity.

5.6.1 Implementation

After simultaneously loading $1.1(1) \times 10^8$ ^{87}Rb and $2.7(3) \times 10^8$ ^{133}Cs atoms into the magnetic trap using the 'push' loading technique, the evaporation trajectories for ^{87}Rb and ^{133}Cs shown in table 5.2 are simultaneously implemented. The resulting atom numbers and phase-space densities for both atomic species are shown in figure 5.14 a and b respectively. For the first five stages of simultaneous evaporation the radial ensemble temperature and number density for both atomic species follow power laws with the same form as those for evaporation in the single species trap (section 5.4.3):

$$\text{PSD} \propto N^{-\gamma} \quad , \tag{5.34}$$

$$T \propto N^{\alpha} \quad , \tag{5.35}$$

where γ and α are the evaporation efficiencies in terms of fractional increase in phase space density and fractional reduction in temperature per fraction of atoms removed from the trap. During the later evaporation stages the ^{87}Rb phase space density and radial temperature reach a plateau at $\simeq 6 \times 10^{-7}$ and $\simeq 10$ μK respectively. This is due to the relatively slow rate of ^{87}Rb evaporation in comparison to that of ^{133}Cs. The fitted evaporation efficiencies to the data of figure 5.14 for each atomic species in the single and two species magnetic trap are shown in table 5.6. Clearly the efficiency of ^{133}Cs
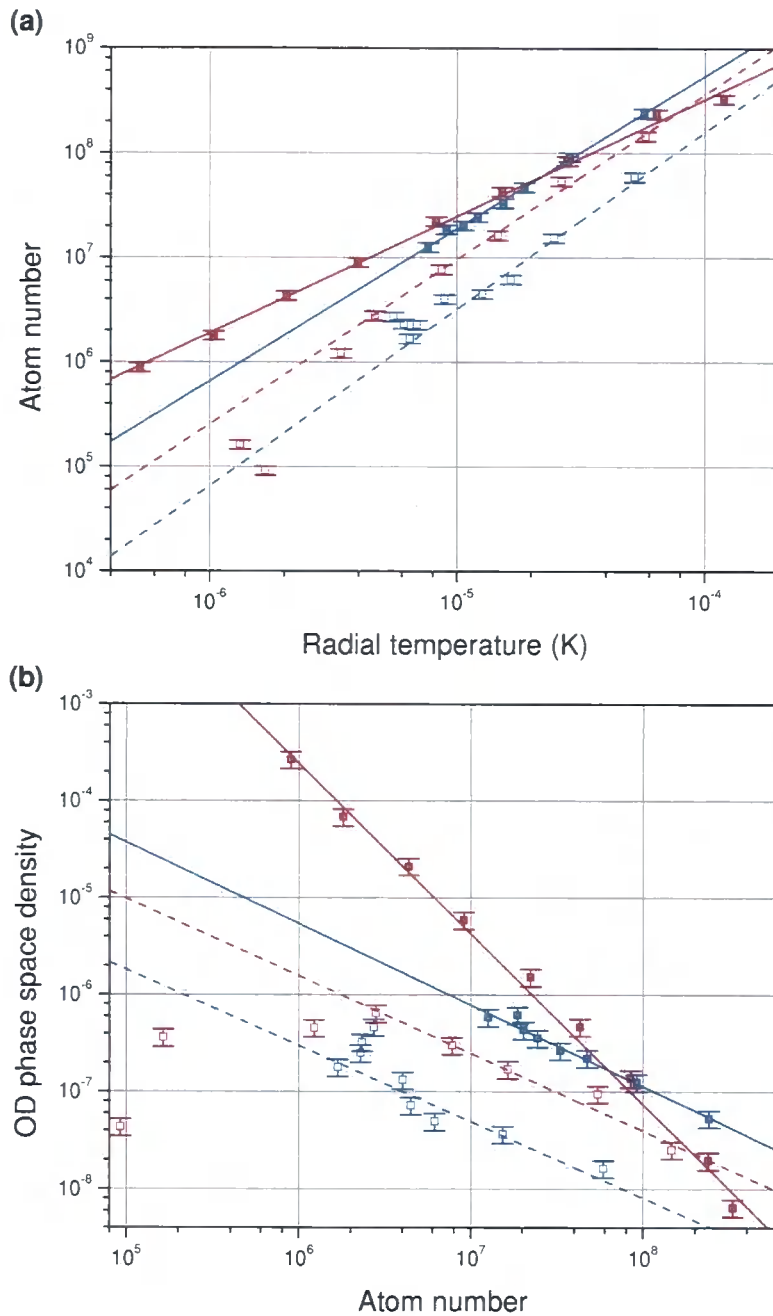
Figure 5.14: The atom number as a function of temperature (a) and phase-space density as a function of number (b) of ^{87}Rb (blue) and ^{133}Cs (red) atom clouds simultaneously evaporated in the magnetic trap following the trajectories of table 5.2 (hollow symbols). Also shown are the corresponding parameters for each species undergoing the same evaporation schemes in the single species trap (solid symbols) along with power-law fits to the single species data (solid lines) and the first five stages of evaporation for the two species data (dashed lines). Clearly the phase-space densities of both species are increased through simultaneous evaporation, however the presence of a second atomic species has a detrimental effect on the number and phase-space density parameters compared to the single species case.

evaporation during the first five evaporation stages is reduced by the presence of ^{87}Rb to be comparable with that of ^{87}Rb alone. This can be seen directly from the markedly different slopes of the single species ^{133}Cs data in figure 5.14 a and b in comparison to the ^{87}Rb alone and two-species curves, which have comparable gradients on the logarithmic scale. After the first five evaporation stages the different rates at which evaporation proceeds for the two atomic species result in consistently lower temperatures of evaporation 'cut' for ^{133}Cs than for ^{87}Rb. Effectively the ^{133}Cs ensemble becomes a heat sink for the ^{87}Rb atoms, maintaining the ^{87}Rb temperature sufficiently below that of the radio-frequency 'cut' to ensure no ^{87}Rb atoms are removed from the trap. As the number of ^{133}Cs atoms drops due to evaporation, the ratio of ^{87}Rb atoms to ^{133}Cs atoms increases (see figure 5.15). At a ^{133}Cs radio-frequency cut temperature of $\simeq 10$ μK this ratio exceeds one, hence below this temperature there are no longer enough ^{133}Cs atoms to absorb the thermal load due to the ^{87}Rb atoms. It is for this reason that simultaneous evaporative cooling following the trajectories of table 5.2 with initial loads of $1.1(1) \times 10^8$ ^{87}Rb and $2.7(3) \times 10^8$ ^{133}Cs atoms is not effective in reducing the phase space densities at temperatures below $\simeq 10$ μK.

	Single species		Two species	
	γ	α	γ	α
^{87}Rb	0.84(8)	0.69(3)	0.78(8)	0.59(3)
^{133}Cs	1.75(3)	0.89(1)	0.80(6)	0.63(3)

Table 5.6: Simultaneous evaporation efficiencies for ^{87}Rb and ^{133}Cs in the single and two species magnetic trap at a B-field at atom cloud centre of B=165.50(6) and B=166.70(6) G for ^{133}Cs and ^{87}Rb respectively. Efficiencies in terms of fractional gain in phase-space density per fraction of atoms removed from the trap (γ) and fractional reduction in temperature per fraction of atoms removed from the trap (α) are shown for the trajectories of table 5.2. The two species efficiencies are for the first five evaporation stages only.

This temperature may be reduced by modifying the evaporation trajectories to maintain temperature coherence of the two species throughout the evaporation process, or altering the ratio of atoms of each species initially loaded into the magnetic trap to reduce the thermal load upon the ^{133}Cs ensemble.
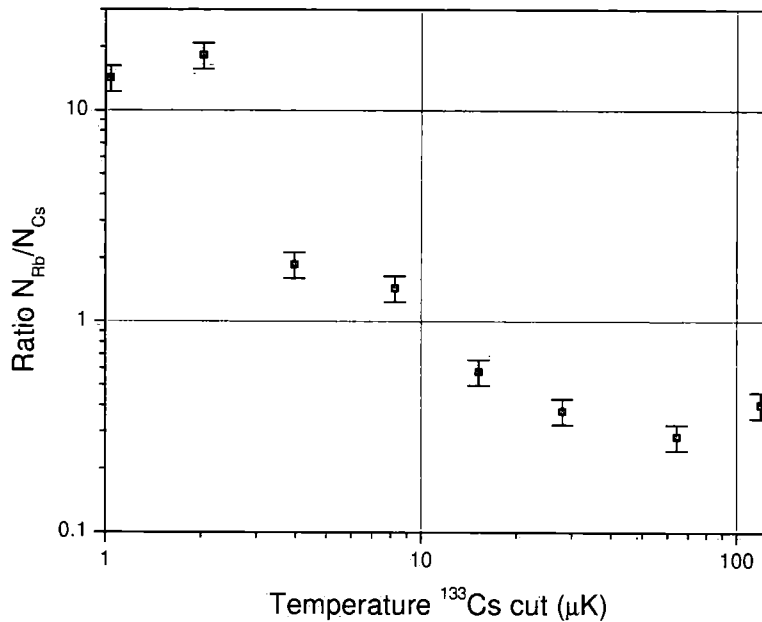
Figure 5.15: Ratio of number of trapped atoms of each species as a function of temperature of ^{133}Cs radio-frequency evaporation cut.

5.6.2   Two Species Magnetic Trap Lifetime

Prior to rigourously optimising the simultaneous evaporation scheme it is prudent to establish to what degree such evaporation enhances the apparatus sensitivity to interspecies resonances. Before embarking upon a Feshbach resonance search it is important to establish whether or not the magnetic field at which the trap is loaded corresponds to the position of a resonance. This is established through measuring the 1/e lifetimes of each atomic species in the two species magnetic trap following simultaneous evaporation. A significant reduction in the lifetime of either species compared to the background lifetime in the single species trap would indicate the presence of additional inelastic loss processes due to the presence of the second atomic species. The number

of atoms of each atomic species remaining in the magnetic trap as a function of time following simultaneous evaporation through five evaporation stages to a temperature of $\simeq 15~\mu$K is shown in figure 5.16. The fitted 1/e lifetimes for ^{87}Rb and ^{133}Cs atoms in the two species magnetic trap are 100(10) and 92(6) s respectively. These are within errors identical to the residual gas collision limited magnetic trap lifetimes for ^{87}Rb and ^{133}Cs in the single species magnetic trap of 86(9) and 103(1) s respectively. Hence there is no evidence of interspecies collisional losses at the loaded magnetic field of B=165.50(6) and B=166.70(6) G for ^{133}Cs and ^{87}Rb respectively.
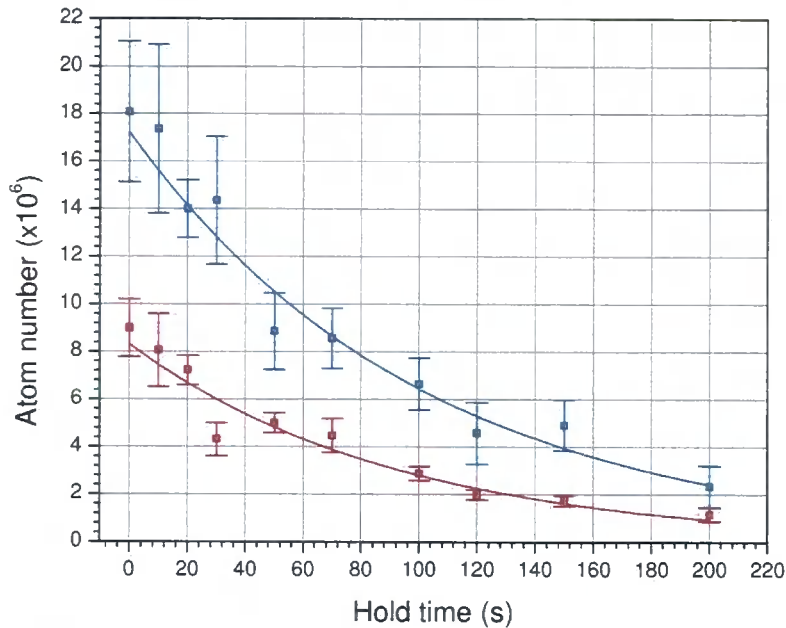
Figure 5.16: Number of ^{87}Rb (blue symbols) and ^{133}Cs (red symbols) atoms remaining in the two-species magnetic trap as a function of duration following simultaneous evaporation to a temperature of $\simeq 15~\mu$K. Exponential fits to these data give 1/e lifetimes of 100(10) and 92(6) s for ^{87}Rb (blue line) and ^{133}Cs (red line) respectively. These lifetimes are in agreement with the single species ^{87}Rb and ^{133}Cs 1/e lifetimes of 86(9) and 103(1) s respectively (section 5.2.2). The evaporation trajectory for ^{87}Rb implemented here is modified from that of table 5.2 to produce comparable optical depths of both atomic species following the fifth evaporation stage.

5.6.3 Thermalisation

One means by which the interspecies elastic collision cross section may be measured is through analysis of thermalisation rates for the two components of an atomic mixture [75]. For the magnetic trap lifetime data (figure 5.16) the radial and axial temperatures of the ^{87}Rb and ^{133}Cs ensembles are shown in figure 5.17 a and b respectively. Although there is little difference in the temperatures of the two atomic ensembles, there is evidence of thermalisation between the radial and axial components of temperature for both species. A simple thermalisation model assumes the axial temperature component T_{ax} remains constant whilst the radial temperature component increases as:

$$T_r = e^{-T/\tau_{th}}T_0 + \left(1 - e^{-T/\tau_{th}}\right) T_{ax} \quad , \tag{5.36}$$

where τ_{th} is the characteristic timescale for thermalisation and T_0 is the radial temperature immediately after evaporation. The thermalisation times for the data of figure 5.16 obtained using this model are shown in table 5.7, along with the calculated single species collision rates. As 2.7 elastic collisions are required to spatially mix the radial and axial components of an atoms energy [102], in the absence of interspecies collisions these thermalisation times should correspond to 2.7 times the elastic collision rate for each individual species. The fact that the number of single species collisions within this time scale is significantly below 2.7 for both species, suggests that the interspecies elastic collision rate is significantly greater than the single species rates.

Species	Thermalisation time (s)	Collision rate (Hz)	Collisions to thermalise
^{87}Rb	10.1(3)	0.041(7)	0.41(7)
^{133}Cs	10.2(4)	0.08(2)	0.8(2)

Table 5.7: Measured thermalisation times for the axial and radial components of ^{87}Rb and ^{133}Cs atom ensembles simultaneously held in the magnetic trap. The number of single species elastic collisions occurring during the thermalisation time is significantly below the 2.7 collisions required for thermalisation of the radial and axial components within a single species trap.
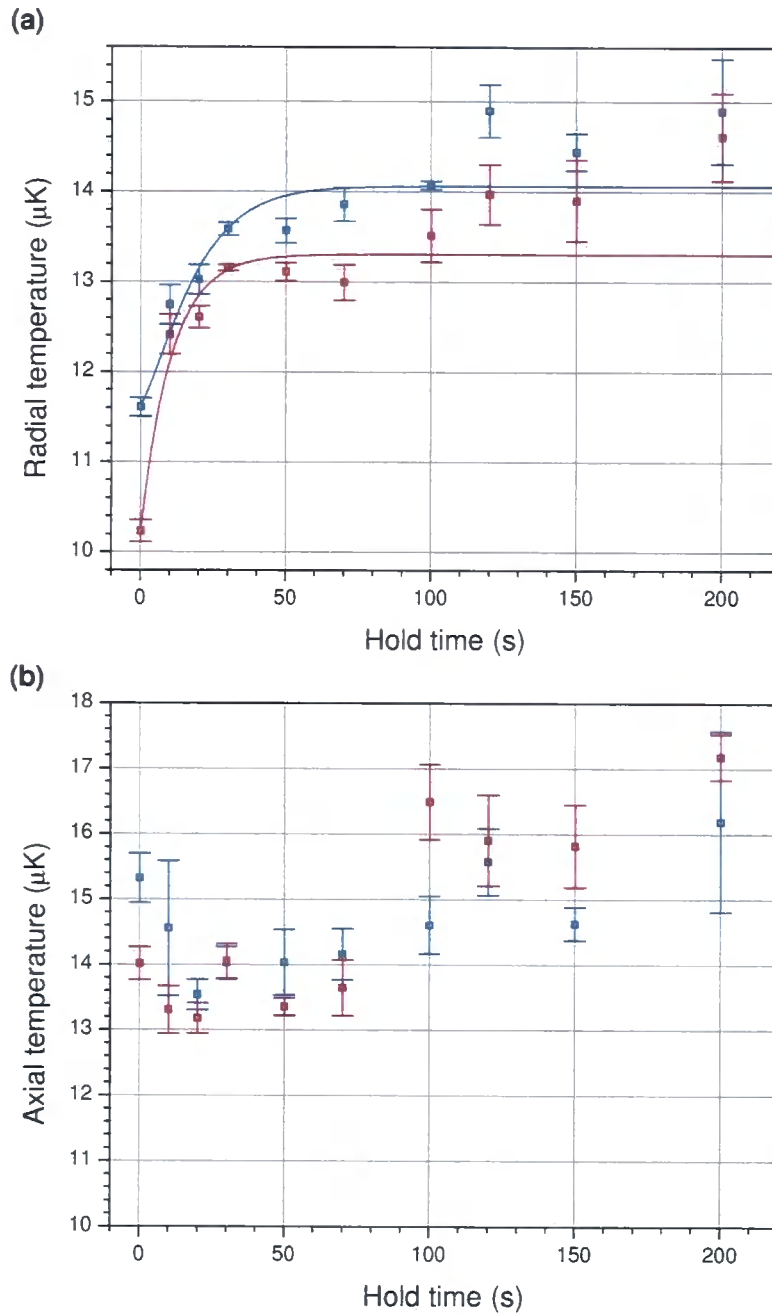
Figure 5.17: The radial (a) and axial (b) temperatures of simultaneously trapped ^{87}Rb (blue symbols) and ^{133}Cs (red symbols) atom clouds as a function of hold duration following simultaneous evaporation to a temperature of $\simeq 15\ \mu$K. Note the increase in radial temperature of each species towards the higher axial temperatures. Also shown are fits to the radial temperature components of ^{87}Rb (blue line) and ^{133}Cs (red line) assuming an exponential reduction in the number of atoms with radial temperature component equal to that at time $T = 0$, and a corresponding increase in the number with equal radial and axial temperature components such that the total atom number is conserved. The fitted $1/e$ thermalisation times for ^{87}Rb and ^{133}Cs are 10.1(3) and 10.2(4) s.

5.7 Feshbach Search at $T = 15$ μK

Having implemented simultaneous evaporation to successfully cool ^{87}Rb and ^{133}Cs to $\simeq 15$ μK and found no evidence of interspecies resonances at the magnetic trap loading field, a further interspecies resonance search was carried out at this reduced temperature. Following simultaneous evaporation of ^{87}Rb and ^{133}Cs to $\simeq 15$ μK the number of atoms of each species remaining as a function of the magnetic trap B-field at the end of a series of two B-field ramps is shown in figure 5.18. The data shows no B-field dependence of the losses of either atomic species over the range investigated. Following the discussion of section 5.3.2, the minimum changes in two-body inelastic interspecies collision rate constants to which the search for interspecies Feshbach resonances at $\simeq 15$ μK is sensitive are $K_{2^{87}\text{Rb}\ ^{133}\text{Cs}} \geq 6(1) \times 10^{-10}$ cm^3 s^{-1} and $K_{2^{133}\text{Cs}\ ^{87}\text{Rb}} \geq 5(1) \times 10^{-10}$ cm^3 s^{-1}. The parameters from which the estimates are calculated are presented in table 5.8. Despite increasing the duration of B-field ramp over which interrogation takes place, the net sensitivity is exactly the same as that obtained at $\simeq 100$ μK. This is due to a combination of effects: Although simultaneous evaporation of both atomic species successfully reduced the ensemble temperatures, the atom number densities of each species decreased. This is due primarily to the reduced efficiencies of the implemented two-species evaporative cooling scheme in comparison to those demonstrated when evaporating ^{133}Cs alone (section 5.6). The gravitational displacement of the two atom clouds also becomes comparable with their $1/e$ radii at the reduced temperature of 15 μK (figure 5.8), reducing the overlap factor to 0.3 at the upper B-field range investigated. The Feshbach search presented here also does not take full advantage of the reduced B-field width probed by the atomic ensembles at this lower temperature. A factor of $\simeq 6$ increase in sensitivity could be obtained through holding the trapped mixture at a fixed B-field for 50 s rather than ramping the field. This sensitivity increase is relatively minor in comparison to that which could be achieved through increasing the atomic densities prior to loading into the magnetic trap using a dark-spot MOT or Raman sideband cooling scheme however.
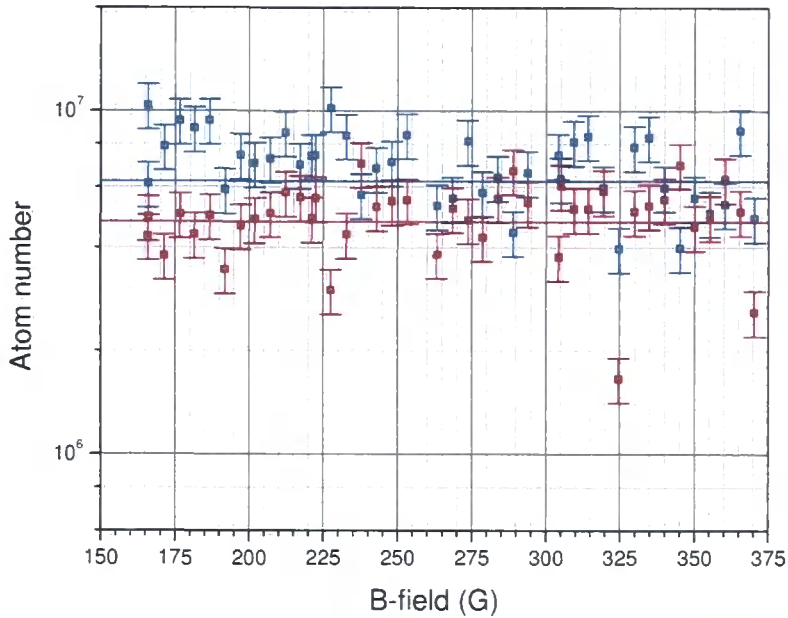
Figure 5.18: Number of ^{87}Rb (blue) and ^{133}Cs (red) atoms in the two-species magnetic trap following simultaneous evaporation to temperature $T \simeq 15\,\mu$K as a function of trap B-field at the end of two B-field ramps. After five stages of simultaneous radio-frequency evaporation at a B-field (at the ^{133}Cs cloud centre) of 165.50(6) G 2.2(3)$\times 10^7$ ^{87}Rb and 8(1)$\times 10^6$ ^{133}Cs atoms remain in the magnetic trap. The B-field is then ramped over a 5 s period to be 5 G away from that of the plotted B-field end point. A 50 s ramp across the 5 G interrogation field range then takes place before atom release and subsequent absorption imaging. Fitting the number of atoms of each species at the end of the B-field ramp to a constant value gives 6.3(1)$\times 10^6$ ^{87}Rb (blue line) and 4.8(1) $\times 10^6$ ^{133}Cs (red line) atoms respectively. Later investigation of regions of B-field around the four most outlying datum points confirmed these deviations to be statistical fluctuations.

(a) Single species ensemble properties

$N_{^{87}Rb}$ = 6.3(1)×10^6	$N_{^{133}Cs}$ = 4.8(1)×10^6
$n_{^{87}Rb\ pk}$ = 7.8(4)×10^8 **cm**$^{-3}$	$n_{^{133}Cs\ pk}$ = 1.20(4)×10^9 **cm**$^{-3}$
$T_{^{87}Rb}$ ≃ 15 μ**K**	$T_{^{133}Cs}$ ≃ 15 μ**K**

(b) Two-species properties

$\langle n_{^{133}Cs}\rangle_{^{87}Rb}$ = 3.6(2)×10^8 cm^{-3}	$\langle n_{^{87}Rb}\rangle_{^{133}Cs}$ = 4.0(3)×10^8 cm^{-3}
0.3 < $F_{^{133}Cs(^{87}Rb)}$ < 0.9	0.3 < $F_{^{87}Rb(^{133}Cs)}$ < 0.9
$B_{w^{87}Rb}$ = 1.5 G	$B_{w^{133}Cs}$ = 1.0 G

(c) Estimated maximum rate constants

$K_{2^{87}Rb\ ^{133}Cs}$ ≤ 6(1)×10^{-10} cm^3 s^{-1}	$K_{2^{133}Cs\ ^{87}Rb}$ ≤ 5(1)×10^{-10} cm^3 s^{-1}

Table 5.8: Interspecies Feshbach resonance search across the magnetic field range $166 < B < 370$ G at 15 μK measurement summary. The measured parameters of ^{87}Rb and ^{133}Cs atomic ensembles during the interspecies Feshbach resonance search of figure 5.18 are shown (a) together with the calculated two-species density, gravitational overlap, and full B-field width over which 90 % of each atomic ensemble is distributed (b) The gravitational overlap varies across the investigated B-field range from 0.9 at the lowest B-field range to 0.3 at the highest B-fields. From these data the sensitivity of the interspecies Feshbach search (comprised of a series of 50 s duration B-field ramps over 5 G intervals) is calculated (c).

Chapter 6

Conclusions and Outlook

Key results of the work detailed in this document are unified in the following pages, along with proposals for future directions of the project for which this work provides a foundation.

6.1   Summary of Presented Work

The achievements presented in this document are two-fold: the development of a robust and versatile apparatus for atomic and molecular ultracold physics, and the characterisation of interactions in an ultracold atomic mixture of ^{87}Rb and ^{133}Cs.

6.1.1   Apparatus Development

A robust apparatus has been developed in which up to 8×10^8 ^{87}Rb and 3×10^8 ^{133}Cs atoms can be independently loaded into a magnetic trap, with residual gas collision limited lifetimes of 100(10) seconds. A simple, novel, optical displacement technique is developed to spatially separate the trapping regions for each atomic species in the two-species science MOT, greatly enhancing the number of atoms which can be simultaneously loaded into the magnetic trap. The magnetic fields and oscillation frequencies for both atomic species at the magnetic trap centre are precisely calibrated allowing accurate determination of ensemble properties through implemented two species frame

transfer absorption imaging, and complimentary calibrated dichroic fluorescence imaging diagnostics. Throughout the construction and optimisation of this apparatus consideration of possible future developments including optical dipole trapping and optical lattice loading has ensured the optical access afforded to the science region of the apparatus is maximised. Hence the general apparatus developed in this work promises to serve this project through to the realisation of quantum degenerate dipolar gases and beyond.

6.1.2 Mixture Characterisation

The ^{87}Rb-^{133}Cs mixture is subject to strong light assisted interspecies collisional losses in a magneto-optical trap, whilst interspecies elastic collisions form the dominant thermalisation route in the magnetically trapped mixture. Clearly ^{87}Rb and ^{133}Cs atoms display interspecies interactions in both trapping regimes. There is, however, no evidence of an interspecies Feshbach resonance within the present apparatus sensitivity range. The differential gravitational sag of the mixture is found to severely limit the magnetic field range over which the two atomic components are coincident at low temperatures. This effect may limit the suitability of atom traps incorporating magnetic levitation in the field of ultracold mixtures and molecules. Efficient evaporative cooling of ^{133}Cs allowed the detection of Feshbach resonances at 118.06(8) G and 133.4(1) G, consistent with measurements made in other experiments. Although simultaneous evaporative cooling of both species following the optimised single species trajectories did not prove favorable, the presence of a significant interspecies elastic collision rate may offer a means by which to improve the evaporative cooling efficiencies for the atomic mixture.

6.2 Project Outlook

During the course of this work many advances have been made in the field of ultracold mixtures and molecules. ^{87}Rb-^{133}Cs is presently a frontrunner in the race towards dipolar molecular Bose-Einstein condensation. It is therefore imperative that the foundations laid in this work are followed by a concerted effort to implement the latest developments within this project.

6.2.1 Project Direction

The recent observation of 23 interspecies Feshbach resonances between ^{87}Rb atoms in the $F = 1$, $m_F = +1$ state and ^{133}Cs atoms in the $F = 3$, $m_F = +3$ state [100], combined with the fact that so far ^{133}Cs has only been condensed in this spin configuration, makes trapping in this combination of absolute ground states highly appealing. Atoms trapped in these states are 'high magnetic field seeking', hence magnetic trapping of this mixture is impossible. Replacing the magnetic trap in the present apparatus with an optical dipole trap would allow this spin combination to be trapped, whilst offering many key advantages, notably trapping frequencies of several kHz (compared to a few hundred Hz radial trapping frequency for a 'tight' Ioffe-Pritchard trap) leading to greatly increased atom number densities and hence elastic collision rates compared to those achievable in a purely magnetic trap. A promising evaporation scheme (which has been used to condense ^{133}Cs) for a mixture within an optical dipole trap is that in which an applied magnetic field gradient effectively 'tilts' the trapping potential to evaporate atoms with minimal reduction in trapping frequency [103]. Following efficient evaporation and adiabatically ramping across an interspecies Feshbach resonance the immediate challenge will be to transfer the ^{87}Rb^{133}Cs vibrationally excited molecules into the rovibrational ground state. Creation of ground state ^{87}Rb^{133}Cs molecules has already been achieved from atoms in a forced Dark SPOT MOT [55], whilst the coherent transfer STIRAP process is expected to have favorable Franck-Condon factors for transfer of Feshbach molecules into the rovibrational ground state [60].

6.2.2 Apparatus Improvements

Although the present apparatus has provided an excellent starting point for the investigation of an ultracold ^{87}Rb-^{133}Cs mixture, implementation of optical trapping will require a significant degree of modification of the apparatus. During this conversion phase a number of modifications to the current apparatus will be carried out, primarily to improve the laser frequency stability [88], and allow access to a greater magnetic field range than is presently realisable (notably to allow access to the predicted broad ^{133}Cs Feshbach

resonance at $\simeq 800$ G). Increasing the atom number density for both atomic species is also a high priority, as high number densities combined with high trapping frequencies should significantly improve the apparatus sensitivity to interspecies Feshbach resonances. This may be achieved through the implementation of a dark SPOT MOT, or two species Raman sideband cooling [100] (or both). In parallel to these improvements, a considerable degree of work must be focussed on the frequency stabilisation of lasers required for the Raman transfer scheme [58].

6.3 Concluding Remarks

Establishing a leading experiment in such a rapidly moving and increasingly complex field as ultracold molecular physics is no mean feat. The rapid dissemination of information and exceedingly high work ethic which permeates atomic physics research is refreshing, exciting, and at times intimidating, with the speed at which research is advancing being a testament to the constructive nature of such close collaboration and collective effort towards common goals. Given the nature of Bose-Einstein condensation this is certainly fitting. Recent breakthroughs in the realisation of ultracold polar molecules have been driven by the desire to penetrate ever deeper into the mysterious world of quantum phenomena, the world in which we all live, even if we don't always realise it.

Appendix A

Optical Components and Polarisation

This appendix contains a brief description of some of the more exotic optics used in this apparatus along with the definition of polarisation to avoid ambiguity.

A.1   Polarisation

The plane of polarisation is defined here as the plane which contains the light beams (figure A.1).

A.2   Acousto-optic Modulators (AOMs)

All acousto-optic modulators used in this apparatus are manufactured by Crystal Technology, Inc. Model 3110-120. The operational centre frequency is 110 MHz with a bandwidth of 24 MHz and active area 2.4 mm 'L' × 0.6 mm 'H'. Each AOM is set up paying close attention to the details in reference [104], notably matching the focused incident beam waist diameter with that specified in the datasheet and the focussed beam geometry with the geometry of the modulators active area.
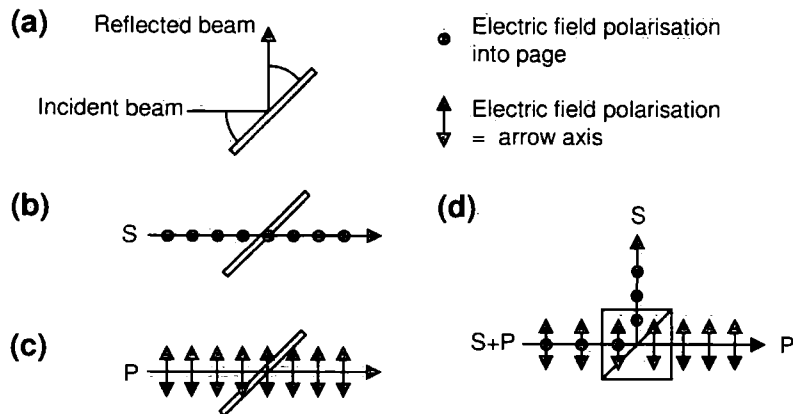
Figure A.1: Linearly polarised light incident on an optical component can split into components with electric field oscillating parallel to the plane of beam incidence (P-polarised light) and perpendicular to the plane of beam incidence (S-polarised light). The plane of beam incidence is the plane in which the beams incident on, and reflected from, an optical component lie. In (a) the optical plane is the plane of this paper. S and P-polarised light are shown in (b) and (c) respectively. An ideal composite polarising beamsplitter cube with dielectric coating on the diagonal axis is shown in (d) to transmit P-polarised light whilst rejecting S-polarised light. Calcite cubes have the opposite behavior.

A.3 Faraday Rotators and Optical Isolators

Faraday rotators employ the Faraday effect [105] in which the axis of linearly polarised light passing through a material with a high Verdet constant in the presence of a magnetic field is rotated in one sense for light traveling parallel to the applied B-field, and in the opposite sense for light traveling anti-parallel to the applied field. The degree of rotation is proportional to the materials Verdet constant, the length of high Verdet constant material and the magnitude of the applied B-field. Thus vertically polarised light after passing through a Faraday rotator set to produce a 45° polarisation rotation, if reflected back into the Faraday rotator will undergo an additional 45° rotation. Hence the reflected light, having passed through the Faraday rotator twice, will be horizontally polarized. Optical isolation is achieved when a pair of polarizers are used in conjunction with a 45° Faraday rotator,

with one at the rotator input and one at the output, both aligned such that light entering the Faraday rotator input with a single linear polarisation is rejected by neither polarizer. Any light entering the transmission port of the output polarizer will be entirely rejected from the isolator assembly.

A.4 Optical Fibres

All optical fibres used in this apparatus are polarisation maintaining single mode with a collimation lens fixed to the fibre input (a 'pigtail' style connector) and an FC system fibre coupler output with both ends of the fibre cleaved and polished at 3.7° to minimise back-reflection. Light is collimated into each fibre coupler using a telescope, routinely achieving coupling efficiencies >70 %. Polarisation purity of the optical fibre output in excess of 21 dB is achieved when the axis of linearly polarised input light is aligned with either the slow or fast axis of the fibre to within $\simeq 0.5°$. Multiple laser beams can simultaneously be coupled into both perpendicular axes of each fibre whilst maintaining individual polarisations in this manner. Strain induced in fibres may result in rotation of polarisation, hence it is important to ensure fibres are fixed securely and the manufacturer's minimum bend radius is adhered to. Fibres used in this apparatus are secured within sections of electrical trunking using adhesive tape.

A.5 Dichroic Beam-splitters

The dichroic beam splitters used in this apparatus, produced by Laseroptik GmbH, transmit light at 780 nm with 98.7(3)% efficiency whilst reflecting that at 852 nm with 99.97(2)% efficiency at an angle of incidence of 45°. This is the case for both S and P polarised light. Stress on the optic can induce significant birefringence, leading to a rotation in the polarisation of light transmitted through it. In order to achieve transmitted polarisation purity in excess of 24 dB it is essential to mount the dichroic beam-splitter in a non-stressing mount (*i.e.*, evenly securing with a retaining ring rather than a stess-inducing locking screw).

Appendix B

Atom Number Calculations

This appendix contains derivations of the expressions used to calculate properties of trapped atom clouds. Section B.1 details calculations relating to atomic fluorescence detection, whilst those used to extract ensemble properties from imaged absorption of a probe beam are presented in section B.2.

B.1   Fluorescence Detection

The power emitted by N two-level atoms[1] illuminated with light of intensity I is:

$$P_{\text{total}} = N \cdot \frac{hc}{\lambda} \cdot \Gamma_{\text{scat}} = N \cdot \frac{hc}{\lambda} \cdot \frac{\Gamma}{2} \frac{\left(\frac{I}{I_S}\right)}{1 + 4(\frac{2\pi\delta}{\Gamma})^2 + \left(\frac{I}{I_S}\right)} \quad , \tag{B.1}$$

where δ is the laser detuning from resonance in MHz, $\Gamma = 1/\tau$ is the natural decay rate of the excited state in radians per second, the intensity is the *total* laser intensity at the atoms (*i.e.* 6 times that of a single MOT beam) and I_S is the saturation intensity defined:

$$I_S = \frac{I}{2} \left(\frac{\Gamma}{\Omega_{\text{Rabi}}}\right)^2 = \frac{\pi h c \Gamma}{3\lambda^3} \quad . \tag{B.2}$$

---

[1] This two-level atom approximation can be improved by including effective Clebsch-Gordan coefficients averaged over all Zeeman sublevels in the I/I_S terms. These coefficients are best determined experimentally, however, and depend on the MOT parameters of the particular setup. The values measured by Townsend *et al.* for ^{133}Cs [106] result in an atom number of $\simeq 1.4 \times$ that calculated using this basic two-level approach.
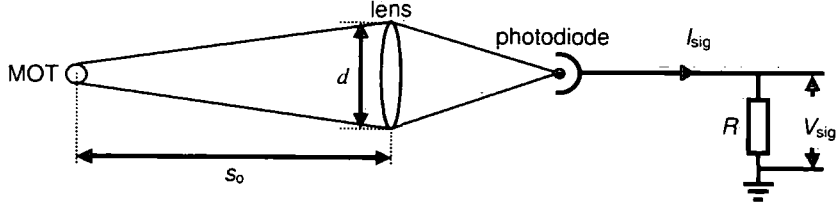
Figure B.1: Fluorescence detection setup. d is the diameter of a lens at distance s_o from the atom cloud. I_{sig} is the photocurrent which produces a voltage V_{sig} across a load resistance R.

The power collected within a solid angle Ω:

$$P_{\text{det}} = \frac{\Omega}{4\pi} \cdot P_{\text{total}} = \frac{1}{4\pi} \cdot \frac{\pi(d/2)^2}{s_o^2} \cdot P_{\text{total}} = \frac{d^2}{16 s_o^2} \cdot P_{\text{total}} \quad , \qquad (B.3)$$

incident on a detector of responsivity $\mathcal{R}(\lambda)$ produces a voltage across a load resistance R:

$$V_{\text{sig}} = I_{\text{sig}} \cdot R = \mathcal{R}(\lambda) P_{\text{det}} \cdot R \quad . \qquad (B.4)$$

Rearranging to give the number of atoms as a function of the measured voltage yields:

$$N = \frac{1}{\mathcal{R}(\lambda) R} \cdot \frac{16 s_o^2}{d^2} \cdot \frac{\lambda}{hc} \cdot \frac{V_{\text{sig}}}{\Gamma_{\text{scatt}}} \qquad (B.5)$$

The parameters of the Durham MOT are:

	^{133}Cs (6^2S$_{1/2} \rightarrow 6^2$P$_{3/2}$)	^{87}Rb (6^2S$_{1/2} \rightarrow 6^2$P$_{3/2}$)	units
I	$6 \times 2.06(4) = 12.7(1)$	$6 \times 2.28(7) = 13.7(4)$	mW cm^{-2}
Δ	$2\pi \cdot 10.5(2)$ MHz	$2\pi \cdot 12.2(2) MHz$	rad s^{-1}
L	176(1)	176(1)	mm
d	28.0(1)	28.0(1)	mm
$\mathcal{R}$	0.54(1)	0.49(1)	A W^{-1}
R	1.000	1.000	MΩ
N	$1.5(3) \times 10^6$	$1.5(2) \times 10^6$	Atoms mV^{-1}

Table B.1: Experimental parameters for ^{87}Rb and ^{133}Cs fluorescence detection.

B.2 Absorption Imaging

The number distribution of atoms as a function of position within a trapped cloud is calculated from the optical depth distribution, where the optical depth (OD) is a measure of the attenuation of an incident probe beam's intensity (here propagating along the y axis) due to the presence of a column of atoms along the propagation axis:

$$I_\mathrm{T}(x, z) = I_0(x, z) \, e^{-\mathrm{OD}(x,z)} \quad , \tag{B.6}$$

where $I_0(x, z)$ is the incident probe laser beam intensity distribution and $I_\mathrm{T}(x, z)$ is the distribution of the laser beams intensity after attenuation by the atom cloud. Thus from each processed absorption image, an optical depth distribution of the form:

$$\mathrm{OD}(x, z) = \ln\left(\frac{I_0(x, z)}{I_\mathrm{T}(x, z)}\right) \quad , \tag{B.7}$$

is obtained. Extracting 'real' parameters of the atom cloud (*i.e.* atom number, atom number density, temperature *etc.*) from such a distribution requires the application of Gaussian statistics in combination with calculation of atomic absorption rates, as described below. Also included is a description of the use of three images to accurately extract the optical depth distribution profile for each atomic species.

B.2.1 Gaussian Statistics

Modeling a cloud of atoms of mass m at temperature T confined in a three dimensional harmonic potential with trap frequencies ω_x, ω_y and ω_z along the x, y and z axes of the trap respectively as a classical gas, the atom number density as a function of position follows a Gaussian distribution:

$$n(x, y, z) = n_\mathrm{pk} \exp\left[\frac{-m}{2k_\mathrm{B}T}\left(\omega_x{}^2 x^2 + \omega_y{}^2 y^2 + \omega_z{}^2 z^2\right)\right] \quad , \tag{B.8}$$

where n_pk is the number density at the trap centre (the peak number density). Integrating equation B.10 across all space the total number of atoms contained in the cloud (N) is obtained as:

$$N = \int_{-\infty}^{\infty}\int_{-\infty}^{\infty}\int_{-\infty}^{\infty} n(x, y, z) \, \mathrm{d}x \, \mathrm{d}y \, \mathrm{d}z = n_\mathrm{pk}\left(\frac{2\pi k_\mathrm{B}T}{m}\right)^{\frac{3}{2}} \cdot \frac{1}{\omega_x \omega_y \omega_z} \quad . \tag{B.9}$$

Conversely from the total number of trapped atoms, the peak number density is calculated as:

$$n_{\text{pk}} = N\omega_x\omega_y\omega_z \left(\frac{m}{2\pi k_{\text{B}}T}\right)^{\frac{3}{2}} \quad . \tag{B.10}$$

The widths of the Gaussian distribution along the x, y and z axes are σ_x, σ_y and σ_z respectively, corresponding the the displacements along each axis at which the number density drops to $n_{\text{pk}} \cdot e^{-1/2}$:

$$m\omega_x{}^2\sigma_x{}^2 = k_{\text{B}}T \quad , \tag{B.11}$$

$$m\omega_y{}^2\sigma_y{}^2 = k_{\text{B}}T \quad \text{and} \tag{B.12}$$

$$m\omega_z{}^2\sigma_z{}^2 = k_{\text{B}}T \quad . \tag{B.13}$$

Thus by measuring the total number of trapped atoms and the width of the number density distribution along each axis the number density and ensemble temperatures may be extracted.

B.2.2 Calculation of Atom Ensemble Parameters

The number of photons absorbed per second from an incident probe laser beam of intensity I mW cm^{-2} by an atom is:

$$\Gamma_{\text{scatt}} = \frac{\Gamma}{2} \frac{\left(\frac{I}{I_{\text{S}}}\right)}{1 + 4(\frac{2\pi\delta}{\Gamma})^2 + \left(\frac{I}{I_{\text{S}}}\right)} \quad , \tag{B.14}$$

where δ is the laser detuning from resonance in MHz, $\Gamma = 1/\tau$ is the natural decay rate of the excited state in radians per second, and I_{S} is the saturation intensity defined in equation B.2. For a resonant laser beam of intensity $I << I_{\text{S}}$ the scattering rate per atom is approximated as:

$$\Gamma_{\text{scatt}} = \frac{\Gamma}{2} \cdot \frac{I}{I_{\text{S}}} = \frac{3\lambda^3}{2\pi hc}I \quad . \tag{B.15}$$

After transmission through a layer of atoms of thickness δy and number density n the laser beam intensity transmitted by the atom layer will be $I = I + \delta I$, where (substituting Γ_{scatt} from equation B.15):

$$\delta I = -n\delta y \Gamma_{\text{scatt}}\frac{hc}{\lambda} = -\frac{3\lambda^2}{2\pi}nI\delta y \quad . \tag{B.16}$$

For a Gaussian atom cloud with number density distribution of equation B.10, rearranging equation B.16 gives:

$$-\frac{\delta I}{I} = \frac{3\lambda^2}{2\pi} n_{\text{pk}} \exp\left[\frac{-m}{2k_{\text{B}}T}\left(\omega_x^2 x^2 + \omega_y^2 y^2 + \omega_z^2 z^2\right)\right]\delta y \quad . \tag{B.17}$$

In the limit of $\delta y \to 0$, $\delta I \to 0$ summing equation B.17 over the full thickness of the Gaussian cloud gives:

$$\int_{I_0(x,z)}^{I_{\text{T}}(x,z)} -\frac{1}{I}\mathrm{d}I = \frac{3\lambda^2}{2\pi}n_{\text{pk}}\exp\left[\frac{-m}{2k_{\text{B}}T}\left(\omega_x^2 x^2 + \omega_z^2 z^2\right)\right]\int_{-\infty}^{\infty}\exp\left[\frac{-m}{2k_{\text{B}}T}\omega_y^2 y^2\right]\mathrm{d}y, \tag{B.18}$$

$$\Rightarrow \quad \ln\left(\frac{I_0(x,z)}{I_{\text{T}}(x,z)}\right) = \frac{3\lambda^2 n_{\text{pk}}}{\omega_y}\exp\left[\frac{-m}{2k_{\text{B}}T}\left(\omega_x^2 x^2 + \omega_z^2 z^2\right)\right]\sqrt{\frac{k_{\text{B}}T}{2\pi m}} \quad , \tag{B.19}$$

where $I_0(x,z)$ and $I_{\text{T}}(x,z)$ are the intensity profiles of the probe laser beam incident upon the atom cloud, and the laser beam transmitted by the cloud respectively. Combining equations B.7 and B.19, the optical depth distribution in the image is shown to be:

$$\text{OD}(x,z) = \frac{3\lambda^2 n_{\text{pk}}}{\omega_y}\exp\left[\frac{-m}{2k_{\text{B}}T}\left(\omega_x^2 x^2 + \omega_z^2 z^2\right)\right]\sqrt{\frac{k_{\text{B}}T}{2\pi m}} \quad . \tag{B.20}$$

The maximum optical depth (OD_{pk}) will occur at the centre of the atom cloud ($x = z = 0$):

$$\text{OD}_{\text{pk}} = \frac{3\lambda^2 n_{\text{pk}}}{\omega_y}\sqrt{\frac{k_{\text{B}}T}{2\pi m}} \quad . \tag{B.21}$$

The displacements along each axis of the image plane at which the optical depth drops to $\text{OD}_{\text{pk}}\cdot e^{-1/2}$ are equal to those at which the number density drops to $n_{\text{pk}}\cdot e^{-1/2}$, *i.e.* the widths of the number density distribution along each axis of the image plane (equations B.11 and B.13) are exactly equal to fitted widths of the optical depth distribution.

Substituting into equation B.21 the expression for n_{pk} given in equation B.10 gives:

$$\text{OD}_{\text{pk}} = \frac{3\lambda^2 N}{4\pi^2}\cdot\frac{m\omega_x\omega_z}{k_{\text{B}}T} \quad . \tag{B.22}$$

Substituting ω_x and ω_z from equations B.11 and B.13 this becomes:

$$\text{OD}_{\text{pk}} = \frac{3\lambda^2 N}{4\pi^2}\cdot\frac{1}{\sigma_x\sigma_z} \quad . \tag{B.23}$$

Conversely, from the measured peak optical depth and fitted $e^{-1/2}$ widths of the optical depth distribution in the image plane (σ_x and σ_z), the number of trapped atoms is calculated as:

$$N = \frac{2\pi \mathrm{OD_{pk}}\sigma_x\sigma_z}{\sigma_0} \quad , \tag{B.24}$$

where $\sigma_0 = 3\lambda^2/2\pi$. As the fitted width along both imaged axes of the optical depth distribution are equal to those of the number density distribution (σ_x and σ_z), the temperature of the atomic sample along each imaged axis of the trap is calculated (from equations B.11 and B.13) as:

$$T_x = \frac{m\omega_x^2\sigma_x^2}{k_\mathrm{B}} \quad \text{and} \tag{B.25}$$

$$T_z = \frac{m\omega_z^2\sigma_z^2}{k_\mathrm{B}} \quad . \tag{B.26}$$

Finally, for the geometry of the baseball magnetic trap which (neglecting gravity) is cylindrically symmetric, with radial trap frequency $\omega_r=\omega_y=\omega_z$, equation B.22 becomes:

$$n_\mathrm{pk} = N\omega_r^2\omega_z \left(\frac{m}{2\pi k_\mathrm{B}T}\right)^{\frac{3}{2}} \quad , \tag{B.27}$$

where the radial and axial temperatures are:

$$T_r = \frac{m\omega_r^2\sigma_r^2}{k_\mathrm{B}} \quad \text{and} \tag{B.28}$$

$$T_\mathrm{ax} = \frac{m\omega_z^2\sigma_z^2}{k_\mathrm{B}} \quad . \tag{B.29}$$

Appendix C

Magnetic Coil Design

C.1 Coil Configuration

C.1.1 Single Coil

A current I passing through a single circular loop of wire produces a magnetic field along the central axis of the loop:

$$B_z = \frac{\mu_0 I R^2}{2\left(R^2 + z^2\right)^{3/2}} \quad , \tag{C.1}$$

where R is the radius of the loop, z is the axial distance from the centre of the loop and μ_0 is the magnetic permeability of free space. By increasing the number of loops of wire (turns) of a single coil, the magnetic field produced by the coil is increased proportionally (assuming for the moment that all turns have identical radial and axial paths). The magnetic field produced by a single coil with N turns is then:

$$B_z = \frac{\mu_0 N I R^2}{2\left(R^2 + z^2\right)^{3/2}} \quad , \tag{C.2}$$

whilst the first three derivatives of magnetic field with respect to axial distance (B-field gradient, curvature, and third derivative respectively) are:

$$\frac{\partial B_z}{\partial z} = \frac{-3\mu_0 N I R^2 z}{2 \left(R^2 + z^2\right)^{5/2}} \quad , \tag{C.3}$$

$$\frac{\partial^2 B_z}{\partial z^2} = \frac{-3\mu_0 N I R^2}{2 \left(R^2 + z^2\right)^{5/2}} \left(1 - \frac{5z^2}{R^2 + z^2}\right) \quad , \tag{C.4}$$

$$\frac{\partial^3 B_z}{\partial z^3} = \frac{15\mu_0 N I R^2 z}{2 \left(R^2 + z^2\right)^{7/2}} \left(3 - \frac{7z^2}{R^2 + z^2}\right) \quad . \tag{C.5}$$

C.1.2 Coil Pair: Same Sense

The magnetic field produced by a single coil is a maximum at the coil centre and drops by 10% at an axial distance $z \simeq 0.27R$. A far more uniform magnetic field can be generated using an identical pair of coils axially separated by a distance S with the current through both coils passing in the same sense. The magnetic field along the axis of a pair of coils positioned at $z = \pm\frac{S}{2}$ is:

$$B_z = \frac{\mu_0 N I R^2}{2 \left(R^2 + \left(z + \frac{S}{2}\right)^2\right)^{3/2}} + \frac{\mu_0 N I R^2}{2 \left(R^2 + \left(z - \frac{S}{2}\right)^2\right)^{3/2}} \quad , \tag{C.6}$$

which at the centre of the coil pair (point P) simplifies to:

$$B_z|_P = \frac{\mu_0 I N R^2}{\left(R^2 + \left(\frac{S}{2}\right)^2\right)^{3/2}} \quad . \tag{C.7}$$

The B-field gradient and third derivative at the centre of the coil pair is zero due to the coil symmetry, whilst the B-field curvature is:

$$\left.\frac{\partial^2 B_z}{\partial z^2}\right|_P = \frac{-3\mu_0 I N R^2}{\left(R^2 + \left(\frac{S}{2}\right)^2\right)^{5/2}} \left(1 - \frac{5\left(\frac{S}{2}\right)^2}{R^2 + \left(\frac{S}{2}\right)^2}\right) \quad . \tag{C.8}$$

This is reduced to zero, and hence the B-field is most uniform, for coils in the Helmholtz configuration:

$$\boxed{\text{Helmoholtz condition: } S = R \quad .} \tag{C.9}$$

The magnetic field uniformity of same-sense coil pairs in the Helmholtz configuration can be found in table C.1.

$\delta B(B_{\mathrm{max}})$	Helmholtz $(S = R)$	Anti-Helmholtz $(S = \sqrt{3}R)$ (reversed)	Max gradient $(S = \sqrt{6}R)$ (reversed)
	z/S	z/S	z/S
0.1 %	± 0.173	± 0.055	± 0.071
0.5 %	± 0.262	± 0.124	± 0.158
1.0 %	± 0.314	± 0.176	± 0.224
5.0 %	± 0.488	± 0.399	± 0.500
10.0 %	± 0.602	± 0.578	± 0.706

Table C.1: The axial distance over which the B-field produced by a current passing through a pair of identical axially separated coils is uniform to a given percentage of the maximum value. The calculated distance is for currents passing in the same sense in coil pairs separated by distances associated with the Helmholtz, anti-Helmholtz, and maximum gradient at fixed separation geometries.

C.1.3 Coil Pair: Opposite Sense

An identical pair of coils axially separated by a distance S positioned at $z = \pm \frac{S}{2}$ with the current through both coils passing in the opposite sense produces a magnetic field:

$$B_z = \frac{\mu_0 I R^2}{2 \left(R^2 + \left(z + \frac{S}{2} \right)^2 \right)^{3/2}} - \frac{\mu_0 I N R^2}{2 \left(R^2 + \left(z - \frac{S}{2} \right)^2 \right)^{3/2}} \quad , \qquad (C.10)$$

which at the centre of the coil pair (point P) is equal to zero due to coil symmetry. The B-field gradient at point P is:

$$\left. \frac{\partial B_z}{\partial z} \right|_{\mathrm{P}} = \frac{-3 \mu_0 I N R^2 \left(\frac{S}{2} \right)}{\left(R^2 + \left(\frac{S}{2} \right)^2 \right)^{5/2}} \qquad (C.11)$$

Uniform Gradient

The curvature and fourth derivative of B-field at the centre of an identical pair of coils with identical currents running in the opposite sense is zero due

Geometry	R/S	$B_{\max}$
Helmholtz	1	1
Anti-Helmholtz (reversed)	$\frac{1}{\sqrt{3}}$	$\frac{5}{7}\sqrt{\frac{15}{7}} \simeq 1.05$
Maximum gradient (reversed)	$\frac{1}{\sqrt{6}}$	$\frac{\sqrt{3}}{2} \simeq 0.87$

Table C.2: Relative size of B-Field at the centre of coil pairs with identical separated and currents passing in the same sense for the Helmholtz, anti-Helmholtz, and maximum gradient at fixed separation geometries. The B-field gradients are expressed relative to that generated by a pair of coils configured to produce the maximum gradient at a fixed separation.

to coil symmetry. The 3rd derivative of magnetic field at the centre of the coil pair is:

$$\left.\frac{\partial^3 B_z}{\partial z^3}\right|_P = \frac{15\mu_0 I N R^2 \left(\frac{S}{2}\right)}{\left(R^2 + \left(\frac{S}{2}\right)^2\right)^{7/2}} \left(3 - \frac{7\left(\frac{S}{2}\right)^2}{R^2 + \left(\frac{S}{2}\right)^2}\right) \quad . \tag{C.12}$$

This is equal to zero, and hence the most uniform gradient is produced, when the anti-Helmholtz condition is satisfied:

$$\boxed{\text{Anti-Helmoholtz condition: } S = \sqrt{3}R \quad .} \tag{C.13}$$

Maximum Gradient

For an identical pair of coils at fixed axial separation S, with identical currents running in the opposite sense, the radius at which the B-field gradient is maximised is found by setting the derivative of gradient with respect to radius equal to zero:

$$\left.\frac{\partial^2 B_z}{\partial z \partial R}\right|_P = \frac{3\mu_0 I N R \left(\frac{S}{2}\right)}{\left(R^2 + \left(\frac{S}{2}\right)^2\right)^{5/2}} \left(2 - \frac{5R^2}{R^2 + \left(\frac{S}{2}\right)^2}\right) = 0 \quad . \tag{C.14}$$

This maximum gradient condition at fixed separation is satisfied when:

$$\boxed{\text{Maximum gradient (fixed separation): } S = \sqrt{6}R \quad .} \tag{C.15}$$

$\delta\frac{\partial B}{\partial z}(\frac{\partial B}{\partial z}{}_{max})$	Helmholtz $(S = R)$ (reversed)	Anti-Helmholtz $(S = \sqrt{3}R)$	Max gradient $(S = \sqrt{6}R)$
	z/S	z/S	z/S
0.1 %	±0.018	±0.244	±0.071
0.5 %	±0.040	±0.365	±0.158
1.0 %	±0.056	±0.435	±0.224
5.0 %	±0.125	±0.655	±0.507
10.0 %	±0.178	±0.784	±0.731

Table C.3: The axial distance over which the B-field gradient produced by a current passing through a pair of identical axially separated coils is uniform to a given percentage of the maximum value. The calculated distance is for currents passing in the opposite sense in coil pairs separated by distances associated with the Helmholtz, anti-Helmholtz, and maximum gradient at fixed separation geometries.

The separation at which the gradient produced by a pair of coils of fixed radius is maximised is found by setting the derivative of gradient with respect to separation equal to zero:

$$\frac{\partial^2 B_z}{\partial z \partial S}\bigg|_P = \frac{-3\mu_0 I N R^2}{2\left(R^2 + \left(\frac{S}{2}\right)^2\right)^{5/2}}\left(1 - \frac{5\left(\frac{S}{2}\right)^2}{R^2 + \left(\frac{S}{2}\right)^2}\right) = 0 \quad . \tag{C.16}$$

This maximum gradient condition at fixed radius is satisfied when:

$$\boxed{\text{Maximum gradient (fixed radius): } S = R} \quad , \tag{C.17}$$

which is identical to the Helmholtz condition. The gradient produced at the centre of the three coil pair configurations is given in table C.4.

C.2 Coil Construction

Different coil winding methods have been employed when winding different magnetic coil types.

Geometry	R/S	$\frac{\partial B_z}{\partial z}\big|_{max}$
Max gradient	$\frac{1}{\sqrt{6}}$	1
Anti-Helmholtz	$\frac{1}{\sqrt{3}}$	$\frac{50}{49}\sqrt{\frac{5}{7}} \simeq 0.86$
Helmholtz (reversed)	1	$\frac{2}{3\sqrt{3}} \simeq 0.38$

Table C.4: Relative size of B-field gradient at the centre equally separated coil pairs with currents passing in the opposite sense for the Helmholtz, anti-Helmholtz, and maximum gradient at fixed separation geometries. The B-field gradients are expressed relative to that generated by a pair of coils configured to produce the maximum gradient at a fixed separation.

Conductor thickness (mm)	Hole diameter (mm)	Conductor cross section (mm^2)	Resistance (mΩ m^{-1})
3.175	2.000	6.939	2.479
4.000	2.750	10.06	1.710

Table C.5: Properties of square cross section copper wire used in magnetic trapping coils. Both types of wire are double wrapped with insulating Kapton film.

C.2.1 Water-cooled Coils

Coils used for magnetic trapping carry currents of a few hundred amps and so must also dissipate large quantities of power in the form of heat. In order to minimise the dissipated power for a given coil current, two different thicknesses of copper wire are used, with conducting cross sections of 6.9 and 10.1 mm^2. Heat is efficiently removed from the coils by continuously pumping cold water through a hole in the centre of the wire. Such wire is cumbersome to work with but can be manipulated using a lathe and a small selection of tools into uniform coils ideal for magnetic trapping applications.
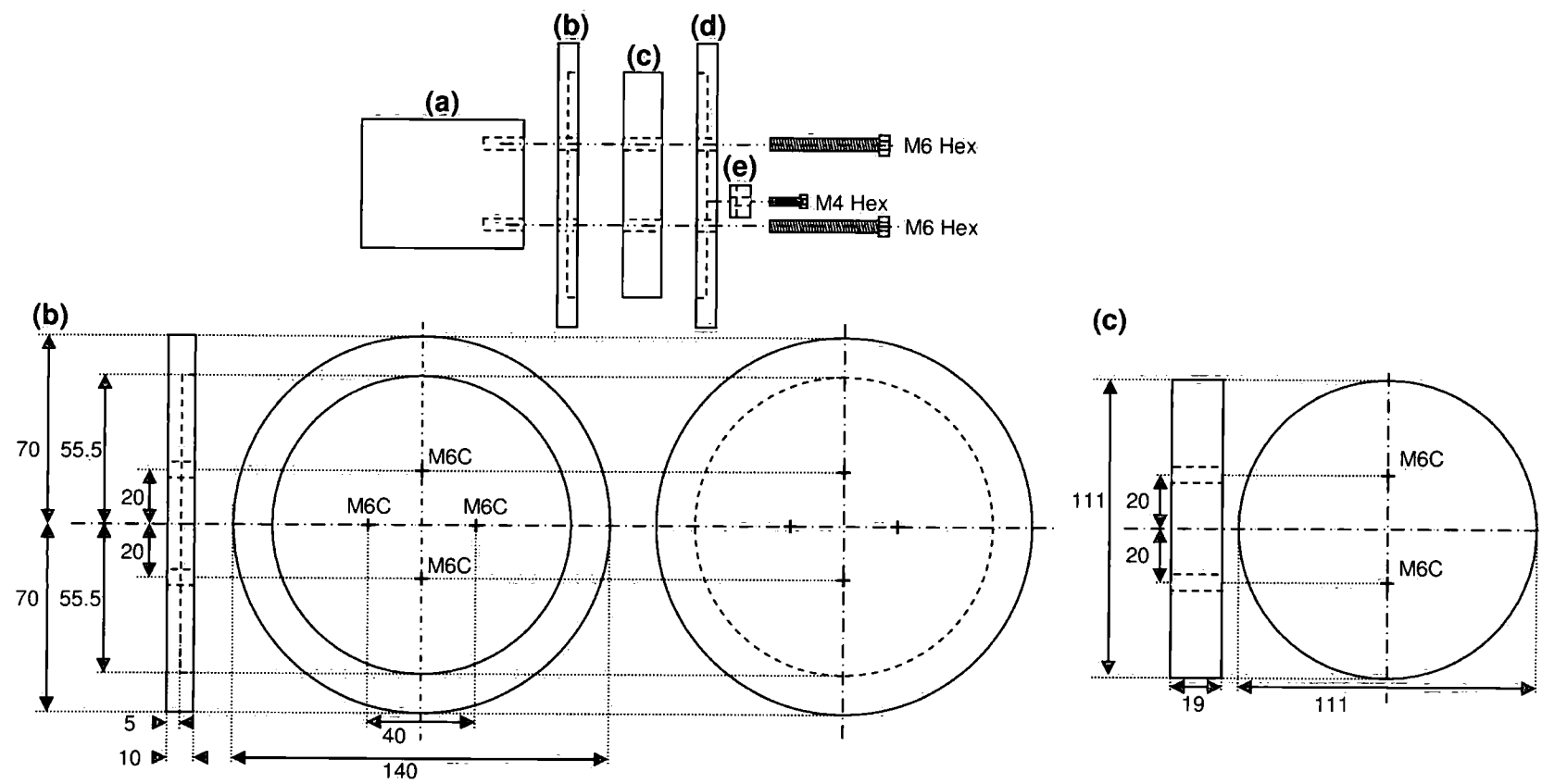
Figure C.1: Vertical bias coil former (i). The coil former is clamped together as shown in the upper schematic, with part (a) clamped into the three jaw chuck of a metal-working lathe. With parts (b) and (e) removed, the first 40 cm of copper wire is loosely wrapped around the former. Part (d) is then fed over the wrapped wire (with the wire passing through the arced slot from the inside face to the outside face). The last section of wrapped wire is bent into position using tool makers clamps such that it is parallel to and flush with the outer face of part (d), whilst the first section of straight wire is bent to be parallel to and flush with the inner face of part(d). The last section of wrapped wire is then clamped onto the outer face of part (d) using clamp (e). The inner faces of parts (b) and (d) and the centre of the radial section of part (c) are greased using silicon grease, and lined with pre-cut Mylar material which is also greased on its outer surfaces. The whole former is then re-assembled in the lathe chuck. At this point the coil is ready to be wound.
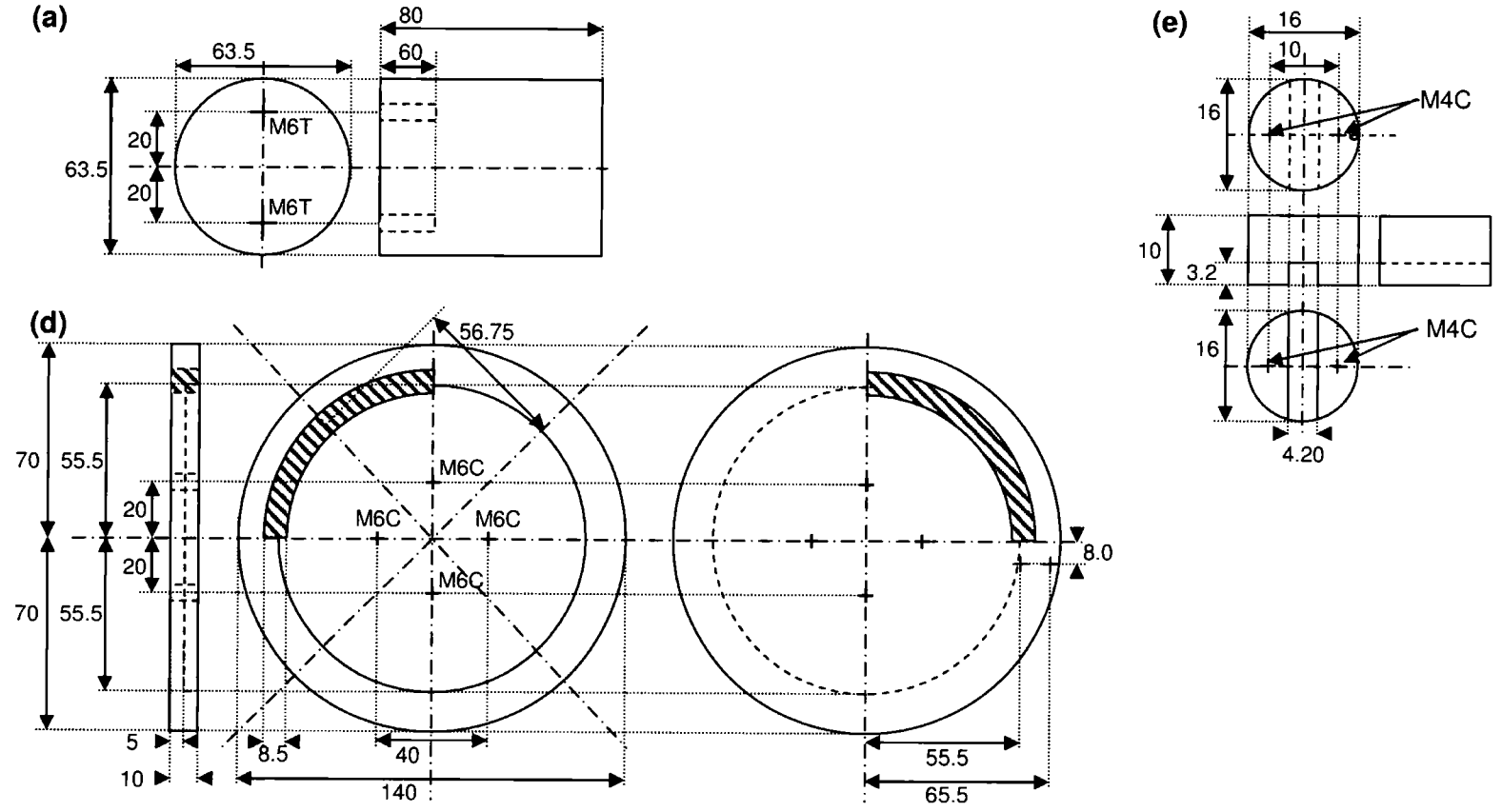
Figure C.2: Vertical bias coil former (*ii*). See caption in figure (C.1).

Principles of Winding

Circular coils are wound with a number of axial turns (loops of equal radial diameter, but axially displaced) and radial turns (loops within the same axial plane which have different radial diameters). A coil pair is described by the number of axial and radial turns of each coil, the inner and outer diameter of the finished coils, and the axial separation of the two coil centres.

Coil Tension

Due to its thickness the wire used for magnetic trapping coils is difficult to bend, whilst the tendency of copper to work-harden makes it very difficult to remove any bends which have been made. Coils used in this work are wound around an aluminium coil-former such as that shown in figures C.1 and C.2. In order to ensure uniform coil construction it is essential to maintain wire tension when winding uniform sections of individual coil turns, and remove tension when changing from one turn to the next (changing axial or radial distance of wire from former centre). The reel of copper wire is mounted on a steel bar supported by two wooden stools to which the bar is clamped $\simeq 1$ m from the lathe bed, with the copper wire fed perpendicular to the lathes rotational axis. In order to maintain tension a G-clamp weighing several kg is hung sequentially from each one of four smaller G-clamps attached uniformly around one face of the copper reel. Hanging G-clamps of different weights varies the wire tension, whilst with no G-clamp the tension is minimised.

Gluing Coils

It is important for coil windings to be firmly held in place, as both the tension in the wound copper and the magnetic forces produced by the coils in-situ will tend to force the turns apart. Due to the complex winding process Araldite 2011 epoxy resin, with a cure time of $\simeq 10$ hours is used to hold coils together. This is applied during the winding process, hence great care must be taken to avoid gluing the wound coils permanently to any component of the coil former. It is for this reason that the coil former is greased and lined as described in figure C.1, and any coil surfaces in contact with the coil former

are not coated with epoxy. The two-part epoxy is applied to wire surfaces in contact with each other from 50 ml disposable cartridges through mixing nozzles using a basic manual cartridge gun and brushed onto the windings to provide a thin, even, tacky surface. This application is carried out after each coil layer is completed when extra epoxy is also injected between adjacent axial turns.

Standard Winding

The standard coil winding described in table C.6 produces a uniform coil with axial thickness greater by one wire width than that of the combined axial turns.

Back-winding

The novel 'back-winding' method proceeds in two separate stages with the same basic technique as used in the 'standard' winding method (table C.6).

- Stage 1: Prior to winding, enough wire to wind the final layer of the coil (turns 7-9 in figure C.3 (d) and (e)) plus $\simeq 60$ cm is loosely wound around the the former, such that this 'excess' has the maximum wind diameter to allow unobstructed rotation of the former in the lathe. Maximising this diameter reduces work-hardening of the copper wire. The unwound copper is then secured in the former as described in figures C.1. It is important to ensure the minimum separation of the coil former side plates (parts (b) and (d) in figure C.1) is $\simeq 1$ mm less than the thickness of $N_{ax} - 1$ turns, where N_{ax} is the required number of axial turns on each radial layer of the finished coil. A coil of $N_{ax} - 1$ axial and N_{rad} radial turns (where N_{rad} is the number of radial layers of the finished coil) is then wound using the 'standard' method (C.6) and left in the lathe overnight for the epoxy to cure.

- Stage 2: The wire between the reel and former is cut $\simeq 60$ cm from the coil former, and loosely wound around the former at the maximum diameter to allow unobstructed former rotation in the lathe. The clamp holding the wire to the former is entirely removed, along with
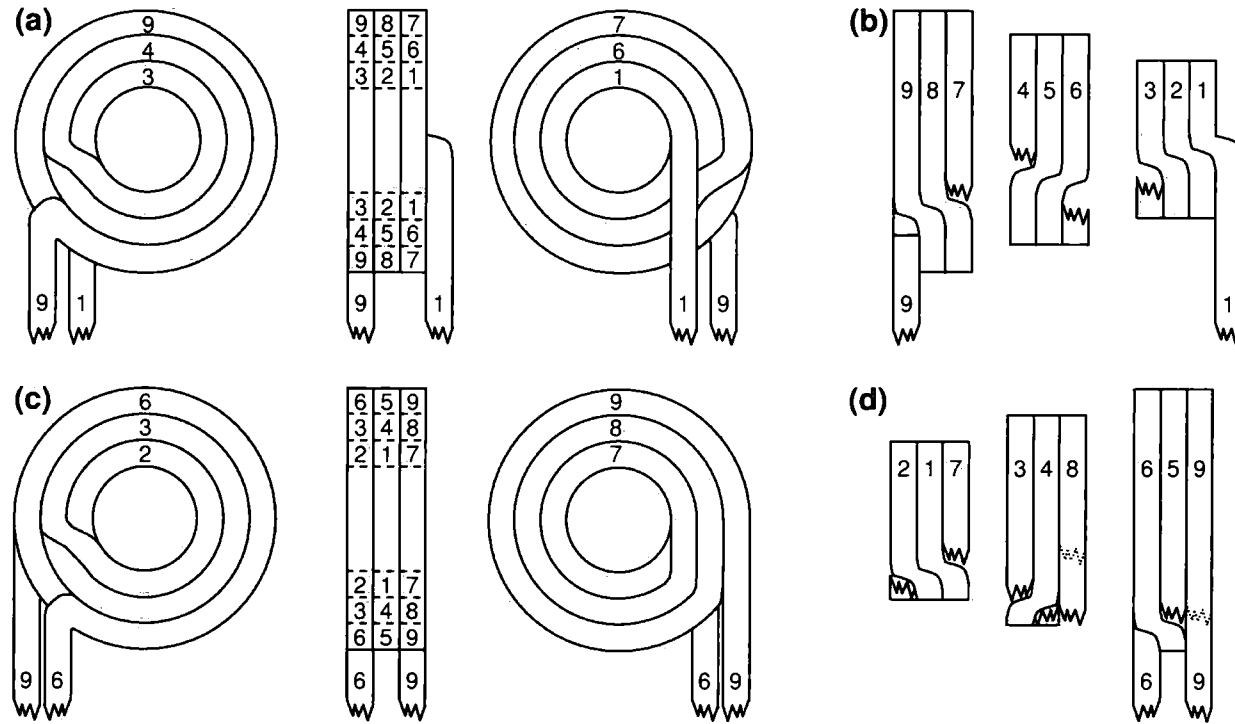
Figure C.3: Winding patterns used for magnetic trapping coils. Two different patterns are used, standard winding(a) and (b), and back-winding (c) and (d). Three projections of the 'standard' winding pattern can be seen in (a), with wire turns numbered in the order they are applied to the coil. Note the wire leading to the first turn projects out of the centre of the coil by one wire thickness. This winding pattern can be completed in a single winding session, as described in table C.6. The composition of each radial layer of the 'standard' winding pattern can be seen in (b). The back winding pattern projections can be seen in (c), with turns numbered in the order in which they are applied to the coil. A full description of the winding process is found in section C.2.1. Note the input and output wires of the back-wound coil both project radially from it, providing a coil axial thickness equal to that of the axial turns alone. This pattern is more complex to implement, and must be wound in two sessions. The composition of each radial layer of the 'back-wound' coil can be seen in (d).

Step	Description
1	Mount copper reel as described in section C.2.1.
2	Mount coil former in lathe chuck and secure copper wire as described in figure C.1.
2	With tension applied to the wire manually rotate lathe chuck clockwise one full turn whilst the copper wire is fed from the reel.
3	Remove tension and use wedge-shaped tool to press the first turn of copper against the inner face of the former to which the wire is clamped at a point $\simeq$ 1 cm before the first revolution is completed.
4	Pull the wire between the former and reel sharply in one continuous movement against the tool through an angle of $\simeq$ 45 °.
5	Raise the end of the most recent turn $\simeq$ 5 mm from the former and place the wedge shaped tool against the opposite face of the wire to that of step 3 and $\simeq$ 1 cm further along the wire path.
6	Pull the wire between the reel and former against the tool sharply in one continuous movement through $\simeq$ 45 ° in the opposite direction to that of step 4, such that this new wire turn is now running parallel to the previous turn.
7	Apply tension to the wire and rotate lathe chuck clockwise one full turn whilst the copper wire is fed from the reel.
8	Repeat steps 3-7 until the first layer of axial turns is complete.
9	Remove tension from the wire and press the tool against the outer radial surface of the final axial turn on the first layer, $\simeq$ 1 cm before this turn meets the previous axial turn.
10	Pull the wire between the reel and former sharply up and away from the former, making a bend through and angle of $\simeq$ 45 °.
11	Raise this bent section of wire from the former and position the wedge shaped tool below the this turn $\simeq$ 1 cm further along the wire path than the position of the bend.
12	Push the wire between the reel and former against the tool such that this new turn is now running radially parallel to the turns of the previous layer.
13	Repeat steps 2-12 until all radial and axial turns are complete.
14	Apply high tension to wire and lock lathe chuck before tightening all former bolts.

Table C.6: Standard coil winding method used for water-cooled magnetic trapping coils.

the rightmost former plate (part (d) in figure C.1). The former is then reassembled in situ with the addition of shim material of one wire thickness between former parts (c) and (d), and with the 'excess' wire now between the coil wound in stage one and former part (d). The final radial coil layer is then wound using the 'standard' method. The final layer is held in place overnight by clamping the remaining 'excess' to the lathe and locking the lathe chuck.

Winding the Baseball Coil

Due to its geometry the baseball coil is wound by hand winding with no mechanical assistance (see figure C.4). Tension is applied to the copper by hand and the wire is bent using toolmakers clamps. The rate at which turns are applied is limited by the curing time of the glue (section C.2.1). Each $\simeq \frac{1}{4}$ of a turn must be left for the curing period prior to winding the next coil section. It is for this reason that winding a nine turn baseball takes approximately one month. Considering this investment of time it is desirable to get the right result first time, hence extreme care should be taken to ensure smooth winding and avoid damage to the wire's Kapton insulation. As with all coil winding, work hardening of the copper wire is to be avoided.

C.2.2 Air-cooled Coils

Some of the coils used in this apparatus are constructed of less cumbersome wire, and require a different winding technique.

Tensioning Coils

Air cooled coils such as solenoids wound with several layers of 0.8 mm diameter enameled copper wire can be wound very efficiently (section C.2.2) if the wire tension is finely controlled. This is achieved by threading the wire reel and compression spring onto one end of a length of M10 studding with a washer and pair of nuts threaded onto the studding at each end of the spring-reel combination. The other end of the studding is clamped onto a stool, which is held firmly in place using weights. The pressure with which
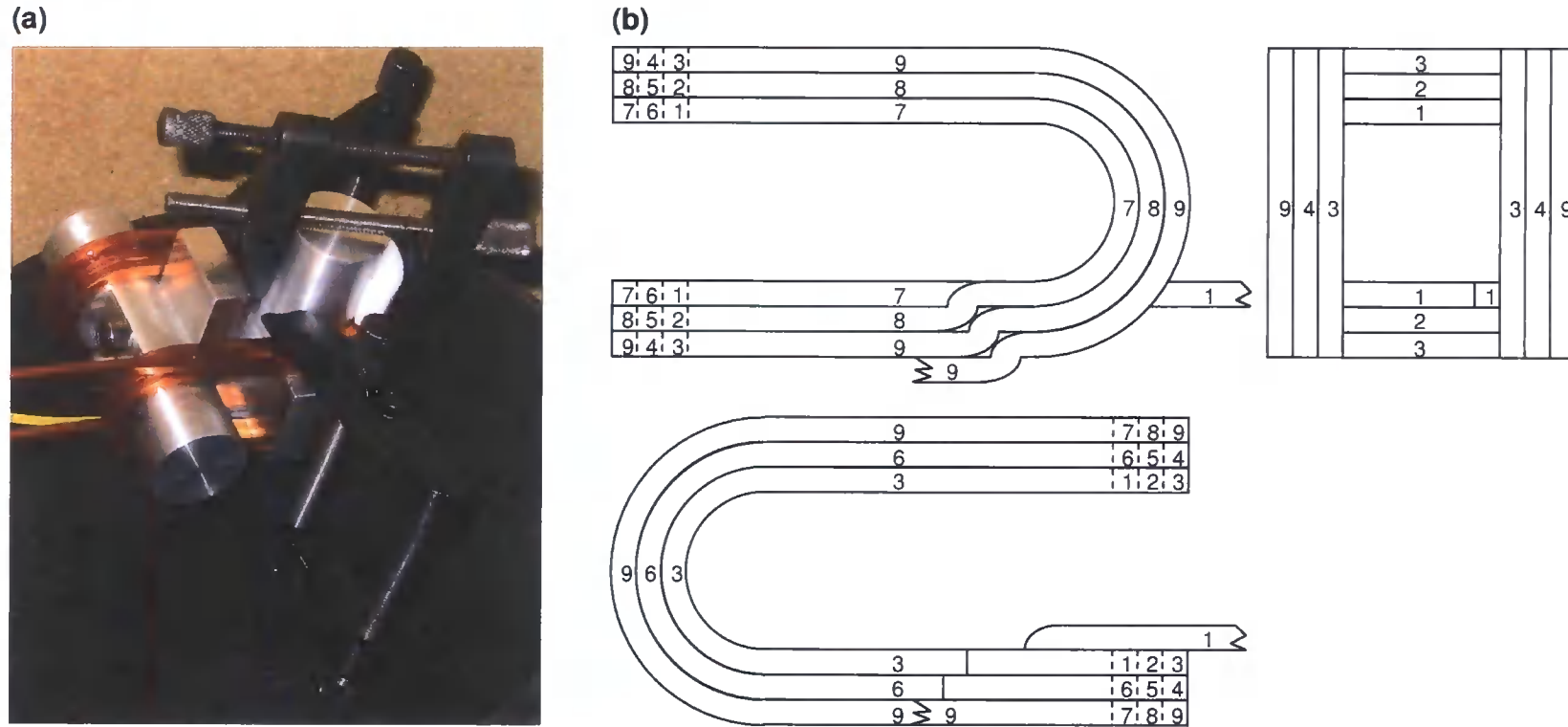
Figure C.4: Winding the baseball coil. The coil is wound in steps of $\simeq \frac{1}{4}$ of a turn, during which the wound wire is glued in place (section C.2.1). Between winding steps the coil is held in position using toolmakers clamps with rubber coated tips to avoid scratching the wire's Kapton insulation. The former around which the coil is wound consists of two aluminium cylinders with diameter equal the inner diameter of the finished baseball radial sections and a series of aluminium plates. The former sections are screwed together such that removing the screws allows the cylinders and plates to be removed from the coil once winding is complete. The winding pattern of the baseball (b) requires the outer turns 4 and 5 to be wound prior to the inner turn 6. This is achieved by using two hollow semi-cylindrical spacers with inner (outer) radial diameters equal to the outer (inner) radial diameter of the former (turn 4 and turn 5 respectively). This can be seen in (a).

the spring is compressed against the reel, and hence the wire tension, can be continuously adjusted by tightening one of the nut pairs against the reel.

DAVLL Solenoid Coils

DAVLL solenoid coils are wound from 0.8 mm diameter enameled copper wire. Brass coil mounts onto which the coils are wound are held firmly in place in a four jaw lathe chuck. The wire is fed onto the cylindrical section of the coil mount and through the slotted insertion hole, before being clamped to the square mount edges using a toolmakers clamp. With the wire reel mounted and tensioned as described in section C.2.1 the coil is wound by manually rotating the lathe chuck and pressing the wound axial turns against one edge of the coil mount. After each axial layer is completed the wire is stepped up onto the wound layer before proceeding to wind across the previous set of windings in the opposite axial direction. Once all axial and radial turns are wound the wire is cut at the reel and fed back through the insertion hole where it is held in place using a cable tie.

C.3 Water-cooling

When the magnetic trap is operating with baseball and bias currents of 200 A and 300 A respectively, the total power generated by these three coils is $\simeq 1.8$ kW. In order to dissipate this amount of power without destroying the coils, cold water is transmitted through a hole in the wire centre (section C.2.1). The rate of water flow is limited by the hole diameter and wire length of each coil, as well as the water pressure drop across the coil, whilst the maximum power dissipation is also dependant on the maximum temperature to which the coil can be safely heated.

C.3.1 Water Flow and Power Dissipation

The energy required to increase 1 litre of water (Mass $m = 1$ kg, specific heat capacity $c_{water} = 4190$ J kg^{-1} K) by a temperature ΔT is:

$$\Delta Q = m c_{water} \Delta T = 4190 \Delta T \quad \text{J} \quad . \tag{C.18}$$

Hence a volumetric flow rate of 1 L s^{-1} of water rising in temperature by ΔT can dissipate a maximum power P of

$$P = 4190\Delta T \quad \textbf{W} \quad . \tag{C.19}$$

The volumetric flow rate of incompressible liquid of viscosity η through a cylindrical pipe of radius R and length L with pressure differential across the pipe of Δp is given by Poiseuille's equation [107]:

$$\frac{\mathrm{d}V}{\mathrm{d}t} = \frac{\pi R^4 \Delta p}{8\eta L} \quad . \tag{C.20}$$

Combining equations C.19 and C.20, the maximum power dissipated by increasing the temperature of water flowing through a cylindrical pipe of radius R and length L with differential pressure Δp between the pipe input and output by temperature ΔT is:

$$P_{\mathrm{max}} = \frac{10^3 c_{\mathrm{water}} \pi R^4 \Delta p \Delta T}{8\eta_{\mathrm{water}} L} \quad . \tag{C.21}$$

Substituting $\eta_{\mathrm{water}} = 1.79 \times 10^{-2}$ Poise $= 1.79 \times 10^{-3}$ N s m^{-2} and $c_{\mathrm{water}} = 4190$ J kg^{-1} K this simplifies to:

$$P_{\mathrm{max}} = 9.192 \times 10^{-4} \left(\frac{\Delta p \Delta T R^4}{L} \right) \quad \textbf{W}. \tag{C.22}$$

For R in mm, L in m and Δp in Pa.

C.3.2 Water Cooling System

Water from a chiller unit enters the laboratory cooling system at a flow rate of $\simeq 30$ L s^{-1} and temperature of $\simeq 15$ °C . Water from the chiller enters the laboratory at $\simeq 70$ PSI (pounds per square inch, 1 PSI $= 6.893 \times 10^3$ Pa), whilst the return to the chiller is also pressurised. This chilled water is distributed through the apparatus through a plumbing manifold, shown in figure C.5. Elements of this manifold are described below.

Barrier Cooler

For magnetic trapping coils, the relatively high volumetric flow of water from the chiller is passed through one chamber of a heat exchanger contained in
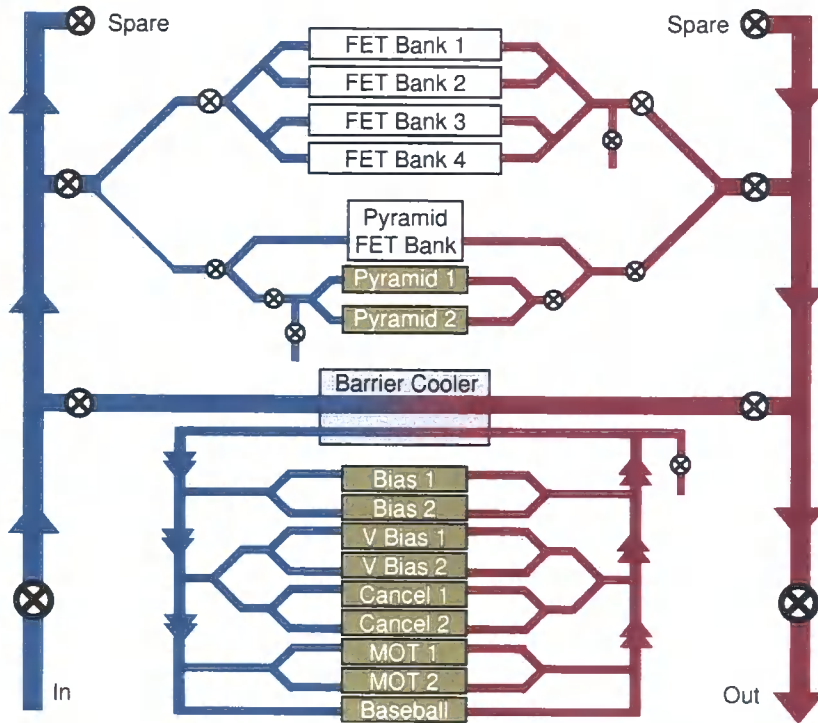
Figure C.5: Plumbing for water cooled coils and FET banks. All magnetic trapping coils and the 2nd MOT coils are supplied with a flow of distilled water via a barrier cooler (section C.3.2). The pyramid MOT coils, pyramid and magnetic trapping FET banks are supplied directly with water from the main laboratory chiller unit.

a barrier cooler. In addition to a heat exchanger, the barrier cooler contains reservoir of distilled water and a pump which transmits the distilled water through a second chamber in the heat exchanger and around a manifold of pipes connected in parallel to all of the magnetic trapping coils in the apparatus. The barrier cooler can maintain a pressure differential between output to the manifold and return to the reservoir of up to $\simeq 55$ PSI. Water from the barrier cooler is output at $\simeq 15$ °C from the heat exchanger. Inputting these pressure and temperature constraints to equation C.22 for the baseball, bias, and vertical bias coils (lengths 3.72 m, 4.78 m and 1.46 m respectively, hole diameters see table C.7) gives maximum power dissipation of 5.1 kW, 14.3 kW and 46.9 kW per coil respectively. This is greater than the maximum required power dissipation of $\simeq 1.8$ kW, and also the rated maximum power dissipation of the barrier cooler (2 kW), hence the barrier cooler is a good

choice for effective cooling of the magnetic trap coils. Without the barrier cooler the maximum coil power dissipations would more than an order of magnitude lower.

Construction and Maintenance

Manifolds of magnetic trapping coils and FET banks are connected to the cooling water supply using push fit pneumatic fittings (of which the Norgren brand is recommended) and 10 mm and 6 mm outer diameter super-flexible pneumatic tubing. Brass nozzles soldered onto the ends of the magnetic trap coils have the appropriate diameters to work in conjunction with these fittings. Connection between manifolds, barrier cooler and chiller is via opaque rubber hose. These connections are secured using 'O-Clips' (also known as two-ear hose clamps), which have proved more secure than jubilee and plastic pipe clips. Any enclosed water system is liable to developing a number of different algae and fungal contaminants, which could easily clog the narrow channels within the coils, and also pose a serious health hazard. A few simple steps can be taken to reduce the chance of this happening:

- Eliminate light completely from system, this includes using only opaque tubing and covering any transparent filter units.

- Ensure chiller unit water is regularly tested for contaminants, and use appropriate decontamination solutions.

- Regularly check any filters and water flow rates.

- Ensure chiller reservoir is isolated from contamination, especially sawdust/paper.

- Check barrier cooler reservoir regularly. Flush out system and renew water if necessary.

- Ensure only to use distilled water in barrier cooler, it is more reactive but less prone to contamination than de-ionised water.

Other recommendations for water cooling are:

- Install a water-flow switch to cut power supply output in the event of a reduction in water flow.

- Install temperature sensors on coils to cut power supply output in case of coil overheating resulting from blockage.

- Use anti-freeze in chiller water to avoid pipe bursts.

- Always wear gloves and goggles when connecting water cooling systems, as contaminants and solvents can be damaging to eyes and skin.

- Do not use any aluminium components in chilled pipe systems as aluminium and distilled water can create contamination (typically black in colour).

C.4 Coil Parameters

The physical parameters of all of the coils used in this work are given in table C.7, whilst the magnetic properties are given in table 3.5.

Coil	Wire thickness (mm)	Hole diameter (mm)	Radius		Straight length		Inner separation (mm)	Radial turns	Axial turns	Total resistance per coil
			Inner (mm)	Outer (mm)	Horizontal (mm)	Vertical (mm)				
Baseball	3.175	2.00	12.5	24.5	43.0	N/A	N/A	3	3.0	9.21 mΩ
Cancellation	4.00	2.75	91.5	96.0	N/A	N/A	55.0	1	3.0	3.01 mΩ
Bias	4.00	2.75	78.0	91.5	N/A	N/A	55.0	3	3.0	8.17 mΩ
Vertical bias	4.00	2.75	53.5	62.5	N/A	N/A	52.0	2	2.0	2.49 mΩ
MOT	3.175	2.00	33.0	47.0	N/A	N/A	54.0	4	4.0	9.97 mΩ
Pyramid MOT	3.175	2.00	51.8	70.6	N/A	N/A	41.3	5	3.2	15.2 mΩ
Grey bias	0.325	N/A	96.0	102.0	N/A	N/A	55.0	6	9.0	2.18 Ω
N-S shims	1.07	N/A	N/A	N/A	209.0	279.0	140.0	5	9.0	210.0 mΩ
E-W shims	1.07	N/A	N/A	N/A	191.2	148.0	290.0	5	9.4	152.0 mΩ
U-D shims	1.07	N/A	112.0	124.0	N/A	N/A	113.6	8	8.5	241.0 mΩ
Pyramid E-W	1.07	N/A	51.8	62.9	N/A	N/A	N/A	10	9.5	164.0 mΩ
Pyramid N-S	1.07	N/A	51.8	62.9	N/A	N/A	N/A	10	9.5	164.0 mΩ
RF 1	1.07	N/A	N/A	N/A	25.0	35.0	N/A	1	1.0	2.30 mΩ
RF 2	1.07	N/A	N/A	N/A	25.0	35.0	N/A	2	1.0	4.60 mΩ
DAVLL solenoid	0.71	N/A	15.0	19.3	N/A		12.0	6	34.5	242.0 mΩ

Table C.7: Dimensions of all coils used in the magnetic trapping apparatus including the number of axial and radial turns (section C.2.1). The pyramid MOT coils are constructed with 2 inner radial layers of 2 axial turns, and 3 outer radial layers of 4 axial turns, hence the non-integer axial turn number. The axial turn number for U-D and E-W 2nd MOT shims is the average number of the axial turns per layer.

^{87}Rb and ^{133}Cs Atomic Data

Name	Symbol	^{87}Rb	^{133}Cs	Units
Atomic mass	m	86.909180520(15)	132.905451931(27)	u
Ground state hyperfine splitting	v_{HFS}	6.83468261090429(9)	9.192631770 (exact)	GHz
Nuclear spin	I	3/2	7/2	GHz
Nuclear g-factor[1]	g_I	-9.951414(10) $\times$ 10^{-4}	-3.9885395(52) $\times$ 10^{-4}	
Fine structure Lande g-factor	g_J	2.0023313(20)	2.00254032(20)	
D2 line transition		$5^2S_{1/2} \rightarrow 5^2P_{3/2}$	$6^2S_{1/2} \rightarrow 6^2P_{3/2}$	
Wavelength (Vacuum)	λ	780.241209686(13)	852.34727582(27)	nm
Natural line width (FWHM)	Γ	$2\pi \cdot 6.065(9)$ MHz	$2\pi \cdot 5.2227(66)$MHz	rad s^{-1}
Saturation intensity	$I_{\mathbf{S}}$	$(m_{\text{F}} = \pm 4$ to $m_{\text{F}}' = \pm 5)$ 1.102(1)	$(m_{\text{F}} = \pm 2$ to $m_{\text{F}}' = \pm 3)$ 1.669(2)	mW cm^{-2}
Doppler temperature	T_{D}	146	125	μK
Recoil temperature	T_r	361.96	198.34	nK

Table C.8: ^{87}Rb and ^{133}Cs atomic structure constants used in this work. Values taken from references [89, 90]

Fine structure Landé g-factors given for ^{87}Rb and ^{133}Cs in the 5^2S$_{1/2}$ and 6^2S$_{1/2}$ states respectively.

Bibliography

[1] S. N. Bose, *Plancks Gesetz und Lichtquantenhypothese*, Z. Phys **26**, 178 (1924).

[2] A. Einstein, *Quantentheorie des Einatomigen Idealen Gases*, Sitzungsber. Kgl. Preuss. Akad. Wiss. , 261 (1924).

[3] M. H. Anderson, J. R. Ensher, M. R. Matthews, C. E. Wieman, and E. A. Cornell, *Observation of Bose-Einstein Condensation in a Dilute Atomic Vapor*, Science. **269**, 198 (1995).

[4] C. C. Bradley, C. A. Sackett, J. T. Tollett, and R. G. Hulet, *Evidence of Bose-Einstein Condensation in an Atomic Gas with Attractive Interactions*, Phys. Rev. Lett. **75**, 1687 (1995).

[5] K. B. Davis *et al.*, *Bose-Einstein Condensation in a Gas of Sodium Atoms*, Phys. Rev. Lett. **75**, 3969 (1995).

[6] S. Chu, *Nobel Lecture: The Manipulation of Neutral Particles*, Rev. Mod. Phys **70**, 685 (1998).

[7] C. Cohen-Tannoudji, *Nobel Lecture: Manipulating Atoms with Photons*, Rev. Mod. Phys **70**, 707 (1998).

[8] W. D. Phillips, *Nobel Lecture: Laser Cooling oand Trapping of Neutral Atoms*, Rev. Mod. Phys **70**, 721 (1998).

[9] K. B. Davis, M. O. Mewes, M. A. Joffe, M. R. Andrews, and W. Ketterle, *Evaporative Cooling of Sodium Atoms*, Phys. Rev. Lett. **74**, 5202 (1995).

[10] W. Ketterle, D. S. Durfee, and D. M. Stamper-Kurn, *Making, Probing and Understanding Bose-Einstein Condensates*, Website, 1999, `http://arxiv.org/abs/cond-mat/9904034v2`.

[11] C. Chin, R. Grimm, P. Julienne, and E. Tiesinga, *Feshbach Resonances in Ultracold Gases*, Website, 2008, `http://www.citebase.org/abstract?id=oai:arXiv:0812.1496v1`.

[12] S. L. Cornish, N. R. Claussen, J. L. Roberts, E. A. Cornell, and C. E. Wieman, *Stable ^{85}Rb Bose-Einstein Condensates with Widely Tunable Interactions*, Phys. Rev. Lett. **85**, 1795 (2000).

[13] T. Weber, J. Herbig, M. Mark, H.-C. Nägerl, and R. Grimm, *Bose-Einstein Condensation of Cesium*, Science **299**, 232 (2003).

[14] J. Denschlag *et al.*, *Generating Solitons by Phase Engineering of a Bose-Einstein Condensate*, Science. **287**, 97 (2000).

[15] S. L. Rolston and W. D. Phillips, *Nonlinear and Quantum Atom Optics*, Nature. **416**, 219 (2002).

[16] M. Mark *et al.*, *Spectroscopy of Ultracold Trapped Cesium Feshbach Molecules*, Phys. Rev. A. **76**, 042514 (2007).

[17] G. Delannoy *et al.*, *Understanding the production of dual Bose-Einstein Condensation with Sympathetic Cooling*, Phys. Rev. A. **63**, 051602(R) (2001).

[18] G. Modugno *et al.*, *Bose-Einstein Condensation of Potassium Atoms by Sympathetic Cooling*, Science. **294**, 1320 (2001).

[19] B. DeMarco and D. S. Jin, *Onset of Fermi Degeneracy in a Trapped Atomic Gas*, Science. **285**, 1703 (1999).

[20] A. G. Truscott, K. E. Strecker, W. I. McAlexander, G. B. Partridge, and R. G. Hulet, *Observation of Fermi Pressure in a Gas of Trapped Atoms*, Science. **291**, 2570 (2001).

[21] S. Jochim *et al.*, *Bose-Einstein Condensation of Molecules*, Science **302**, 2101 (2003).

[22] M. Greiner, C. A. Regal, and D. S. Jin, *Emergence of a Molecular Bose-Einstein Condensate from a Fermi Gas*, Nature **426**, 537 (2003).

[23] S. B. Papp, J. M. Pino, and C. E. Wieman, *Studying a Dual-Species BEC with Tunable Interactions*, Phys. Rev. Lett. **101**, 040402 (2008).

[24] J. M. Hutson and P. Soldán, *Molecule Formation in Ultracold Atomic Gases*, Int. Rev. Phys. Chem. **25**, 497 (2006).

[25] J. Deiglmayr, A. Grochola, M. Repp, and K. M *Formation of Ultracold Polar Molecules in the Rovibrational Ground State.*

[26] K.-K. Ni *et al.*, *A High Phase-Space-Density Gas of Polar Molecules*, Science. **322**, 231 (2008).

[27] K. Winkler *et al.*, *Coherent Optical Transfer of Feshbach Molecules to a Lower Vibrational State*, Phys. Rev. Lett. **98**, 043201 (2007).

[28] J. J. Hudson, B. E. Sauer, M. R. Tarbutt, and E. A. Hinds, *Measurement of the Electron Electric Dipole Moment Using YbF Molecules*, Phys. Rev. Lett. **89**, 023003 (2002).

[29] T. Zelevinsky, S. Kotochigova, and J. Ye, *Precision Test of Mass-Ratio Variations with Lattice-Confined Ultracold Molecules*, Phys. Rev. Lett. **100**, 043201 (2008).

[30] D. DeMille *et al.*, *Enhanced Sensitivity to Variation of m_e/m_p in Molecular Spectra*, Phys. Rev. Lett. **100**, 043202 (2008).

[31] R. V. Krems, *Molecules Near Absolute Zero and External Field Control of Atomic and Molecular Dynamics*, Int. Rev. Phys. Chem. **24**, 99 (2005).

[32] D. DeMille, *Quantum Computation with Trapped Polar Molecules*, Phys. Rev. Lett. **88**, 067901 (2002).

[33] C. J. Pethick and H. Smith, *Bose-Einstein Condensation in Dilute Gases* (Cambridge, 2002).

[34] W. Ketterle, *Nobel Lecture: When Atoms Behave as Waves: Bose-Einstein Condensation and the Atom Laser*, Rev. Mod. Phys **74**, 1131 (2002).

[35] F. Dalfovo, S. Giorgini, L. P. Pitaevskii, and S. Stringari, *Theory of Bose-Einstein Condensation in Trapped Gases*, Rev. Mod. Phys **71**, 463 (1999).

[36] T. Kraemer *et al.*, *Evidence for Efimov Quantum States in an Ultracold Gas of Caesium Atoms*, Nature. **440**, 315 (2006).

[37] M. Mark *et al.*, *Efficient Creation of Molecules from a Bose-Einstein Condensate*, Europhysics Letters **69**, 706 (2005).

[38] C. S. Adams and E. Riis, *Laser Cooling and Trapping of Neutral Atoms*, Prog. Quant. Electron. **21**, 1 (1997).

[39] H. J. Metcalf and P. van der Straten, *Laser Cooling and Trapping* (Springer, 2002), pp. 137–140.

[40] J. Schoser and A. Bat *Intense Source of Cold Rb Atoms From a Pure Two-Dimensional Magneto-Optical Trap.*

[41] J. Arlt, O. Maragò, S. Webster, S. Hopkins, and C. Foot, *A Pyramidal Magneto-Optical Trap as a Source of Slow Atoms*, Opt. Comm. **157**, 303 (1998).

[42] H. J. Lewandowski, D. M. Harber, D. L. Whitaker, and E. A. Cornell, *Simplified System for Creating a Bose-Einstein Condensate*, J. Low. Temp. Phys. **132**, 309 (2003).

[43] M. Greiner, I. Bloch, and T. W. H *Magnetic Transport of Trapped Cold Atoms Over a Large Distance.*

[44] W. Petrich, M. Anderson, J. Ensher, and E. Cornell, *Behaviour of Atoms in a Compressed Magneto-Optical Trap*, J. Opt. Soc. Am. B. **1**, 1332 (1994).

[45] M. T. DePue, S. L. Winoto, D. J. Han, and D. S. Weiss, *Transient Compression of a MOT and High Intensity Fluorescent Imaging of Optically Thick Clouds of Atoms*, Opt. Comm. **180**, 73 (2000).

[46] J. Dalibard and C. Cohen-Tannoudji, *Laser Cooling Below the Doppler Limit by Polarization Gradients: Simple Theoretical Models*, J. Opt. Soc. Am. B **6**, 2023 (1989).

[47] W. H. Wing, *On Neutral Partical Trapping in Quasistatic Electromagnetic Fields*, Prog. Quant. Electron. **8**, 181 (1984).

[48] R. Grimm, M. Weidermüller, and Y. B. Ovchinnikov, *Optical Dipole Traps for Neutral Atoms*, Adv. Atom. Mol. Opt. Phys **42**, 95 (2000).

[49] F. Riboli and M. Modugno, *Topology of the Ground State of Two Interacting Bose-Einstein Condensates*, Phys. Rev. A. **65**, 063614 (2002).

[50] C. J. Myatt, E. A. Burt, R. W. Ghrist, E. A. Cornell, and C. E. Wieman, *Production of Two Overlapping Bose-Einstein Condensates by Sympathetic Cooling*, Phys. Rev. Lett. **78**, 586 (1997).

[51] H. L. Bethlem and G. Meijer, *Production and Application of Translationally Cold Molecules*, Int. Rev. Phys. Chem. **22**, 73 (2003).

[52] J. Doyle, B. Friedrich, R. V. Krems, and F. Masnou-Seeuws, *Editorial: Quo Vadis, Cold Molecules?*, Eur. Phys. J. D **31**, 149 (2004).

[53] H. L. Bethlem *et al.*, *Alternating Gradient Focusing and Deceleration of Polar Molecules*, J. Phys. B. **39**, R263 (2006).

[54] K. M. Jones, E. Tiesinga, P. D. Lett, and P. S. Julienne, *Ultracold Photoassociation Spectroscopy: Long-Range Molecules and Atomic Scattering*, Rev. Mod. Phys **78**, 483 (2006).

[55] J. M. Sage, S. Sainis, T. Bergeman, and D. DeMille, *Optical Production of Ultracold Polar Molecules*, Phys. Rev. Lett. **94**, 203001 (2005).

[56] W. Salzmann, U. Poschinger, R. Wester, and M. Weidemüller, *Coherent Control with Shaped Femtosecond Laser Pulses Applied to Ultracold Molecules*, Phys. Rev. A. **73**, 023414 (2006).

[57] M. W. Zwierlein, J. R. Abo-Shaeer, A. Schirotzek, C. H. Schunck, and W. Ketterle, *Vortices and Superfluidity in a Strongly Interacting Fermi Gas*, Nature. **435**, 1047 (2005).

[58] K. Bergmann, H. Theuer, and B. W. Shore, *Coherent Population Transfer Among Quantum States of Atoms and Molecules*, Rev. Mod. Phys **70**, 1003 (1998).

[59] F. Lang, K. Winkler, C. Strauss, R. Grimm, and J. H. Denschlag, *Ultracold Triplet Molecules in the Rovibrational Ground State*, Phys. Rev. Lett. **101**, 133005 (2008).

[60] W. C. Stwalley, *Efficient Conversion of Ultracold Feshbach-Resonance-Related Polar Molecules into Ultracold Ground State (X $^1\Sigma^+$ v=0, J=0) Molecules*, Eur. Phys. J. D. **31**, 221 (2004).

[61] A. R. Allouche *et al.*, *Theoretical Electronic Structure of RbCs Revisited*, J. Phys. B. **33**, 2307 (2000).

[62] P. Julienne and co-workers at NIST Gaithersburg, Private communication.

[63] D. J. McCarron, I. G. Hughes, P. Tierney, and S. L. Cornish, *A Heated Vapor Cell Unit for Dichroic Atomic Vapor Laser Lock in Atomic Rubidium*, Rev. Sci. Inst. **78**, 093106 (2007).

[64] A. Millett-Sikking, I. G. Hughes, P. Tierney, and S. L. Cornish, *DAVLL Lineshapes in Atomic Rubidium*, J. Phys. B. **40**, 187 (2006).

[65] M. L. Harris, P. Tierney, and S. L. Cornish, *Magnetic Trapping of a Cold Rb-Cs Atomic Mixture*, J. Phys. B. **41**, 035303 (2008).

[66] T. W. Hänsch and A. L. Schawlow, *Cooling of Gases by Laser Radiation*, Opt. Comm. **13**, 68 (1975).

[67] D. J. Wineland and W. M. Itano, *Laser Cooling of Atoms*, Phys. Rev. A. **20**, 1521 (1979).

[68] H. J. Metcalf and P. van der Straten, *Laser Cooling and Trapping* (Springer, 1999).

[69] D. Sesko, T. Walker, C. Monroe, A. Gallagher, and C. Wieman, *Collisional Losses from a Light-Force Atom Trap*, Phys. Rev. Lett. **63**, 961 (1989).

[70] W. Ketterle, K. B. Davis, M. A. Joffe, A. Martin, and D. E. Pritchard, *High Densities of Cold Atoms in a* Dark *Spontaneous-Force Optical Trap*, Phys. Rev. Lett. **70**, 2253 (1993).

[71] R. Loudon, *The Quantum Theory of Light, 3rd Edition.* (Oxford University Press, 2004), pp. 65–68.

[72] G. K. Woodgate, *Elementary Atomic Structure.* (Oxford University Press, 2002), pp. 186–194.

[73] J. Dalibard, *Collisional Dynamics of Ultra-Cold Atomic Gases*, Bose-Einstein Condensation in Atomic Gases , 321 (1999).

[74] C. Buggle, J. Léonard, W. von Klitzing, and J. T. M. Walraven, *Interferometric Determination of the s- and d-wave scattering amplitudes in ^{87}Rb*, Phys. Rev. Lett. **93**, 173202 (2004).

[75] M. Anderlini *et al.*, *Sympathetic Cooling and Collisional Properties of a Rb-Cs Mixture*, Phys. Rev. A. **71**, 061401 (2005).

[76] J. Goldwin *et al.*, *Measurement of the Interaction Strength in a Bose-Fermi Mixture with ^{87}Rb and ^{40}K*, Phys. Rev. A. **70**, 021601 (2004).

[77] S. Kotochigova, E. Tiesinga, and P. S. Julienne, *Relativistic ab initio Treatment of The Second-Order Spin-Orbit Splitting of the $a^3\Sigma_u^+$ Potential of Rubidium and Cesium Dimers*, Phys. Rev. A. **63**, 012517 (2000).

[78] G. Thalhammer *et al.*, *Long-Lived Feshbach Molecules in a Three-Dimensional Optical Lattice*, Phys. Rev. Lett. **96**, 050402 (2006).

[79] M. Theis *et al.*, *Tuning the Scattering Length with an Optically Induced Feshbach Resonance*, Phys. Rev. Lett. **93**, 123001 (2004).

[80] C. E. Wieman and L. Hollberg, *Using Diode Lasers for Atomic Physics*, Rev. Sci. Instrum. **62**, 1 (1991).

[81] L. Ricci *et al.*, *A Compact Grating-Stabilized Diode Laser System for Atomic Physics*, Opt. Comm **117**, 541 (1995).

[82] A. S. Arnold, J. S. Wilson, and M. G. Boshier, *A Simple Extended-Cavity Diode Laser*, Rev. Sci. Inst. **69**, 1236 (1998).

[83] K. J. Weatherill, *A CO_2 Laser Lattice Experiment for Cold Atoms*, PhD thesis, Durham University, 2007.

[84] B. Cherón, H. Gilles, J. Hamel, O. Moreau, and H. Sorel, *Laser Frequency Stabilization using Zeeman Effect*, J. Physique III **4**, 401 (1994).

[85] K. L. Corwin, Z.-T. Lu, C. F. Hand, R. J. Epstein, and C. E. Wieman, *Frequency-Stabilized Diode Laser with the Zeeman Shift in an Atomic Vapor*, Appl. Opt. **37**, 3295 (1998).

[86] G. D. Rovera, G. Santarelli, and A. Clarion, *Laser Diode System Stabilized on the Caesium D_2 Line*, Rev. Sci. Instrum. **65**, 1502 (1994).

[87] G. C. Bjorklund, *Frequency-Modulation Spectroscopy: a New Method for Measureing Weak Absorptions and Dispersions*, Opt. Lett. **5**, 15 (1980).

[88] D. J. McCarron, S. A. King, and S. L. Cornish, *Modulation Transfer Spectroscopy in Atomic Rubidium*, Meas. Sci. Technol. **19**, 1 (2008).

[89] D. Steck, *Rubidium 87 D line data*, Website, 2003, http://george.ph.utexas.edu/~dsteck/alkalidata/rubidium87numbers.1.6.pdf.

[90] D. Steck, *Cesium D Line Data*, Website, 2003, http://george.ph.utexas.edu/~dsteck/alkalidata/cesiumnumbers.1.6.pdf.

[91] P. F. Griffin, *Laser Cooling and Loading of Rb into A Large Period, Quasi-Electrostatic, Optical Lattice*, PhD thesis, Durham University, 2005.

[92] N. Lunblad *et al.*, *Two Species Cold Atomic Beam*, J. Opt. Soc. Am. B. **21**, 3 (2003).

[93] A. M. Thomas, *Ultra-cold Collisions and Evaporative Cooling of Caesium in a Magnetic Trap*, PhD thesis, University of Oxford, 2004.

[94] M. L. Harris, *Realisation of a Cold Mixture of Rubidium and Caesium*, PhD thesis, Durham University, 2008.

[95] J. Weiner, *Cold and Ultracold Collisions in Quantum Microscopic and Mesoscopic Systems.* (Cambridge University Press, 2003), pp. 58–87.

[96] P. Lett *et al.*, *Hyperfine Structure Modifications of Collisional Losses from Light-Force Atom Traps*, J. Phys. B. **28**, 65 (1995).

[97] M. W. Mancini, A. R. L. Caires, G. D. Telles, V. S. Bagnato, and L. G. Marcassa, *Trap Loss Rate for Heteronuclear Cold Collisions in Two Species Magneto-Optical Trap*, Eur. Phys. J. D. **30**, 105 (2004).

[98] A. J. Kerman, J. M. Sage, S. Sainis, T. Bergeman, and D. DeMille, *Production of Ultracold, Polar RbCs* Molecules via Photoassociation*, Phys. Rev. Lett. **92**, 033004 (2004).

[99] M. S. Santos *et al.*, *Simultaneous Trapping of Two Different Atomic Species in a Vapor-Cell Magneto-Optical Trap*, Phys. Rev. A. **52**, R4340 (1995).

[100] K. Pilch *et al.*, *Observation of Interspecies Feshbach Resonances in an Ultracold Rb-Cs Mixture*, Website, 2008, http://www.citebase.org/abstract?id=oai:arXiv.org:0812.3287.

[101] C. Chin, *Cooling, Collisions and Coherence of Cold Cesium Atoms in a Trap*, PhD thesis, Stanford University, 2001.

[102] C. R. Monroe, E. A. Cornell, C. A. Sackett, C. J. Myatt, and C. E. Wieman, *Measurement of Cs-Cs Elastic Scattering at $T = 30$ μK*, Phys. Rev. Lett. **70**, 414 (1993).

[103] C.-L. Hung, X. Zhang, N. Gemelke, and C. Chin, *Fast, Runaway Evaporative Cooling to Bose-Einstein Condensation in Optical Traps*, Phys. Rev. A. **78**, 011604 (2008).

[104] Crystal Technology, Inc, *Acousto-Optic application note modulator model 3000 series*, Website, 2006, http://www.crystaltechnology.com/docs/AO_Modulator3000_appnote.pdf.

[105] E. Hecht, *Optics, 4th Edition.* (Addison Wesley, 2002), pp. 366–368.

[106] C. G. Townsend, N. H. Edwards, C. J. Cooper, K. P. Zetie,, and C. J. Foot, *Phase-Space Density in the Magneto-Optical Trap*, Phys. Rev. A. **52**, 1423 (1995).

[107] H. D. Young, R. A. Freedman, T. R. Sandin, and A. L. Ford, *University Physics.* (Addison-Wesley, 2000), pp. 446–448.

Nomenclature

List of Abbreviations

ϕ Diameter

AMD   Alkali metal dispensers

AOM   Acousto-optic modulators

AR   Anti-reflection

BCS   Bardeen-Cooper-Schrieffer

BEC   Bose-Einstein condensation

CCD   Charge-coupled device

CMOT   Compressed magneto-optical trap

DAQ   Data acquisition

DAVLL   Dichroic atomic vapour laser lock.

EOM   Electro-optical modulator.

FET   Field-effect transistor

FWHM   Full width of peak at half maximum height

GPE   Gross-Pitaevskii equation

GPIB   General purpose interface bus

HR   High-reflection

ID   Inner diameter

Laser   Light amplification by stimulated emission of radiation

MOT   Magneto-optical trap

OD   Optical depth

OP   Optical pumping

PBS   Polarising beam-splitting cube

Piezo   Piezoelectric actuator

PSD   Phase-space density

PSI   Pounds per square inch

RF   Radio frequency

STIRAP Stimulated Raman adiabatic passage

List of Constants

η_{water}	Viscosity of water at 20 °C	1.79×10^{-2} **Poise**
μ_0	Magnetic permeability of free space	$4\pi \times 10^{-7}$ **N A^{-2}**
μ_{B}	Bohr magneton	$9.27400915(23) \times 10^{-24}$ **J T^{-1}**
ρ_{copper}	Resistivity of copper	$1.72(1) \times 10^{-8}$ **Ω m**
a_0	Bohr radius	$5.2917720859(36) \times 10^{-11}$ **m**
c	Speed of light in vacuum	2.99792458×10^{8} **m s^{-1}**
c_{water}	Resistivity of water	4.19×10^{3} **J kg^{-1}**
g	Acceleration due to gravity	9.80665(adopted value) **m s^{-1}**
h	Planck's constant	$6.62606896(33) \times 10^{-34}$ **J s**

List of Conversion Factors

$\hbar$	$= h/2\pi =$	$1.054571628(53) \times 10^{-34}$	**J s**
$0\,°C$	$=$	273.15	**°K**
1 G	$=$	1×10^{-4}	**Tesla**
1 Poise	$=$	1×10^{-1}	**N s m^{-2}**
1 PSI	$=$	6.893×10^{3}	**Pa**

List of Variables

α	Evaporation efficiency (Density)	
β	Magnetic field gradient	**G cm^{-1}**
β_i	MOT loss rate coefficient	**cm^3 s^{-1}**
Δ	Interaction parameter	
δ	Laser detuning	**Hz**
ϵ_i	Energy	**J**
Γ	Natural linewidth (FWHM)	**rad s^{-1}**
γ	Evaporation efficiency (PSD)	
γ	Magnetic field curvature	**G cm^{-2}**
γ	Residual gas collision rate	**Hz**
Γ_{scatt}	Photon scattering rate	**s^{-1}**
λ	Wavelength	**nm**
λ_{dB}	de Broglie wavelength	**m**
$\mathcal{E}_0$	Electric field	**N C^{-1}**
d	Transition dipole moment	**C m**
$\mathcal{R}$	Responsivity	**A W^{-1}**
μ	Chemical potential	**J**
μ	Magnetic moment	**J T-1**
Ω	Rabi frequency	**rad s^{-1}**
ω_{r}	Radial trap frequency	**rad s^{-1}**
ψ	Wave function	
τ_{th}	Thermalisation time	**s**

r	Vector position	
a	Scattering length	**m**
B	Magnetic field	**G**
B_w	Probed magnetic field width	**G**
F	Force	**N**
F	Fractional number density overlap	
F	Total atom angular momentum quantum number	
f	frequency	**Hz**
g	Mean field energy	**J m^3**
I	Current	**A**
I	Intensity	**mW cm^{-2}**
k	Wavenumber	**cm^{-1}**
K_2	Two body inelastic collision rate constant	**cm^3 s^{-1}**
K_3	Three body inelastic collision rate constant	**cm^6 s^{-1}**
L	Length	**m**
L	MOT loading rate	**s^{-1}**
M	Magnification	
m	Atomic mass	**kg**
m_F	Total atom magnetic quantum number	
N	Number of atoms	
n	Number density	**cm^{-3}**
P	Power	**W**
P	Probability	

p	Momentum	kg m s^{-1}
p	Pressure	N m^{-2}
Q	Energy	J
R	Radius	m
r	Radial distance	m
T	Temperature	$^\circ\text{K}$
t	Time	s
V	Voltage	V
w	$1/e^2$ radius	mm
z	Axial distance	m
OD	Optical depth	
PSD	Phase space density	

List of Products

440 A power supply 6690A	Agilent Technologies, Inc
580 A power supply 6681A	Agilent Technologies, Inc
Analogue interface PCI-6713	National Instruments Corp.
AOM Model 3110-120	Crystal Technology, Inc
Araldite 2011 50 ml cartridge	Onecall
CCD Camera Andor iXon 885	Andor Technology PLC
Dichroic mirror	Laseroptik GmbH
Digital interface PCI-DIO-32-HS	National Instruments Corp.
GPIB interface PCI-GPIB	National Instruments Corp.
Hall-effect sensor SCNL181	Honeywell Int.
Kapton adhesive tape	RS Components Ltd
Laser current driver EW1206 (-ve)	Central Electronics, Oxford
Laser current driver EW1291 (+ve)	Central Electronics, Oxford
Magnetic trap feedback EW1282	Central Electronics, Oxford
Magnetic trap reference EW1285	Central Electronics, Oxford
MOSFET STE180NE10	Onecall
O-Clips	Springmasters Limited
Photodiode BPX65	Onecall
Photodiode circuit EW1287	Central Electronics, Oxford
Photodiode DET36A	Thorlabs Ltd. UK
Piezo driver EW1145	Central Electronics, Oxford
RF signal generator E4400B	Agilent Technologies, Inc

Temperature controller MPT 2500	Wavelength Electronics
Toolmakers clamps	Onecall
Vacuum feedthrough ZEFT34A	VG Scientia Holdings AB
Voltage Level Multiplexer	Central Electronics, Oxford
Voltage Switching Unit EW1288	Central Electronics, Oxford

List of Suppliers

Agilent Technologies, Inc	`http://www.agilent.com/`
Andor Technology PLC	`http://www.andor.com/`
Central Electronics, Oxford	`http://www.physics.ox.ac.uk/electronics/`
Crystal Technology, Inc	`http://www.crystaltechnology.com`
Honeywell International Inc	`http://www.honeywell.com/`
Laseroptik GmbH	`http://www.laseroptik.de`
National Instruments Corporation	`http://www.ni.com/`
Onecall	`http://onecall.farnell.com`
Optiglass Ltd.	`http://www.optiglass.com/`
RS Components Ltd	`http://uk.rs-online.com/web/`
Springmasters Limited	`http://www.springmasters.com/`
Thorlabs Ltd. UK	`http://www.thorlabs.com/`
VG Scientia Holdings AB	`http://www.vgscienta.com`
Wavelength Electronics, Inc	`http://www.teamwavelength.com/`

Index